EVALUATION OF REACTIVITY FEEDBACKS DUE TO CORE DEFORMATION IN FAST REACTORS

by

Tian Jing

A Dissertation

Submitted to the Faculty of Purdue University
In Partial Fulfillment of the Requirements for the degree of

Doctor of Philosophy

School of Nuclear Engineering
West Lafayette, Indiana
May 2018

THE PURDUE UNIVERSITY GRADUATE SCHOOL
STATEMENT OF COMMITTEE APPROVAL

Dr. Won Sik Yang, Chair
School of Nuclear Engineering, Purdue University
Dr. Chan Choi
School of Nuclear Engineering, Purdue University
Dr. Hany S. Abdel-Khalik
School of Nuclear Engineering, Purdue University
Dr. Xiangxiong Zhang
Department of Mathematics, Purdue University
Dr. Taek K. Kim
Department of Nuclear Systems Analysis, Argonne National Laboratory

Approved by:
Dr. Seungjin Kim
Head of the Graduate Program

To my family

TABLE OF CONTENTS

LIST OF TABLES

LIST OF FIGURES

ABSTRACT

Author: Jing, Tian. PhD
Institution: Purdue University
Degree Received: May 2018
Title: Evaluation of Reactivity Feedbacks Due to Core Deformation in Fast Reactors.
Major Professor: Won Sik Yang

In order to meet the worldwide demands on sustainable energy, new generation of nuclear reactor systems has been proposed to continue the benefit of nuclear power for electricity production. Sodium-cooled fast reactor (SFR) is one of the most promising candidate among those reactor concepts for both energy production and minimizing radioactive nuclear waste and features inherent safety potential. To ensure inherent safety characteristics of SFR, accurate evaluation of reactivity feedbacks is essential. However, accurate evaluation of the negative reactivity induced by the core radial expansion and assembly bowing remains challenging. SFR has a relatively large coolant temperature rise, and thus the resulting temperature gradients lead to differential thermal expansion of the assembly duct walls that, along with the irradiation creep and swelling, result in the bowing of assembly. The deformation of assembly induces feedback reactivity that, with careful design of the core constraint system, is often a significant portion of negative feedback reactivity to guarantee inherent safety. However, during the operation of the SFR, a large number of assemblies are distorted in a complex manner, making the prediction of the bowing reactivity a very difficult task. The large uncertainty in predicting the negative assembly bowing reactivity limits the range of design space and inhibits the incorporation of the innovative features in advanced SFR design.

The objective of this doctoral work is to develop a perturbation theory method for accurate and efficient evaluation of the feedback reactivity induced by SFR core deformation. The pre-calculated assembly bowing reactivity coefficient could be adopted by the safety analysis tools for more realistic modeling of the SFR dynamic behavior during anticipated transient without scram (ATWS) events. The improved simulation accuracies will contribute to reducing the economic penalties due to the conservative design margins to accommodate the prediction uncertainties.

The major challenge in using perturbation theory method to calculate the assembly bowing reactivity worth is the evaluation of the bi-linearly weighted reaction rate integral for a perturbed geometry. Direct adoption of the conventional perturbation theory method based on the material property changes in the original mesh grid requires material homogenization in the meshes where discontinuous material boundaries are included due to assembly displacement. Especially for applications with realistic heterogeneous assembly model, the boundaries for discontinuous materials such as fuel, cladding, coolant, duct, etc. would intersect with millions of meshes, making numerical evaluations of the reaction integrals within such meshes extremely difficult. In this dissertation, we bypass this obstacle by formulating the first-order perturbation theory under the ‘Lagrangian frame of reference’, noticing that, in this case, the material is not changed in property but only displaced. The equivalence of such formula is shown to the conventional first-order perturbation theory formula by applying a coordinate transformation to map the original mesh in ‘Eulerian coordinates’ to ‘Lagrangian coordinates’. The new formula provides unique convenience for modeling heterogeneous assembly displacements. The perturbation theory formulation is based on neutron transport approximation, which is more adequate than diffusion approximation for analyzing fast reactor where the anisotropic scattering effect is large.

The key practice of the proposed perturbation theory method is to convert the problem of calculating material property perturbation to the problem of evaluating the difference of the fluxes to which materials are exposed at original and perturbed locations. To determine the flux distributions, we employed the variational nodal transport code VARIANT and the unstructured geometry transport code PROTEUS-SN. Continuous forward and adjoint flux distributions in the core are determined from VARIANT calculations with a core model of homogenized assemblies. The heterogeneous assembly fluxes at both original and shifted positions are then reconstructed by combining the VARIANT solution with the finite element-based form functions of scalar flux obtained from PROTEUS-SN single assembly calculations. The discontinuous material distribution in an assembly is also represented based on the same finite element meshes adopted in the PROTEUS-SN code. Numerical tests showed that these reconstructed fluxes agree well with the full core heterogeneous solution of the PROTEUS-SN code.

We developed a computer code named RAINBOW (ReActivity INduced by assembly BOWing) applying the proposed perturbation theory method. RAINBOW reads forward and adjoint fluxes from VARIANT and PROTEUS-SN solutions and reconstructs the heterogeneous flux distributions, with which it computes assembly segment displacement worth coefficients in six directions normal to the hexagonal assembly duct walls. RAINBOW also has a capability to calculate the reactivity worth of fuel axial expansion. The fuel axial expansion module applies the material density perturbation to each axially expanded assembly segment.

The verification of the RAINBOW code was performed by comparing the perturbation results with the direct subtractions between eigenvalues of both unperturbed and perturbed cases. The reference eigenvalues were calculated by both MCNP6 Monte Carlo simulation and PROTEUS-SN deterministic calculation, both of which can model distorted heterogeneous assembly configurations. The verification tests are performed based on two-dimensional (2D) and three-dimensional (3D) mini-core problems that are derived from Advanced Burner Test Reactor (ABTR). Statistical analysis indicated that the RAINBOW results are statistically consistent with the MCNP6 results. The perturbation calculation results also agree well with the PROTEUS-SN results.

In summary, this doctoral work developed a transport theory-based perturbation theory method resolving the long-standing challenge of effectively assessing feedback reactivity effect due to core geometry change. The practice of the proposed perturbation method achieves the same level of accuracy for three-dimensional heterogeneous core with several orders of magnitude smaller computational time compared to the direct subtraction of eigenvalues obtained from whole-core transport simulations with MCNP or PROTEUS-SN.

1. INTRODUCTION

This introductory chapter discussing the background, motivation, and the objective of the presented thesis is structured as follows. Section 1.1 provides a general introduction to the sodium-cooled fast reactor (SFR). Section 1.2 discusses the physical implications in the viewpoint of SFR safety. The reactivity feedback phenomena due to material property change and core geometry change are presented in Section 1.3 and Section 1.4, respectively. Finally, Section 1.5 provides the motivation and objective.

1.1 Sodium-Cooled Fast Reactor

Nuclear power has been playing an important role in electricity production since 1960s. Currently, there are 449 commercial nuclear power plants in operation with a total net installed capacity of 392 GWe (11% of the world capacity) [1]. The use of nuclear power results in a significant reduction in the environmental impact of the electricity generation. The majority of the operating nuclear power plants features thermal spectra and one-through fuel cycle. As they retired, new nuclear system will be needed to continue the benefit of nuclear power and to meet the increasing demand on the sustainable energy. The new generation nuclear power system is expected to be far more advantageous compared to the current light water reactor (Generation-II/III reactor system) in terms of sustainability, safety, economics, physical protection and nonproliferation considerations. The Generation-IV International Forum (GIF) members identified six types of Generation-IV reactor systems: very high temperature reactor (VHTR), gas-cooled fast reactor (GFR), sodium-cooled fast reactor (SFR), lead-cooled fast reactor (LFR), molten salt reactor (MSR) and super-critical water-cooled reactor (SCWR). [2]

As shown in Table 1.1, over half of the six Generation-IV systems (GFR, SFR and LFR) feature a fast-neutron spectrum and closed fuel cycle for effective utilization of uranium resource and management of hazardous nuclear waste. The neutronics characteristics provide the fast-neutron reactor system with a higher degree of sustainability than the operating advanced light water reactors (ALWRs) that utilize only a tiny fraction (< 1%) of natural uranium in the fuel for energy production while generate and accumulate significant amount of long-lived nuclear waste. Specifically, higher fission-to-capture ratio together with greater number of neutrons released per fission in the fast neutron region produced more excess neutron that can be utilized to convert fertile U-238 to fissile Pu-239. By recycling the discharged fuel, almost all fissionable isotopes in the fuel can be utilized for energy production in fast reactor excluding a small reprocessing loss. On the other hand, fast reactor can also be designed for the mission of destroying transuranics (TRU) because of the high fission-to-capture ratio. Considering the exceptional capability of effective breeding fissile materials and burning hazardous nuclear waste, the development of fast reactor systems was assigned a high priority by the GIF.

Table 1.1 Overview of Six Types of Generation-IV Nuclear Reactor Systems [2]

Generation-IV reactor type	Neutron spectrum	Coolant material	Fuel cycle
VHTR	Thermal	Helium	Open
GFR	Fast	Helium	Closed
SFR	Fast	Sodium	Closed
LFR	Fast	Lead	Closed
MSR	Fast/Thermal	Fluoride salts	Closed
SCWR	Thermal/Fast	Water	Open/Closed

Among the three Generation-IV fast reactor systems, SFRs (as shown in Figure 1.1) are the most mature technology. [3] In the early development of nuclear power, the fast reactor systems that could make the best use of available uranium resource was proceeded in higher priority, since large part of uranium deposits had not been discovered and it was believed, at that time, that the uranium reserves were limited. The very high energy density in fast reactor requires an efficient manner for heat transfer. Liquid sodium was selected as coolant because of its low melting point (98 °C), low capture cross-section and good compatibility with structural materials. Since 1950s, over 20 experimental and prototype SFRs have been constructed and operated world-widely, which achieved around 400 reactor-years of accumulated operation experience until 2010. In recent years, there is a renewed interest in SFRs. China, Russia and India have constructed CEFR, BN-800 and PFBR, respectively. Significant design efforts have been designated in BN-1200 in Russia, ASTRID in France and PGSFR in South Korea. Widespread interests in SFRs have resulted in its dominant occupation in the international fast reactor community.

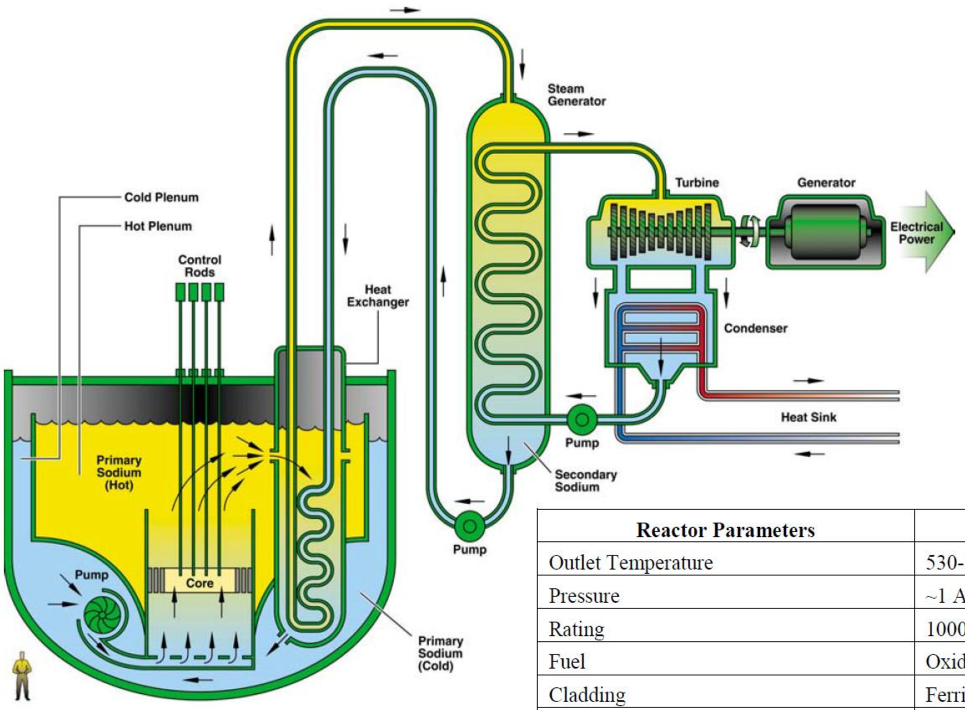

Reactor Parameters	Reference Value
Outlet Temperature	530-550 °C
Pressure	~1 Atmospheres
Rating	1000-5000 MWth
Fuel	Oxide or metal alloy
Cladding	Ferritic or ODS ferritic
Average Burnup	~150-200 GWD/MTHM
Conversion Ratio	0.5-1.30
Average Power Density	350 MWth/m^3

Figure 1.1 Sodium Cooled Fast Reactor and Design Parameters [2]

1.2 SFR Safety Implications

Enhancing safety and maintaining reliable operation is an essential priority in the development of the next-generation power systems. The safety consideration of SFR is different from that of the conventional LWR. The SFR system consists of primary and secondary sodium circulation systems. The primary-loop system can be designed in either pool-type or loop-type configurations. Both options provide large sodium thermal inertia to ensure sufficient margin to the sodium boiling temperature. The secondary loop serves as a barrier between the radioactive primary-loop sodium and the tertiary loop water or steam to prevent radioactive release in case of sodium-water interaction. A major safety advantage of SFR is the low-pressure in the primary-loop system that eliminates the concern of the loss of coolant accident (LOCA) for the LWR. In addition, the coolant temperature rise across the core of SFR is around 100 °C ~150 °C that is significant larger than 30~35 °C in LWR. This promotes the natural circulation of the coolant for the decay heat removal.

On the other hand, the neutronic characteristics of fast neutron spectrum poses unique challenges to the SFR safety. In LWR, the core is designed based on an optimal fuel-to-moderate ratio. The reactor is operated in an under-moderated condition that guarantee a negative temperature coefficient of reactivity. On the contrast, the coolant temperature coefficient is often positive in SFR. In case of coolant temperature rise, the reduction of sodium density results in a hardened spectrum. The increase in number of neutron released per fission (η) with incident neutron energy causes positive reactivity insertion, which can possibly overwhelm the negative reactivity induced by the increase of neutron leakage. Especially in a large SFR where the leakage effect is small, the coolant temperature coefficient and the sodium void worth can be positive.

The neutron mean-free path in the fast spectrum is order of magnitude larger than that in the LWR and the spatial self-shielding effect is significantly less important. The long mean free path makes local reactivity perturbations affect the whole core, and the large leakage fraction makes the reactivity change sensitive to a core geometry change. Since the fast reactor core is not in the most reactive configuration, the fuel compaction could be a source of positive reactivity insertion.

SFR features inherent safety potential as demonstrated in the EBR-II SHRT test [4] and the FFTF inherent safety tests [5]. The inherent safety is the capability of nuclear reactor system, given an upset condition, to initiate recovery action and return a safe state depending on only natural forces. The main criteria of the inherent safety capability are passive shutdown of the reactor and passive removal of decay heat with sufficient thermal and structural margins.

Properly designed SFR with inherent safety characteristics can even survive unprotected transient scenarios that are classified as transient over power (UTOP) and transient under cooling (UTUC) events, including loss of flow (ULOF) and loss of heat sink (LOHS). All these unprotected transients are anticipated transient without scram (ATWS) events [6]. The key to successful prevention of core damage in these unprotected transient scenarios is the reliance on passive mechanisms of specific core design to restore the balance between reactor power production and the system cooling. Such passive mechanisms include:

1. Core inherent reactivity feedbacks to reduce power with increased core temperatures.

2. Functions of passive shutdown systems, such as self-actuated shutdown system (SASS) [7], gas expansion modules (GEMs) [8, 9] and enhanced CRDL thermal expansion system [10].
3. Natural circulation of coolant for decay heat removal.

The inherent reactivity feedback mechanisms are essential to terminate the fission chain reaction and keep the core temperatures within safety domains. The reactivity feedback is mainly in response to core temperature excursion that results in both material property changes and core deformation. The following sections discuss several major components of the reactivity feedback that are of primary importance to SFRs.

1.3 Reactivity Feedback Phenomena Due to Material Property Change

1.3.1 Doppler Feedbacks

The Doppler broadening with increased temperature of the resonance cross sections for all reactions (absorption, fission, scattering, etc.) in all materials of the core accounts for part of the temperature feedbacks in SFRs. With increased material temperature, the resonance width is broadened, and the resonance height is reduced due to the thermal motions of the resonance nuclei. The Doppler broadening does not change the energy integral of resonance cross section itself, but it does reduce the energy self-shielding, resulting in an increase in reaction rate [11]. For the fertile or non-fuel materials, the increase in absorption reaction rate due to Doppler broadening lead to a decrease in core reactivity. For the fissile material, the reactivity effects of increased capture and fission reactions have opposite signs, resulting in a minor net effect. Thus, the Doppler effects greatly depend on the fuel composition, especially the fertile-to-fissile ratio. In fast breeder reactors with significant amount of U-238, there is a large negative Doppler coefficient mainly due to the resonance broadening of U-238 absorption cross section. The Doppler coefficient becomes less negative with decreasing fertile-to-fissile ratio. In the extreme case of uranium-free burner reactor, the Doppler coefficient is almost zero or slightly positive [12]. The Doppler coefficient is strongly affected by the spectrum since the resonance height decreases with increasing energy. Thus, the magnitude of Doppler effects is smaller with harder spectrum.

The magnitude of the Doppler coefficient is not constant but decreases with increased temperature. The reactivity change rate due to fuel temperature change can be approximated as

$$\frac{d\rho}{dT} = \frac{C_D}{T^a}. \tag{1.1}$$

In oxide-fueled fast reactors, the Doppler coefficient is almost inversely proportional to the temperature, i.e. $a = 1$ [6]. The Doppler constant C_D can be evaluated from the reactivity change by doubling the fuel temperature. The reactivity change can be written as

$$\Delta\rho = \int_{T_f}^{2T_f} \frac{d\rho}{dT}(T)dT = \int_{T_f}^{2T_f} \frac{C_D}{T} dT = C_D \ln 2. \tag{1.2}$$

1.3.2 Coolant Expansion Feedbacks

The sodium density reduction or sodium void resulting from coolant temperature rise introduces feedback reactivity, which can be either positive or negative depending on the competing effects of spectrum hardening, increase in leakage and reduction in sodium capture. Spectrum hardening effect introduces positive reactivity because the fissile η and threshold fertile fission will increase with incident neutron energy in fast energy regime. The increase in leakage is always negative effect and has strong spatial dependence. The leakage effect is small at the core central region while it is relatively large near the core periphery. The reduction in sodium capture is a positive effect on reactivity but relatively small in magnitude compared with the first two effects. The evaluation of the sodium density coefficient is generally calculated using the first-order perturbation theory for small density change, while the sodium void worth is calculated using the exact perturbation theory with cross sections generated at the sodium voided condition to account for the spectral shift.

In a large sodium-cooled fast breeder reactor, in which the neutron leakage is small, the sodium temperature coefficient and sodium void worth are positive. Extensive studies have been performed for the design options to reduce the sodium void worth [13]. The general design alternatives include change in composition for softer spectrum, having large sodium plenum above active core, reducing core height-to-diameter ratio [14], or applying heterogeneous core configuration [15]. However, these options either exhibit core physics performance trade-offs or result in more complex core design with higher capital cost.

1.4 Reactivity Feedback Phenomena Due to Core Geometry Change

1.4.1 Fuel Axial Expansion

The fuel axial expansion is caused by thermal expansion of fuel or cladding with an increase in fuel or cladding temperature. It is considered as a prompt reactivity feedback as fuel Doppler feedback for a power transient accident since it is a direct response of fuel temperature change. Thus, it has a significant impact on the power transient accident. The fuel axial expansion increases the active core height while decreases the fuel nuclide densities. The fuel thermal expansion results in two effects. The increase in fuel volume increases the geometrical buckling thus introduces a positive reactivity while the decrease in fuel nuclide densities increases the migration area and introduces a negative reactivity. In a simple homogenized one-group model, the effective multiplication factor k_{eff} can be approximated by

$$k_{eff} = k_{\infty} P_{NL} = \frac{\nu \Sigma_f}{\Sigma_a} e^{-B^2 M^2} \tag{1.3}$$

where k_{∞} is multiplication factor for infinite medium, P_{NL} is the non-leakage probability. The migration area M^2 is inversely proportional to the square of material density, and B^2 is the geometrical buckling, which is inversely proportional to the square of the core linear dimension. An increased core height slightly increases the core inventory of sodium coolant, thus increases the neutron absorption in sodium, resulting in a slightly decrease in the infinite multiplication factor. The fractional increase of the sodium coolant inventory decreases with increasing core height, thus the negative reactivity effect due to increased sodium inventory is inversely proportional to the core height. However, the increased sodium coolant inventory has a negative impact on the migration area, thus the axial leakage is reduced, resulting in a positive reactivity effect that is proportional to the core height cubed. With an increased fuel height, the axial buckling reduces while the migration area increases. The fractional decrease in the axial buckling is equal to the fractional increase in the migration area resulting in a zero net effect on axial leakage. The increased migration area also increases the radial leakage, yielding a negative reactivity effect that is inversely proportional to core height and square of core radius. In addition, the axial expansion of fuel also results in a effective insertion of control rods that remain at the same location, introducing an additional negative reactivity effect.

The above conceptual discussion of fuel axial expansion can be further developed to a simple analytical model for estimating the fuel axial expansion coefficient [16]. However, as illustrated in Figure 1.2, the fuel assembly axial expansions may not be uniform because of the varying fuel temperature from assembly to assembly depending on the radial power shape and the flow orifice. It is necessary to evaluate the fuel axial expansion coefficients for individual fuel assemblies.

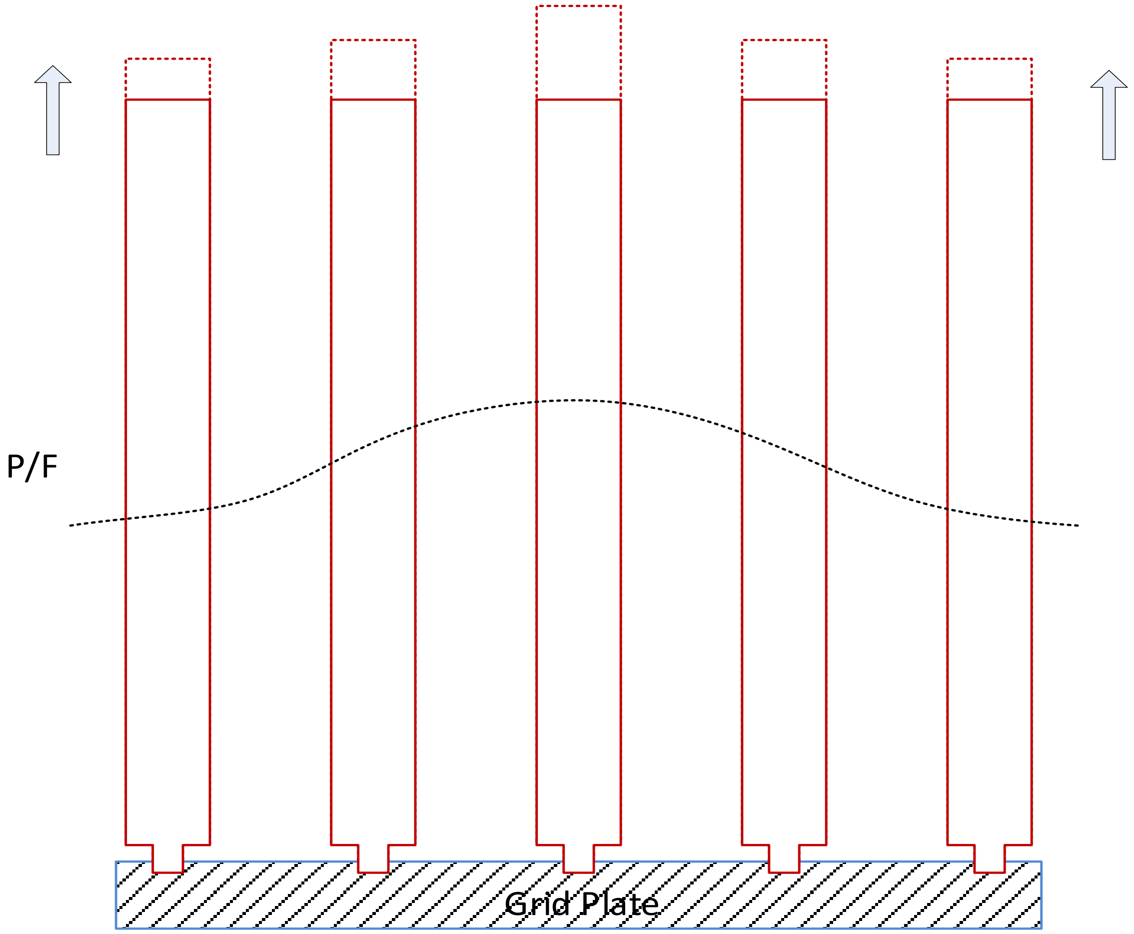

Figure 1.2 Fuel Axial Expansion with Increased Fuel Temperature

1.4.2 Core Radial Expansion

In SFRs, the reactivity feedback due to core radial expansion is one of the most important reactivity feedback phenomena [17]. The core radial expansion due to the grid plate thermal expansion is in response to core inlet coolant temperature rise. The time scale of the core response to the radial expansion of grid plate is in the order of several tens of seconds. The grid plate expansion increases the spacing between assemblies and results in a dilation of the active core as shown in Figure 1.3. Negative reactivity is introduced by the core grid plate radial expansion mainly due to the increased axial leakage and moving fuel from regions with higher reactivity worth to regions with lower reactivity worth. Radial expansion of the reactor core provides a large portion of the negative reactivity feedbacks that are essential for passive shutdown of a SFR during unprotected transients.

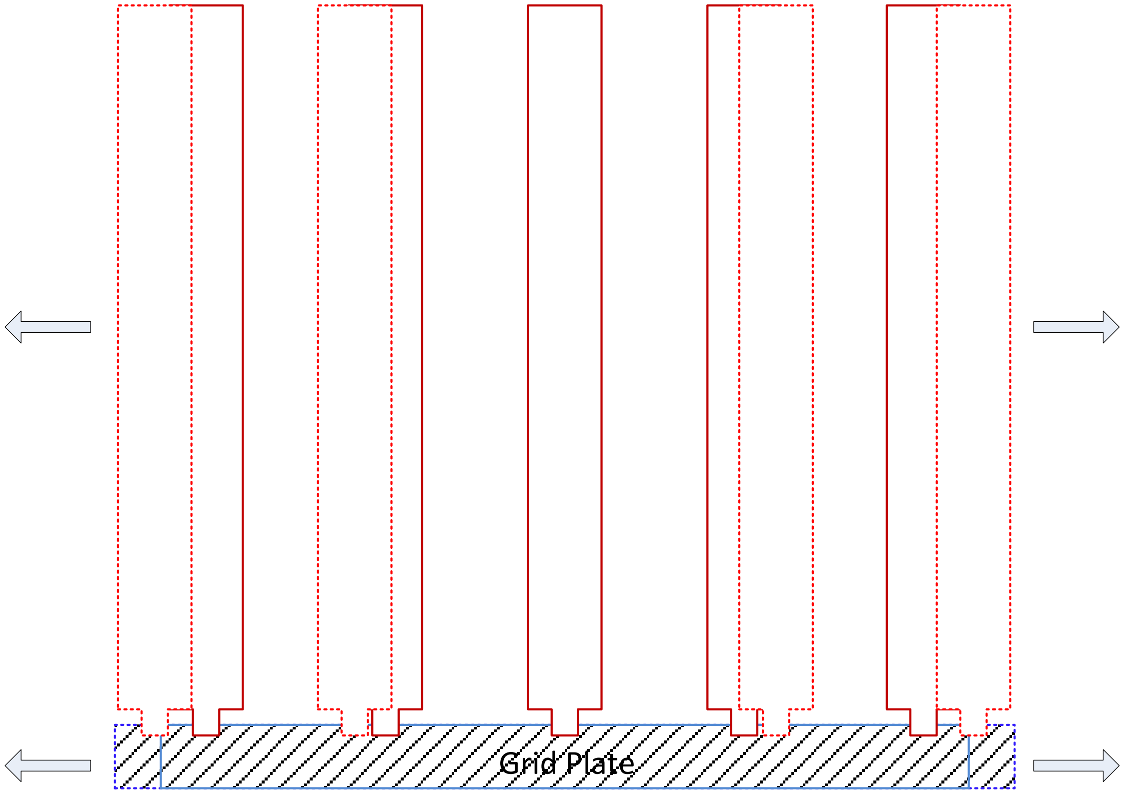

Figure 1.3 Uniform Dilation of Core Due to Grid Plate Radial Expansion

1.4.3 Assembly Bowing

In addition to the uniform dilation of the core due to grid plate radial expansion, the change in assembly duct wall temperature and irradiation swelling cause assembly deformation. Each assembly is subjected to a bending moment due to the temperature difference of opposite hexagonal duct walls of the assembly. The hotter duct wall will thermally expand more compared to the colder wall in the opposite side, resulting in a deflection of the assembly from its original shape. The core deformation is featured by an assembly bowing or flowering depending on the design of the core restraint systems [18]. An important objective of core restraint system design is to control assembly motion such that the reactivity insertion due to assembly bowing is negative during a power transient. There are several core restraint system designs result in different bowing reactivity feedback effects: restrained bowing, limited free bowing and free flowering.

In the restrained bowing design, the assembly is fixed at the top by the top load pad (TLP) as shown in Figure 1.4. In the core with an idealized radial power profile, the thermal gradient of the core decreases radially outward from the center. The side of the fuel assembly that is closer to the core center will be subjected to a larger thermal expansion and the assembly tends to bow towards the core center. The inward bowing of the fuel assembly inserts a positive reactivity and this core design has a positivity power coefficient.

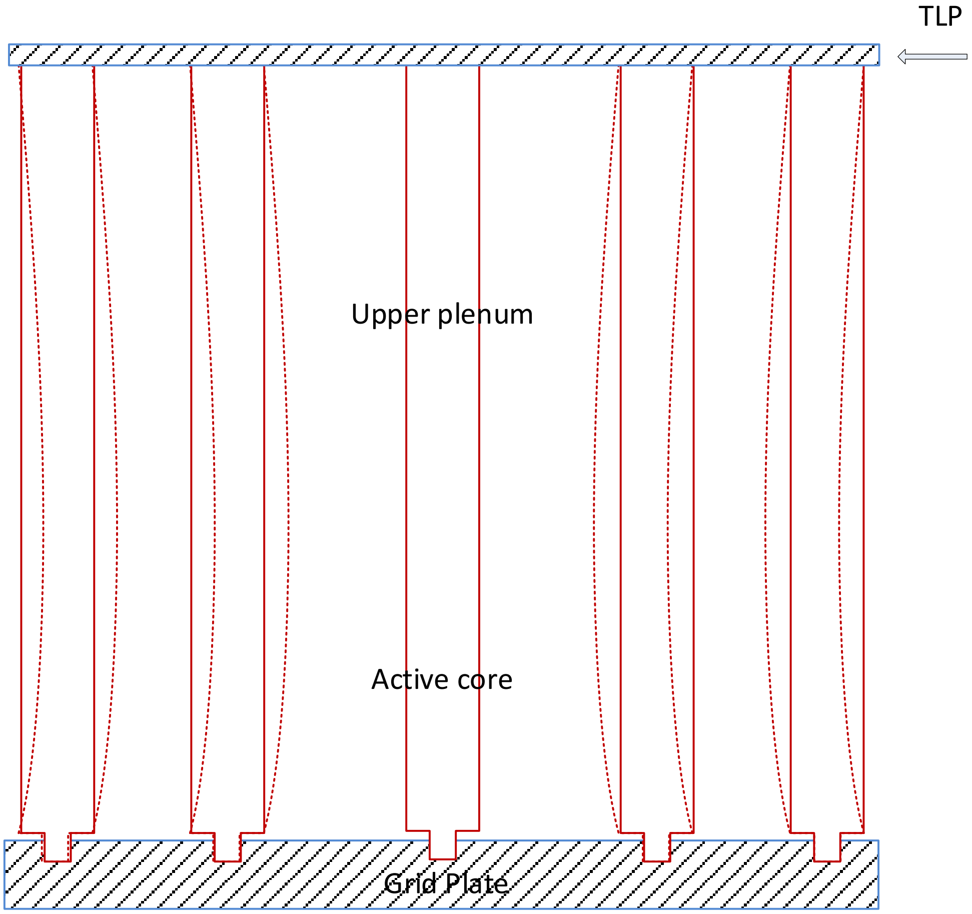

Figure 1.4 Inward Bowing of the Assembly Restrained at Top and Bottom

The free flowering design poses no radial constraint to the top of the assemblies. When the radial temperature gradient increases, the fuel assemblies have a free bending in the outward direction until they interact with the shield assemblies as shown in Figure 1.5. This design results in a monotonically more negative reactivity insertion as the power-to-flow ratio (P/F) increases. The main disadvantage of the free flowering design is the lack of physical bound against lateral motions in case of a seismic event and has a potential difficulty to maintain alignment and tolerance in large cores [19].

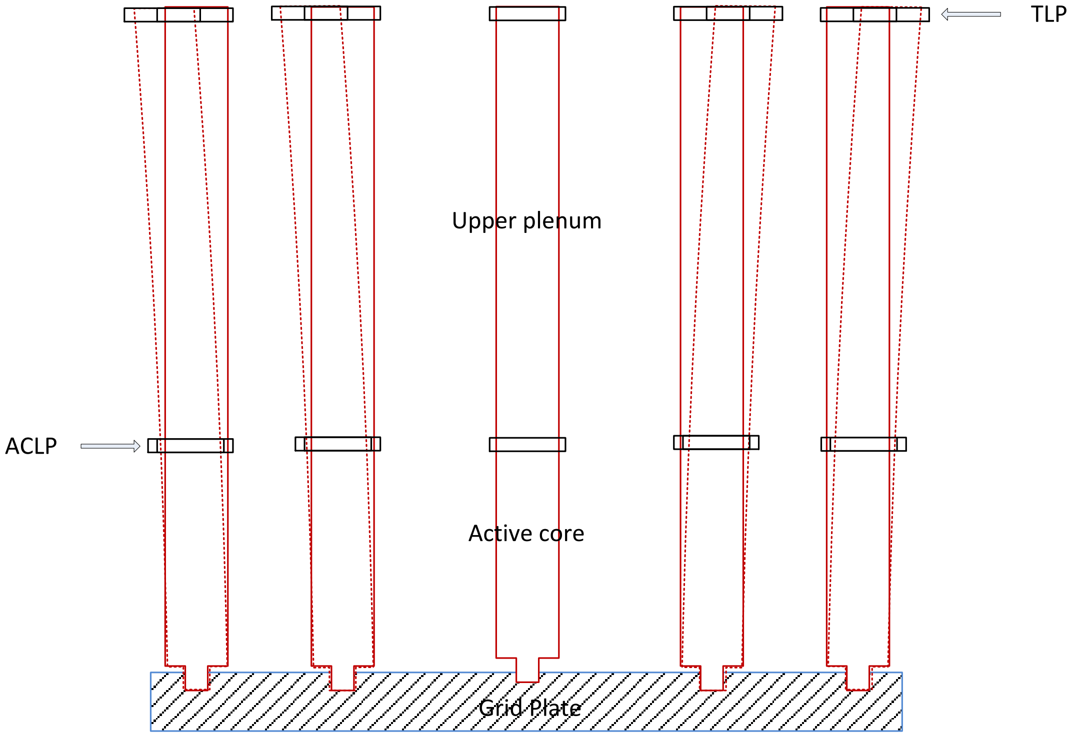

Figure 1.5 Free Flowering Design of Core Restraint System

The limited free bow design shown in Figure 1.6 features three lateral constraints at different elevations. At the core bottom, the coolant inlet nozzle end of assembly is clamped at the core grid plate. Load pads are provided on the assembly duct above the active core (ACLP) and at the top of the assembly (TLP) to carry the load of assembly bowing and to provide spacing between assemblies. Restraint rings attached to the core barrel at the TLP and ACLP elevations are also provided to limit the excessive radial expansion. Unlike the free flowering design, the limited free bow design results in a complex dependence of the bowing reactivity on the P/F ratio (i.e., temperature gradient). As the P/F starts to increase from zero, a negative reactivity is induced due to the flowering of assemblies until the duct contacts the TLP restraint ring. After contacting the top restraint ring only, the active core region of the duct bows inward with further increase in P/F, which temporarily increases the reactivity. The inward bowing continues until the ducts contact at the ACLP. When all the interior ducts contact at the ACLP, the core is "locked up" and no further compaction can occur. Subsequent increase in P/F causes an outward bowing of the active core region and decreases the reactivity. The FFTF and CRBRP designs adopted the limited free bow design [20].

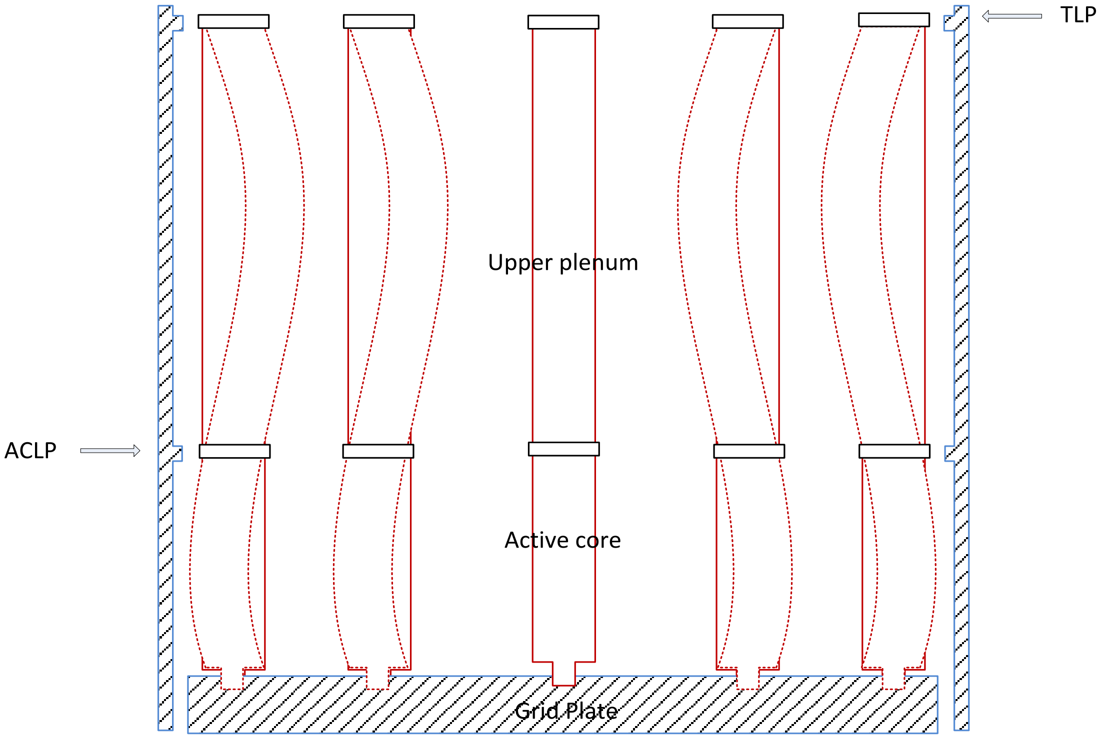

Figure 1.6 Limited Free Bowing Design of Core Restraint System

1.5 Motivation and Objective

As discussed in the previous section, SFRs have a large coolant temperature rise. The resulting temperature gradients lead to differential thermal expansion of the assembly duct walls that, along with the irradiation creep and swelling of the duct walls, results in the bowing of the assembly. Accurate evaluation of the assembly bowing reactivity also provides useful information for the core restraint system design to ensure safe operation. In 1955, experiments on Experimental

Breeder Reactor-I (EBR-1) was performed to study the prompt positive reactivity effect by changing the coolant flow. The core experienced a partial melt accident during the experiment. Subsequent analysis indicated that lowered coolant flow rate resulted in a temperature change across the core causing the center of the fuel to bow inward with fuel rod restrained both at the bottom and top. The movement of the fuel to the higher importance region induces a positive feedback reactivity [21]. Later, in the design of The Experimental Breeder Reactor-II (EBR-II) core, outward dimples were added to fuel ducts near the core centerline to avoid core compaction.

The deformation of assembly induces feedback reactivity that, with careful design of the core restraint system, is often a significant portion of negative feedback reactivity to guarantee inherent safety. However, accurate evaluation of the reactivity induced by the core deformation is difficult. Especially, in large power reactors where hundreds of assemblies are distorted in a complex manner, the prediction of bowing reactivity is a notoriously difficult task. For example, during 1989 and 1990, four fast and oscillating reactivity transients was observed in the French reactor PHENIX [22]. Figure 1.7 shows the power signal during the negative reactivity transient (NRT). Then, significant investigations were performed involving 200 man-years to find the explanations of these Negative Reactivity Transient. The conclusion is that the most likely reason is the core flowering.

In principle, the feedback reactivity due to core deformation can be quantified by Monte Carlo (MC) simulations for the base and perturbed core cases. However, it is not practical since a huge number of histories are required to reduce the statistical uncertainty to a satisfactory level for a reliable estimation of a small reactivity change. The feedback reactivity due to core deformation can also be assessed using a deterministic neutronics analysis code that has a capability to represent the heterogeneous core geometry explicitly, for example a transport code based on the unstructured finite element method (FEM) such as the PROTEUS-SN code [23] developed at ANL that applies the state-of-the-art numerical techniques to reduce computational burdens for realistic reactor core modeling. However, such a FEM-based code requires an excessive memory for explicit modeling of practically large cores. Furthermore, these methods cannot be used for a practical transient analysis since a MC simulation or deterministic core calculation needs to be performed for every possible deformed core configuration.

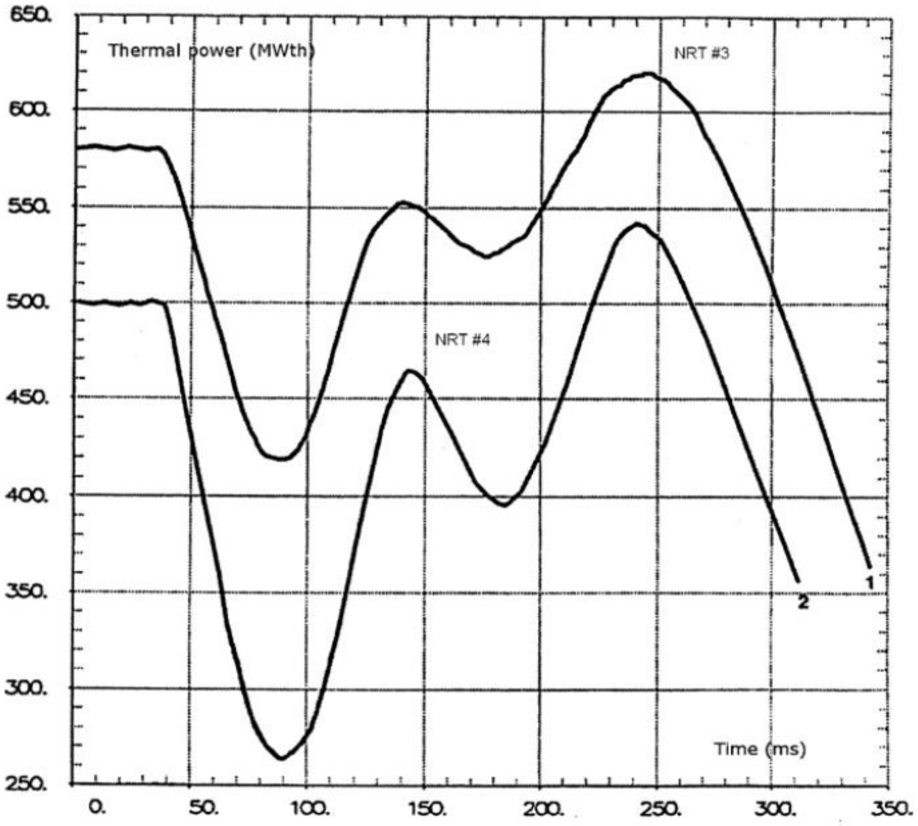

Figure 1.7 Power Signal Recorded During NRT [22]

The objective of the proposed thesis work is to develop a perturbation theory method for accurate and efficient calculation of feedback reactivity due to core deformation. The proposed method will be implemented to a computer code that can be connected with the structure analysis code such as the NUBOW-3D code [24, 25] to improve its capability for modeling the feedback reactivity of core deformation. The enhanced computational capabilities will allow to explore a broader range of design space and to incorporate innovative design features, and the improved prediction accuracies will contribute to reducing the economic penalties due to the conservative design margins to accommodate the prediction uncertainties.

2. LITERATURE REVIEW ON PERTURBATION THEORY METHOD FOR ASSEMBLY BOWING REACTIVITY EVALUATION

Perturbation theory is a widely used mathematical tool in science and engineering for estimating a given response variation due to small changes of input parameters. The earliest use of perturbation theory can be traced back to the 18th century. It was proposed in celestial mechanics for solving the moon-earth-sun three-body problem. In the 20th century, the perturbation methods were adopted to solve new problems arising during the development of quantum mechanics [26]. Since then, the perturbation theory has been developed to a standard method used in classical and quantum mechanics for providing approximated solutions of PDEs that have no exact analytical solution. In classical and quantum mechanics, the equations of interest are mostly self-adjoint. The perturbation theory was firstly introduced to the area of reactor physics by Eugene Wigner. In his classic paper published in 1945 [27], he proposed application of perturbation theory for non-self-adjoint equations. In neutronics area, the perturbation theory is usually used to calculate the reactivity coefficients, in which the eigenvalue is the response parameters of interest with given input changes. The perturbation theory was also generalized to various types of applications for computing response parameters other than eigenvalues, such as kinetic parameters [28], sensitivity coefficients [29], and burnup-dependent responses [30]. The perturbation theory for such purposes is known as the generalized perturbation theory (GPT) [31].

Depending on the quantity perturbed for a reactor system, the perturbation theory can be classified into two major categories: the material property perturbation and core geometry perturbation. In this thesis work, we focused on the core geometry perturbation. Before the proposed work, there are several attempts to model the core deformation based on perturbation theory method, including triangular homogenization scheme, boundary perturbation theory, ‘virtual density theory’ (or ‘similarity theory’), mesh projection-based method and coordinate transformation method.

2.1 Triangular Homogenization Scheme

The triangular homogenization scheme was developed by P. J. Finck at Argonne National Laboratory [32]. It uses the forward and adjoint fluxes determined using the triangular-z finite difference option of the DIF3D code [33, 34] with six triangular meshes per hexagonal assembly.

For each hexagonal assembly, six perturbed cross sections are created by applying a correction factor to the so called “triangular homogenization scheme”, which calculates the cross sections for each triangular mesh by volume weighting of the homogenized assembly zone and the inter-assembly gap sodium zone as illustrated in Figure 2.1. The correction factor is determined to preserve the mass displacement in each triangular mesh. The unperturbed fluxes and adjoint fluxes are assumed linear within the assembly.

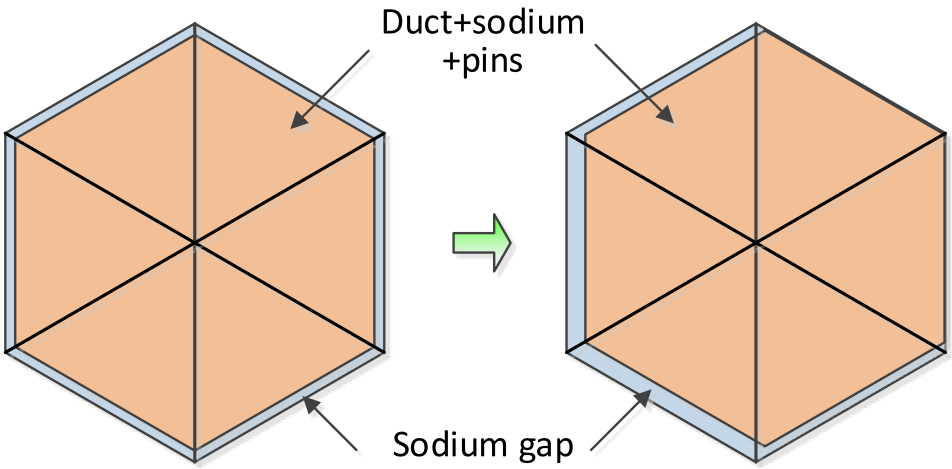

Figure 2.1 Illustration of Homogenized Assembly Displacement and Triangular Homogenization Scheme

2.2 Boundary perturbation theory

The original development of the boundary perturbation theory was performed by Larsen, Pomraning and Rahnema at 1980s. In the first paper published by Larsen and Pomraning [35], the perturbation formulation to calculate the first-order reactivity change by a small perturbation in the external boundary of the reactor system was developed for both diffusion and transport theory. The internal boundary perturbation problem was firstly investigated by Pomraning and Rahnema. However, they found that in diffusion theory the classical first-order perturbation formalism fails to produce correct results for first-order change in the eigenvalue due to internal boundary shift [36]. Later, Pomraning provided correct first-order classical perturbation formula to handle the interface perturbation [37]. The internal boundary perturbation problem was finally treated in a more rigorous manner by Rahnema using the transformation operator technique [38]. More recent studies on internal boundary perturbation problem were performed by Favorite [39]. In his work, the presented equation for estimating the eigenvalue sensitivity to reactor system dimension was shown to be very similar to the earlier results obtained by Rahnema. The main difference which is also the main limitation of his equation is that it only accommodates uniform expansions or contractions of a surface while Rahnema's formula can also be used for the translation and rotation of a surface. Then, Favorite adopted Rahnema's formula to estimate the eigenvalue sensitivity to the translation of a sphere by dividing it into a positive component (bulging in 'front') and a negative component (the collapsing 'behind") as shown in Figure 2.2. The results showed that the formula worked very well for each component separately, but it did not produce accurate estimates for total translation [40]. He also applied the formula to the Zeus [41] model. The conclusion is similar to the previous one drawn from the sphere translation problem that the equation should be applied cautiously for the problems involving multiple surface shifting.

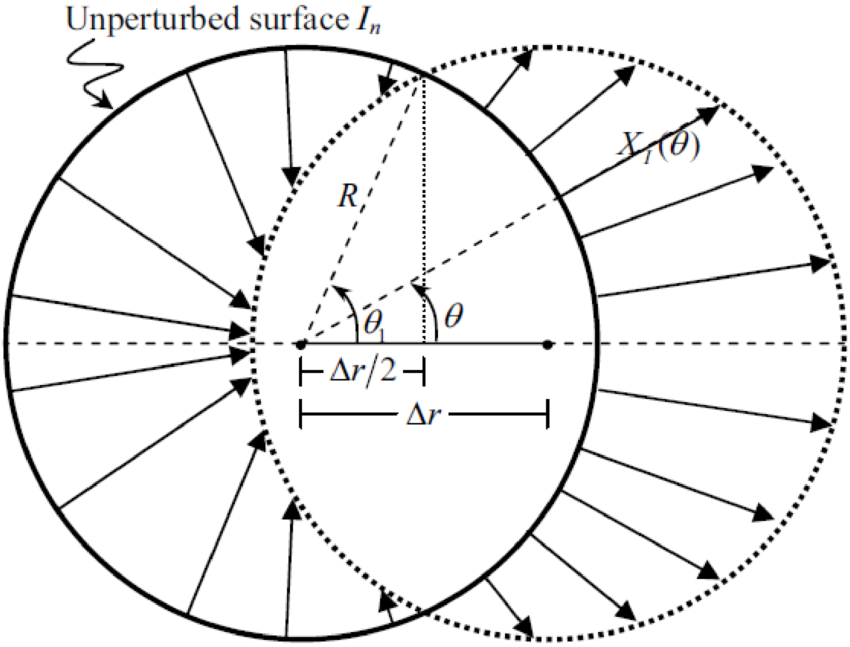

Figure 2.2 Illustration of The Tanslation of A Sphere [40]

2.3 'Virtual Density' Theory

Another approach to handle the geometrical effects on reactivity is to convert the core geometry change to the material density change when applying perturbation theory. The theoretical basis for this method is so called the 'principle of similarity', which is originated during the Manhattan project and later was developed by Shikhov around 1960 [42]. In 2000s, Cullen published two reports on this topic, which contains several numerical examples for homogenous core expansion

[43, 44]. However, in the Western nuclear community, this principle has only been used to perform criticality calculation in early days and almost never been used in perturbation theory for calculation of reactivity coefficients. On the other hand, the ‘principle of similarity’ has been frequently applied to the calculation of reactivity coefficients by Soviet Union nuclear community since Shikhov firstly proposed this concept. This law is also adopted in the design of BN-800 [45].

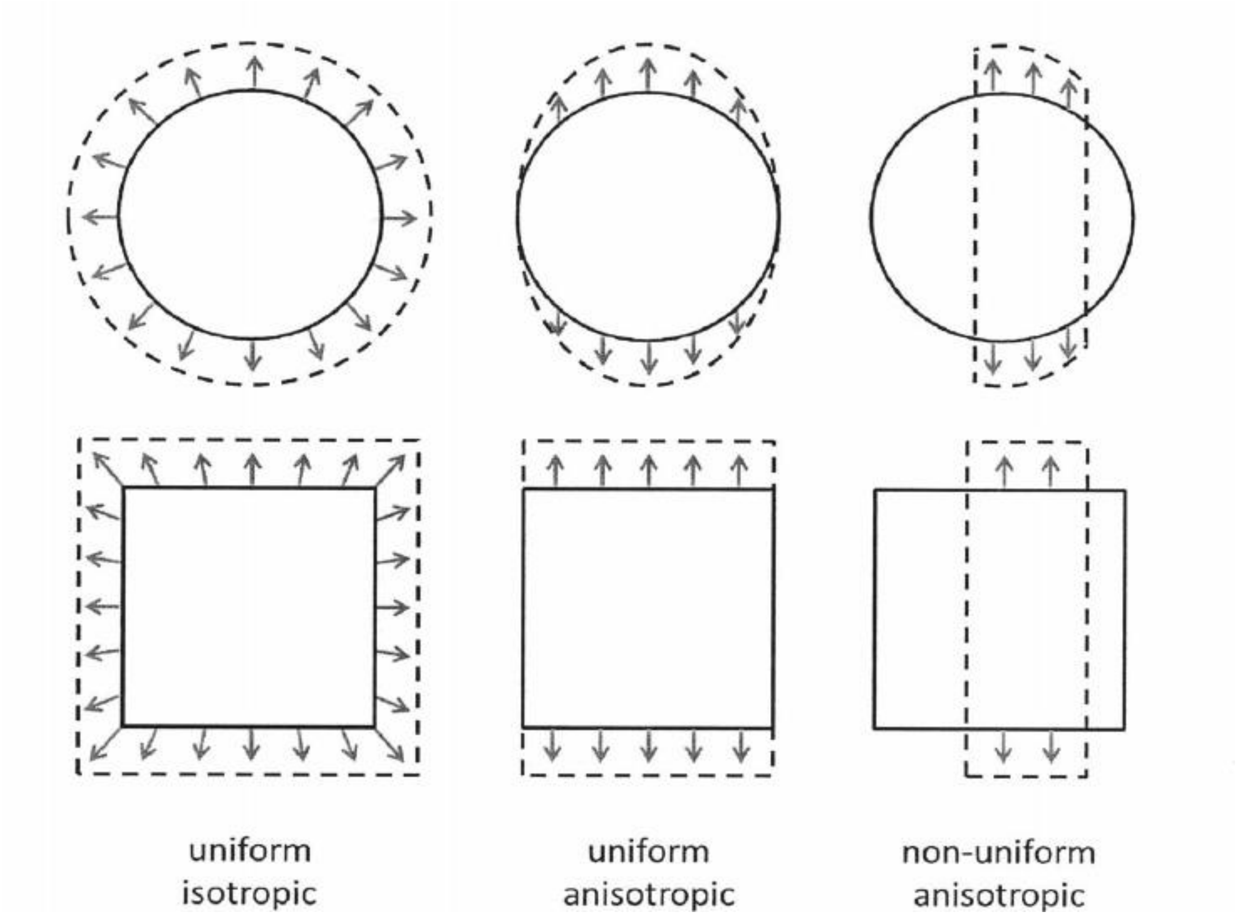

Figure 2.3 Illustration of ‘Uniform Isotropic’, ‘ Uniform Anisotropic’ and Non-Uniform Anisotropic’ Geometrical Expansion [49]

Recently, M. Reed at MIT performed an extensive study in the development and application of the ‘virtual density’ theory [46, 47, 48, 49, 50, 51]. As pictured in Figure 2.3, the geometrical change can be divided into three categories. The ‘uniform isotropic’ and uniform anisotropic’ expansion problems have been solved in either Western or Soviet Union literatures. Reed’s work generalized the application of the ‘virtual density’ theory to ‘non-uniform anisotropic’ swelling and expansion.

However, the work is entirely based on diffusion approximation, which may not be sufficient for fast reactor applications. In addition, the ‘virtual density’ theory is used for thermal expansion, but not for displacement problem.

2.4 Mesh Projection-Based Method

The very recent effort on modeling the bowing reactivity was the mesh projection-based method proposed by Gentili [51, 53]. In this method, an assembly is treated as a hexagon with homogeneous medium surrounded by sodium. As the assembly shifted, part of the volume (V_B) initially occupied by it will be replaced by sodium and vice versa for part of the sodium coolant (V_A) as shown in Figure 2.4. Then, the classical perturbation theory formula is used to estimate the reactivity change due to the material density perturbation in these volumes. The proposed perturbation formulation is based on the diffusion approximation even though the forward and adjoint fluxes are solved from both the diffusion and transport equations.

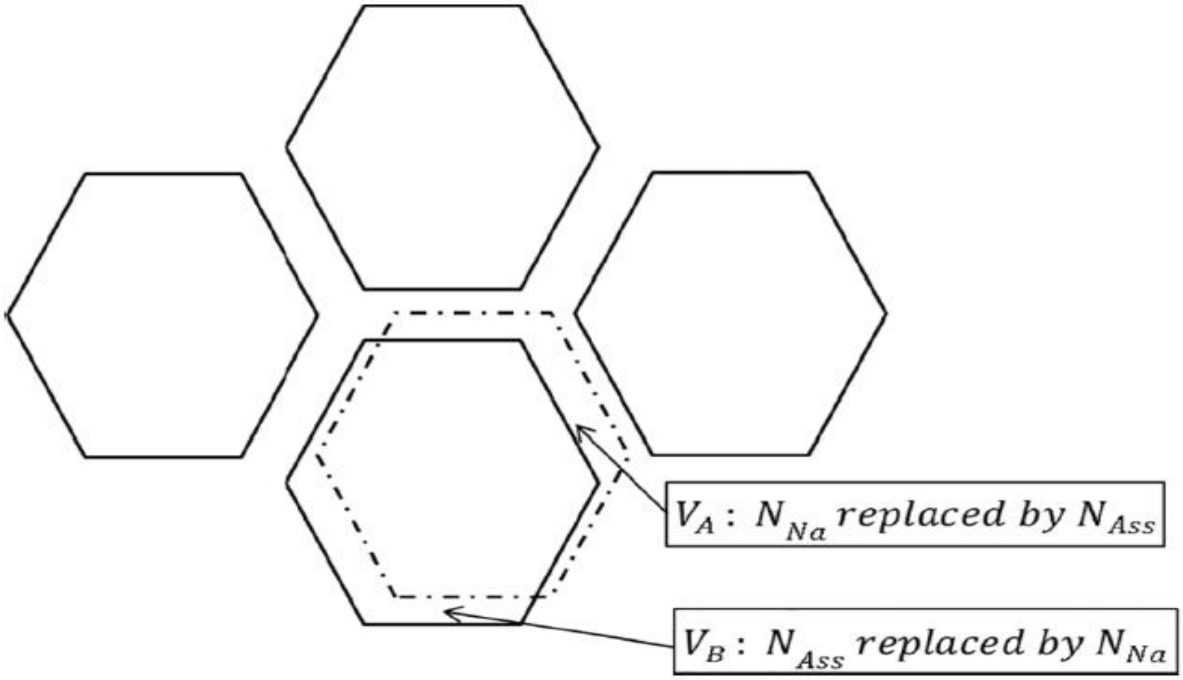

Figure 2.4 Assembly Displacement Representation of Mesh Projection-based Method [51]

This method was tested on central flowering of PHENIX core assemblies. This is the most realistic application of the bowing reactivity evaluation method on practical reactor model found in available literatures. The results were compared with Monte Carlo simulation results and showed a decent agreement. However, the heterogeneous effects of the within assembly structure (fuel pins, coolant and assembly duct) cannot be naturally taken into account.

2.5 Coordinate Transformation Method

In the mid-1980s, G. M. Greenman at ANL presented a new approach for calculating reactivity feedback due to core assembly bowing in LMFBRs [54, 55]. His central idea is very similar to what we adopted in this thesis work, which is to apply a coordinate transformation on the reactivity integral for the perturbed state to map the material distribution back to its original state. The first-order perturbation expression for reactivity is written as

$$\delta(1/k) = \frac{\left\langle \phi^*(r), H(r-\Delta n)\phi(r) \right\rangle}{\left\langle \phi^*(r), F(r)\phi(r) \right\rangle}, \tag{2.1}$$

where H is the diffusion operator, F is the fission operator, ϕ^* and ϕ are the adjoint and forward scalar fluxes, respectively. By applying the coordinated transformation

$$r' = r - \Delta n\,. \tag{2.2}$$

One can obtain an alternative first-order perturbation expression:

$$\delta(1/k) = \frac{\left\langle \phi^*(r+\Delta n), H(r)\phi^*(r+\Delta n) \right\rangle}{\left\langle \phi^*(r), F(r)\phi^*(r) \right\rangle}. \tag{2.3}$$

Equation (2.3) indicates that the shift in the discontinuous material distribution can be transformed into a shift in discontinuous flux distribution. However, the method is developed under diffusion theory. The continuous distribution of the flux is constructed from finite difference results obtained from the DIF3D code.

2.6 Summary

In this chapter, we reviewed the perturbation theory methods in existing literatures for application of evaluating the feedback reactivity due to core deformation. The characteristic and limitation of these methods are summarized in Table 2.1. Based on this review, the author concludes that, to the best of the author’s knowledge, there is no existing perturbation theory method that fulfills all the objective defined in this study for accurate and efficient evaluation of the feedback reactivity due to core deformation.

Table 2.1 Summary of Existing Perturbation Theory Method for Core Deformation in Literatures

Method	Applications	Limitations
Triangular Homogenization scheme	Assembly displacement	Diffusion approximation; Homogeneous assembly model
Boundary Perturbation Theory	External boundary perturbation (thermal expansion) Internal boundary translation (Assembly displacement)	Failed to produce reasonable results for internal closed surface translation
Virtue Density Theory	Assembly swelling	It is well developed only under diffusion approximation and not applicable to assembly displacement problems
Mesh Projected-based Method	Assembly displacement	Homogeneous assembly model
Coordinate Transformation Method	Assembly displacement	Diffusion approximation; Homogeneous assembly model

3. PERTURBATION THEORY METHOD FOR CORE DEFORMATION REACTIVITY COEFFICIENT

This section presents the new perturbation theory method for evaluating the reactivity due to assembly displacement. The perturbation calculation is performed by tracking the material movement, which is analogous to the "Lagrangian frame of reference" in a fluid field. This scheme provides a unique convenience for modeling heterogeneous assembly displacements by eliminating the need to consider complex intersections of discontinuous material boundary and the geometrical meshes.

3.1 Method of Evaluating Assembly Bowing Reactivity

Finite difference approach is used for modeling the axial distortion of the bowed assembly as shown in Figure 3.1. The assembly is divided into multiple axial segments and allowed different amount of displacement for individual segments.

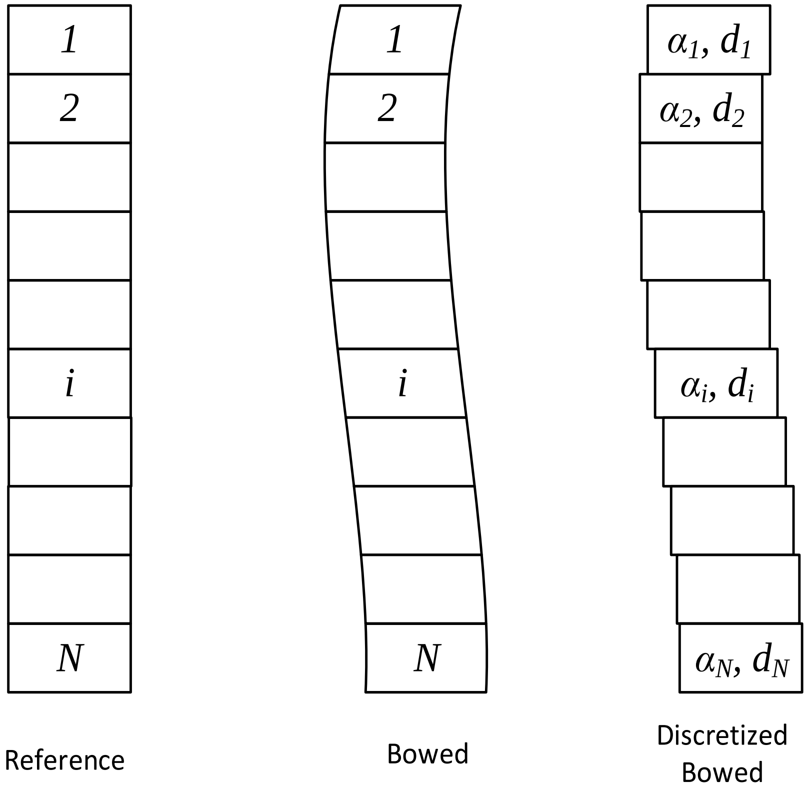

Figure 3.1 Illustration of Axial Segments of Original and Bowed Assembly

Assuming that the reactivity changes linearly with small assembly displacements, the reactivity change due to assembly bowing can be calculated by combining a set of pre-calculated reactivity worth coefficients of each assembly segment per unit displacement in each of six directions normal to the duct wall surfaces and the actual displacements of individual segments. The assembly bowing reactivity ρ_A can be written as

$$\rho_A = \sum_{i=1,N} \vec{\alpha}_i \cdot \vec{d}_i \,, \tag{3.1}$$

where $\vec{\alpha}_i$ is directional bowing reactivity coefficient for assembly segment i and $\vec{d}_i$ is directional displacement vector for assembly segment i.

In order to calculate ρ_A, two pieces of information are required. One is the displacement in each segment of deformed assembly from its original position that can be obtained from a structural analysis code such as NUBOW-3D. The other is the reactivity worth coefficients for the direction in which the assembly segments are displaced. The directional bowing reactivity coefficients can be evaluated for six directions that are normal to the assembly duct using perturbation theory method. A displacement in an arbitrary direction can be decomposed into the two directions normal to the hexagonal duct that are neighboring to that direction.

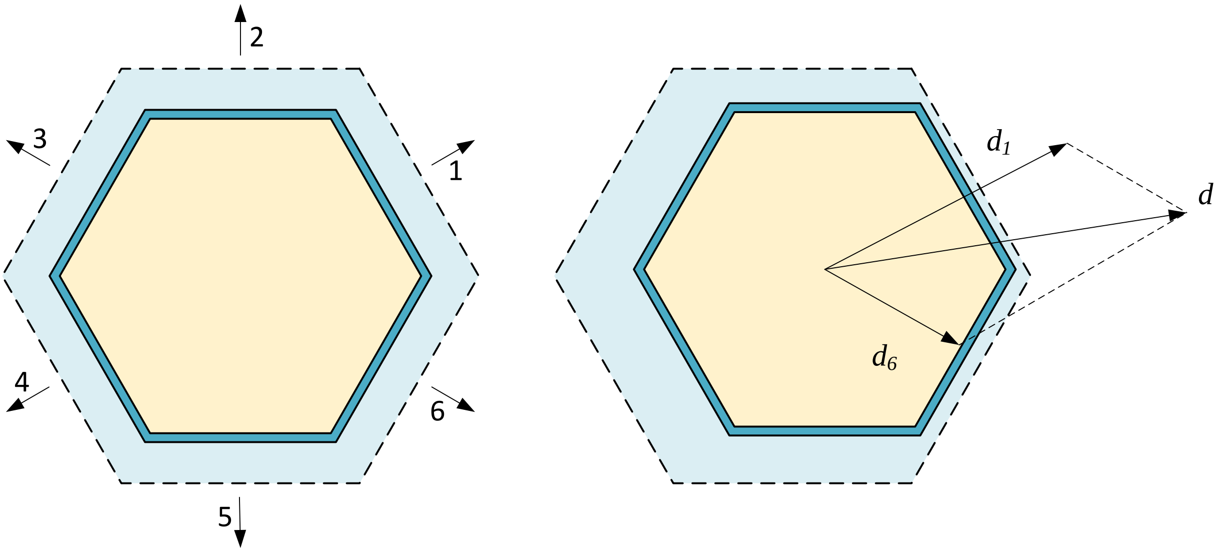

Figure 3.2 Illustration of Radial Configurations of Original (Left) and Displaced (Right) Assembly Due to Bowing

Figure 3.2 presents an example of such decomposition. Consider a displacement of an assembly segment by a distance d in the direction shown in Fig. 3.2. This displacement can be treated as a vector sum of a displacement in the direction one by a distance d_1 and a displacement in the direction six by a distance d_6 . The reactivity worth due to this assembly segment displacement can be written as

$$\rho_{A,i} = \alpha_1 \cdot d_1 + \alpha_6 \cdot d_6 . \tag{3.2}$$

The perturbation theory method for evaluating the directional bowing reactivity coefficients for assembly segments is described in the following sections.

3.2 Basic Perturbation Theory Formulation

The λ-mode eigenvalue equation for neutron transport in a multiplying system can be written as

$$\begin{aligned}&\hat{\Omega}\cdot\nabla\psi_0(\vec{r},E,\hat{\Omega})+\Sigma_{0,t}(\vec{r},E)\psi_0(\vec{r},E,\hat{\Omega})\\&=\sum_{l=0}^{L}\sum_{k=-l}^{l}Y_{lk}(\hat{\Omega})\int dE'\Sigma_{sl}(\vec{r},E'\to E)\psi_{lk0}(\vec{r},E')+\frac{\lambda_0}{4\pi}\chi_0(E)\int dE'\nu\Sigma_{0,f}(\vec{r},E')\phi_0(\vec{r},E')\end{aligned}, \tag{3.3}$$

with the vacuum boundary condition

$$\psi_0(\vec{r},E,\hat{\Omega}) = 0, \qquad \vec{r}\in\partial V, \qquad \hat{\Omega}\cdot\hat{n}\le 0 . \tag{3.4}$$

The adjoint equation of Eq. (3.3) is given by

$$\begin{aligned}&-\hat{\Omega}\cdot\nabla\psi_0^*(\vec{r},E,\hat{\Omega})+\Sigma_{0,t}(\vec{r},E)\psi_0^*(\vec{r},E,\hat{\Omega})\\&=\sum_{l=0}^{L}\sum_{k=-l}^{l}Y_{lk}(\hat{\Omega})\int dE'\Sigma_{sl}(\vec{r},E\to E')\psi_{lk0}^*(\vec{r},E')+\frac{\lambda_0}{4\pi}\nu\Sigma_{0,f}(\vec{r},E)\int dE'\chi_0(E')\phi_0^*(\vec{r},E')\end{aligned}, \tag{3.5}$$

with the vacuum boundary condition

$$\psi_0^*(\vec{r},E,\hat{\Omega}) = 0, \qquad \vec{r}\in\partial V, \qquad \hat{\Omega}\cdot\hat{n}\ge 0 . \tag{3.6}$$

The subscript 0 in the above equations refers to the original unperturbed system. V is the problem domain and ∂V is the domain boundary. $\hat{n}$ is the unit normal vector at the boundary surfaces. $\psi(\vec{r},E,\hat{\Omega})$ and $\psi^*(\vec{r},E,\hat{\Omega})$ are the forward and adjoint neutron angular flux of energy E , position $\vec{r}$ and angle $\hat{\Omega}$. Σ_t is the total cross section, $\nu\Sigma_f$ is the number of neutron per fission multiplied by fission cross section and χ is the fission spectrum. The scattering kernel is expanded using spherical harmonics $Y_{lk}(\hat{\Omega})$. ψ_{lk} and ψ_{lk}^* are the spherical harmonics moments of the forward and adjoint angular fluxes. Σ_{sl} is the scattering cross section for Legendre moment of order l .

It was shown that the fundamental eigenvalues of forward and adjoint transport equations are equal [56]. Equation (3.3) and Eq. (3.5) can be written in operator notation as

$$\boldsymbol{A}_0\psi_0 - \lambda_0\boldsymbol{F}_0\psi_0 = 0\,, \tag{3.7}$$

and

$$\boldsymbol{A}_0^*\psi_0^* - \lambda_0\boldsymbol{F}_0^*\psi_0^* = 0\,, \tag{3.8}$$

where $\boldsymbol{A}_0$ and $\boldsymbol{F}_0$ are the neutron loss and migration operator and the fission operator, respectively. $\boldsymbol{A}_0^*$ and $\boldsymbol{F}_0^*$ are the adjoint operators of $\boldsymbol{A}_0$ and $\boldsymbol{F}_0$, respectively. The adjoint operators are defined by the following inner products:

$$\left\langle \boldsymbol{A}_0^*\psi_0^*, \psi_0 \right\rangle = \left\langle \psi_0^*, \boldsymbol{A}_0\psi_0 \right\rangle, \tag{3.9}$$

and

$$\left\langle \boldsymbol{F}_0^*\psi_0^*, \psi_0 \right\rangle = \left\langle \psi_0^*, \boldsymbol{F}_0\psi_0 \right\rangle, \tag{3.10}$$

where the inner products indicate an integration over space, angle and energy domains.

Consider a perturbed system of which loss/migration and fission operators are given by

$$\boldsymbol{A}' = \boldsymbol{A}_0 + \delta\boldsymbol{A}\,, \tag{3.11}$$

and

$$\boldsymbol{F}' = \boldsymbol{F}_0 + \delta\boldsymbol{F}\ . \tag{3.12}$$

The forward neutron transport equation for the perturbed system can be written as

$$\boldsymbol{A}'\psi' - \lambda'\boldsymbol{F}'\psi' = 0\,, \tag{3.13}$$

with the perturbed eigenvalue and eigenfunction

$$\lambda' = \lambda_0 + \delta\lambda\,, \tag{3.14}$$

and

$$\psi' = \psi_0 + \delta\psi\ . \tag{3.15}$$

The vacuum boundary condition in Eq. (3.4) is also used for the perturbed system since the external boundaries are unperturbed. Integrating Eq. (3.13) with adjoint flux weighting over space, angle and energy domains yields

$$\left\langle \psi_0^*, (\boldsymbol{A}' - \lambda' \boldsymbol{F}')\psi' \right\rangle = 0 . \tag{3.16}$$

Inserting Eq. (3.11), Eq. (3.12) and Eq. (3.14). in Eq. (3.16) and using Eq. (3.9) and Eq. (3.10), we have

$$\left\langle \psi_0^*, (\delta \boldsymbol{A} - \delta\lambda \boldsymbol{F}_0 - \delta \boldsymbol{F} \lambda_0 - \delta\lambda \delta \boldsymbol{F})\psi' \right\rangle = 0 . \tag{3.17}$$

Therefore, the exact expression of the eigenvalue perturbation can be obtained as

$$\delta\lambda = \frac{\left\langle \psi_0^*, \left(\delta \boldsymbol{A} - \lambda_0 \delta \boldsymbol{F}\right)\psi' \right\rangle}{\left\langle \psi_0^*, (\boldsymbol{F}_0 + \delta \boldsymbol{F})\psi' \right\rangle} = \frac{\left\langle \psi_0^*, \left(\delta \boldsymbol{A} - \lambda_0 \delta \boldsymbol{F}\right)\left(\psi_0 + \delta\psi\right) \right\rangle}{\left\langle \psi_0^*, (\boldsymbol{F}_0 + \delta \boldsymbol{F})\left(\psi_0 + \delta\psi\right) \right\rangle} . \tag{3.18}$$

Neglecting the terms that are higher than first-order of the product of $\delta \boldsymbol{A}$, $\delta \boldsymbol{F}$, and $\delta\psi$, the eigenvalue perturbation $\delta\lambda$ can be obtained as

$$\delta\lambda = \frac{\left\langle \psi_0^*, \left(\delta \boldsymbol{A} - \lambda_0 \delta \boldsymbol{F}\right)\psi_0 \right\rangle}{\left\langle \psi_0^*, \boldsymbol{F}_0 \psi_0 \right\rangle} . \tag{3.19}$$

The reactivity change $\delta\rho$ is defined by the change in the off-criticality between the unperturbed and perturbed system,

$$\delta\rho = \left(1 - \frac{1}{k'}\right) - \left(1 - \frac{1}{k}\right) = (1 - \lambda') - (1 - \lambda) = -\delta\lambda . \tag{3.20}$$

Therefore, the first order perturbation formula for the reactivity can be obtained as

$$\delta\rho = -\frac{\left\langle \psi_0^*, \left(\delta \boldsymbol{A} - \lambda_0 \delta \boldsymbol{F}\right)\psi_0 \right\rangle}{\left\langle \psi_0^*, \boldsymbol{F}_0 \psi_0 \right\rangle} . \tag{3.21}$$

3.3 Perturbation Theory Method for Assembly Bowing

3.3.1 Lagrangian Scheme for Evaluating the Reactivity Worth of Material Movements

The proposed perturbation theory method focuses on evaluating the reactivity changes induced by the material movement of an assembly as shown in Figure 3.3. The reactivity changes are determined by the differences in reaction rates before and after material relocations. Conceptually, the reaction rate is similar to some physical quantity of a material element in continuum mechanics that is subject to a space-time-dependent velocity field. Therefore, the time rate of changes in reaction rate can be described by the substantial (or material) derivative. The physical meaning of the substantial derivative is the change rate of a quantity (reaction rate in this case) as experienced by an observer that is moving along with the flow (assembly material movement in this case). The observations made by a moving observer are affected by the stationary time rate of change of the property, which is zero in this case since the total amount of materials is conserved and the microscopic cross sections are assumed unperturbed. What is observed also depends on where the observer goes as it floats along with the flow. If the flow takes the observer into a region where, for example, the local flux is higher, then the observed amount of reaction rate will be higher due to this change in location. The reaction rate change before and after material relocations can be obtained by integrating its substantial derivative over a period when the material movement goes on.

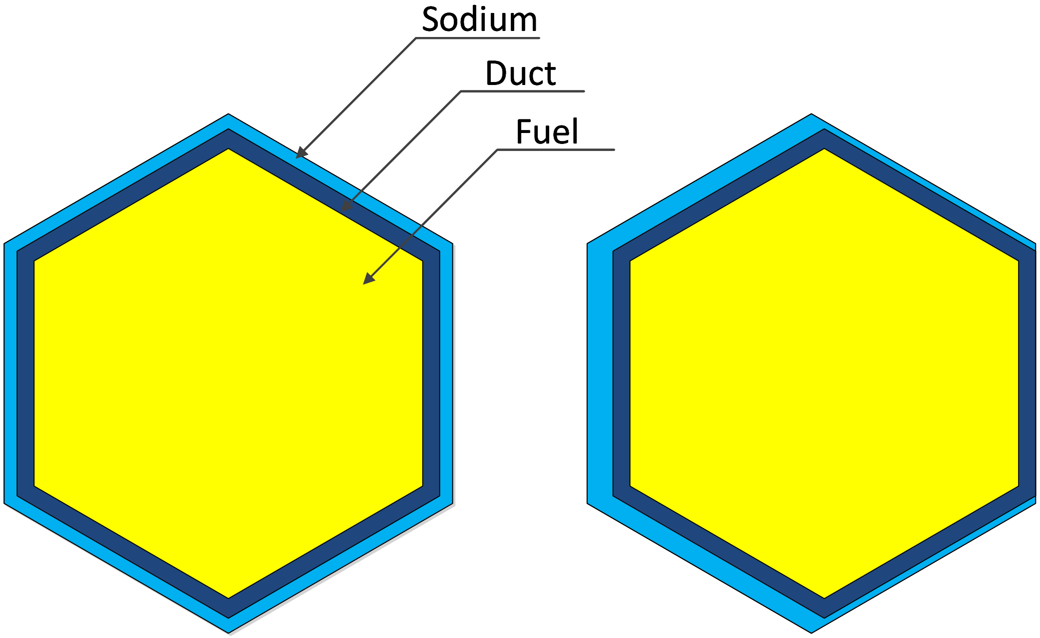

Figure 3.3 Original (Left) and Displaced Assembly (Right) Configurations

The substantial derivative can be formulated based on Eulerian or Lagrangian types of descriptions of continuum deformation. It can be seen that the classical perturbation theory formulation in Eq. (3.21) is derived under the Eulerian frame. In the perturbed system, the materials are relocated in the spatial domain while the total mass of the materials are conserved. In addition, the microscopic cross sections are assumed unperturbed. By taking advantages of these properties, Eq. (3.21) is reformulated by using the Lagrangian frame of reference to simplify the numerical treatment of the perturbation with finite element spatial discretization.

In the Eulerian description, the focus is on the reference configuration, giving attention to what is occurring at a fixed point in space as time progresses, instead of giving attention to individual materials as they move through space and time. In Eulerian type of expression, the substantial derivative is

$$\frac{\mathrm{D}}{\mathrm{D}t} q(x_0,t) = \frac{\partial}{\partial t} q(x_0,t) + \frac{dx_0}{dt} \nabla q(x_0,t) \ . \tag{3.22}$$

In this particular case,

$$q(x_0,t) = \boldsymbol{M}(x_0,t)\psi(x_0) \, , \tag{3.23}$$

where M is reaction operator such as fission, capture and scattering and x_0 is a fixed point at the initial configuration such that $dx_0 / dt = 0$. Thus, the convection term is zero and the substantial derivative is only the time derivative of the reaction rate:

$$\frac{\mathrm{D}}{\mathrm{D}t}[\boldsymbol{M}(x_0,t)\psi(x_0)] = \frac{\partial}{\partial t}[\boldsymbol{M}(x_0,t)\psi(x_0)] \, . \tag{3.24}$$

The total change in reaction rate at position x_0, $\delta R(x_0)$, can be obtained by integrating the equation over the time interval of material movement, that is

$$\delta R(x_0) = \int_{t_1}^{t_2} \frac{\partial}{\partial t}[\boldsymbol{M}(x_0,t)\psi(x_0)]dt = \boldsymbol{M}(x_0,t)\psi(x_0)\Big|_{t_1}^{t_2} = \delta\boldsymbol{M}(x_0)\psi(x_0) \, , \tag{3.25}$$

where $\delta\boldsymbol{M}(x_0)$ is the operator change at position x_0 before and after the assembly displacement. This reaction rate change yields Eq. (3.21) for the first order perturbation theory based on operator perturbation. Evaluation of Eq. (3.21) involves determining the material property changes at each spatial point. It is straightforward for the case that the material is stationary and changes are only in the local nuclide density or microscopic cross sections, such as for Doppler effects or coolant density coefficient. However, for the case of material movement, it becomes extremely difficult to determine the material property changes in each discretized spatial element, since the interface between different materials may intersect with the spatial element in the perturbed configuration.

In the Lagrangian description, the positions and reaction rates of the nuclides are described in terms of the material or referential coordinates and time. An observer standing in the referential frame of moving objective observes the changes in the position and reaction rates as the material body moves in space as time progresses. The substantial derivative in the Lagrangian type of expression is

$$\frac{\mathrm{D}}{\mathrm{D}t}Q(x,t)=\frac{\partial}{\partial t}Q(x,t)+\frac{dx}{dt}\nabla Q(x,t)\,, \tag{3.26}$$

where

$$Q(x,t)=\boldsymbol{M}(x)\psi(\chi^{-1}(x,t)) \tag{3.27}$$

and x is the spatial coordinate attached to the material. The coordinate x can be mapped to the initial coordinate x_0 as

$$x=\chi(x_0,t)\,. \tag{3.28}$$

Thus,

$$\frac{dx}{dt}=\frac{\partial}{\partial t}\chi(x_0,t)=v \tag{3.29}$$

is the velocity of material movement.

The substantial derivative of reaction rate for a material element is given by

$$\frac{\mathrm{D}}{\mathrm{D}t}[\boldsymbol{M}(x)\psi(\chi^{-1}(x,t))]=\frac{\partial}{\partial t}[\boldsymbol{M}(x)\psi(\chi^{-1}(x,t))]+v\nabla[\boldsymbol{M}(x)\psi(\chi^{-1}(x,t))]\,. \tag{3.30}$$

The first term in the right-hand side of Eq. (3.30) is equal to zero since there is no production or destruction of material in the system and the microscopic cross sections of materials are constant with time. Integrating the equation over the time interval of material movement yields the reaction rate change before and after the assembly displacement. $\delta R(x)$ can be written as

$$\delta R(x)=\int_{t_1}^{t_2}dt\frac{dx}{dt}\nabla[\boldsymbol{M}(x)\psi(\chi^{-1}(x,t))]=\boldsymbol{M}(x)\psi(\chi^{-1}(x,t))\Big|_{t_1}^{t_2}=\boldsymbol{M}(x)\delta\psi(x)\,, \tag{3.31}$$

where $\delta\psi(x)$ is the difference in flux experienced by the material before and after assembly displacement. The above equation indicates that the calculation of the reaction rate change can be accomplished by evaluating the fluxes at different positions in the spatial domain. Consequently, the reactivity change can be expressed as

$$\Delta\rho = -\frac{\left\langle \psi^*, \left(\delta\boldsymbol{A} - \lambda\delta\boldsymbol{F}\right)\psi \right\rangle}{\left\langle \psi^*, \boldsymbol{F}\psi \right\rangle} \Leftrightarrow -\frac{\left(\left\langle \tilde{\psi}^*, \boldsymbol{A}\tilde{\psi} \right\rangle - \left\langle \psi^*, \boldsymbol{A}\psi \right\rangle\right) - \left(\left\langle \tilde{\psi}^*, \lambda\boldsymbol{F}\tilde{\psi} \right\rangle - \left\langle \psi^*, \lambda\boldsymbol{F}\psi \right\rangle\right)}{\left\langle \psi^*, \boldsymbol{F}\psi \right\rangle}, \tag{3.32}$$

where $\tilde{\psi}$ and $\tilde{\psi}^*$ are the forward and adjoint fluxes at the shifted position of a material element that was originally exposed to ψ and ψ^* at the base position.

3.3.2 Discretized Formulations of the Perturbation Theory Method

Equation (3.32) requires evaluation of the two perturbation terms. The loss and migration term is defined as

$$\Delta I_A = \left\langle \psi^*, \delta\boldsymbol{A}\psi \right\rangle = \left\langle \tilde{\psi}^*, \boldsymbol{A}\tilde{\psi} \right\rangle - \left\langle \psi^*, \boldsymbol{A}\psi \right\rangle. \tag{3.33}$$

Similarly, the fission term is defined as

$$\Delta I_F = \left\langle \psi^*, \delta\boldsymbol{F}\psi \right\rangle = \left\langle \tilde{\psi}^*, \boldsymbol{F}\tilde{\psi} \right\rangle - \left\langle \psi^*, \boldsymbol{F}\psi \right\rangle. \tag{3.34}$$

The inner product in the above equations denotes the integral over space, angle and energy variables. Numerical evaluation of such integrals requires discretization on those variables. The discretization of the perturbation formula in space domain is based on unstructured finite element meshes. Within each finite element, the flux is represented using its averaged value and material homogenized cross sections are assumed constant.

Based on the spatially discretized formulation, the equivalence between the Lagrangian and Eulerian schemes can be further explained by the following example. Considering the fission term in Eq. (3.34), the integral over spatial domain can be approximated as the summation over all finite element meshes. Therefore, the fission term can be rewritten as

$$\Delta I_F = \sum_{i=1}^{N} \psi_i^* \delta\boldsymbol{F}_i \psi_i = \sum_{i=1}^{N} \psi_i^* \left(\boldsymbol{F}_i^p - \boldsymbol{F}_i^b\right)\psi_i = \sum_{i=1}^{N} \psi_i^* \boldsymbol{F}_i^p \psi_i - \sum_{i=1}^{N} \psi_i^* \boldsymbol{F}_i^b \psi_i, \tag{3.35}$$

where $\boldsymbol{F}_i^b$ and $\boldsymbol{F}_i^p$ represent the base and perturbed fission operator at mesh i. For sufficiently fine spatial discretization, the material shift from a mesh j to another mesh i can be defined by a mapping

$$i = I(j). \tag{3.36}$$

The perturbed fission operator at mesh i can be written as the unperturbed fission operator at mesh j as

$$\boldsymbol{F}_i^{\,p} = \boldsymbol{F}_j^{b} = \boldsymbol{F}_{I^{-1}(i)}^{b} . \tag{3.37}$$

Substituting Eq. (3.37) into Eq. (3.35) and changing the summation indices of the second term, we have

$$\sum_{i=1}^{N} \psi_i^{\,*} \boldsymbol{F}_{I^{-1}(i)}^{b} \psi_i - \sum_{i=1}^{N} \psi_i^{\,*} \boldsymbol{F}_i^{b} \psi_i = \sum_{i=1}^{N} \psi_i^{\,*} \boldsymbol{F}_{I^{-1}(i)}^{b} \psi_i - \sum_{j=1}^{N} \psi_j^{\,*} \boldsymbol{F}_j^{b} \psi_j . \tag{3.38}$$

In the first term of the right side of Eq. (3.38), the summation over mesh i attached to the fluxes can be converted to the summation over mesh j attached to the fission operator (i.e. material):

$$\sum_{i=1}^{N} \psi_i^{\,*} \boldsymbol{F}_{I^{-1}(i)}^{b} \psi_i = \sum_{j=1}^{N} \psi_{I(j)}^{*} \boldsymbol{F}_j^{b} \psi_{I(j)} . \tag{3.39}$$

As a result, the fission term can be rewritten as

$$\sum_{i=1}^{N} \psi_i^{\,*} \boldsymbol{F}_i^{\,p} \psi_i - \sum_{i=1}^{N} \psi_i^{\,*} \boldsymbol{F}_i^{b} \psi_i = \sum_{j=1}^{N} \psi_{I(j)}^{*} \boldsymbol{F}_j^{b} \psi_{I(j)} - \sum_{j=1}^{N} \psi_j^{\,*} \boldsymbol{F}_j^{b} \psi_j = \sum_{j=1}^{N} \boldsymbol{F}_j^{b} \left(\psi_{I(j)}^{*} \psi_{I(j)} - \psi_j^{\,*} \psi_j \right). \tag{3.40}$$

In general, the shifted finite element mesh may not overlap the finite element at the new location in the original mesh structure, thus the element-averaged forward and adjoint fluxes $\tilde{\psi}_j$ and $\tilde{\psi}_j^{*}$ at the new location would not be equal to the element-averaged fluxes $\psi_{I(j)}$ and $\psi_{I(j)}^{*}$ at the mesh i. Therefore, the element-averaged fluxes $\tilde{\psi}_j$ and $\tilde{\psi}_j^{*}$ are re-evaluated using the VARIANT and PROTEUS-SN solutions. With the re-evaluated element-averaged fluxes, we have

$$\left\langle \psi^{*}, \delta \boldsymbol{F} \psi \right\rangle = \sum_{i=1}^{N} \psi_i^{\,*} \delta \boldsymbol{F}_i \psi_i = \sum_{j=1}^{N} \boldsymbol{F}_j \left(\tilde{\psi}_j^{*} \tilde{\psi}_j - \psi_j^{*} \psi_j \right). \tag{3.41}$$

Similarly, the loss and migration term can be written as

$$\left\langle \psi^{*}, \delta \boldsymbol{A} \psi \right\rangle = \sum_{i=1}^{N} \psi_i^{\,*} \delta \boldsymbol{A}_i \psi_i = \sum_{j=1}^{N} \boldsymbol{A}_j \left(\tilde{\psi}_j^{*} \tilde{\psi}_j - \psi_j^{*} \psi_j \right). \tag{3.42}$$

Figure 3.4 illustrates a simple example where materials 2 to 4 are shifted in material 1. In this figure, an illustrative flux distribution is also given. The Eulerian scheme focuses on the material change in each spatial mesh to which a flux value is given, whereas the Lagrangian scheme focuses on the change in the flux exposed to each material. For example, with the Eulerian scheme, the perturbation of the fission term due to material displacement can be evaluated as

$$\left\langle \psi^{*}, \delta \boldsymbol{F} \psi \right\rangle = [\psi_2^{*}(\boldsymbol{F}_1 - \boldsymbol{F}_2)\psi_2] + [\psi_3^{*}(\boldsymbol{F}_2 - \boldsymbol{F}_3)\psi_3] + [\psi_4^{*}(\boldsymbol{F}_3 - \boldsymbol{F}_4)\psi_4] + [\psi_5^{*}(\boldsymbol{F}_4 - \boldsymbol{F}_1)\psi_5] . \tag{3.43}$$

On the other hand, with the Lagrangian scheme, the perturbation of the fission term can be equivalently written as

$$\begin{aligned}\left\langle \psi^*, \delta \boldsymbol{F}\psi \right\rangle =& (\psi_3^* \boldsymbol{F}_2 \psi_3 - \psi_2^* \boldsymbol{F}_2\psi_2) + (\psi_4^*\boldsymbol{F}_3\psi_4 - \psi_3^*\boldsymbol{F}_3\psi_3) \\ &+ (\psi_5^*\boldsymbol{F}_4\psi_5 - \psi_4^*\boldsymbol{F}_4\psi_4) + (\psi_2^*\boldsymbol{F}_1\psi_2 - \psi_5^*\boldsymbol{F}_1\psi_5)\end{aligned} . \tag{3.44}$$

The spherical harmonic expansion for the angular variable are applied. Since the fission source is isotropic, the fission term ΔI_F can be written in terms of forward and adjoint scalar fluxes as

$$\Delta I_F = \iiint dE dE' dV \chi(E) N(\vec{r}) \nu\sigma_f(E') \left[\tilde{\phi}^*(\vec{r}, E)\tilde{\phi}(\vec{r}, E') - \phi^*(\vec{r}, E)\phi(\vec{r}, E') \right] . \tag{3.45}$$

The integral over energy and space are numerically evaluated by a summation over the finite element mesh i and energy groups g and g':

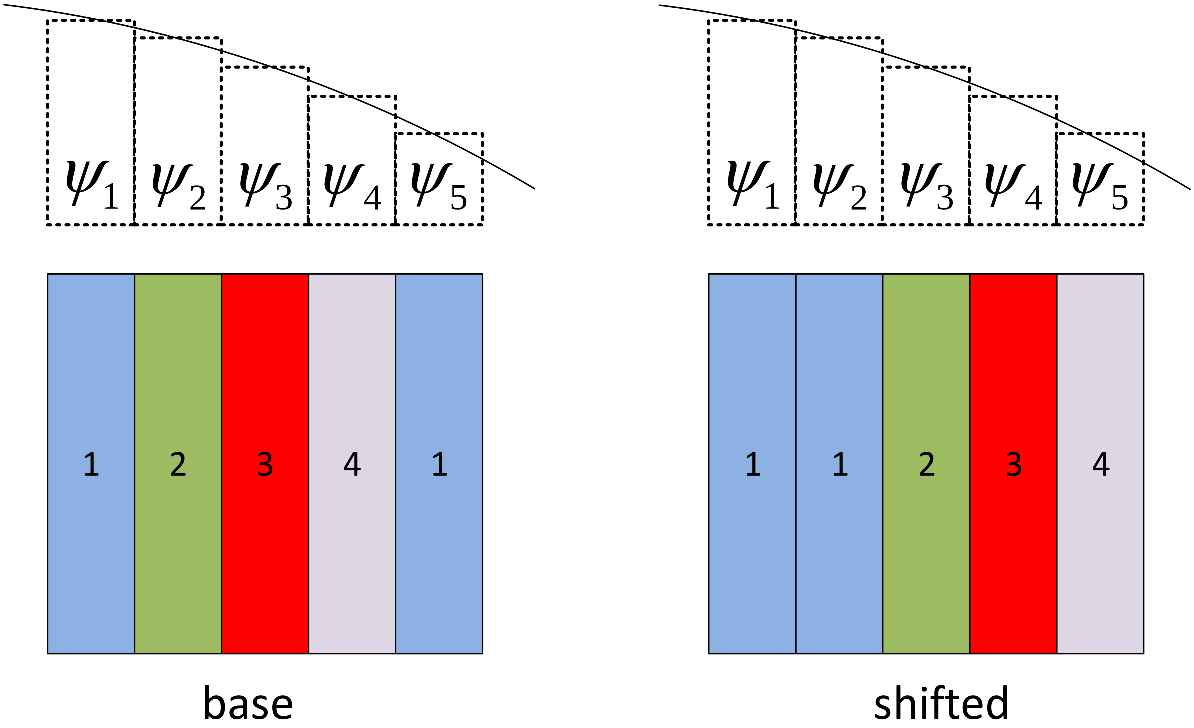

base

shifted

Figure 3.4 Multi-mesh Example of Material Relocation

$$\Delta I_F = \sum_g \chi(g) \sum_{g'} \sum_i N(i) \nu\sigma_f(i, g') \left[\tilde{\phi}(i, g')\tilde{\phi}^*(i, g) - \phi(i, g')\phi^*(i, g) \right] V_e(i) , \tag{3.46}$$

where $V_e(i)$ is the volume of the finite element mesh i.

The loss and migration term ΔI_A can be expressed as the total reaction term minus the scattering source term:

$$\Delta I_A = \Delta I_T - \Delta I_S \, , \tag{3.47}$$

where ΔI_T and ΔI_S are the total and scattering terms, which are defined as

$$\Delta I_T = \iint dVdEN(\vec{r})\sigma_t(\vec{r},E)\int d\hat{\Omega}\left[\tilde{\psi}^*(\vec{r},E,\hat{\Omega})\tilde{\psi}(\vec{r},E,\hat{\Omega}) - \psi^*(\vec{r},E,\hat{\Omega})\psi(\vec{r},E,\hat{\Omega})\right], \tag{3.48}$$

and

$$\Delta I_S = \iint dVdE\sum_{l=0}^{L}\sum_{k=-l}^{l}\int dE'N(\vec{r})\sigma_{s,l}(\vec{r},E'\to E)\left[\tilde{\psi}_{lk}^*(\vec{r},E)\tilde{\psi}_{lk}(\vec{r},E') - \psi_{lk}^*(\vec{r},E)\psi_{lk}(\vec{r},E')\right]. \tag{3.49}$$

For the scattering source term, the spatial and energy integration can be done in a similar manner to that of the fission term ΔI_F. By taking into account the space and energy discretization, we have

$$\Delta I_S = \sum_{g}\sum_{g'}\sum_{i} N(i)\sum_{l=0}^{L}\sigma_{s,l}(i,g'\to g)\sum_{k=-l}^{l}\left[\tilde{\phi}_{lk}(i,g')\tilde{\phi}_{lk}^*(i,g) - \phi_{lk}(i,g')\phi_{lk}^*(i,g)\right]V_e(i)\, , \tag{3.50}$$

where $\phi_{lk}(i,g)$ and $\phi_{lk}^*(i,g)$ (same with $\tilde{\phi}_{lk}(i,g)$ and $\tilde{\phi}_{lk}^*(i,g)$) are discretized angular moment in space and energy, which can be obtained by evaluating the VARIANT solutions stored in the NHFLUX and NAFLUX datasets at reference and shifted positions.

The expression of numerical evaluation of ΔI_T can be obtained in a similar way to derive ΔI_S. The angular fluxes $\psi(\hat{\Omega})$ and $\psi^*(\hat{\Omega})$ were expanded in terms of spherical harmonics as

$$\psi(\vec{r},E,\hat{\Omega}) = \sum_{l=0}^{L}\sum_{k=-l}^{l}\psi_{lk}(\vec{r},E)Y_{lk}(\hat{\Omega}) \tag{3.51}$$

and

$$\psi^*(\vec{r},E,\hat{\Omega}) = \sum_{l=0}^{L}\sum_{k=-l}^{l}\psi_{lk}^*(\vec{r},E)Y_{lk}^*(\hat{\Omega})\, . \tag{3.52}$$

Using the orthogonal relation of spherical harmonics

$$\int d\hat{\Omega}Y_{lk}(\hat{\Omega})Y_{l'k'}^*(\hat{\Omega}) = \delta_{ll'}\delta_{kk'}\, , \tag{3.53}$$

we have

$$\begin{aligned}&\int d\hat{\Omega}\left[\tilde{\psi}^*(\vec{r},E,\hat{\Omega})\tilde{\psi}(\vec{r},E,\hat{\Omega}) - \psi^*(\vec{r},E,\hat{\Omega})\psi(\vec{r},E,\hat{\Omega})\right] \\ &= \sum_{l=0}^{L}\sum_{k=-l}^{l}\left[\tilde{\psi}_{lk}^*(\vec{r},E)\tilde{\psi}_{lk}(\vec{r},E) - \psi_{lk}^*(\vec{r},E)\psi_{lk}(\vec{r},E)\right]\end{aligned}\, . \tag{3.54}$$

Inserting Eq. (3.54) into Eq.(3.48), we have

$$\Delta I_T = \iint dVdE \sum_{l=0}^{L} \sum_{k=-l}^{l} N(\vec{r})\sigma_t(\vec{r},E)\left[\tilde{\psi}_{lk}^*(\vec{r},E)\tilde{\psi}_{lk}(\vec{r},E) - \psi_{lk}^*(\vec{r},E)\psi_{lk}(\vec{r},E)\right]. \tag{3.55}$$

By taking into account the space and energy discretization, the total reaction term can be written as

$$\Delta I_T = \sum_g \sum_i N(i)\sigma_t(i,g) \sum_{l=0}^{L} \sum_{k=-l}^{l} \left[\tilde{\phi}_{lk}(i,g)\tilde{\phi}_{lk}^*(i,g) - \phi_{lk}(i,g)\phi_{lk}^*(i,g)\right] V_e(i) . \tag{3.56}$$

In summary, a set of discretized perturbation formula for calculation of the reactivity worth of shifting assembly n was obtained as

$$\Delta\rho(n) = -\frac{\Delta I_A(n) - \Delta I_F(n)}{I_F} , \tag{3.57}$$

$$\Delta I_A(n) = \Delta I_T(n) - \Delta I_S(n) \ , \tag{3.58}$$

$$I_F = \left\langle \psi^*, F\psi \right\rangle \ , \tag{3.59}$$

$$\begin{cases} \Delta I_T\left(n\right) = \sum\limits_g \sum\limits_i N(n,i)\sigma_t(n,i,g) \sum\limits_{l=0}^{L} \sum\limits_{k=-l}^{l} \begin{bmatrix} \tilde{\phi}_{lk}(n,i,g)\tilde{\phi}_{lk}^*(n,i,g) - \\ \phi_{lk}(n,i,g)\phi_{lk}^*(n,i,g) \end{bmatrix} V_e(n,i) \\ \Delta I_S\left(n\right) = \sum\limits_g \sum\limits_{g'} \sum\limits_i N(n,i) \sum\limits_{l=0}^{L} \sigma_{s,l}(n,i,g' \to g) \sum\limits_{k=-l}^{l} \begin{bmatrix} \tilde{\phi}_{lk}(n,i,g')\tilde{\phi}_{lk}^*(n,i,g) - \\ \phi_{lk}(n,i,g')\phi_{lk}^*(n,i,g) \end{bmatrix} V_e(n,i) \\ \Delta I_F\left(n\right) = \sum\limits_g \chi(n,g) \sum\limits_{g'} \sum\limits_i N\left(n,i\right)\nu\sigma_f\left(n,i,g'\right) \begin{bmatrix} \tilde{\phi}_{00}(n,i,g')\tilde{\phi}_{00}^*(n,i,g) - \\ \phi_{00}(n,i,g')\phi_{00}^*(n,i,g) \end{bmatrix} V_e(n,i) \\ I_F = \sum\limits_n \sum\limits_g \chi(n,g) \sum\limits_{g'} \sum\limits_i N\left(n,i\right)\nu\sigma_f\left(n,i,g'\right)\phi_{00}(n,i,g')\phi_{00}^*(n,i,g)V_e(n,i) \end{cases} , \tag{3.60}$$

where N is the nuclide density, σ_t is the total cross section, σ_s is the scattering cross section, $\nu\sigma_f$ is the fission yield cross section, χ is the fission spectrum and V_e is the volume of the finite element. ϕ_{lk} and $\tilde{\phi}_{lk}$ are the angular flux moments at the original and shifted locations. Similarly, ϕ_{lk}^* and $\tilde{\phi}_{lk}^*$ are the adjoint angular flux moments at the original and shifted locations. ϕ_{00} and ϕ_{00}^* are the forward and adjoint scalar fluxes. The indices n, g, i and l in Eq. (3.60) represent the node number, the energy group number, the finite element number, and the Legendre order, respectively. Equations (3.57) to Eq. (3.60) are the final expressions that are used in the numerical implementation of the first order perturbation theory method for calculating the reactivity worth of assembly displacement.

3.4 Perturbation Theory Method for Fuel Axial Expansion

The fuel axial expansion results in perturbations of material property in three regions as shown in Figure 3.5. The original fuel nuclide density is reduced in the fuel region. Part of boundary sodium is replaced by expanded fuel region. Part of fission gas plenum region is replaced by bond sodium.

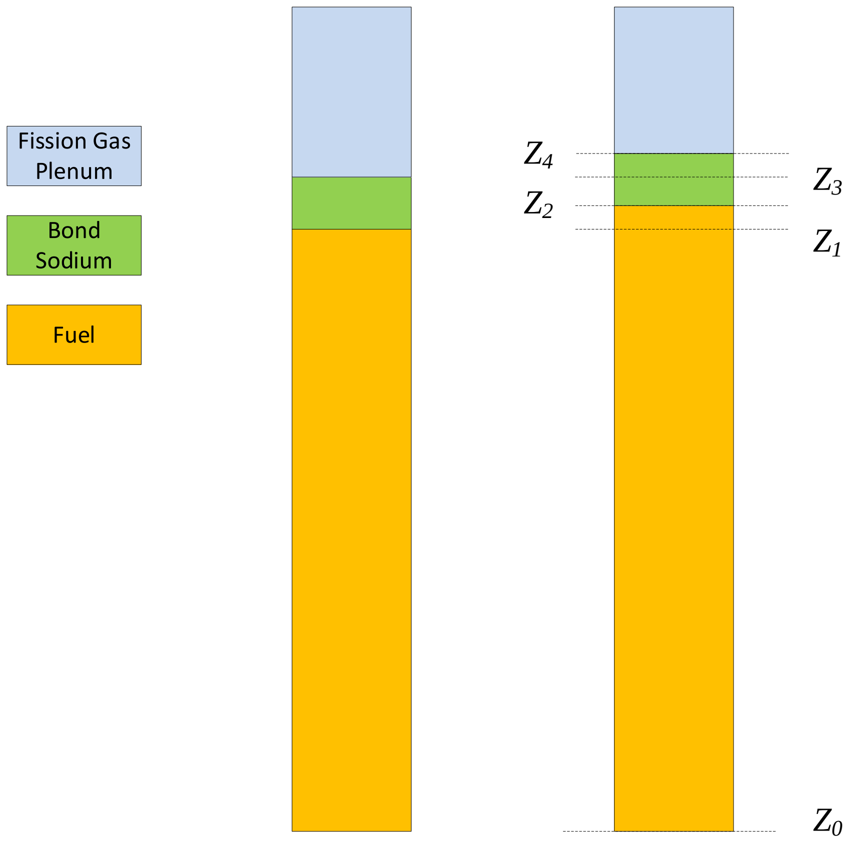

Figure 3.5 Illustration of Fuel Axial Expansion Model

The reactivity worth due to fuel axial expansion can be calculated by applying the conventional perturbation theory method for material property perturbation to the three perturbed regions. For the original fuel region, the reactivity change $\Delta\rho_{i,\,fuel}$ due to the nuclide density change in assembly i can be write as

$$\Delta\rho_{i,fuel} = \frac{\int_{z_0}^{z_1} \psi_i^*(z)\left[A'_{i,f}(z) - A_{i,f}(z)\right]\psi_i(z)dz}{I_F}, \tag{3.61}$$

where ψ_i and ψ_i^* are forward and adjoint fluxes in assembly i, $A_{i,f}$ and $A'_{i,f}$ represent the original and perturbed transport operator for fuel assembly i. I_F is the whole core fission integral defined by Eq. (3.59). Similarly, the reactivity perturbation for perturbed bond sodium and perturbed fission gas plenum regions are given by

$$\Delta\rho_{i,sodium} = \frac{\int_{z_1}^{z_2} \psi_i^*(z)\left[A'_f(z) - A_s(z)\right]\psi_i(z)dz}{I_F}, \tag{3.62}$$

and

$$\Delta\rho_{i,fission\_gas\_plenum} = \frac{\int_{z_3}^{z_4} \psi_i^*(z)\left[A_s(z) - A_{fg}(z)\right]\psi_i(z)dz}{I_F}. \tag{3.63}$$

The reactivity worth of fuel axial expansion can be obtained by combining the three components

$$\Delta\rho_{i,axial\_expansion} = \Delta\rho_{i,fuel} + \Delta\rho_{i,sodium} + \Delta\rho_{i,fission\_gas\_plenum} \tag{3.64}$$

Note that the perturbation method presented in this section produces the reactivity coefficients of fuel axial expansion for individual fuel assemblies. The whole core reactivity change due to fuel axial expansion can be calculated by combining the fuel axial expansion coefficients and the magnitude of axial expansions for individual assemblies.

4. REACTIVITY FEEDBACK EFFECTS DUE TO CORE DEFORMATION

A series of investigations was performed to develop an efficient and accurate procedure for assessing the feedback reactivity due to core deformation. We investigated the reactivity effects of assembly bowing, core grid-plate radial expansion, fuel axial expansion and assembly duct radial expansion. We also studied the assembly heterogeneity effect on assembly displacement worth and fuel axial expansion worth. An investigation on the additivity of the assembly displacement worth has been performed to qualify the idea of using pre-calculated assembly displacement worth coefficients for evaluating the bowing reactivity.

4.1 Assembly Bowing

4.1.1 Heterogeneity Effect

The proposed perturbation theory method aims at accurately evaluating the reactivity worth due to displacement of heterogeneous assembly. In this section, we investigated the assembly heterogeneity effect on the reactivity change due to assembly displacement. The heterogeneity effect on the reactivity worth of displaced assemblies was investigated using the Advanced Burner Test Reactor (ABTR) [58] problem and a three-dimensional (3D) mini-core problem that was derived from the ABTR with reduced number of assemblies and core height. The reactivity change caused by assembly displacement was obtained by direct eigenvalue comparisons between the base and shifted assembly cases. Three assembly models with different heterogeneity levels were used: original heterogeneous assembly, partially heterogeneous assembly, and homogeneous assembly.

4.1.1.1 Advanced Burner Test Reactor (ABTR) Problem

The configuration of the reference 250 MWt ABTR metal core design is shown in Figure 4.1. It consists of 54 driver assemblies fueled with weapons-grade plutonium, 78 reflectors, 48 shields, 10 control assemblies and 9 test assemblies. The material test assemblies are filled with reflector assemblies and the test-fuel assemblies are fueled with the TRU recovered from light water reactor (LWR) spent fuel instead of weapons-grade plutonium. The circular core barrel and surrounding sodium are represented by 54 background hexagonal assemblies (barrel) without axial heterogeneity. The calculations were performed using the MCNP6 [59] code with ENDFVII.0

library [60]. MCNP6 simulations were carried out with one million neutrons per cycle and 1550 active and 450 inactive cycles. The multiplication factors converged with a standard deviation of one pcm.

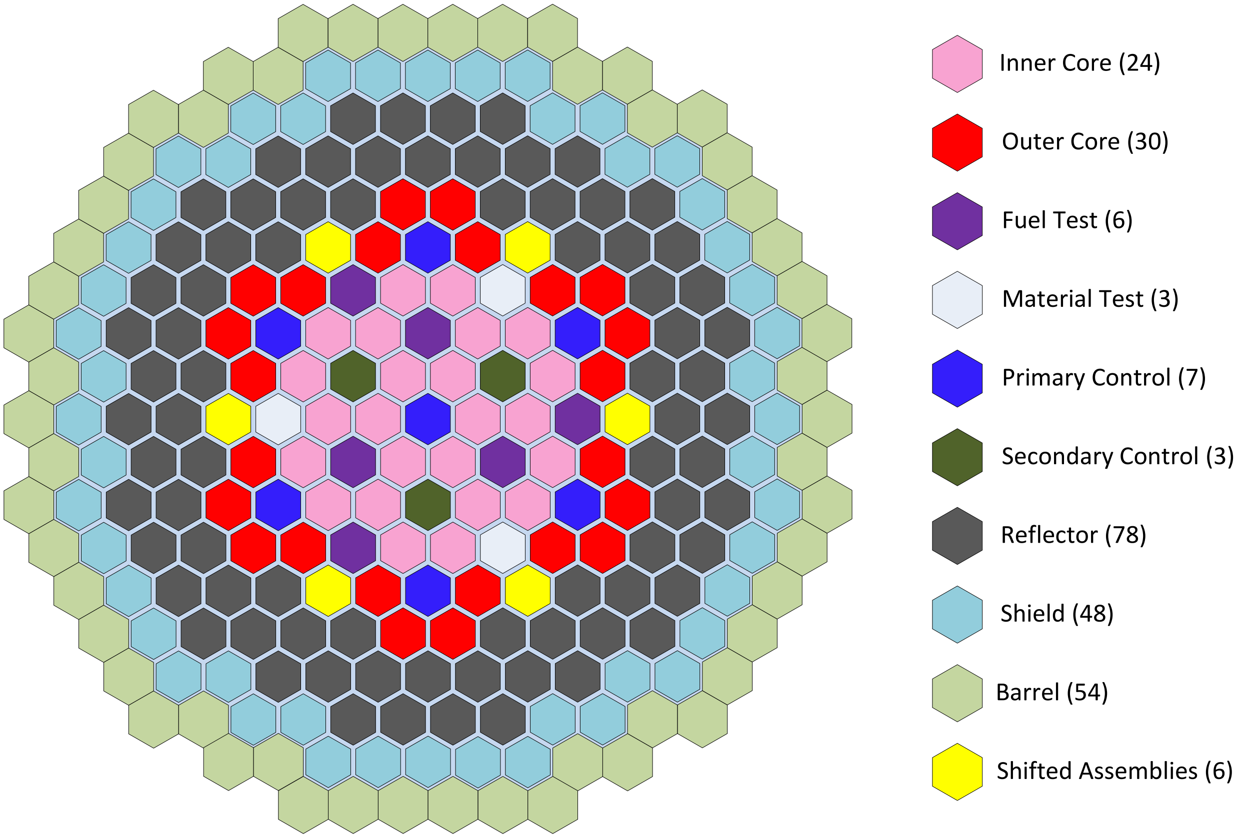

Figure 4.1 Radial Layout of ABTR Core Model

The reactivity changes due to displacing the outer core fuel assemblies marked with yellow color in Figure 4.1 were examined. Both individual and simultaneous displacements of these six assemblies were considered. The selected outer core fuel assemblies were shifted radially outward by 2 mm, which is less than the inter-assembly sodium gap thickness of 4 mm. For this small displacement, an assembly shift does not involve rearrangement of the neighboring assemblies. The axial configurations of the base and the shifted fuel assembly are shown in Figure 4.2. The fuel assembly were divided into six axial regions in MCNP6 simulations: lower structure, lower reflector, fuel, bond sodium, upper gas plenum and upper structure regions (from the bottom to the top). Homogenized models were used for the upper and lower structure regions. Three different heterogeneity levels were used for the upper gas plenum, bond sodium, fuel and lower reflector regions. For the homogeneous model, each axial segment of assembly was homogenized while the inter-assembly sodium gap was explicitly modeled. For the partially heterogeneous model, only the interior region of the duct was homogenized while the duct wall and the inter-assembly sodium gap were explicitly modeled. For the heterogeneous model, each fuel pin and duct wall were explicitly represented. The three models of base and shifted assemblies are compared in Figure 4.3. In these calculations, heterogeneous models were used for control, reflector, shield and test assemblies while the barrel assemblies were homogenized.

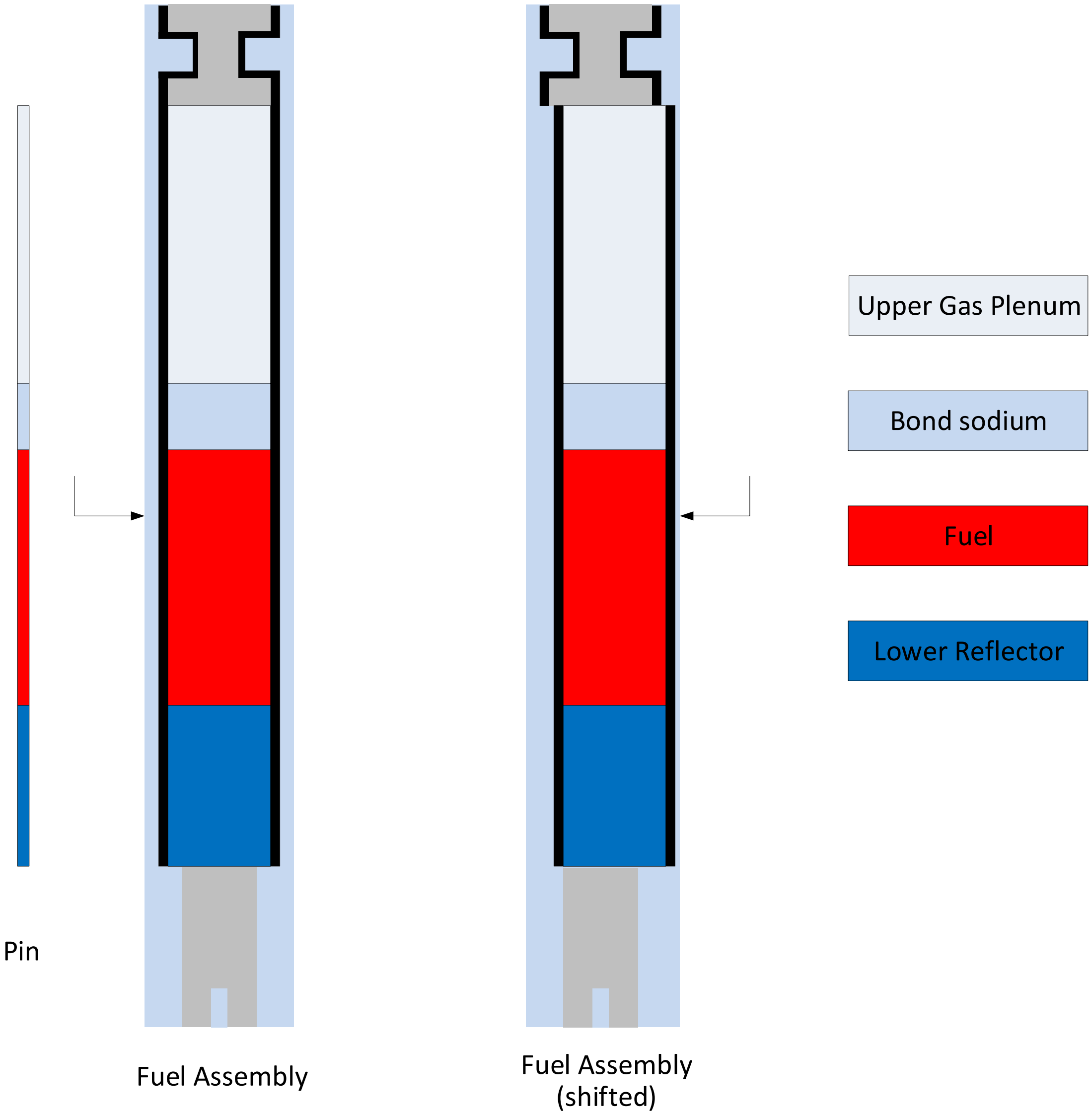

Figure 4.2 Fuel Assembly Axil Profiles

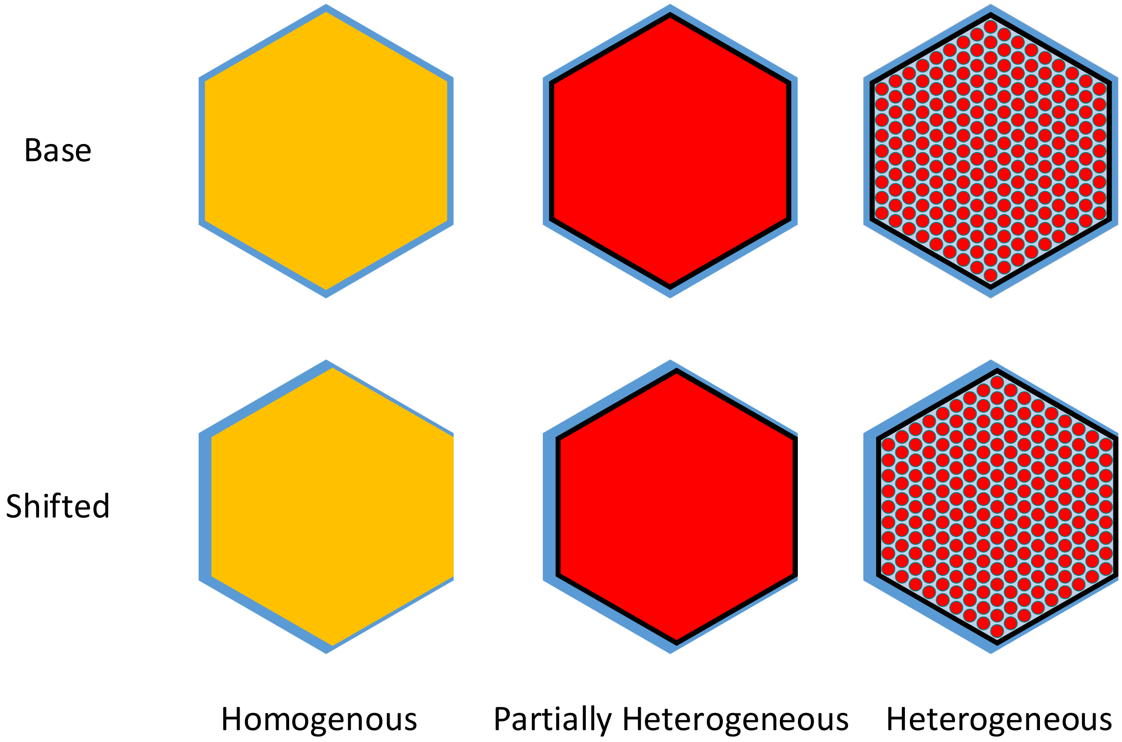

Figure 4.3 Base and Shifted Assembly Radial Layouts with Three Levels of Heterogneity

Table 4.1 compares the estimated fuel pin and duct wall heterogeneity effects of an outer fuel assembly with the results in Reference 61. It can be seen that the duct heterogeneity effect on the multiplication factor is significantly larger than that of fuel pins. The duct wall heterogeneity effect is 238 pcm and the fuel pin heterogeneity effect is 69 pcm, yielding a total assembly heterogeneity effect of 307 pcm. These results are consistent with the benchmark results presented in Reference 61, which were obtained using MCNP5 with ENDF/B-V cross section library.

Table 4.1 Duct and Fuel Pin Heterogeneity Effects of Outer Core Assembly on Multiplication Factor of ABTR

	MCNP6 & ENDF/B-VII.0	MCNP5 & ENDF/B-V [61]
Duct (pcm)	238 ± 1.4	249 ± 34
Pins (pcm)	69 ± 1.4	52 ± 34
Total (pcm)	307 ± 1.4	301 ± 36

Table 4.2 summarizes the assembly heterogeneity effects on the eigenvalue and assembly displacement worth. The reactivity change is about 5 pcm for single outer fuel assembly

displacement and about 30 pcm for six assembly displacements. The heterogeneity effect of fuel pins on the reactivity change due to fuel assembly displacements is practically zero, and the heterogeneity effect of duct wall is -2 pcm for the single assembly displacement and -3 pcm for the displacement of 6 assemblies. In other words, the assembly displacement worth determined with the partially heterogeneous assembly model is the same to the value obtained with the heterogeneous assembly model, but a slightly overestimated value is obtained with the homogeneous model. However, the reactivity change is very small even for the case of six assemblies displaced, and the difference in estimated assembly displacement worth between the homogeneous and heterogeneous models is comparable to the MCNP6 standard deviation. Further studies would be needed with larger perturbations.

Table 4.2 Assembly Homogenization Effects on Fuel Assembly Displacement Worth in ABTR

	Homogeneous		Partially Hetero.		Heterogeneous	
Multiplication Factors	mean	STD	mean	STD	mean	STD
Base	1.03582	0.00001	1.03820	0.00001	1.03889	0.00001
Single Assembly Shifted	1.03576	0.00001	1.03816	0.00001	1.03885	0.00001
Six Assemblies Shifted	1.03551	0.00001	1.03792	0.00001	1.03861	0.00001
Displacement Worth (pcm)	mean	STD	mean	STD	mean	STD
Single Assembly	-6	1.4	-4	1.4	-4	1.4
Six Assemblies	-31	1.4	-28	1.4	-28	1.4

4.1.1.2 Three-Dimensional Mini-Core Problem

In order to introduce larger perturbations, the homogenization effect on the assembly displacement worth was examined for a 3D mini-core problem. This mini-core problem was derived from the ABTR benchmark problem with reduced number of assemblies, axial complexity and core height. Figure 4.4 shows the radial layout of the mini-core. The core has an extruded geometry in axial direction. The core height is 84.4 cm. The mini-core has three rings of inner fuel assemblies, three rings of reflector assemblies and approximately one ring of barrel assemblies taken from ABTR model. The reactivity worth of a single assembly displacement was ~25 pcm for the fuel assembly located at the third ring, which is much larger than that for an ABTR outer fuel assembly due to the smaller core size and thus a larger leakage effect in the mini-core model. With this mini-core model, the physical effect of assembly homogenization on the assembly displacement worth could be well separated from the statistical errors of Monte Carlo simulations. With the original nuclide densities of ABTR, the significantly reduced amount of fuel in the core makes the mini-core deeply subcritical. Thus, another critical mini-core problem was devised by increasing the plutonium atomic fraction in the fuel from 16% to 23%. The fuel composition of the critical mini-core is presented in Appendix A.

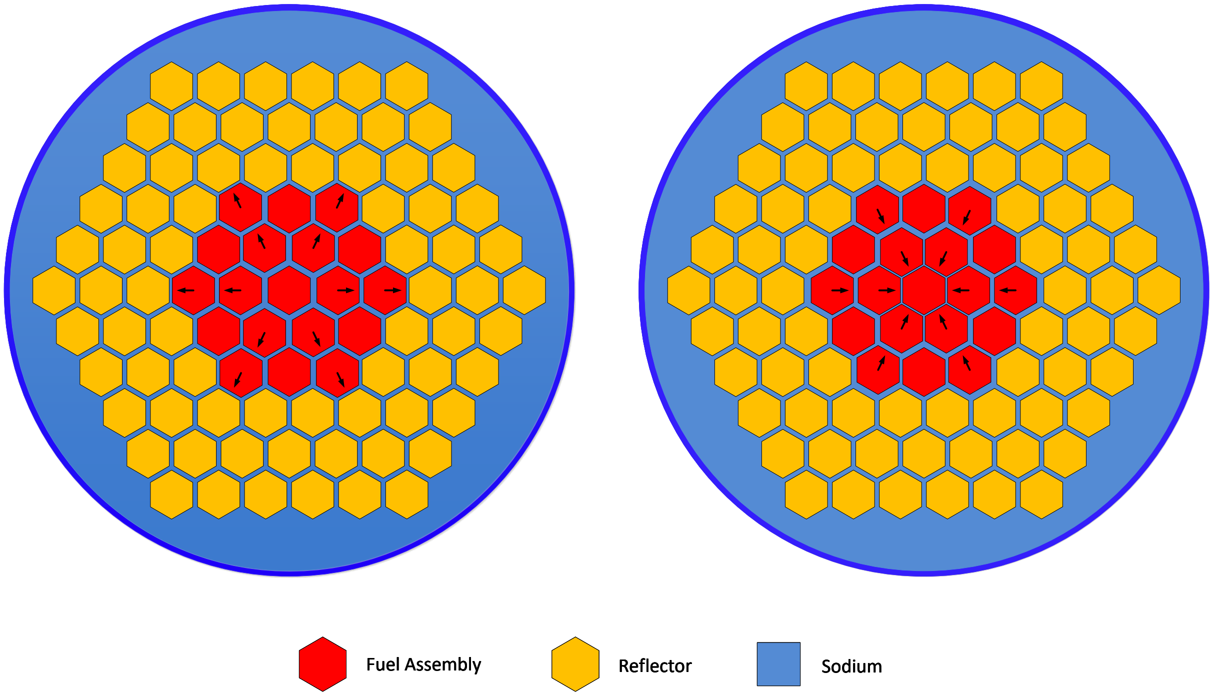

Figure 4.4 Radial Layout of Mini-Core Model with Fuel Assemblies Shifted Radially Outwards (Left) and Inwards (Right) from Core Center

Twelve fuel assemblies located at the second and third rings of the core were displaced radially inwards or outwards from the core center by 2 mm. The shifted assemblies were marked with arrows in Figure 4.4. The single assembly displacement worth was also calculated for one fuel assembly at the third ring. The neutronics simulations were performed using the MCNP6 code with the ENDF/B-VII.0 library. The simulations were carried out with one million neutrons per cycle and 1550 active and 450 inactive cycles. The eigenvalue converged with one pcm standard deviation. Homogenization effects of fuel and reflector assemblies were separately examined using two core configurations. Both fuel and reflector assemblies were represented heterogeneously in one configuration as shown in the left figure of Figure 4.5, but the reflector assemblies were homogenized in the other configuration as shown in the right figure of Figure 4.5. As in the ABTR case, the reactivity change due to fuel assembly displacements were evaluated using three different heterogeneity levels. In the first core configuration, the three different assembly models were used for both fuel and reflector assemblies, but in the second configuration, they were used only for fuel assemblies while retaining the homogenized reflector assemblies.

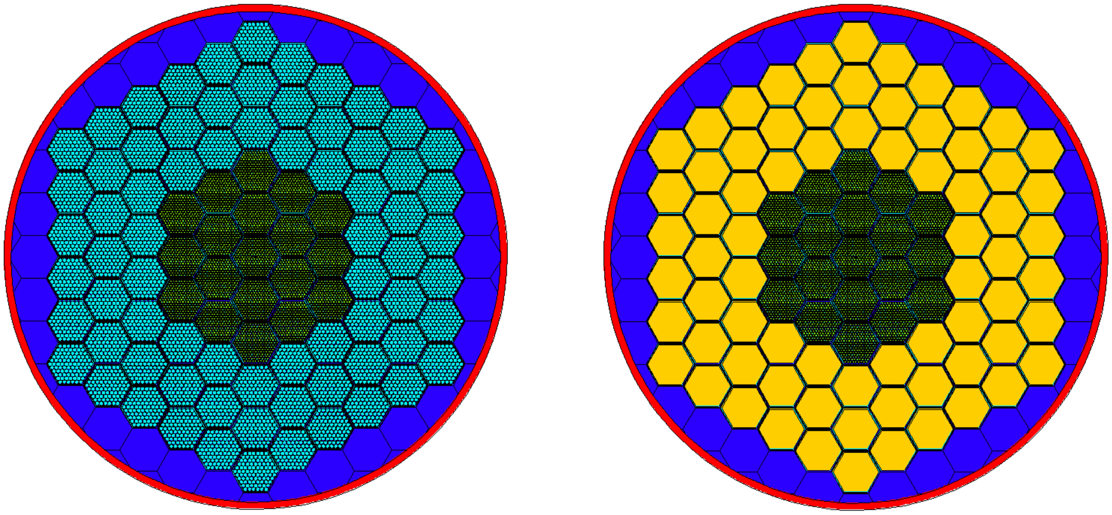

Figure 4.5 MCNP6 Models of Mini-Core with Heterogeneous Fuel and Reflector Assemblies (Left) and with Heterogeneous Fuel and Homogeneous Reflector Assemblies (Right)

Table 4.3 and Table 4.4 show the homogenization effects of fuel and reflector assemblies investigated with the first core configuration. Table 4.3 shows the fuel and reflector assembly homogenization effects on the reactivity worth of displaced fuel assemblies for the subcritical mini-core with original ABTR nuclide densities. For the displacement of single fuel assembly in the third fuel ring, the three different assembly models yielded the same displacement worth around -24 pcm within two standard deviations. That is, the heterogeneity effects of duct walls and fuel pins on the reactivity worth of the displaced fuel assembly are practically zero. When the twelve fuel assemblies were displaced inwards, the homogeneous, partially heterogeneous, and fully heterogeneous assembly models yielded reactivity changes of 296, 280, and 282 pcm, respectively. When the twelve fuel assemblies were displaced outward, the corresponding reactivity changes are -293, -284, and -278 pcm, respectively. These results indicate that the heterogeneity effect of fuel pins on the reactivity change due to fuel assembly displacement is negligible, and the heterogeneity effect of duct walls is 5.7% of the displacement worth for the outward displacement and 3.2% of the displacement worth for the inward displacement.

Similarly, Table 4.4 shows the fuel and reflector assembly homogenization effects on the reactivity worth of displaced fuel assemblies for the critical mini-core with increased plutonium fraction in the fuel. Since the increased fissile fraction increases the fuel worth, the reactivity worth of the fuel assembly displacement is larger than that in the subcritical mini-core. For the displacement of single fuel assembly, the three different assembly models yielded the same displacement worth around -31 pcm within two standard deviations. That is, the heterogeneity effects of duct walls and fuel pins on the reactivity worth of the displaced fuel assembly are practically zero. When the twelve fuel assemblies were displaced inwards, the homogeneous, partially heterogeneous, and fully heterogeneous assembly models yielded reactivity changes of 347, 330, and 326 pcm, respectively. When the twelve fuel assemblies were displaced outward, the corresponding reactivity changes are -344, -332, and -328 pcm, respectively. The estimated heterogeneity effect of fuel pins on the reactivity change due to fuel assembly displacement is negligible, and the heterogeneity effect of duct walls is 5.2% of the displacement worth for the outward displacement and 3.7% of the displacement worth for the inward displacement.

Table 4.3 Fuel and Reflector Assembly Homogenization Effects on Fuel Assembly Displacement Worth in Subcritical Mini-Core with Original Nuclide Densities

	Homogeneous		Partially Hetero.		Heterogeneous	
Multiplication Factors	mean	STD	mean	STD	mean	STD
Base	0.80899	0.00001	0.81343	0.00001	0.81658	0.00001
Shifted Inwards	0.81195	0.00001	0.81623	0.00001	0.81940	0.00001
Shifted Outwards	0.80606	0.00001	0.81059	0.00001	0.81380	0.00001
Single Assembly Outwards	0.80875	0.00001	0.81317	0.00001	0.81634	0.00001
Displacement Worth (pcm)	mean	STD	mean	STD	mean	STD
Shifted Inwards	296	1.4	280	1.4	282	1.4
Shifted Outwards	-293	1.4	-284	1.4	-278	1.4
Single Assembly Outwards	-24	1.4	-26	1.4	-24	1.4

Table 4.4 Fuel and Reflector Assembly Homogenization Effects on Fuel Assembly Displacement Worth in Critical Mini-Core with Increased Plutonium Fraction

	Homogeneous		Partially Hetero.		Heterogeneous	
Multiplication Factors	mean	STD	mean	STD	mean	STD
Base	0.99912	0.00001	1.00406	0.00001	1.00751	0.00001
Shifted Inwards	1.00259	0.00001	1.00736	0.00001	1.01077	0.00001
Shifted Outwards	0.99568	0.00001	1.00074	0.00001	1.00423	0.00001
Single Assembly Outwards	0.99878	0.00001	1.00376	0.00001	1.00720	0.00001
Displacement Worth (pcm)	mean	STD	mean	STD	mean	STD
Shifted Inwards	347	1.4	330	1.4	326	1.4
Shifted Outwards	-344	1.4	-332	1.4	-328	1.4
Single Assembly Outwards	-34	1.4	-30	1.4	-31	1.4

Table 4.5 summarizes the duct and pin heterogeneity effects of fuel and reflector assemblies on the multiplication factor itself. In the subcritical core with the original ABTR nuclide densities, the heterogeneity effect of fuel and reflector assembly ducts on eigenvalue is 444 pcm and that of fuel and reflector pins is 315 pcm, yielding a total assembly heterogeneity effect of 759 pcm. For the critical core with increased plutonium fraction in the fuel, the duct heterogeneity effect is 494 pcm and the pin heterogeneity effect is 345 pcm, yielding a total assembly heterogeneity effect is 839 pcm. It can be seen that for both mini-cores, the assembly homogenization consistently increases the multiplication factor and the duct heterogeneity effect is significantly larger than the pin heterogeneity effect. It is also noted that both the duct and pin heterogeneity effects are larger in the critical core with increased plutonium fraction since the increased fissile fraction increases the fuel worth and thus the effects of mixing the fuel with coolant and subsequently with duct become more significant.

Table 4.5 Duct and Pin Heterogeneity Effects of Fuel and Reflector Assemblies on Multiplication Factor of Mini-Cores

	Subcritical Core	Critical Core
Duct (pcm)	444 ± 1.4	494± 1.4
Pins (pcm)	315± 1.4	345± 1.4
Total (pcm)	759± 1.4	839± 1.4

Table 4.6 and Table 4.7 show the fuel assembly homogenization effects investigated with the second core configuration. Table 4.6 shows the fuel assembly homogenization effects on the reactivity worth of displaced fuel assemblies for the subcritical mini-core with original ABTR nuclide densities. It can be seen that the reactivity changes due to the three different displacements of fuel assemblies are very similar to the corresponding values in Table 4.3, which were obtained with homogenizing both fuel and reflector assemblies. These results indicate that the displacement worth of fuel assemblies is independent of the reflector assembly homogenization. The estimated heterogeneity effect of fuel pins on the reactivity change due to fuel assembly displacement is negligible, and the heterogeneity effect of duct walls is 5.7% of the displacement worth for the outward displacement of 12 fuel assemblies and 2.1% for the inward displacement of 12 fuel assemblies.

Table 4.6 Fuel Assembly Homogenization Effects on Fuel Assembly Displacement Worth in Subcritical Mini-Core with Original Nuclide Densities

	Homogeneous		Partially Hetero.		Heterogeneous	
Multiplication Factors	mean	STD	mean	STD	mean	STD
Base	0.81082	0.00001	0.81343	0.00001	0.81689	0.00001
Shifted Inwards	0.81378	0.00001	0.81623	0.00001	0.81971	0.00001
Shifted Outwards	0.80792	0.00001	0.81059	0.00001	0.81404	0.00001
Single Assembly Outwards	0.81056	0.00001	0.81317	0.00001	0.81664	0.00001
Displacement Worth (pcm)	mean	STD	mean	STD	mean	STD
Shifted Inwards	296	1.4	280	1.4	282	1.4
Shifted Outwards	-290	1.4	-284	1.4	-285	1.4
Single Assembly Outwards	-26	1.4	-26	1.4	-24	1.4

Table 4.7 shows the fuel assembly homogenization effects on the reactivity worth of displaced fuel assemblies for the critical mini-core with increased plutonium fraction in the fuel. It can be seen that the reactivity changes due to the three different displacements of fuel assemblies are very similar to the corresponding values in Table 4.4, which were obtained with homogenizing both fuel and reflector assemblies. These results again indicate that the displacement worth of fuel assemblies is independent of the reflector assembly homogenization. The estimated heterogeneity

effect of fuel pins on the reactivity change due to fuel assembly displacement is negligible, and the heterogeneity effect of duct walls is 3.1% of the displacement worth for the outward displacement of 12 fuel assemblies and 3.6% for the inward displacement of 12 fuel assemblies.

Table 4.7 Fuel Assembly Homogenization Effects on Fuel Assembly Displacement Worth in Critical Mini-Core with Increased Plutonium Fraction

	Homogeneous		Partially Hetero.		Heterogeneous	
Multiplication Factors	mean	STD	mean	STD	mean	STD
Base	1.00138	0.00001	1.00406	0.00001	1.00782	0.00001
Shifted Inwards	1.00478	0.00001	1.00736	0.00001	1.01109	0.00001
Shifted Outwards	0.99794	0.00001	1.00074	0.00001	1.00453	0.00001
Single Assembly Outwards	1.00105	0.00001	1.00376	0.00001	1.00750	0.00001
Displacement Worth (pcm)	mean	STD	mean	STD	mean	STD
Shifted Inwards	340	1.4	330	1.4	327	1.4
Shifted Outwards	-344	1.4	-332	1.4	-329	1.4
Single Assembly Outwards	-33	1.4	-30	1.4	-32	1.4

Table 4.8 summarizes the duct and pin heterogeneity effects of fuel assemblies on the multiplication factor itself. In the subcritical core, the heterogeneity effect of fuel assembly ducts on eigenvalue is 261 pcm and that of fuel pins is 346 pcm, yielding a total assembly heterogeneity effect of 607 pcm. For the critical core with increased plutonium fraction in the fuel, the fuel assembly duct heterogeneity effect is 268 pcm and the fuel pin heterogeneity effect is 376 pcm, yielding a total assembly heterogeneity effect is 644 pcm. For both the subcritical and critical mini-cores, the heterogeneity effect of fuel assembly ducts is about 100 pcm smaller than the heterogeneity effect of fuel pins. By comparing with the results in Table 4.5, it can be deduced that the heterogeneity effect of reflector assembly ducts is 183 pcm for the subcritical mini-core and 226 pcm for the critical mini-core while the heterogeneity effect of reflector pins is -31 pcm for both cores. These results indicate that in reflector assemblies, the duct heterogeneity effect is significantly larger than the pin heterogeneity effect. The heterogeneity effect of fuel pins on the multiplication factor is larger than that of fuel assembly ducts, but the pin heterogeneity effects in the reference and displaced fuel assemblies are almost the same and hence cancelled out for the

reactivity worth of fuel assembly displacement. As a result, the duct heterogeneity effect becomes predominant for the reactivity worth of fuel assembly displacement.

Table 4.8 Duct and Pin Heterogeneity Effects of Fuel Assemblies on Multiplication Factor of Mini-Cores

	Subcritical Core	Critical Core
Duct (pcm)	261 ± 1.4	268 ± 1.4
Pins (pcm)	346± 1.4	376± 1.4
Total (pcm)	607± 1.4	644± 1.4

The reactivity change caused by assembly displacement can be estimated by the perturbed neutron balance caused by the changes in the competing reaction and leakage rates. Thus, the reactivity change can be written in terms of those components as follows:

$$total\ effect = fission\ production - absorption - axial\ leakage - radial\ leakage\,, \tag{4.1}$$

where the elastic and inelastic scattering terms are not included since they have negligible contribution to the neutron balance in the case of assembly displacement that involves no spectral shift. The contributions of individual reaction and leakage components to the reactivity change were estimated using the reaction rate and current tallies in the reference and displaced assembly cases. In MCNP6 simulations, the tallied reaction rates were normalized to one fission neutron produced in the whole core (i.e. $\nu\Sigma_f\phi_{core} = 1$). As a result, the reactivity change due to the changes in fission production and absorption rates is the variations of the reaction rates tallied in the shifted assembly cells. The leakage contribution to the displacement worth is the change in the neutron leakage at the radial and axial boundary surfaces of the core. Each components of the assembly displacement worth can be expressed as

$$\Delta\rho_{fission\_production} = \frac{\Delta(\nu\Sigma_f\phi)_{shifted\_assembly}}{(\nu\Sigma_f\phi)_{core}}\,, \tag{4.2}$$

$$\Delta\rho_{absorption} = \frac{\Delta(\Sigma_a\phi)_{shifted\_assembly}}{(\nu\Sigma_f\phi)_{core}/k}\,, \tag{4.3}$$

$$\Delta\rho_{leakage,\ radial/axial} = \frac{\Delta L_{radial/axial\ surface\ of\ core}}{(\nu\Sigma_f\phi)_{core}/k}\,. \tag{4.4}$$

Table 4.9 shows the contributions of fission production, absorption and leakage on the reactivity worth of fuel assembly displacement evaluated with homogeneous, partially heterogeneous and heterogeneous assembly models. This evaluation was performed for the critical mini-core with increased plutonium fraction in the fuel while considering the reflector heterogeneity, that is, for the case presented in Table 4.3 . A single fuel assembly located at the third ring of the core was shifted outwards by 2 mm. As shown in Table 4.9, the contributions of fission production, absorption, axial and radial leakages to the assembly displacement worth were -30, -14, 11, and 4 pcm, respectively. The summation of these four components yields a total reactivity worth of -30 pcm, which is very close to the value of -31 pcm determined from the reference and perturbed multiplication factors. This result indicates that the reactivity worth of a single assembly displacement can be approximately determined by the reaction rates in the perturbed domain without considering the variations in the reaction rates in the regions outside the perturbed domain. The partially heterogeneous and homogeneous assembly models reduce the fission production and absorption contributions by -2 and -1 pcm, respectively, compared to the heterogeneous assembly model, while they reduce the axial leakage contribution by -2 pcm. The partially heterogeneous assembly model reduces the radial leakage contribution by -1 pcm while the homogeneous assembly model increases the radial leakage contribution by 3 pcm. As a result, the partially heterogeneous model increases the displacement worth by 1 pcm, and the homogeneous assembly model reduces the displacement worth by 3 pcm, which amounts to 10% of the displacement worth.

Table 4.9 Assembly Heterogeneity Effects on Fission Production, Absorption and Leakage Components of Fuel Assembly Displacement Worth

$\Delta\rho$ (pcm)	Homogeneous	Partially Hetero.	Heterogeneous
Fission production	-32.05±0.59	-32.49±0.60	-30.11±0.60
Absorption	-14.41±0.23	-14.68±0.23	-14.52±0.24
Total leakage	15.60±1.47	12.10±1.44	14.10±1.43
Axial leakage	8.90±0.00	9.30±0.00	10.60±0.00
Radial leakage	6.7±1.47	2.80±1.44	3.5±1.43
Sum	-33.24±1.60	-29.91±1.57	-29.69±1.57
$1/k'_{eff} - 1/k_{eff}$	**-34±1.4**	**-30±1.4**	**-31±1.4**

In summary, this study indicates that the heterogeneity effect of fuel pins on the reactivity worth of fuel assembly displacement is relatively small. Thus, the partially heterogeneous assembly configuration will be adopted for the perturbation calculations

4.1.2 Additivity

In the proposed method, the overall feedback reactivity induced by assembly bowing is calculated by summing the reactivity worth of displacement over all assembly segments under the assumption that the additivity holds for reactivity worth due to individual assembly segment displacement. We use the 3D mini-core model presented in section 4.1.1.2, with partially heterogeneous assembly model, to verify the additivity. As shown in Figure 4.6, six fuel assemblies in the second ring and six assemblies in the third ring (marked with black arrow) are moved outwards from the core center by 2 mm.

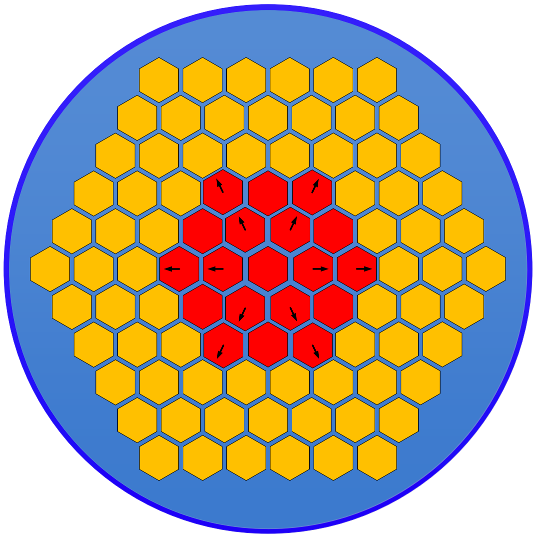

Figure 4.6 Radial Layout of Mini-Core Model with Fuel Assemblies Shifted Radially Outwards from Core Center

The overall feedback reactivity induced by shifting these twelve assembly are calculated in two ways using MCNP6 code. In the first method, we calculate the eigenvalues for both the base and perturbed cases with all twelve assemblies displaced. The total feedback reactivity is calculated by the subtraction between the base and perturbed eigenvalues. In the second method, the individual assemble displacement worth is calculated first, and the total feedback reactivity is calculated by adding up the displacement worth of the twelve assemblies. The eigenvalues of the base and perturbed cases are shown in Table 4.10 and the reactivity worth due to assembly displacements are given in Table 4.11. The reactivity worth of single assembly at ring 2 and ring 3 displaced by 2 mm are -29.8±1.4 pcm and -25.8±1.4 pcm, respectively, resulting in a total reactivity worth of -333.4±4.8 pcm. The total reactivity worth calculated by the eigenvalue difference between the base case and the perturbed case of all twelve assemblies shifted is -330.4±1.4. The total reactivity worth estimated by the two methods agree well with each other indicating that the reactivity worth calculated by summing individual segment displacement worth introduces a negligible error compared with the direct calculation result.

Table 4.10 Effective Multiplication Factors for Base and Perturbed Cases

Effective Multiplication Factors	Mean	STD
Base	1.00406	0.00001
Single Assembly Outwards (ring 2)	1.00380	0.00001
Single Assembly Outwards (ring 3)	1.00376	0.00001
All 12 Assemblies Outwards	1.00074	0.00001

Table 4.11 Reactivity Changed due to Single and Twelve Assembly Displacements

Worth (pcm)	Mean	STD
Single Assembly Outwards (ring 2)	-29.8	1.4
Single Assembly Outwards (ring 3)	-25.8	1.4
Sum	-333.4	4.8
All 12 Assemblies Outwards	-330.4	1.4

4.2 Core Grid Plate Radial Expansion

In this section, we investigate the reactivity effect due to the core grid plate radial expansion. The calculations are performed based on a two-dimensional mini-core model that is derived from ABTR core. The radial layout of the mini-core model is shown in Figure 4.7. The mini-core model has three rings of fuel assembly with the same composition as ABTR outer fuel assemblies, three rings of reflector assembly and one ring of barrel assemblies adopted from ABTR core. Partially

Heterogeneous and homogeneous assembly models are used for fuel and reflector assemblies and fully homogeneous model is used for barrel assembly. The calculations are performed using MCNP6 code. In the radial expanded case, the assembly pitch is increase by 1%, 2% and 3%. For the calculations with partially heterogeneous assembly model, the assembly duct and inside region remain the same while the volume of inter-assembly gap sodium is increased. In the calculation with homogenized assembly model, the fuel and structure volume fractions are reduced while the sodium volume fraction is increased.

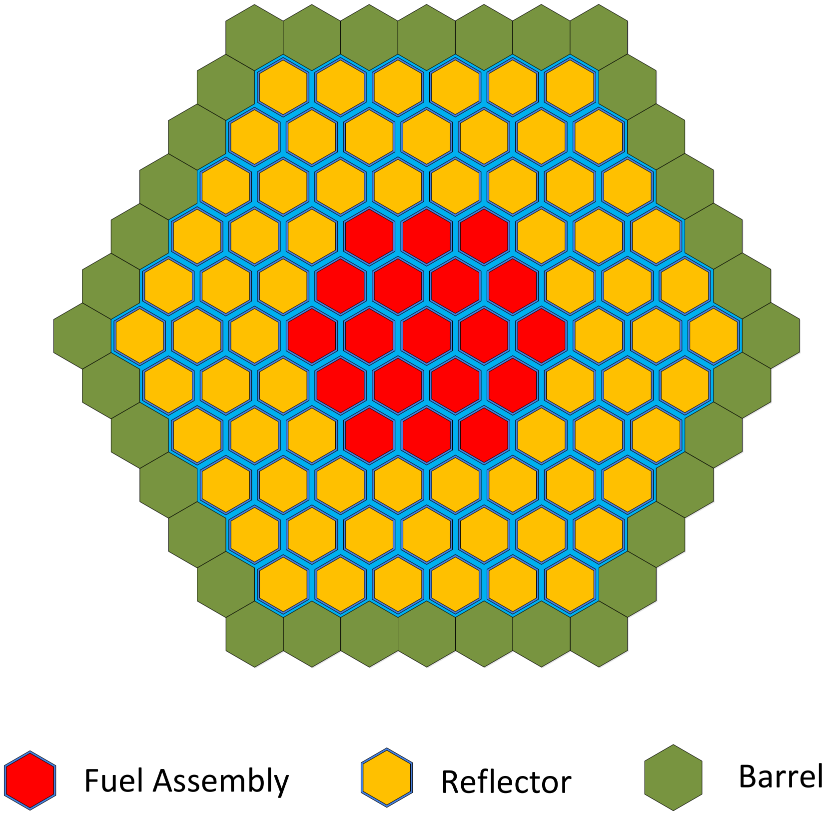

Figure 4.7 Two-Dimensional Mini-Core Model

Table 4.12 and Table 4.13 present the effective multiplication factors for the base and radially expanded cores and the feedback reactivity due to the radial expansion based on homogeneous and heterogeneous assembly models, respectively. The reactivity changes due to the radial expansion of the core grid plate by 1%, 2% and 3% are -438 pcm, -877 pcm and -1317 pcm, respectively, for the homogeneous assembly model and -437 pcm, -874 pcm and -1308 pcm, respectively, for the heterogeneous model. The assembly heterogeneity has negligible effect on the core radial expansion reactivity.

Table 4.12 Effective Multiplication Factors and Reactivity Worth for Radially Expanded Core with Homogenized Assembly Models

	Effective k	STD	Worth (pcm)	STD (pcm)
Base	1.00918	0.00001	0	1.4
Expand by 1%	1.00474	0.00001	-437.89	1.4
Expand by 2%	1.00033	0.00001	-876.66	1.4
Expand by 3%	0.99594	0.00001	-1317.30	1.4

Table 4.13 Effective Multiplication Factors and Reactivity Worth for Radially Expanded Core with Heterogeneous Assembly Models

	Effective k	STD	Worth (pcm)	STD (pcm)
Base	1.00918	0.00001	0	1.4
Expand by 1%	1.00474	0.00001	-437.89	1.4
Expand by 2%	1.00033	0.00001	-876.66	1.4
Expand by 3%	0.99594	0.00001	-1317.30	1.4

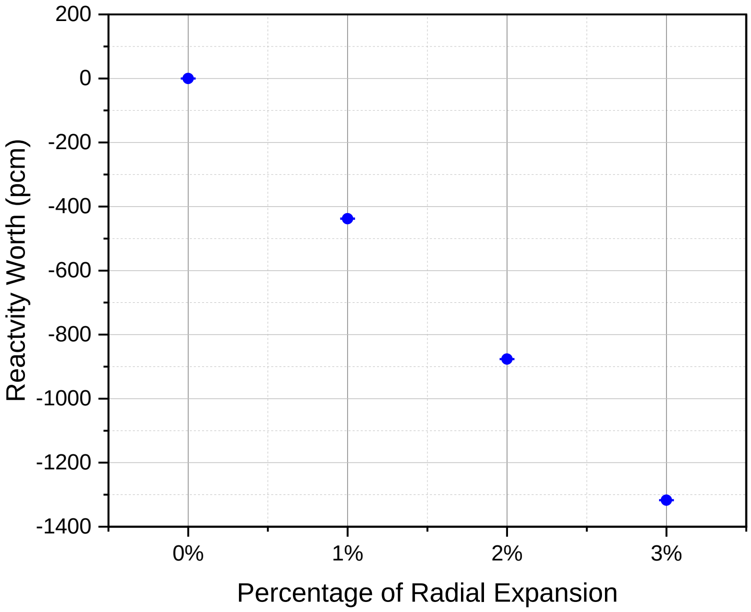

Figure 4.8 Linearity of the Radial Expansion Worth with Respect to Grid Plate Radial Expansion

The magnitude of the radial expansion worth increases linearly with the grid plate radial expansion up to 3% of expansion as shown in Figure 4.8. However, it is not clear whether the linearity result of this small mini-core problem can be generalized to realistically large core problems. Fortunately, the grid plate thermal expansion results in a whole core expansion that can be represented by an integrated radial expansion worth. Thus, the feedback reactivity due to core radial expansion can be calculated by direct modeling of the radially expanded core model.

4.3 Fuel Axial Expansion

The 2D mini-core model described in the previous section was extended to a 3D model with heterogeneous axial regions as shown in Figure 4.9. The active core region is extruded by 80 cm in the axial direction. Above the fuel region is the bound sodium and fission gas plenum with lengths of 20 cm and 70 cm, respectively. There are upper and lower structure materials at the top and bottom of the core.

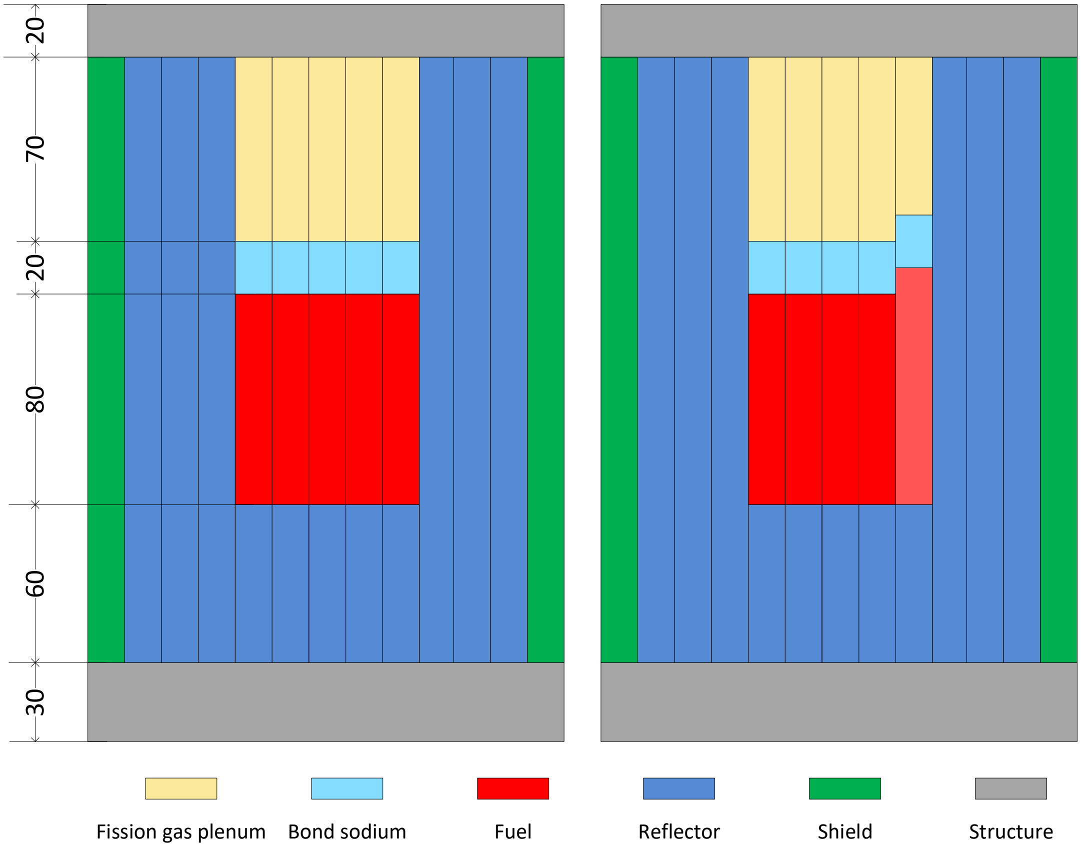

Figure 4.9 Axial Regions of The Mini-Core Model

We investigate the fuel pin heterogeneity effect on the reactivity worth duel to fuel assembly axial expansion. A single fuel assembly located at a corner of the third ring is expanded by 1%, resulting in a 0.8 cm increase in length of the fuel region. The bond sodium region is shifted upward by 0.8 cm and the length of the fission gas plenum is reduced by 0.8 cm, correspondingly. Table 4.14 and Table 4.15 show the effective multiplication factors of the base and axially expanded fuel models and the reactivity worth due to the fuel axial expansion. The results in Table 4.14 are calculated based on the fully heterogeneous assembly model while the fully homogeneous model is used for obtaining the results in Table 4.15. It was observed that the MCNP6 results vary significantly more than the reported standard deviation of 1 pcm since the reported MCNP6 standard deviation is significantly underestimated due to the assumption that the fission source is independent from cycle to cycle [62]. Therefore, the MCNP6 simulations were repeated for six times using different random seed numbers to obtain more reliable results. The results in Table 4.14 show that the statistical standard deviation is significantly larger than the reported MCNP6 standard deviations. The statistical standard deviation is 2.42 pcm for the base case and 1.17 pcm for the axial expansion case although the standard deviation reported by MCNP6 is one pcm for individual runs.

Table 4.14 Reactivity Worth Due to 1% Axial Expansion of Single Fuel Assembly in The Third Ring (Fully Heterogeneous Assembly Model)

	Base	STD	1% axial exp.	STD	Worth (pcm)
Seed 1	1.02861	0.00001	1.02847	0.00001	-13.23
Seed 2	1.02863	0.00001	1.02849	0.00001	-13.23
Seed 3	1.02865	0.00001	1.02848	0.00001	-17.01
Seed 4	1.02866	0.00001	1.02849	0.00001	-15.12
Seed 5	1.02865	0.00001	1.02850	0.00001	-15.12
Seed 6	1.02868	0.00001	1.02850	0.00001	-17.01
Mean	1.02865		1.02849		-14.97
STD (pcm)	2.42		1.17		2.69

Table 4.15 Reactivity Worth Due to 1% Axial Expansion of Single Fuel Assembly in The Third Ring (Fully Homogeneous Assembly Model)

	Base	STD	1% axial exp.	STD	Worth (pcm)
Seed 1	1.02181	0.00001	1.02167	0.00001	-13.41
Seed 2	1.02180	0.00001	1.02168	0.00001	-11.49
Seed 3	1.02183	0.00001	1.02166	0.00001	-16.28
Seed 4	1.02180	0.00001	1.02164	0.00001	-15.33
Seed 5	1.02181	0.00001	1.02165	0.00001	-15.33
Seed 6	1.02185	0.00001	1.02166	0.00001	-17.24
Mean	1.02182		1.02166		-14.85
STD (pcm)	1.41		1.64		2.17

The statistical uncertainties become a significant error source when investigating a small reactivity effect. If we compare the axial expansion worth between fully heterogeneous and fully homogeneous cases calculated by a single pair of MCNP6 simulations, the heterogeneity effect can amount to several percent in maximum that is larger than the reported standard deviation, indicating there might be some physical effect. However, if we further reduced the statistical error by taking average of the six mean values of effective multiplication factors, we obtain nearly identical axial expansion worth between fully heterogeneous and fully homogeneous cases. Thus, we conclude that the assembly heterogeneity effect on fuel axial expansion worth is insignificant.

The above results indicate that fully homogeneous model is adequate for evaluating the assembly axial expansion worth. Thus, the axial expansion worth of each assembly can be evaluated using perturbation theory based on the forward and adjoint flux distributions calculated by the VARIANT code based on homogenized assembly model. We calculate the reactivity worth for a 3% axial fuel expansion using the MCNP6 and VARIANT codes. A relatively larger expansion was considered to avoid the possible convergence problem of VARIANT caused by a spoiled geometry of very large aspect ratio. The results are shown in Table 4.16. The MCNP6 simulations were performed with eight different random seed numbers with each calculation converged to a reported standard deviation of 2 pcm. The final effective multiplication factors obtained from MCNP6 calculations are calculated by taking the average of the eight mean effective multiplication factors of MCNP6 outputs. The fuel axial expansion worth is calculated by subtraction of the averaged effective multiplication factors between the base and axially expanded cases. The fuel axial expansion worth evaluated using VARIANT code is -44.7 pcm that agrees very well with the MCNP6 result of -44.6 pcm.

In the present work, we proposed to use first-order perturbation theory method for evaluating the fuel axial expansion worth. Thus, we investigate the linearity of the fuel axial expansion worth with the magnitude of the assembly axial expansion to show the adequacy of using the first-order perturbation theory. We calculated the reactivity worth induced by 1%, 2% and 3% axial expansions of a fuel assembly. Considering the metal fuel thermal expansion coefficient and the possible fuel temperature rise, the fuel axial expansion is unlikely to exceed 3%. Table 4.17 shows the effective multiplication factors for the base and axially expanded fuel cases as well as the fuel axial expansion worth that are calculated using MCNP6 code with a partially heterogeneous model. The magnitude of the fuel axial expansion worth increases linearly with the fuel axial expansion as shown in Figure 4.10.

Table 4.16 Fuel Assembly Axial Expansion Worth of 3% Expansion Evaluated Using MCNP6 and VARIANT Code

	Base	STD	3% axial exp.	STD	Worth (pcm)
Seed 1	1.02182	0.00002	1.02142	0.00002	-38.3
Seed 2	1.02181	0.00002	1.02136	0.00002	-43.1
Seed 3	1.02185	0.00002	1.02133	0.00002	-49.8
Seed 4	1.02183	0.00002	1.02138	0.00002	-43.1
Seed 5	1.02185	0.00002	1.02139	0.00002	-44.1
Seed 6	1.02184	0.00002	1.02135	0.00002	-46.9
Seed 7	1.02176	0.00002	1.02130	0.00002	-44.1
Seed 8	1.02181	0.00002	1.02132	0.00002	-46.9
Mean	1.02182		1.02136		-44.6
STD (pcm)	1.41		3.96		4.94
VARIANT	1.020028		1.019563		-44.7
Errors (pcm)	179.3		179.3		0.15

Table 4.17 Reactivity Worth of Fuel Assembly Axial Expansion by 1%, 2% and 3%

	k_{eff}	STD	Worth	STD (pcm)
Base	1.02461	0.00001	0	1.4
Expand by 1%	1.02447	0.00001	-13.34	1.4
Expand by 2%	1.02430	0.00001	-29.54	1.4
Expand by 3%	1.02412	0.00001	-46.70	1.4

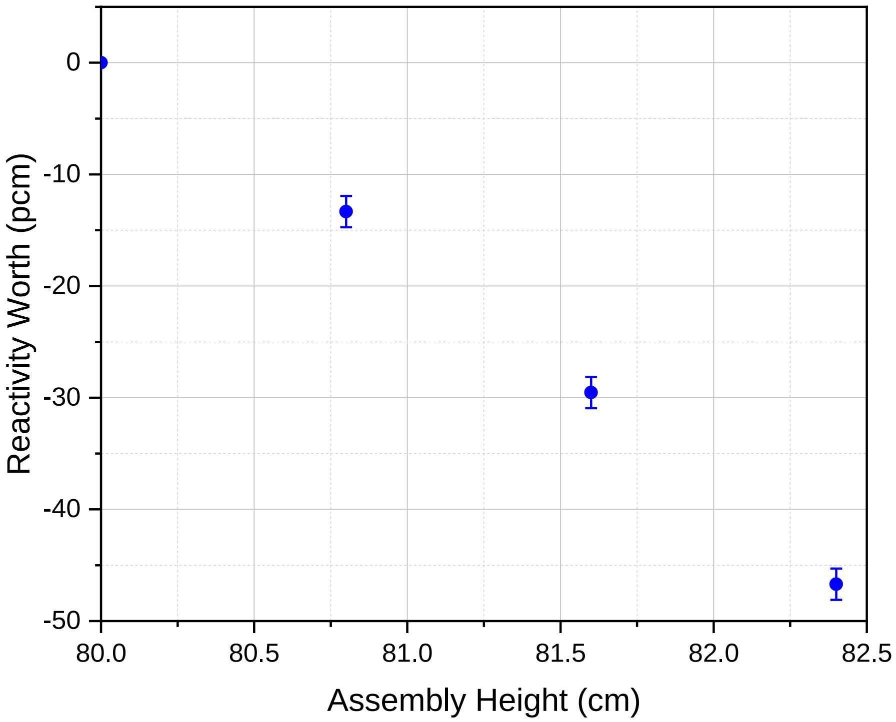

Figure 4.10 Linearity of The Reactivity Worth of Aixal Expansion with Respect to the Axial Expansion

4.4 Assembly Duct Radial Expansion

In this section, we study the reactivity effect due the radial expansion of the assembly duct. The 2D mini-core model presented in section 4.2 is used for the calculations. We expand the duct wall of the assembly 8 by 1% and 2% as shown in Figure 4.11. The partially heterogeneous assembly model is adopted. The fuel assembly duct radial expansion increases the duct thickness and the flat-to-flat distance of the assembly such that the coolant content within the expanded assembly is increased while the inter-assembly gap sodium volume is reduced.

Table 4.18 shows the feedback reactivity due to assembly duct radial expansion evaluated using the MCNP6 and PROTESU-SN codes. The MCNP6 results show that the reactivity worth due to 1% assembly duct radial expansion is only 1 pcm, which is within the one standard deviation, indicating that the difference is likely due to MC statistical error. The calculations are also performed using the PROTEUS-SN deterministic code to eliminate the effect of statistical uncertainty. The result for 1% and 2% duct radial expansion is 0.401 pcm and 0.885 pcm, respectively. Based on this result, we conclude that the duct radial expansion worth is so small compared to other components of core deformation (i.e., assembly displacement, axial fuel expansion, and radial expansion of grid plate) that it can be neglected.

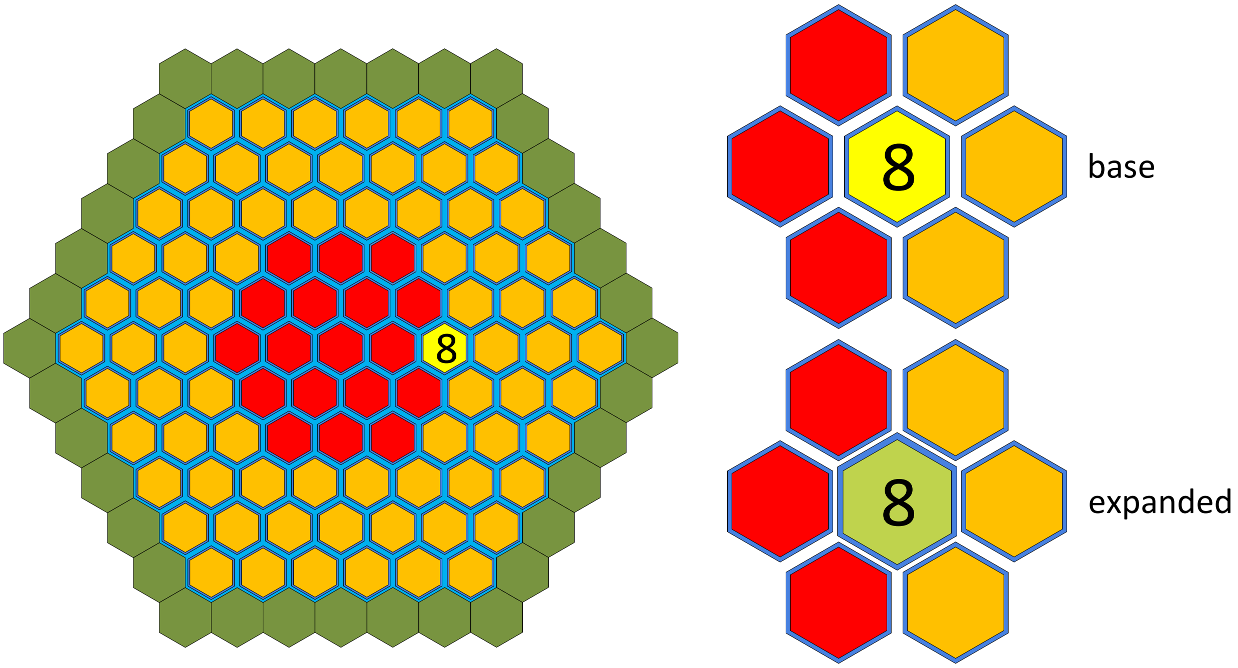

Figure 4.11 Two-Dimension Mini-Core Model for Investigation of Duct Radial Expansion Effect on Reactivity

Table 4.18 Feedback Reactivity Due to Assembly Duct Radial Expansion Evaluated Using MCNP6 and PROTEUS-SN Codes

	MCNP6	PROTEUS-SN	
	1% duct radial exp.	1% duct radial exp.	2% duct radial exp.
Base	1.00918±0.00001	1.00527950	1.00527950
Perturbed	1.00919±0.00001	1.00527545	1.00527056
worth (pcm)	-0.982±1.4	0.401	0.885

5. RECONSTRUCTION OF HETEROGENEOUS FLUX DISTRIBUTION

In the proposed perturbation theory method for evaluating the reactivity changes due to assembly displacements, the heterogeneous real and adjoint flux distributions are needed. The real and adjoint fluxes for heterogeneous core configurations can be reconstructed by combining the VARIANT transport solutions for homogenized-assembly core models and the PROTEUS-SN solutions for heterogeneous single-assembly models. In this section, the heterogeneous flux reconstruction method is presented, and the accuracy of the reconstructed flux distributions are examined by comparing with the reference heterogeneous flux distributions obtained from PROTEUS-SN whole core calculations.

5.1 Heterogeneous Flux Reconstruction Method

The fission and loss terms in Eq. (3.60) are evaluated using the angular fluxes obtained from whole-core VARIANT calculations with homogenized assembly models and single-assembly PROTEUS-SN calculations with heterogeneous assembly models and reflective boundary conditions. The angular fluxes in Eq. (3.60) are expanded in spherical harmonics series as in the VARIANT code. The forward and adjoint flux distributions in the heterogeneous assemblies in the core are approximately determined by combining the flux distributions in homogenized assemblies obtained from the whole-core transport solution of VARIANT with the form functions obtained from PROTEUS-SN calculations. Assuming that the local heterogeneity effects on the higher-order angular flux moments are negligible, the form functions are applied to the scalar fluxes only and the higher-order angular flux moments are obtained from the reconstructed VARIANT fluxes.

Using the PROTEUS-SN flux solution defined on the vertices of finite elements, the intra-element flux distributions are determined by combining the vertex values with the shape functions depending on the finite element type. The element-averaged fluxes are then obtained by integrating the intra-element flux distributions. Currently, only two types of extruded finite elements based on three-node linear element and four-node bilinear element have been implemented. The element types with more nodes and/or higher order will be included in the future if necessary. A description on the post-processing of PROTEUS-SN results can be found in Appendix B.

The finite element meshes of the PROTEUS-SN model to represent a heterogeneous assembly configuration are superimposed on the VARIANT solutions, which are given in terms of expansion coefficients for the set of basis polynomials. For a scalar flux $\phi_g^k(\vec{r})$ of group g in node k, the VARIANT solution can be written as:

$$\phi_g^k(\vec{r}) = \sum_m f_m(\vec{r})\zeta_{g,m}^k , \tag{5.1}$$

where $f_m(\vec{r})$'s are the basis polynomials and $\zeta_{g,m}^k$'s are the corresponding expansion coefficients. The VARIANT global solution is evaluated at the vertices of each element for both the base and shifted positions. The element-averaged fluxes are then determined using the same procedure used in evaluating the element-averaged fluxes of the PROTEUS-SN solution discussed in Appendix B.

The evaluated VARIANT and PROTEUS-SN solutions are then multiplied to yield a full core heterogeneous flux distribution. The combined element-averaged scalar flux $\bar{\phi}_C(i,g)$ of group g in element i is obtained as

$$\bar{\phi}_C(i,g) = \bar{\phi}_V(i,g)\bar{\phi}_P(i,g) , \tag{5.2}$$

where $\bar{\phi}_V(i,g)$ and $\bar{\phi}_P(i,g)$ are the element-averaged forward fluxes evaluated from the VARIANT and PROTEUS-SN solutions, respectively. Since the form function obtained from the PROTEUS-SN single assembly heterogeneous calculation modifies only the spatial distribution of the VARIANT full core solution, the combined flux should have the same assembly-averaged spectrum as the VARIANT solution. Thus, the combined flux of each energy group is normalized such that its integrated value over the assembly of interest is the same as the VARIANT solution. The reconstructed element-averaged flux $\bar{\phi}_R(i,g)$ in the heterogeneous assembly configuration for group g in element i is obtained as

$$\bar{\phi}_R(i,g) = \frac{\sum_k \bar{\phi}_V(k,g)A(k)}{\sum_k \bar{\phi}_C(k,g)A(k)} \bar{\phi}_C(i,g) , \tag{5.3}$$

where $A(k)$ is the area of the element k . This reconstructed forward flux is used in the perturbation calculations. The reconstructed element-averaged adjoint flux is obtained by following the same procedure as for the forward flux.

5.2 Numerical Test of Flux Reconstruction Method

5.2.1 Two-Dimensional Mini-Core Models

Three distinct transport calculations were performed to determine the reconstructed heterogeneous flux distributions and the reference heterogeneous solutions: (1) VARIANT calculation for 2D mini-core with homogenized assemblies, (2) PROTEUS-SN calculation for 2D partially heterogeneous fuel assembly with reflective boundary conditions, and (3) PROTEUS-SN calculation for 2D mini-core with partially heterogeneous assemblies. Figure 5.1 shows the radial layouts of the mini-core models used for VARIANT and PROTEUS-SN calculations. In the VARIANT calculations, each fuel or reflector assembly and inter-assembly gap sodium within a hexagonal node was homogenized as shown in Figure 5.1 (A). In PROTEUS-SN calculations, fuel or reflector pins were homogenized with coolant as shown in Figure 5.1 (B).

5.2.2 Multi-group Cross Section Generation

Two sets of multi-group cross section were generated for the VARIANT calculations with homogenized assemblies and the PROTEUS-SN calculations with partially heterogeneous assemblies, respectively. The cross section set for VARIANT calculation was generated using the MC^2-3 code [63, 64] with the TWODANT [65] transport calculation option to account for the region-to-region spectral transition effects. The TWODANT calculation was performed in one-dimensional cylindrical geometry with three different regions as shown in Figure 5.2 (A). The radii of the core, reflector and barrel region are determined to conserve the corresponding volumes in the VARIANT model in Figure 5.2 (A). A region-wise broad group cross section set for PROTEUS-SN heterogeneous model calculation were generated using the MC^2-3 code with the MOC transport calculation option [66] to take into account the duct heterogeneity effect. The computational model used for the MOC transport calculation is shown in Figure 5.2 (B). The fuel and reflector assembly models are consistent with those in the PROTEUS-SN calculation model while the outer ring of barrel assemblies was modified to form a hexagonal outer boundary because of available boundary conditions in the MOC transport solver. The broad group cross sections of fuel assemblies were also used for the PROTEUS-SN single-assembly calculations.

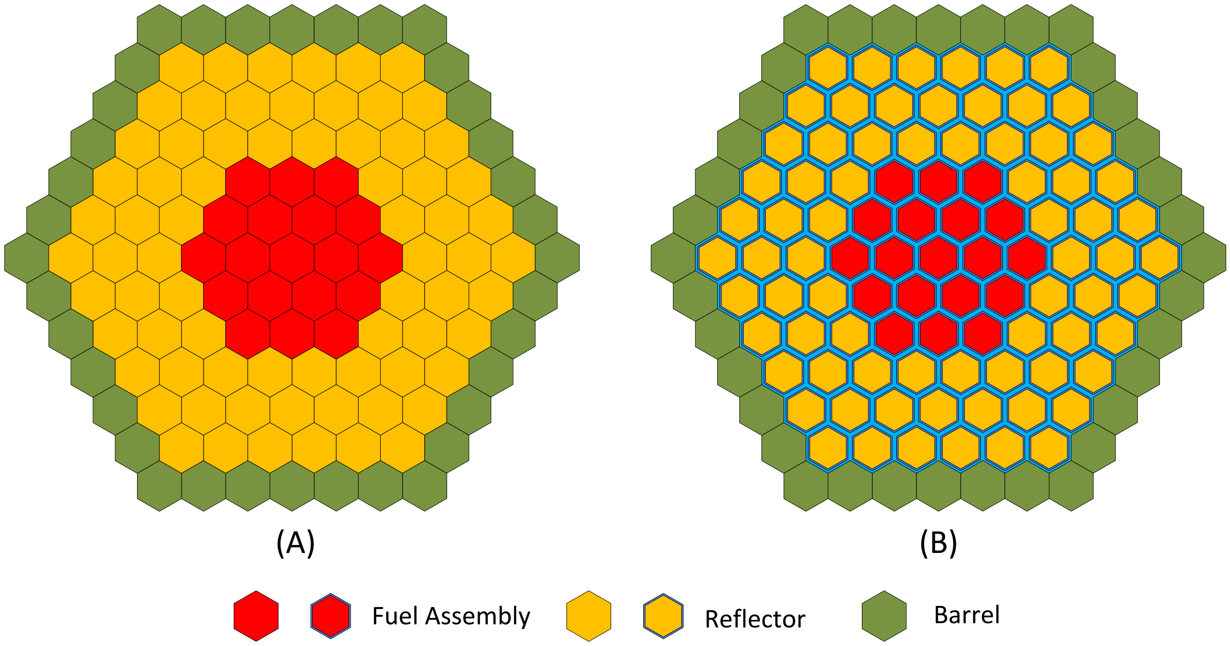

Figure 5.1 Radial Layouts of 2D Mini-Core Models for VARIANT (A) and PROTEUS-SN (B) Calculations

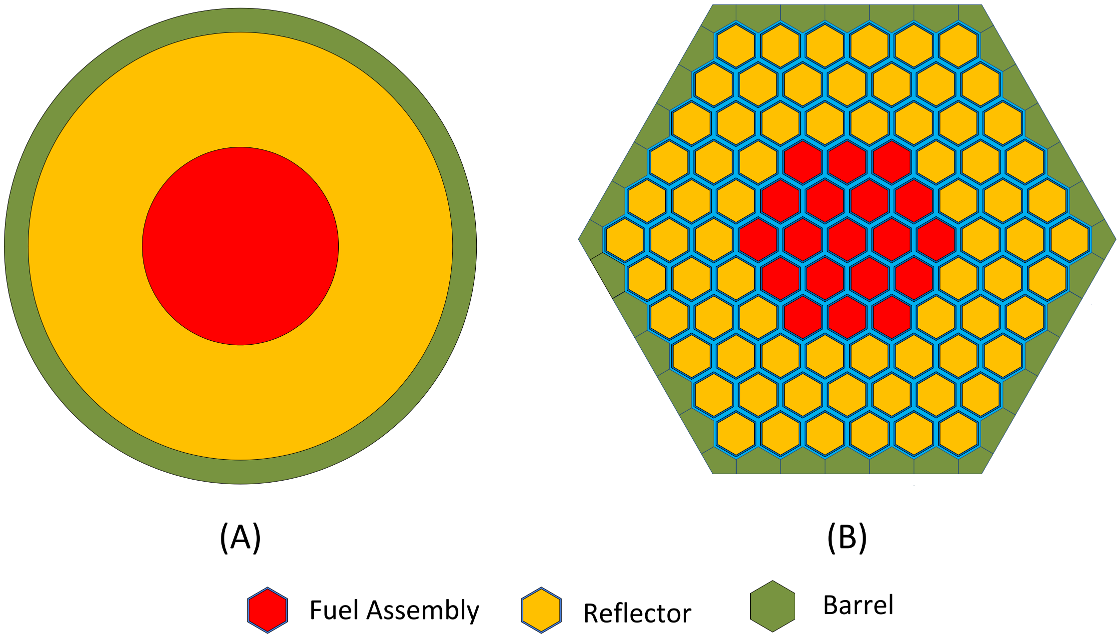

Figure 5.2 Radial Layouts of 2D Mini-Core Models for TWODANT (A) and MC^2-3/MOC (B)

The reference solutions of the 2D mini-core problems used for the VARIANT, PROTEUS-SN, TWODANT and MC^2-3/MOC calculations were obtained using the MCNP6 code with ENDF/B-VII.0 library. The eigenvalue results are summarized in Table 5.1. The reference eigenvalues for the 2D mini-core problem with full barrel assemblies for VARIANT calculation and the 1D cylindrical core for TWODANT calculation are 1.00622±0.00004 and 1.00883±0.00006. The 1D cylindrical core model used in TWODANT calculation for broad-group cross section generation for VARIANT calculations yields a 261 pcm larger eigenvalue than the 2D mini-core problem for VARIANT calculations. The reference eigenvalue for the 2D mini-core with full barrel assemblies for PROTEUS-SN calculations is 1.00916±0.00004. On the other hand, the 2D mini-core with half barrel assemblies used in MC^2-3/MOC calculation to generate broad-group cross sections for PROTEUS-SN calculations yields an eigenvalue of 1.00683±0.00004. The boundary modification reduces the eigenvalue by 233 pcm, but its impact on the heterogeneity effect is negligible. Both the full and half barrel boundaries result in ~300 pcm for the heterogeneity effect of fuel and reflector assembly ducts.

Table 5.1 MCNP6 Reference Solutions for Mini-Core Problems Used for VARIANT, PROTEUS-SN, TWODANT and MC^2-3/MOC Calculations

	2D Mini-Core with Full Barrel	2D Mini-Core with Half Barrel	1D Cylindrical Core
Homogenous assembly	1.00622±0.00004	1.00387±0.00004	1.00883±0.00006
Heterogeneous assembly	1.00916±0.00004	1.00683±0.00004	N/A
Heterogeneity effect (pcm)	-294	-298	N/A

The accuracy of the broad-group cross sections generated with MC^2-3 was examined by comparing to the reference cross sections determined from the tallies of MCNP6 calculation for the 2D mini-core problem with partially heterogeneous assemblies. Using the 33-group structure shown in Appendix C, two sets of broad-group cross sections were generated with MC^2-3. One set was generated using the MOC transport option, which allows the generation of broad group cross sections for local regions (e.g., fuel, cladding, coolant, etc.) using the ultrafine group (UFG, 2082) transport solution for heterogeneous assembly models. Using the 2D mini-core model with partially heterogeneous assemblies, 33-group cross sections were generated for fuel, duct and inter-assembly gap regions. The other set was generated with the TWODANT transport calculation option of MC^2-3 for the 1D cylindrical core model with homogenized compositions. Note that the local heterogeneity effects are not taken into account in the second set of cross sections.

Table 5.2 compares the eigenvalues obtained from TWODANT and MC^2-3/MOC calculations with the MCNP6 reference solutions. TWODANT and MC^2-3/MOC calculations produce UFG fluxes to be used in collapsing UFG cross sections to 33-group cross sections for VARIANT and PROTEUS-SN calculations. Relatively coarse meshes were used in TWODANT calculation due to the memory limitation and in MC^2-3/MOC calculation to reduce the computational time. In the MC^2-3/MOC calculation, a ray spacing of 0.05 cm, 18 azimuthal angles and 4 polar angles were used. In the TWODANT calculation, the spatial mesh interval of around 1.5 cm was used. A scattering order of 5 was used in both TWODANT and MC^2-3/MOC calculations. TWODANT overestimated the eigenvalue by 462 pcm, and MC^2-3/MOC overestimated the eigenvalue by more than 600 pcm for both problems with heterogeneous and homogeneous assemblies, indicating the eigenvalues are not fully converged due to the coarse spatial discretization. However, the global spectral shift associated with these eigenvalue errors would not affect significantly the broad-group cross sections generated in 33, 70 and 116 groups in this study since the broad-group cross sections are determined by the within-group spectrum in each broad group.

Table 5.2 Comparison of the Eigenvalues Calculated from TWODANT and MC^2-3/MOC Solver with MCNP6 Reference Solutions

	Eigenvalues	MCNP6 reference	Difference (pcm)
TWODANT, 1D cylinder	1.01345	1.00883±0.00006	462
MC^2-3/MOC, Hom. assembly	1.01038	1.00387±0.00004	651
MC^2-3/MOC, Het. assembly	1.01370	1.00683±0.00004	687

Figure 5.3 compares 33-group U-238 total cross sections in fuel region generated with MC^2-3/MOC, MC^2-3/TWODANT and MCNP6 tallies. Figure 5.4 compares the relative errors of U-238 total cross sections in fuel region generated by MC^2-3/MOC and MC^2-3/TWODANT with MCNP6 standard deviations. For the groups in the above resonance energy range (groups 1 to 10), both MC^2-3 cross sections agree well with MCNP6 reference values. In the resolved and unresolved resonance energy ranges (groups 11 to 31), the cross sections generated with MC^2-3/MOC for 2D heterogeneous core model agree well with the reference cross sections obtained from MCNP6.

However, the cross sections generated with MC^2-3/TWODANT for 1D cylindrical core model with homogenized compositions show 5% and 8% errors in groups 27 and 28, respectively, where the second and third resonances of U-238 located. This is due to the local heterogeneity effect neglected in the MC^2-3/TWODANT calculation. The thermal group (group 33) cross section shows a relatively large error since the lower energy boundary for slowing-down calculation of the current MC^2-3 is 0.414 eV and thus the group 33 cross section of MC^2-3 is for an energy interval from 0.417 eV to 0.414 eV while the MCNP6 cross section is for the energy interval below 0.417 eV. However, this error would not affect the core calculation results since the neutron flux level in thermal group is negligible in fast spectrum reactors.

Figure 5.5 shows 33-group Pu-239 fission cross sections in fuel region generated with MC^2-3/MOC, MC^2-3/TWODANT and MCNP6 tallies. Figure 5.6 compares the relative errors of Pu-239 fission cross sections in fuel region generated by MC^2-3 with MCNP6 standard deviations. Similar to the U-238 total cross sections, the Pu-239 fission cross sections generated with MC^2-3 agree well with the MCNP6 reference values in the above resonance energy range (groups 1 to 20). In the resonance groups (groups 21 to 32), the cross sections obtained with MC^2-3/MOC agree well with the MCNP6 reference values. However, the cross sections obtained with MC^2-3/TWODANT show a maximum error of 10% in the group 29 since the local heterogeneity effect was neglected. The thermal group cross section shows a large error for the same reason discussed above for U-238 total cross section.

Figure 5.7 shows 33-group Fe-56 total cross sections in fuel region generated with MC^2-3/MOC, MC^2-3/TWODANT and MCNP6 tallies. Figure 5.8 compares the relative errors of Fe-56 total cross sections in fuel region generated with MC^2-3 with MCNP6 standard deviations. The cross sections obtained with MC^2-3/MOC agree well with the MCNP6 reference values. Both MC^2-3/MOC and MC^2-3/TWODANT yield errors up to 3% in the group 6, but the cross section in the group 6 is only 2.44 barns and thus the absolute error is negligible.

Figure 5.9 shows 33-group Na-23 total cross sections in fuel region generated with MC^2-3/MOC, MC^2-3/TWODANT and MCNP6 tallies. Figure 5.10 compares the relative errors of the Na-23 total cross sections in fuel region generated with MC^2-3 with MCNP6 standard deviations. Na-23 has a large elastic resonance at around 2.8 keV that results in a peek of Na-23 total cross section in the group 18. The cross sections generated with MC^2-3/MOC agree well with the reference MCNP6 cross sections except for the thermal group, which are not important in fact reactors. The cross sections generated with MC^2-3/TWODANT without considering the local heterogeneity effects show a maximum error of 1% in the group 18.

In summary, the comparison of the 33-group cross sections generated with MC^2-3 with the reference MCNP6 cross sections indicate that the MC^2-3 code with the MOC calculation option produce accurate multi-group cross sections for partially heterogeneous assemblies. In addition, the local heterogeneity effects should be taken into account in generating region dependent broad-group cross sections.

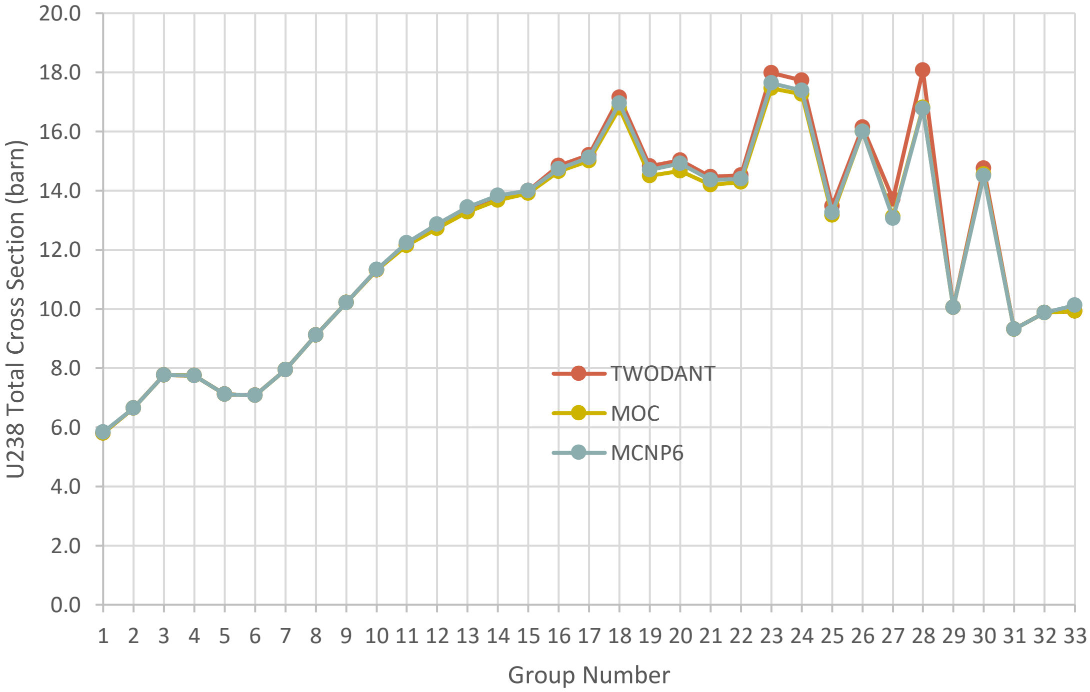

Figure 5.3 Comparison of U-238 Total Cross Sections in Fuel Region Generated with MC^2-3/MOC, MC^2-3/TWODANT and MCNP6 Tallies

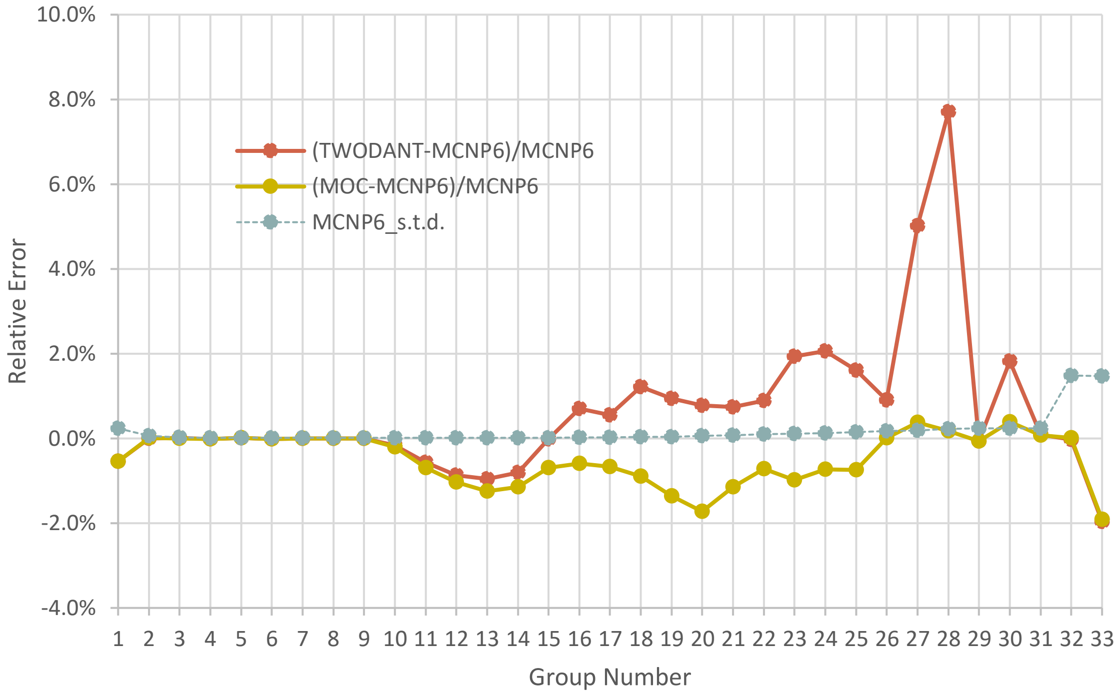

Figure 5.4 Comparison of Relative Errors of U-238 Total Cross Sections in Fuel Region Generated with MC^2-3/MOC and MC^2-3/TWODANT with MCNP6 Standard Deviations

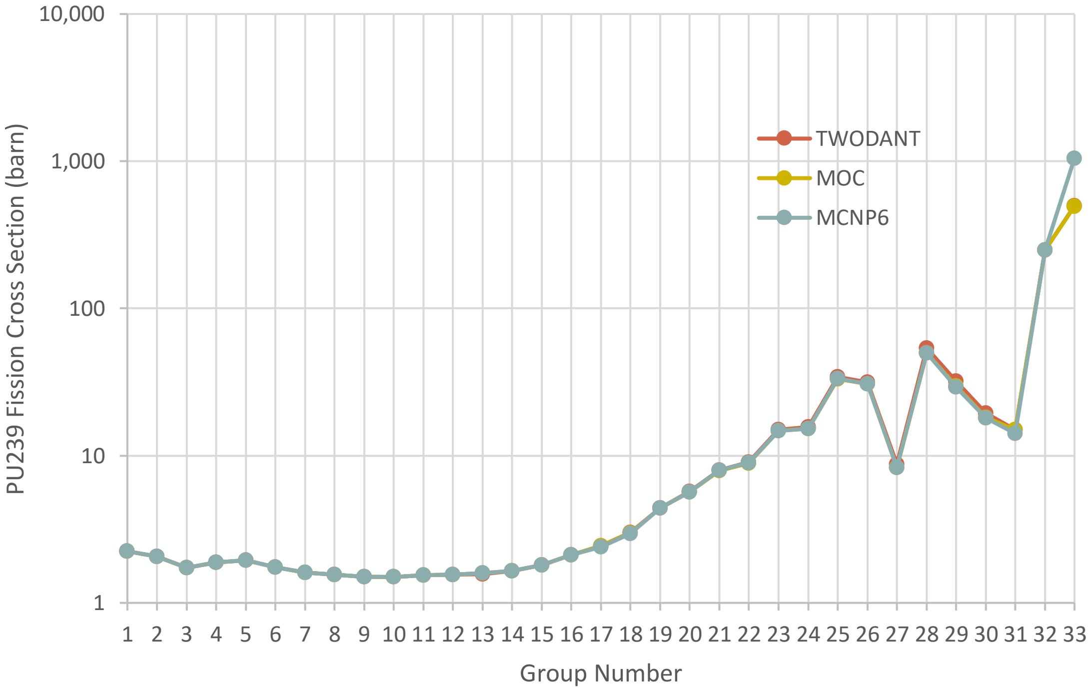

Figure 5.5 Comparison of Pu-239 Fission Cross Sections in Fuel Region Generated with MC^2-3/MOC, MC^2-3/TWODANT and MCNP6 Tallies

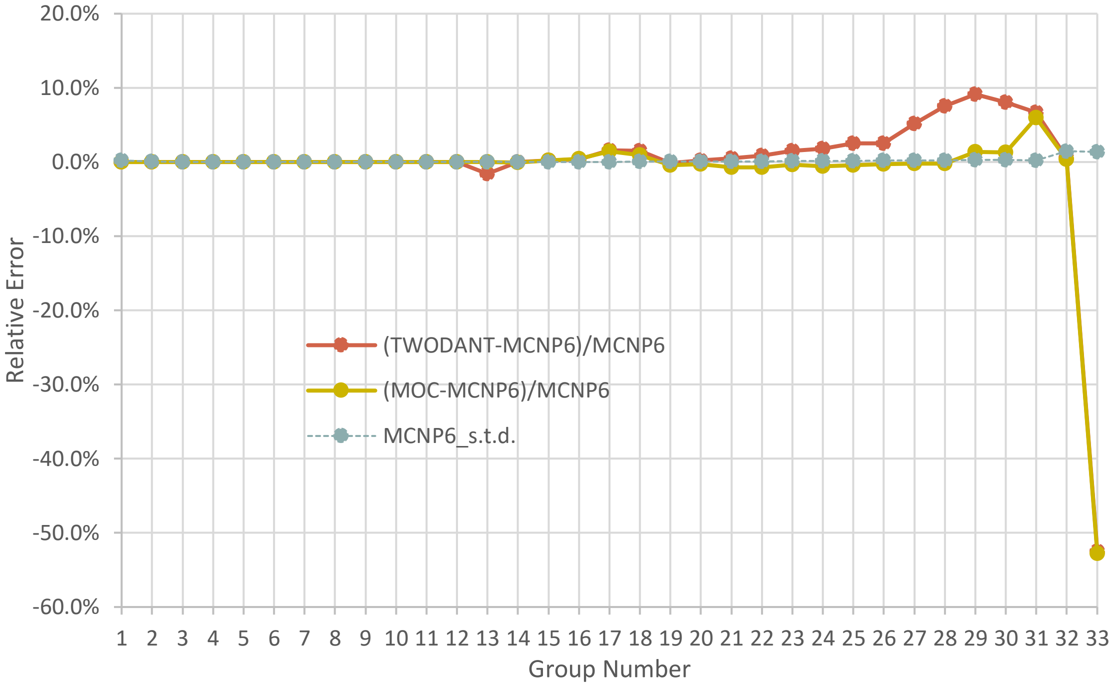

Figure 5.6 Comparison of Relative Errors of Pu-239 Fission Cross Sections in Fuel Region Generated with MC^2-3/MOC and MC^2-3/TWODANT with MCNP6 Standard Deviations

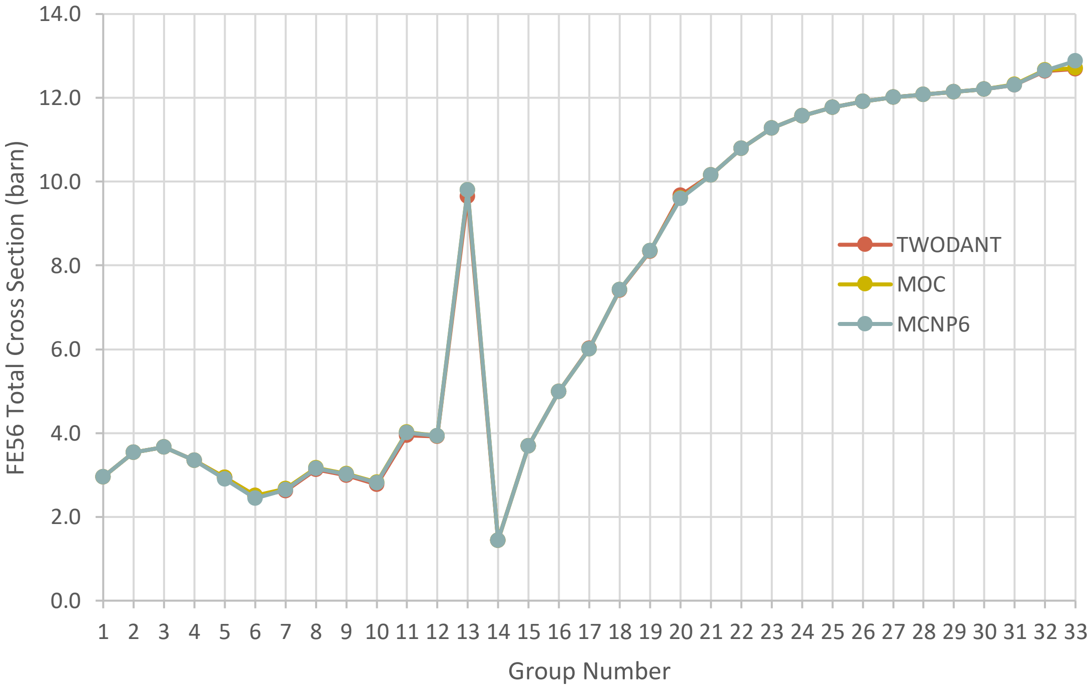

Figure 5.7 Comparison of Fe-56 Total Cross Sections in Fuel Region Generated with MC^2-3/MOC, MC^2-3/TWODANT and MCNP6 Tallies

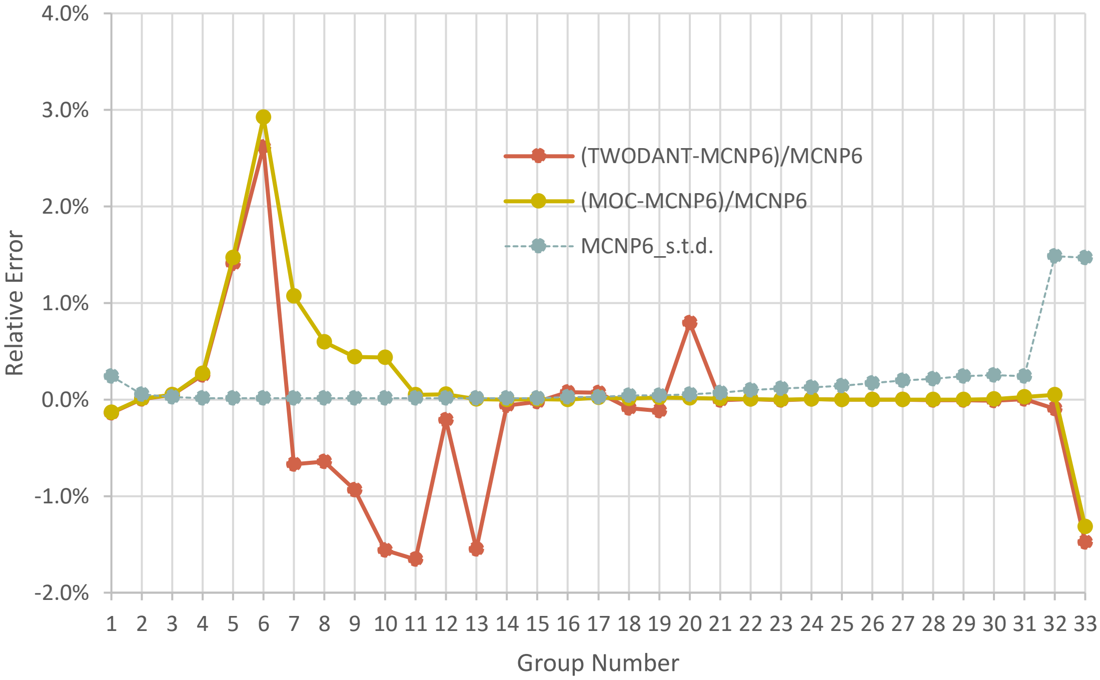

Figure 5.8 Comparison of Relative Errors of Fe-56 Total Cross Sections in Fuel Region Generated with MC^2-3/MOC and MC^2-3/TWODANT with MCNP6 Standard Deviations

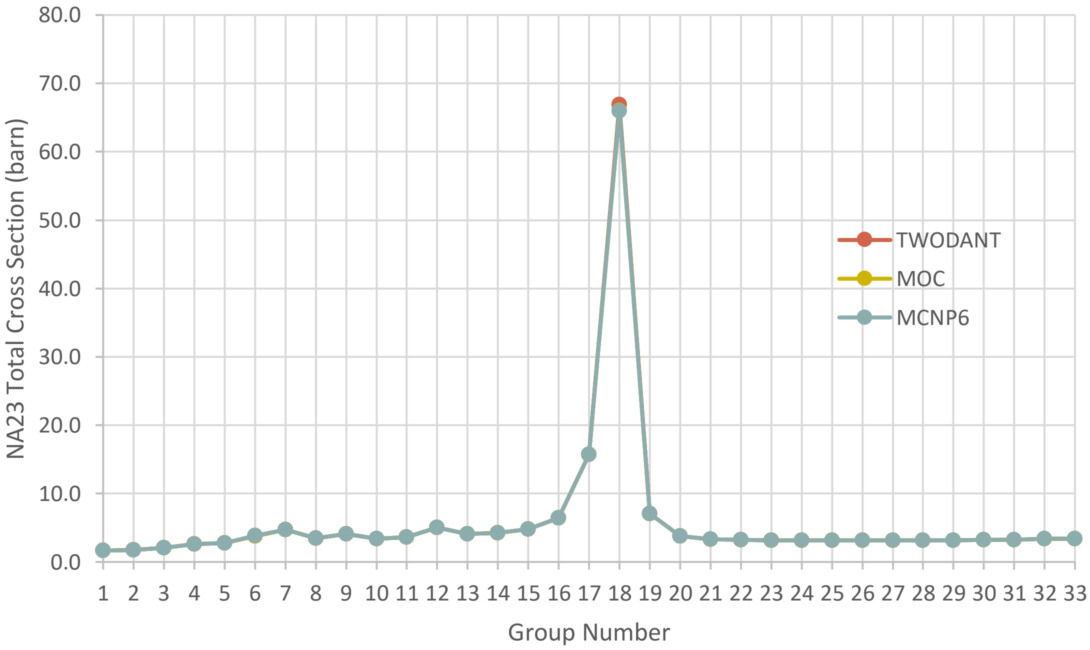

Figure 5.9 Comparison of Na-23 Total Cross Sections in Fuel Region Generated with MC^2-3/MOC, MC^2-3/TWODANT and MCNP6 Tallies

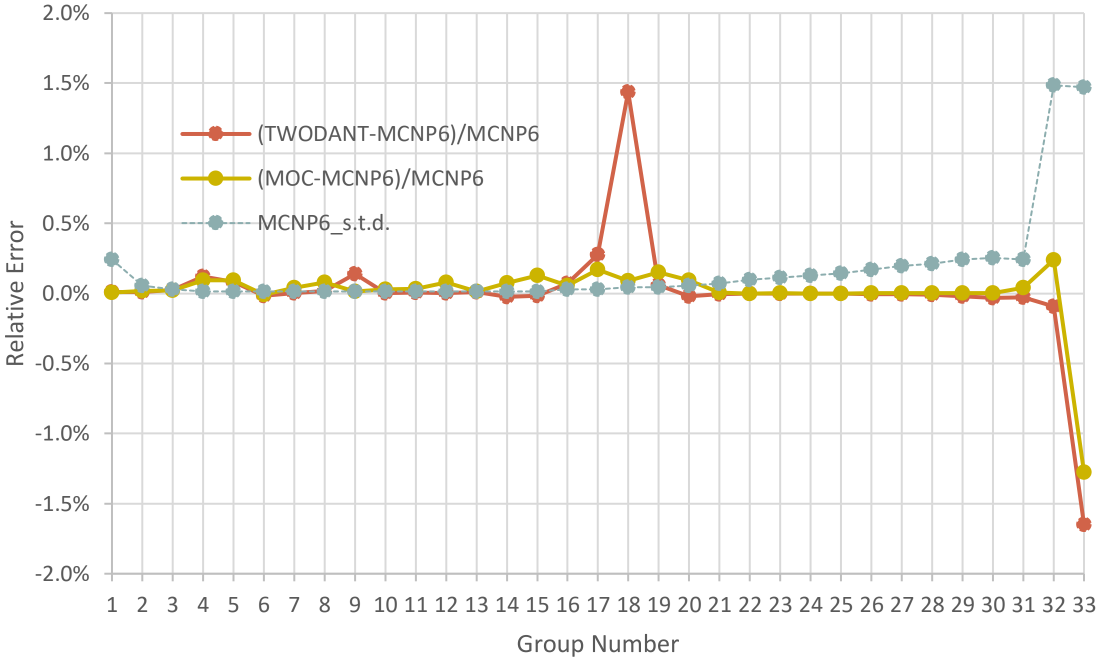

Figure 5.10 Comparison of Relative Errors of Na-23 Total Cross Sections in Fuel Region Generated with MC^2-3/MOC and MC^2-3/TWODANT with MCNP6 Standard Deviations

5.2.3 Two-Dimensional Mini-Core Solutions

The transport solution for the 2D mini-core problem with homogeneous assemblies shown in Figure 5.1 (A) was obtained using the VARIANT code with the broad-group cross sections generated with MC^2-3/TWODANT. The sensitivity studies on the number of energy groups and the spatial and angular approximations for intra-nodal flux distributions were also performed. Table 5.3 and Table 5.4 show the eigenvalue results of the 33 and 70 group VARIANT calculations, respectively, obtained with different spatial and angular approximations. The eigenvalue errors relative to the MCNP6 reference solution 1.00622±0.00004 are also included. The three numbers in the spatial approximation present the polynomial orders for the intra-nodal source distribution, the intra-nodal flux distribution, and the nodal interface current distribution (source-flux-current approximation).

The angular approximation represents the spherical harmonics order for the angular approximation of intra-nodal flux distribution. It can be seen that the VARIANT solutions converge with increasing polynomial order and increasing spherical harmonics order. However, the converged solutions show some deviations from the MCNP6 reference solution because of the multi-group approximation. The converged 33-group solution shows an eigenvalue error of ~200 pcm. This error is reduced to ~10 pcm when the number of energy groups is increased to 70.

Table 5.3 Eigenvalues of 33-Group VARIANT Calculations for 2D Mini-Core with Homogeneous Assemblies vs. Spatial and Angular Approximations

	Angular approximation	Spatial approximation				
		4-6-1	6-6-1	6-6-2	7-7-2	4-8-3
Eigenvalue	P1	0.99515	0.99514	0.99513	0.99513	0.99513
	P3	1.00398	1.00396	1.00394	1.00395	1.00396
	P5	1.00426	1.00424	1.00419	1.00421	1.00424
	P7	1.00435	1.00433	1.00427	1.00430	1.00433
Error (pcm)	P1	-1107	-1108	-1109	-1109	-1109
	P3	-224	-226	-228	-227	-226
	P5	-196	-198	-203	-201	-198
	P7	-187	-189	-195	-192	-189

Table 5.4 Eigenvalues of 70-Group VARIANT Calculations for 2D Mini-Core with Homogeneous Assemblies vs. Spatial and Angular Approximations

	Angular approximation	Spatial approximation				
		4-6-1	6-6-1	6-6-2	7-7-2	4-8-3
Eigenvalue	P1	0.99699	0.99696	0.99695	0.99695	0.99698
	P3	1.00602	1.00596	1.00594	1.00595	1.00600
	P5	1.00631	1.00624	1.00619	1.00630	1.00628
	P7	1.00641	1.00633	1.00628	1.00630	1.00638
Error (pcm)	P1	-923	-926	-927	-927	-924
	P3	-20	-26	-28	-27	-22
	P5	9	2	-3	8	6
	P7	19	11	6	8	16

The transport solutions for the 2D mini-core problem with partially heterogeneous assemblies and the single fuel assembly model were calculated using the PROTEUS-SN code with the broad-group cross sections generated with MC^2-3/MOC. The PROTEUS-SN code uses the multi-group approximation for energy discretization, the finite element method for spatial discretization, and the discrete ordinate method for angular discretization. Before solving the 2D mini-core problem with partially heterogeneous assemblies, sensitivity studies were performed using the 2D mini-core with homogeneous assemblies. With mesh sensitivity studies, a mesh grid of 168704 finite elements was selected. Further refinement of the mesh changed the eigenvalue by only one pcm. Further sensitivity studies on the number of energy groups and the angular cubature were performed to find the converged solutions. Table 5.5 summarizes the eigenvalues of PROTEUS-SN calculations obtained with different angular cubature and numbers of energy groups. The eigenvalue errors relative to the MCNP6 reference solution 1.00622±0.00004 are also included. For angular integrations, the Legendre-Chebyshev cubature was used. L5T5 cubature appears an adequate approximation. It can be seen that the eigenvalue approaches an asymptotic value with increasing number of energy groups.

Table 5.5 Eigenvalues of PROTEUS-SN Calculations for 2D Mini-Core with Homogenized Assemblies vs. Angular Cubature and Number of Energy Groups

	Number of groups	Angular cubature	
		L5T5	L7T35
Eigenvalue	33	1.00307	1.00310
	70	1.00509	1.00512
	116	1.00598	1.00599
Error (pcm)	33	-315	-312
	70	-113	-110
	116	-24	-23

PROTEUS-SN calculations were performed for the 2D mini-core problem with partially heterogeneous assemblies by varying the number of energy groups. Table 5.6 shows the heterogeneity effect of the 2D mini-core estimated by PROTEUS-SN with different numbers of groups. It can be seen that with increasing number of groups, the eigenvalue converges to the

MCNP6 reference value for both homogenized and partially heterogeneous assembly cases. On the other hand, the eigenvalue differences between the homogenous and partially heterogeneous assembly cases remain almost constant since the errors induced by the multi-group approximation are canceled out in the subtraction of the eigenvalues. The heterogeneity effect estimated by PROTEUS-SN is ~70 pcm smaller than the MCNP6 reference result.

Table 5.6 Comparison of Heterogeneity Effects of 2D Mini-Core Estimated with PROTEUS-SN Calculations with Different Number of Groups and MCNP6 Results

Code	PROTEUS-SN			MCNP6 Reference
Number of Groups	33	70	116	
Homogeneous Assembly	1.00307	1.00509	1.00598	1.00622±0.00004
Errors (pcm)	315	113	24	
Heterogeneous Assembly	1.00528	1.00734	1.00821	1.00916±0.00004
Errors (pcm)	388	182	95	
Heterogeneity Effect (pcm)	221	224	222	294±6

Based on the above analysis results, a set of parameters for spatial, angular and energy approximation were selected for the VARIANT and PROTEUS-SN calculations as summarized in Table 5.7. The mesh used for the PROTEUS-SN single assembly calculation is the same with the mesh used for the fuel assembly in the PROTEUS-SN mini-core calculation. In the next section, the flux solutions of VARIANT mini-core calculation and PROTEUS-SN single assembly calculation will be used for constructing the global heterogeneous flux and the results will be compared with the reference flux solution obtained from the PROTEUS-SN calculation for 2D mini-core with partially heterogeneous assemblies.

Table 5.7 Computational Parameters Used in VARIANT and PROTESU-SN Calculations

	VARIANT (Mini-core)	PROTEUS-SN (Mini-core)	PROTEUS-SN (Single Assembly)
Number of groups	33	33	33
Spatial approximation	6-6-1	168,704 elements	1394 elements
Angular approximation	P5	L5T5	L5T5
Scattering order	5	5	5

5.2.4 Reconstructed Heterogeneous Flux Distributions

The overall procedure for assessing the accuracy of the reconstructed heterogeneous flux is shown in Figure 5.11. The finite element meshes for a fuel assembly in the 2D mini-core was used for representing the spatial distribution of the heterogeneous flux within an assembly.

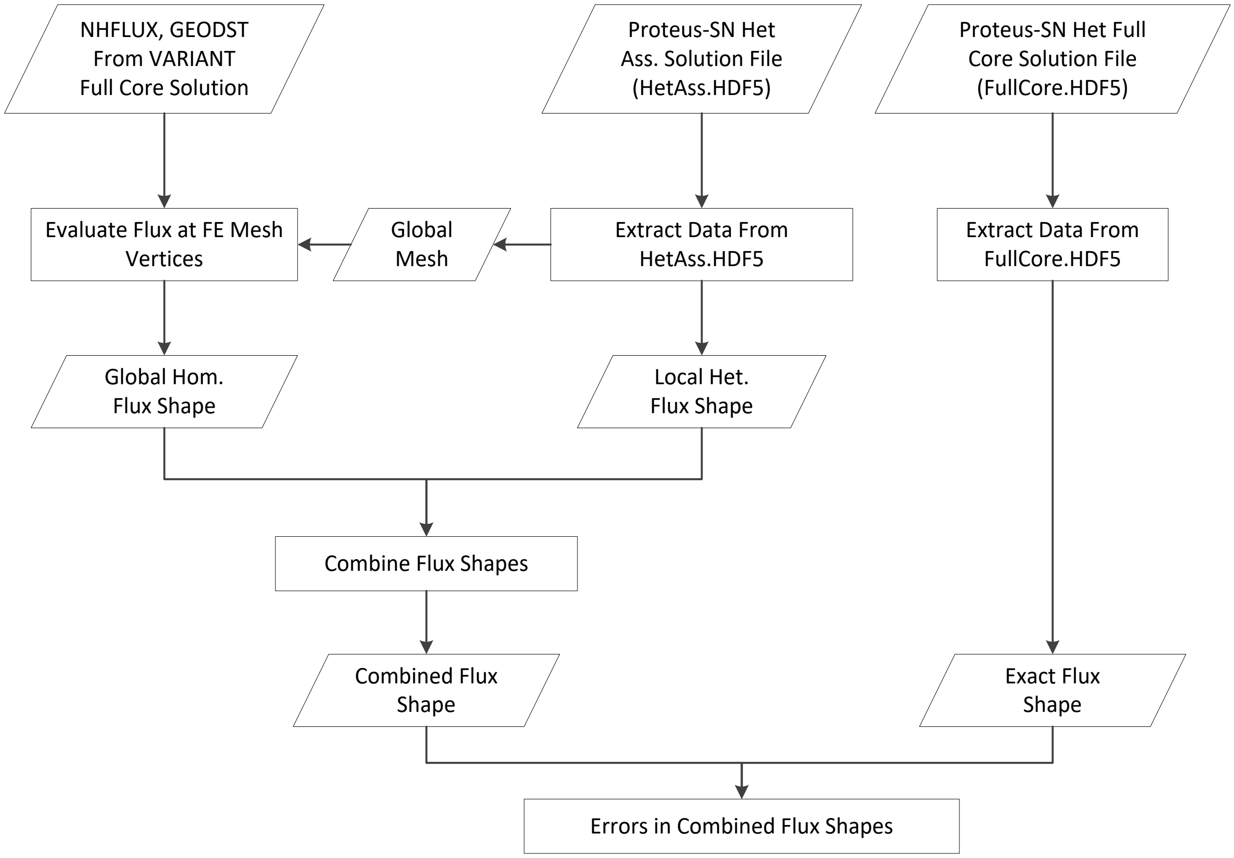

Figure 5.11 Procedures for Assessing the Accuracy of the Reconstructed Heterogeneous Flux

In the PROTEUS-SN calculation for a single heterogeneous assembly, the flux solutions are given at the vertices of finite element meshes and the full solutions were stored in the hierarchical data format (HDF5) [67, 68]. A computational module was developed to extract the flux solutions from the HDF5 output file. Then, the element-averaged or -integrated flux was obtained by integrating the flux distribution over the element determined from the flux values at the vertices and the shape functions of the given element type. To combine the PROTEUS-SN assembly solution with VARIANT global solution, the finite element meshes used for PROTEUS-SN were superimposed on the VARIANT solution for each node (homogenized assembly). The full-core flux solution and geometry information of the VARIANT calculation are stored in the NHFLUX and GEODEST files. The VARIANT flux evaluation module calculates the fluxes at arbitrary points when their global coordinates are given. The VARIANT global flux was evaluated at the vertices of each element. The element-integrated flux was obtained following the same procedure used in evaluating the element-integrated flux of PROTEUS-SN solutions. The reconstructed heterogeneous flux from VARIANT and PROTEUS-SN solutions was then compared with the reference heterogeneous flux calculated using PROTEUS-SN code based on heterogeneous whole core model.

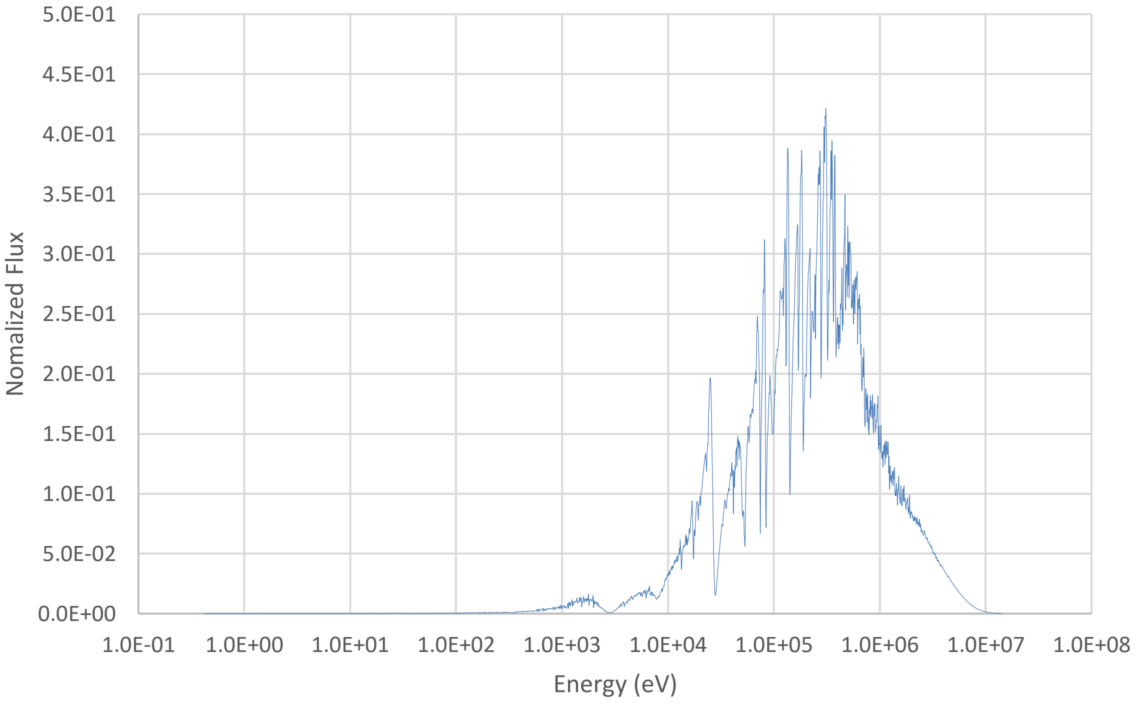

Figure 5.12 Neutron Spectrum in Fuel Assembly of 2D Mini-Core Problem

As shown in Figure 5.12, the neutron spectrum is concentrating in the energy range from 1 keV to 10 MeV. Therefore, it was decided to examine the accuracy of the combined flux distributions for groups 5, 9, and 19. The combined flux shapes were constructed and compared with the reference flux shapes for two fuel assemblies: one at the core center and the other at the core periphery (i.e., the third fuel ring). The latter fuel assembly shows larger variations in the global flux distributions. Each group flux was normalized such that its integrated value over the assembly of interest is one, and thus the spectral difference was not considered. Since the form function obtained from the PROTEUS-SN single assembly heterogeneous calculation modifies the spatial distribution of the VARIANT full core solution, the combined flux will have the same spectrum as the VARIANT solution. The absolute values of the combined flux for each group can be obtained by multiplying the normalized flux shape and the total group flux of VARIANT.

Figure 5.13, Figure 5.15 and Figure 5.17 show the global VARIANT flux shape, the local PROTEUS-SN flux shape, the combined flux shape and the reference flux shape of the fuel assembly at the core center for the groups 5, 9 and 19, respectively. The color represents the magnitude of the element-averaged fluxes. The errors in the element-averaged fluxes of the reconstructed flux from the VARIANT solution and the combined flux are also presented in Figure 5.14, Figure 5.16 and Figure 5.18 for the groups 5, 9 and 19, respectively. Similarly, Figure 5.19, Figure 5.21 and Figure 5.23 show the global VARIANT flux shape, the local PROTEUS-SN flux shape, the combined flux shape and the reference flux shape of the fuel assembly at the core periphery for the groups 5, 9 and 19, respectively. The corresponding errors in the element-averaged fluxes of the reconstructed flux from the VARIANT solution and the combined flux are shown in Figure 5.20, Figure 5.22 and Figure 5.24 for the groups 5, 9 and 19, respectively.

Table 5.8 summarizes the maximum relative errors in the normalized element-averaged fluxes of the fuel assembly at the core center. The maximum error in the reconstructed flux from the VARIANT solution is ~7.6% occurred in group 19, which is mainly due to the assembly homogenization. By comparing the errors in the reconstructed VARIANT flux and the combined flux, it can be seen that the group 19 flux shows a significant local heterogeneity effect because of the relatively short neutron mean free path. The maximum error in the group 19 is reduced to ~1.8% in the combined flux shape since the local heterogeneity information is reflected through the single assembly PROTEUS-SN solution. This result suggests that the single assembly PROTEUS-SN solution provides good local heterogeneity information. The results in Figure 5.14, Figure 5.16 and Figure 5.18 also show that the use of PROTEUS-SN single assembly solution reduces the errors in the reconstructed VARIANT flux significantly by providing local heterogeneity information.

Table 5.9 summarizes the maximum relative errors in the normalized element-averaged fluxes of the fuel assembly at the core periphery, which shows significant flux variations across the assembly. The maximum error in the reconstructed VARIANT solution is 6.9%, which occurs in group 19. The maximum error in the combined flux shape is 4.6% and occurs in group 5. The errors in the combined flux shape are relatively larger in this core periphery assembly than in the central fuel assembly. These results indicate that the reflective boundary conditions used in the PROTEUS-SN single assembly calculation is not adequate since this fuel assembly is surrounded by fuel and reflector assemblies. In order to improve the accuracy, the form function to represent the local heterogeneity information needs to be obtained from the PROTEUS-SN calculation for a supercell composed of the target assembly of interest and six surrounding assemblies.

Table 5.8 Maximum Relative Error in Normalized Element-Averaged Fluxes of Fuel Assembly at Core Center

	VARIANT	Combined solution
Group 5	0.0338	0.0182
Group 9	0.0090	0.0047
Group 19	0.0755	0.0181

Table 5.9 Maximum Relative Error in Normalized Element-Averaged Fluxes of Fuel Assembly at Core Periphery

	VARIANT	Combined solution
Group 5	0.0653	0.0456
Group 9	0.0103	0.0059
Group 19	0.0690	0.0209

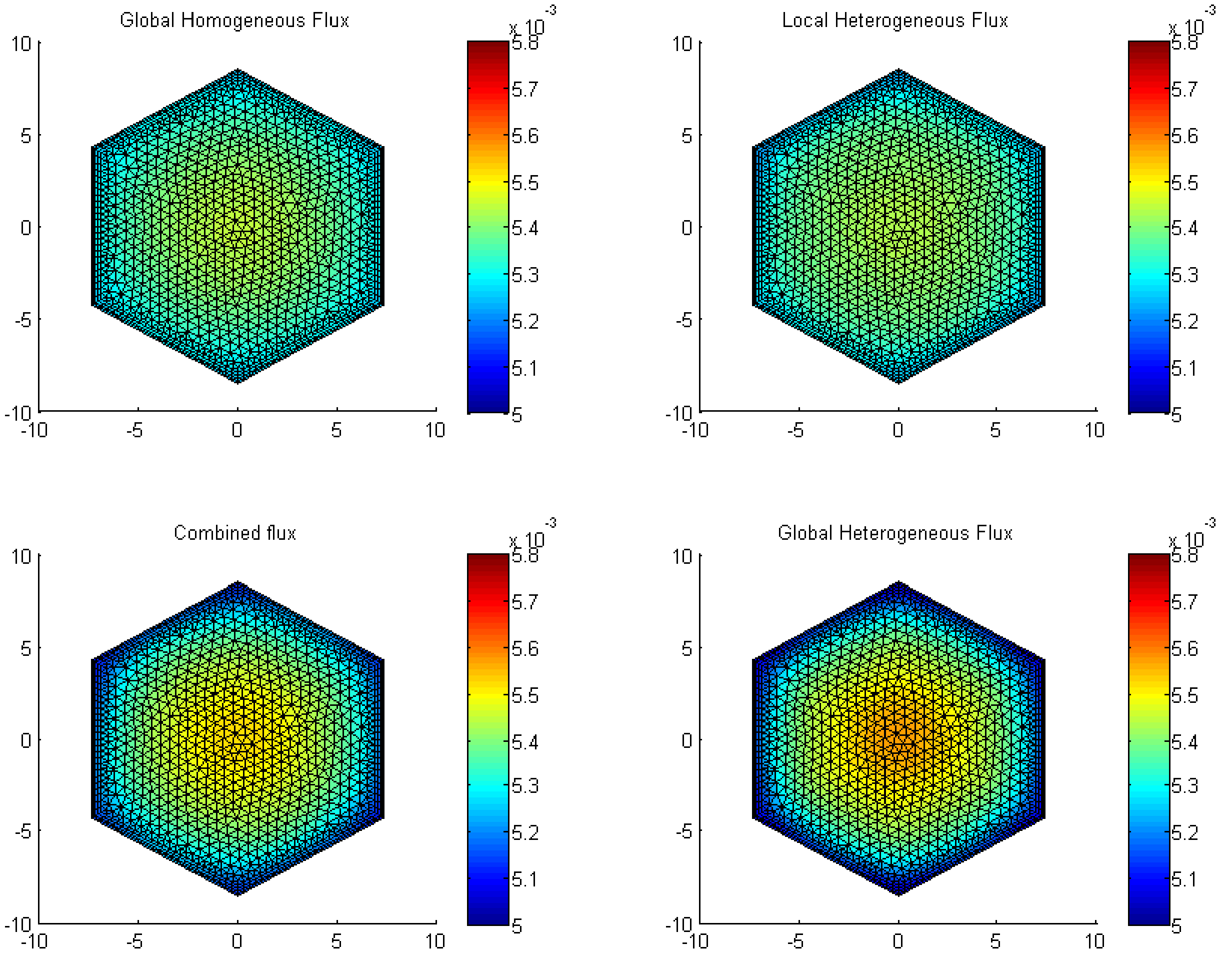

Figure 5.13 Combined and Reference Distributions of Group 5 Flux in Fuel Assembly at Core Center

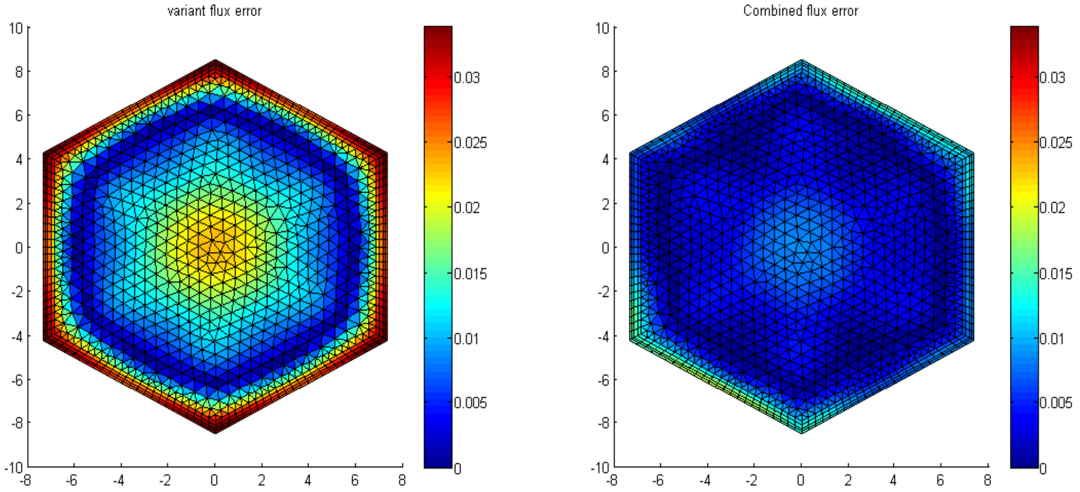

Figure 5.14 Relative Error in Element-Averaged Group 5 Fluxes in Fuel Assembly at Core Center

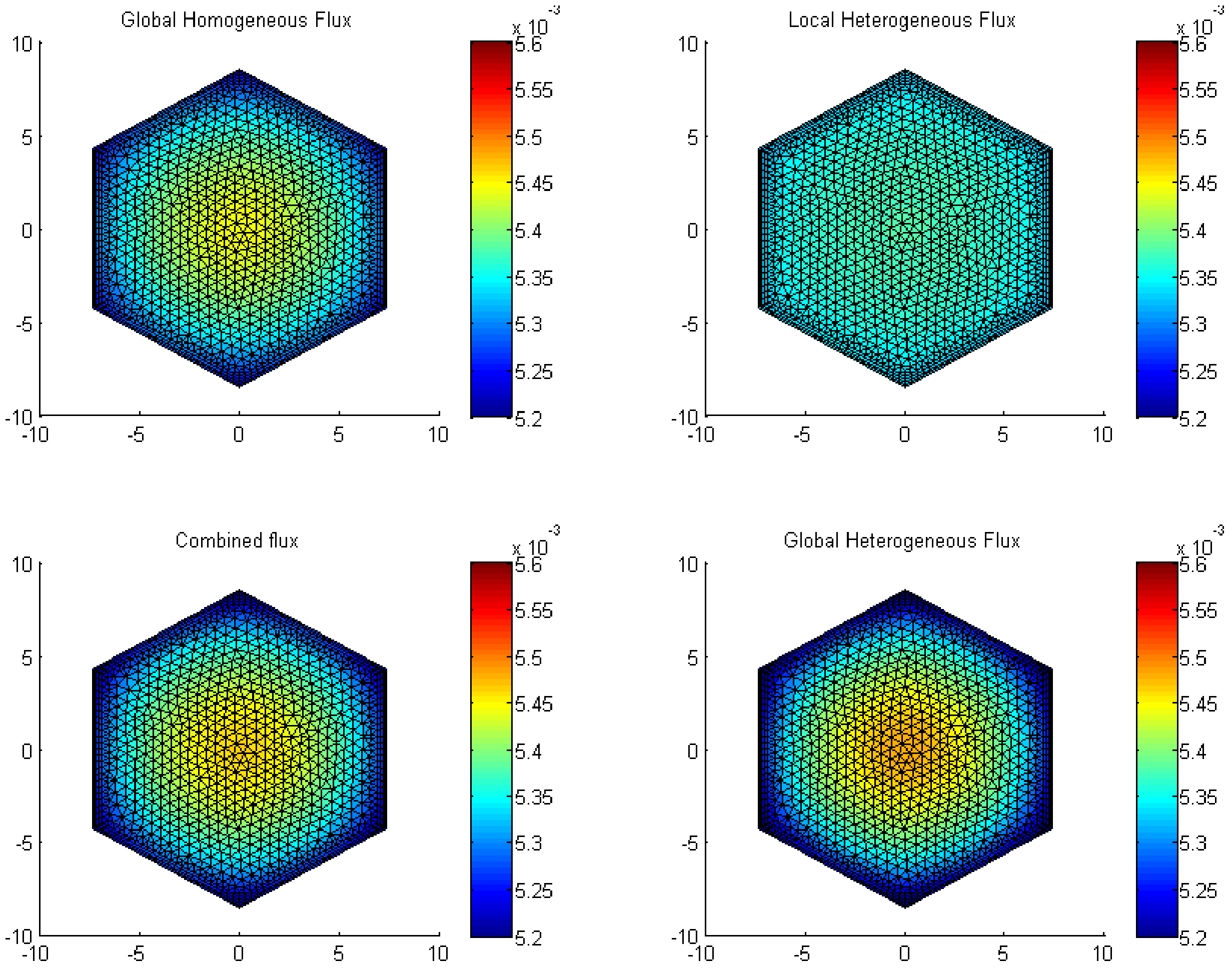

Figure 5.15 Combined and Reference Distributions of Group 9 Flux in Fuel Assembly at Core Center

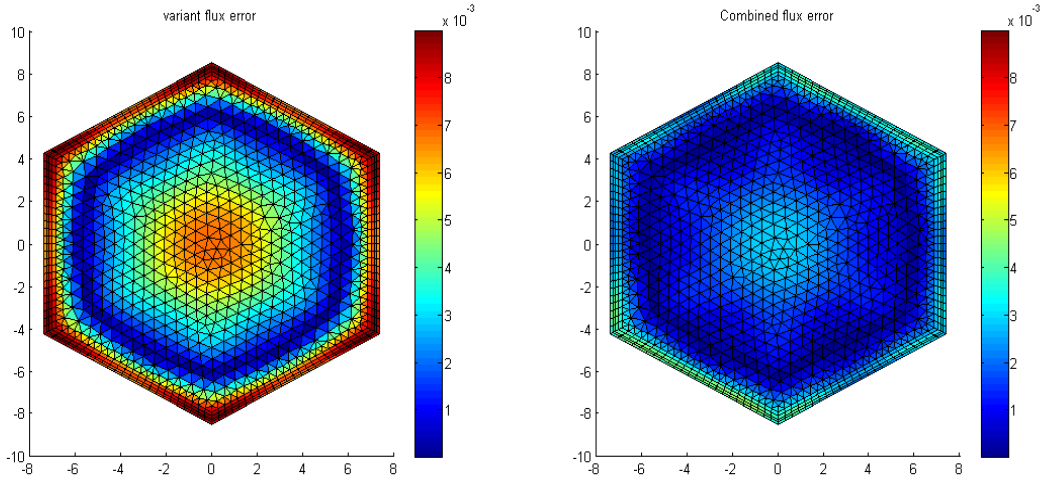

Figure 5.16 Relative Error in Element-Averaged Group 9 Fluxes in Fuel Assembly at Core Center

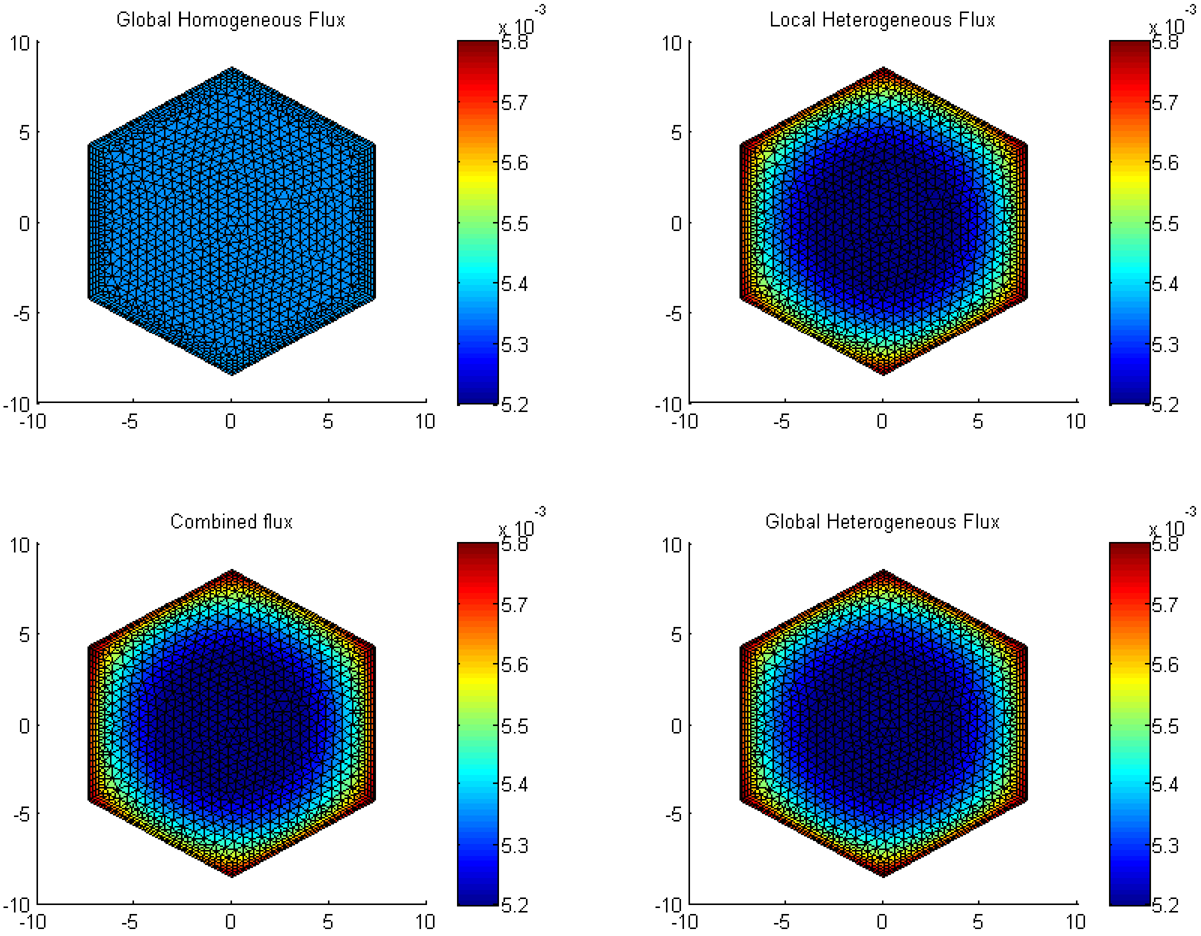

Figure 5.17 Combined and Reference Distributions of Group 19 Flux in Fuel Assembly at Core Center

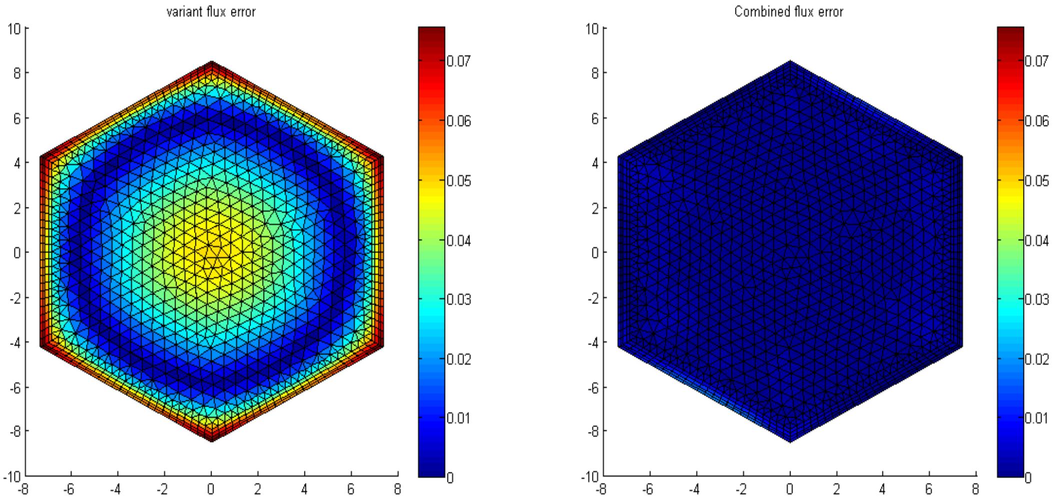

Figure 5.18 Relative Error in Element-Averaged Group 19 Fluxes in Fuel Assembly at Core Center

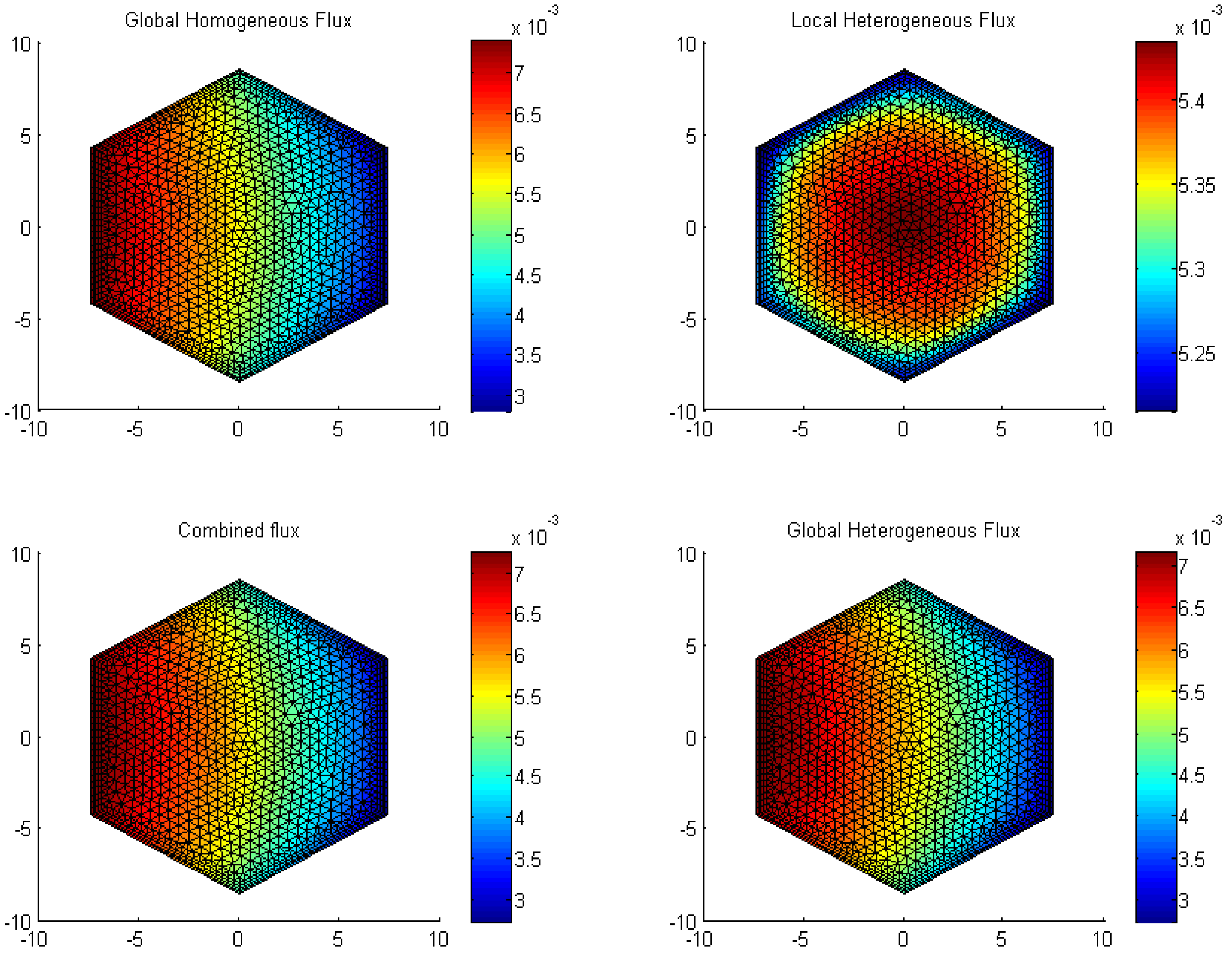

Figure 5.19 Combined and Reference Distributions of Group 5 Flux in Fuel Assembly at Core Periphery

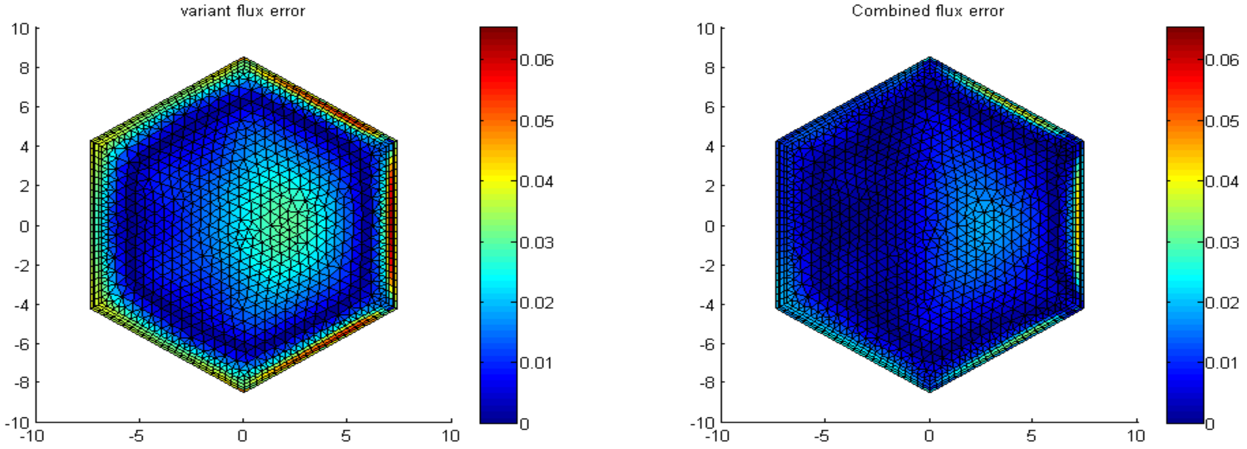

Figure 5.20 Relative Errors in Element-Averaged Group 5 Fluxes in Fuel Assembly at Core Periphery

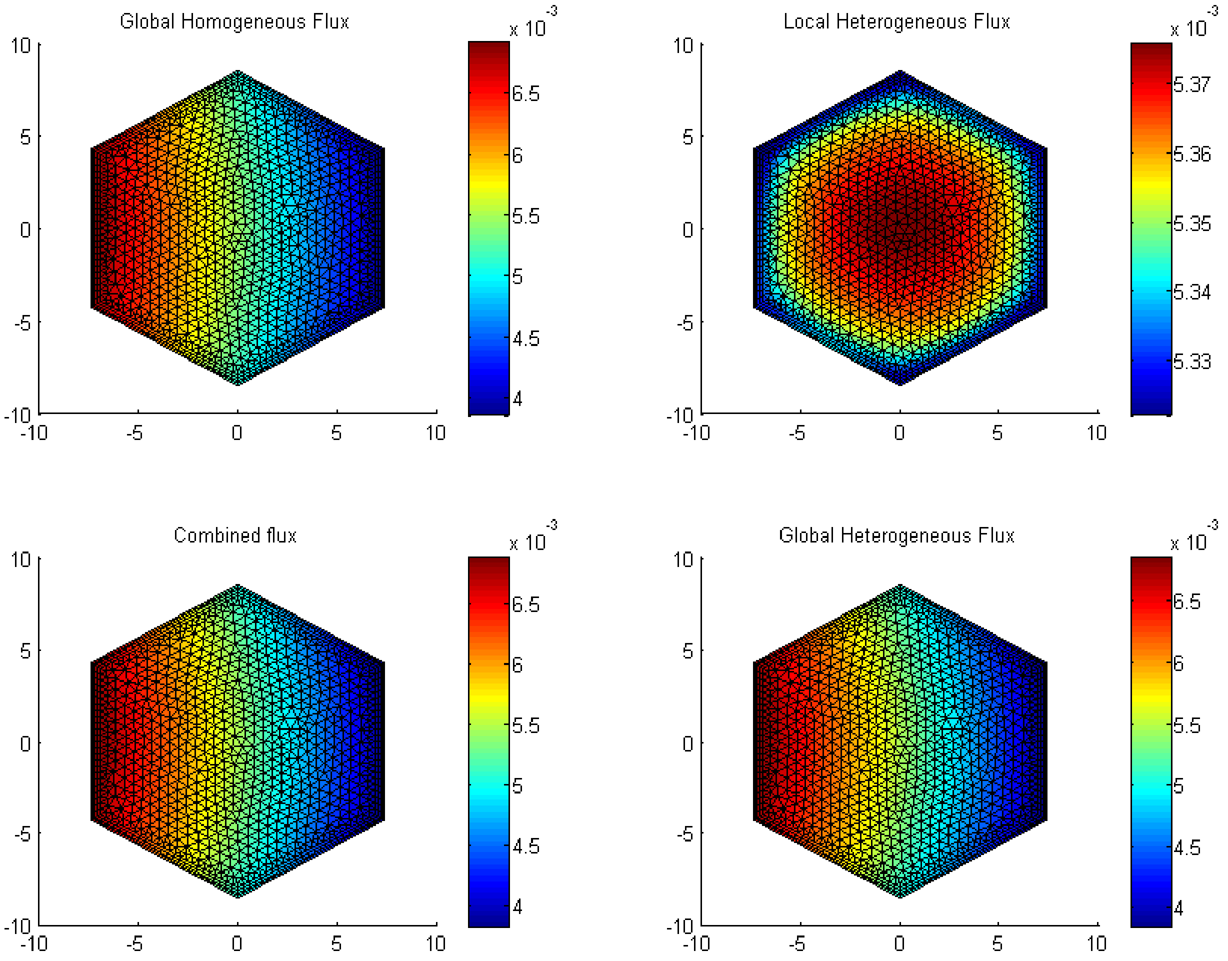

Figure 5.21 Combined and Reference Distributions of Group 9 Flux in Fuel Assembly at Core Periphery

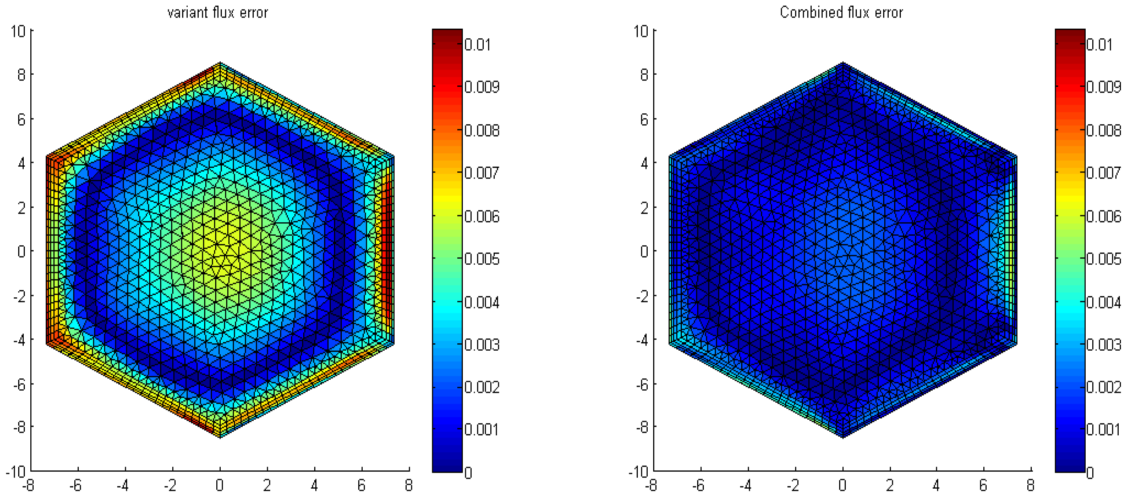

Figure 5.22 Relative Errors in Element-Averaged Group 9 Fluxes in Fuel Assembly at Core Periphery

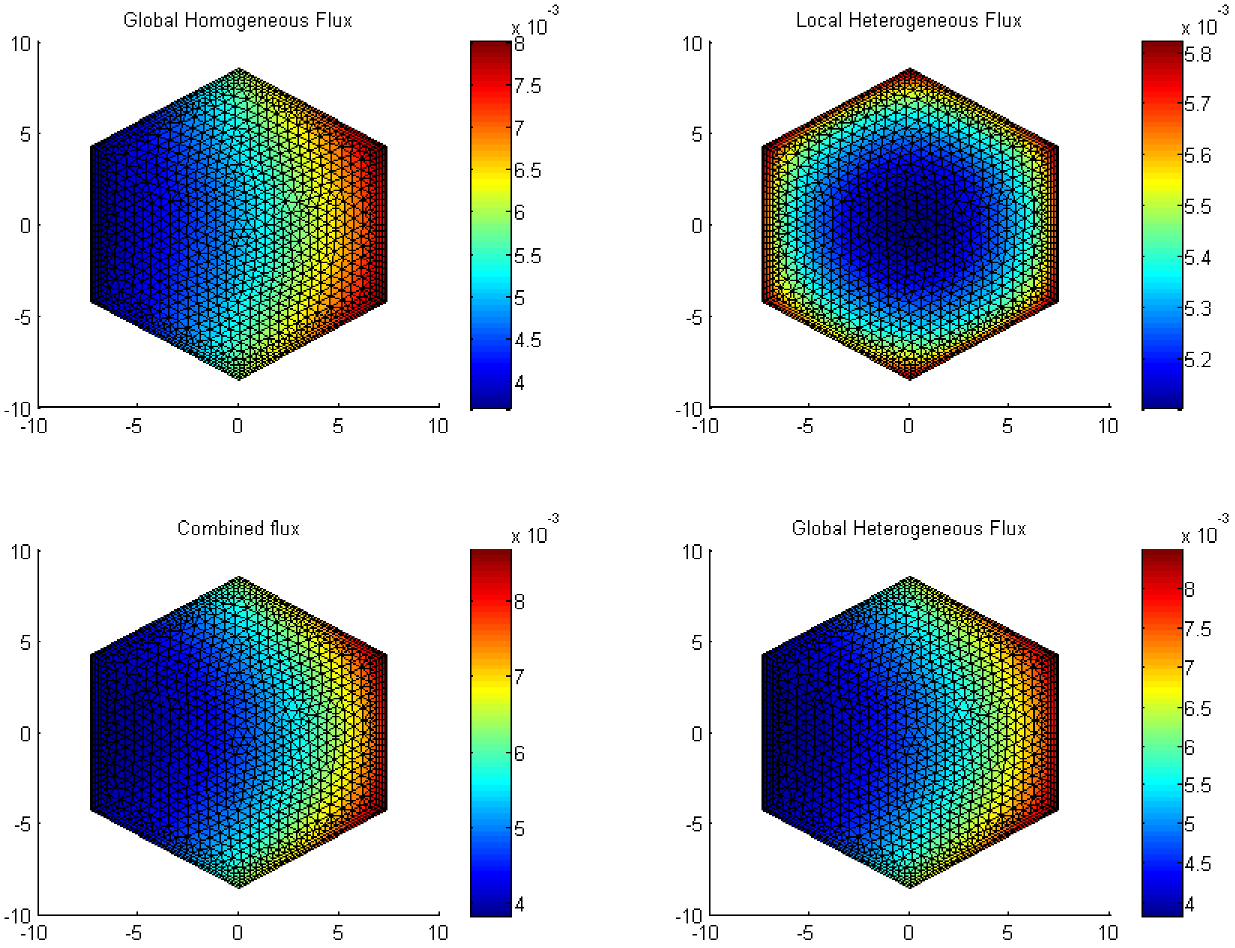

Figure 5.23 Combined and Reference Distributions of Group 19 Flux in Fuel Assembly at Core Periphery

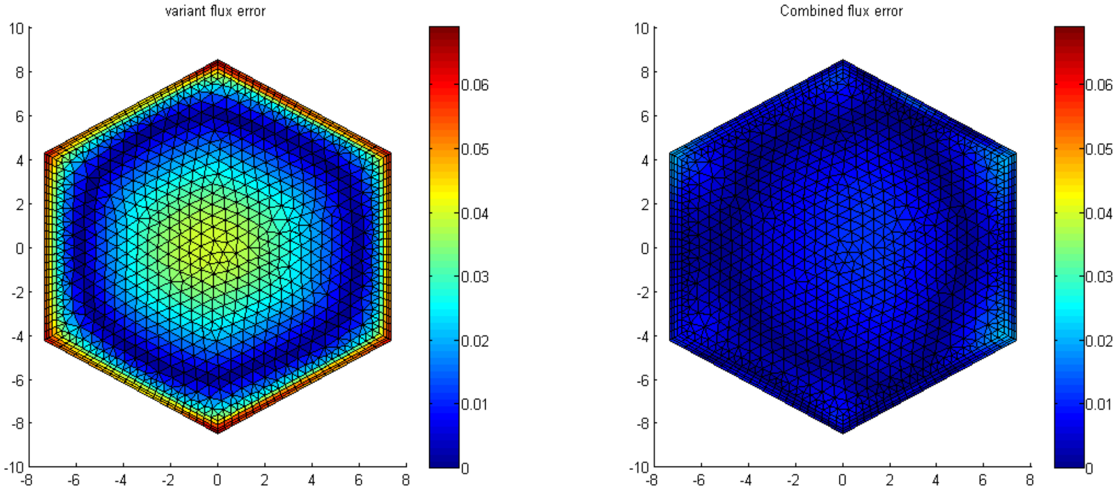

Figure 5.24 Relative Error in Element-Averaged Group 19 Fluxes in Fuel Assembly at Core Periphery

6. DEVELOPMENT OF RAINBOW CODE

6.1 Overview of RAINBOW Code

The perturbation calculation scheme for calculating the reactivity change due to assembly displacement described in Chapter 3 has been implemented into a computer program named RAINBOW (ReActivity INduced by assembly BOWing). The RAINBOW code is programmed in FORTRAN 95 and developed on PC Windows in Intel Parallel Studio XE environment. The RAINBOW code should also work on any Linux system with trivial modifications if necessary.

The RAINBOW code structure and data flow are shown in Figure 6.1. The RAINBOW code requires one general input file and four CCCC (Committee on Computer Code Coordination) binary interface files [69]. The four binary interface files are the microscopic cross section file ISOTXS, the geometry description file GEODST, the nodal flux solution file NHFLUX, and the nodal adjoint flux solution file NAFLUX, and they are obtained from the VARIANT calculation. It also requires the assignment input and HDF5 output files of PROTUES-SN code. The HDF5 output file can be replaced by a FormFE file if it is available. RAINBOW code contains mainly four modules: the input processing module, the flux reconstruction module, the macroscopic cross section calculation module, and the perturbation calculation module.

6.2 RAINBOW Modules

6.2.1 Input Processing Module

The input processing module preprocesses the interface files to extract the data for the succeeding computations. It adopts several I/O modules for CCCC interface files in the ARC (Argonne Reactor Computation) code package to preprocess the NHFLUX, NAFLUX, GEODST and ISOTXS files. NHFLUX contains the spatial expansion coefficients for the forward scalar flux and higher order angular moments. The coefficients are extracted and stored into the variable USER_NHFLUX that is defined in a derived type following the NHFLUX file format. Since the adjoint flux is written in the same format in NAFLUX as the forward flux, it is treated in the same way and stored into the variable USER_NAFLUX. It is noted that NAFLUX contains the raw data generated by solving the adjoint neutron transport equation using forward neutron transport solver

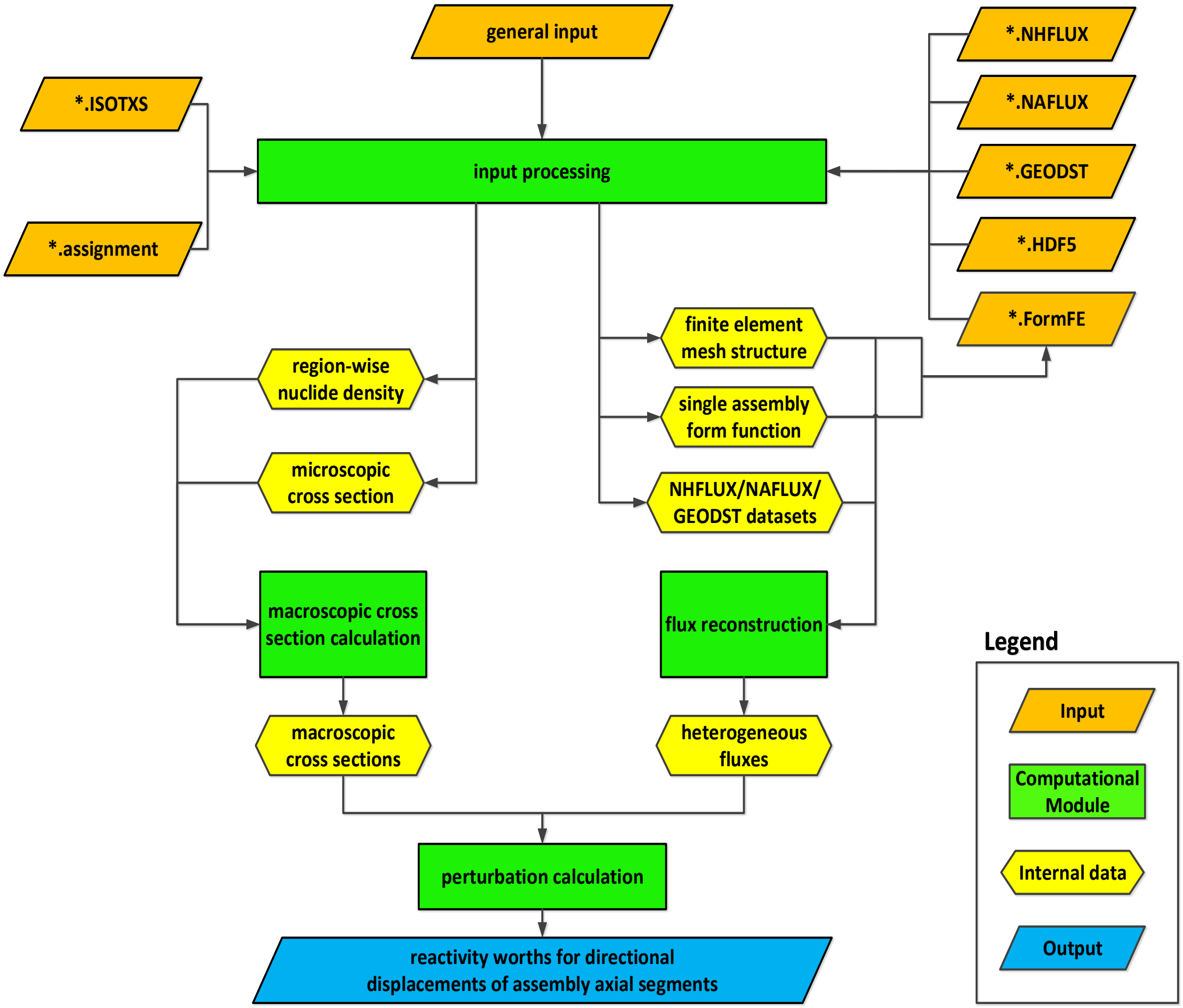

Figure 6.1 RAINBOW Code Structure and Data Flow

by reversing the energy group order and the angular direction. To evaluate the adjoint flux based on NAFLUX dataset, the energy group number should be reversed and the sign of odd-parity angular flux moments should be flipped. The GEODST file that contains the geometrical information of the core model is extracted into the variable USER_GEODST. The ISOTXS file that contains the microscopic cross sections for each isotope is read into the variable RAINBOW_ISOTXS.

The HDF5 output file of the PROTEUS-SN code is required for the first run of the RAINBOW code to provide the heterogeneous forward and adjoint form functions of each single assembly. The PROTEUS-SN solutions are defined in each finite element vertex. The intra-element flux distribution is determined by the vertex values combined with the shape function depending on the finite element type. The element-averaged flux is then obtained by integrating the intra-element flux distribution. Currently, the RAINBOW code accepts only two types of extruded finite elements based on three-node linear element and four-node bilinear element. The element types with more nodes and/or higher order could be included in the future development of RAINBOW code if necessary. With the HDF5 interface file, the input processing part also generates a FormFE file containing the following information: 1) assembly heterogeneous form functions of forward and adjoint fluxes in each finite element, 2) finite element vertex coordinates, and 3) global identification number for each finite element vertex that links the vertex identification number to the finite element identification number. Once the FormFE file is generated, the RAINBOW code can be executed by providing the FormFE file instead of the HDF5 interface file to avoid duplicate processing of the PROTEUS-SN output data for the same assembly model. The assembly form functions and the associate finite element mesh structure are stored in the variable PROTEUS_Solution. The variables PROTEUS_Solution, USER_NHFLUX, USER_NAFLUX and USER_GEODEST are passed to the flux reconstruction module for computing the combined heterogeneous forward and adjoint fluxes used in the perturbation calculations.

The input processing module also adopts the assignment input file of the PROTEUS-SN code to obtain the compositions of heterogeneous assembly model. The assignment file provides three types of information, which are sufficient for calculating the homogenized nuclide densities for each heterogeneous block (e.g., regions such as fuel, duct and coolant). The MATERIAL_DEF card recursively defines the materials based on the isotopes appearing in the ISOTXS dataset, which are stored in the variable RAINBOW_Materials. The REGION_ALIAS card links a material to a block, which is stored in the variable RAINBOW_MaterialToBlock. The REGION_PROPERTY card assigns atom densities to a block, which is stored in the variable RAINBOW_MeshBlockProperties.

6.2.2 Macroscopic Cross Section Calculation Module

The HMG4C module of the VARIANT code generates the macroscopic cross section dataset COMPXS based on the data contained in the CCCC datasets ISOTXS, NDXSRF, ZNATDN and DLAYXS. However, a heterogeneous assembly configuration is required to calculate the reactivity change due to assembly displacement. Thus, the macroscopic cross section dataset COMPXS from VARIANT calculation with fully homogenized-assembly model cannot be directly used for RAINBOW calculations. Instead, the perturbation calculations should be based on the heterogeneous assembly configuration used in PROTEUS-SN calculations. Therefore, the subroutines of the PROTEUS-SN code for calculating macroscopic cross sections of blocks are adopted in this module. The calculation procedure is shown in Figure 6.2. The module accepts RAINBOW_Materials, RAINBOW_ALIAS, and RAINBOW_MeshBlockProperties together with RAINBOW_ISOTXS that are passed from the input processing module. The macroscopic cross sections for each block are finally calculated by multiplying the isotopic nuclide densities with associate microscopic cross sections and summing over all isotopes in the block.

6.2.3 Heterogeneous Flux Reconstruction Module

The heterogeneous flux reconstruction module contains the subroutines that produce the element-averaged forward and adjoint fluxes based on heterogeneous assembly configuration by combining the PROTEUS-SN single assembly solution and the VARIANT full core solution. The overall procedure of flux reconstruction is shown in Figure 6.4. The finite element (FE) meshes are used for representing the spatial distribution of the heterogeneous flux within a fuel assembly. The finite element meshes used for the PROTEUS-SN code were superimposed on the VARIANT solution for each node (homogenized assembly). The global VARIANT solutions are processed node by node following the assembly ordering in the NHFLUX dataset as shown in Figure 6.3. Figure 6.3

also shows the global frame of reference (X-Y), the origin of which is at the core center, and the local frame of reference (X'-Y'), the origin of which is at each assembly center.

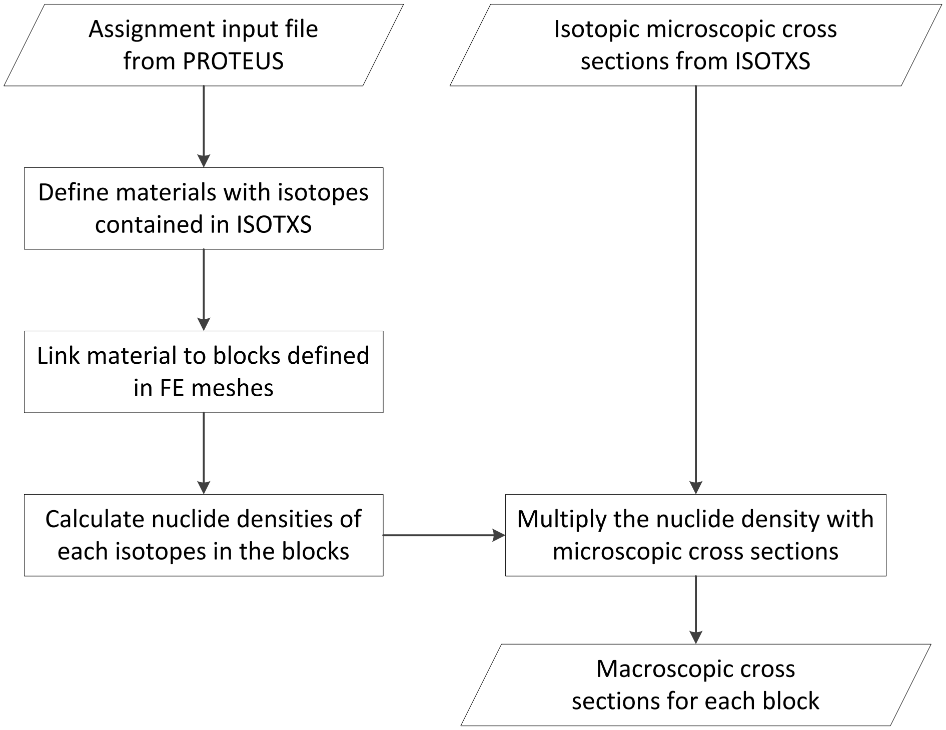

Figure 6.2 Procedures for Calculating the Macroscopic Cross Sections for Each Block

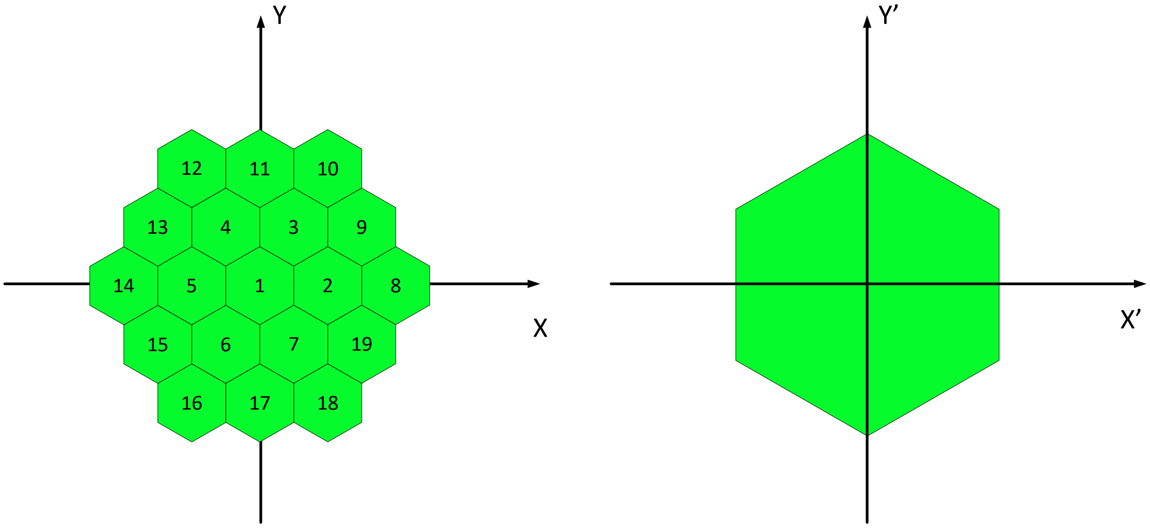

Figure 6.3 Example of Node Ordering in NHFLUX Dataset and the Frames of Reference for FE Meshes

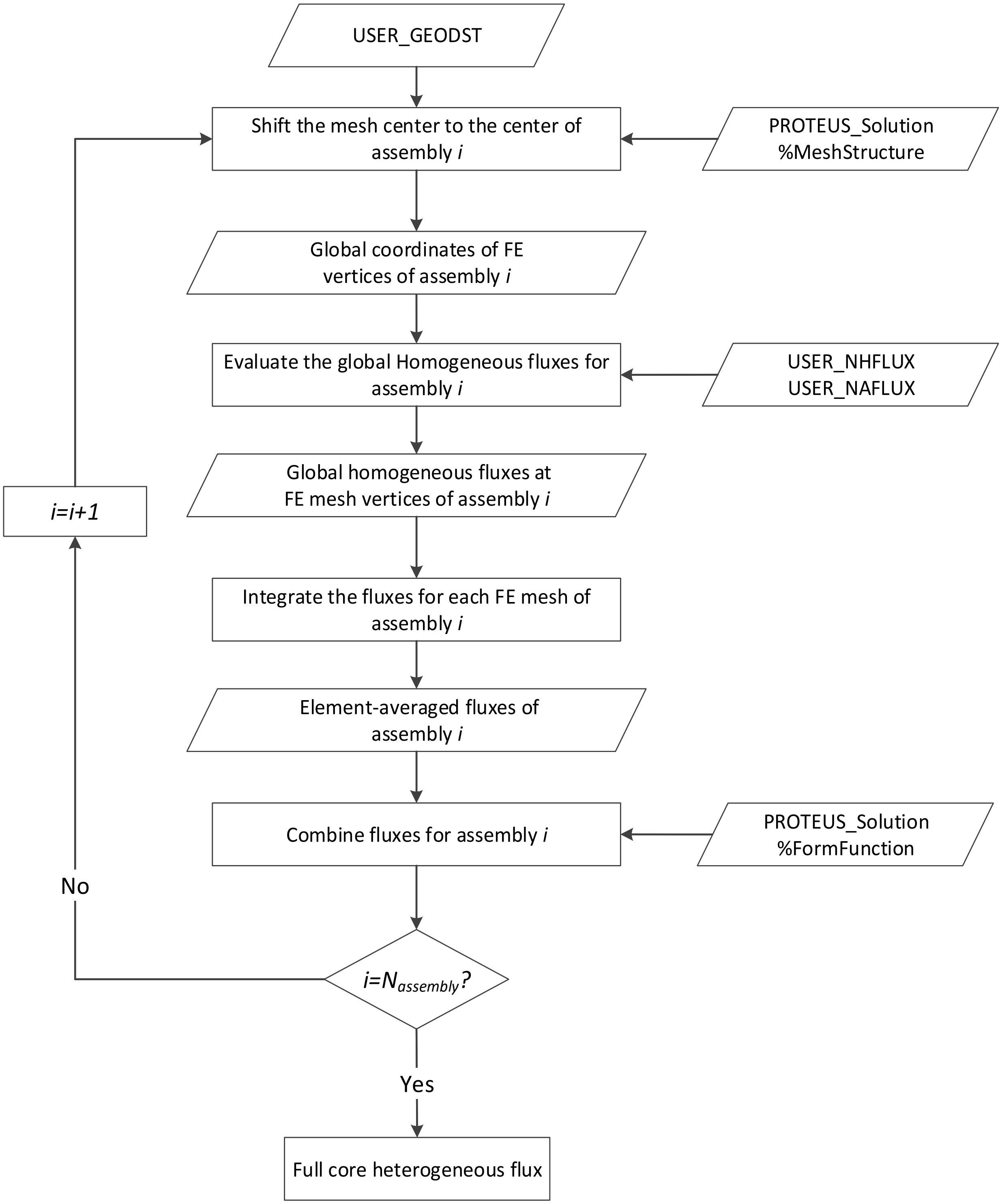

Figure 6.4 Procedures for Reconstruction of Global Heterogeneous Flux

The flux evaluation subroutine takes the coordinates in the global frame of reference as input, while the FE meshes from PROTEUS-SN calculation are defined in the local frame of reference. The FE mesh coordinates at the global frame of reference for individual assembly are determined by adding the node center coordinates in the global frame of reference to the FE mesh local coordinates. The VARIANT global flux is evaluated at the vertices of each element. The element-averaged flux is determined following the same procedure used in evaluating the element-averaged flux of the PROTEUS-SN solution. The evaluated VARIANT and PROTEUS-SN solutions are then combined to yield a full core heterogeneous flux distribution based on the flux reconstruction method described in Chapter 5.

6.2.4 Perturbation Calculation Module

The designed perturbation calculation module in the RAINBOW code contains two procedures for bowing reactivity coefficient and for fuel axial expansion.

6.2.4.1 Bowing reactivity coefficient

The perturbation calculation for assembly displacement produces the reactivity change for a small shift of each axial segment of each assembly. The perturbation calculations are performed by shifting each assembly segment in each of six directions normal to the duct wall surfaces by a user-specified amount. Then, the reactivity change for assembly displacement in any given direction can be approximated by the linear combination of the reactivity changes in the selected six directions normal to duct wall surfaces as discussed in Section 3.1.

The procedure for the perturbation calculations of the reactivity changes due to assembly displacements is shown in Figure 6.5. The calculation starts from evaluating the bilinear-weighted fission production term I_F over the whole core, which provides the denominator of the perturbation formula. The numerator includes the perturbations of the fission production term and the loss and migration term. The loss and migration term equals to the absorption term plus the out-scattering term minus the in-scattering term, which is equivalent to the total reaction terms subtracting the scattering source term. The perturbations of the bilinear-weighted reaction rates and the reactivity changes are calculated by following the loops over the six directions, assembly axial segments and assemblies. For each axial segment, the spatial integration of a bilinear-weighted reaction rate perturbation over the node is approximated by the production of the integrated value at the node mid-plane and the node height. The node height should be sufficiently small, and the bilinearly weighted reaction rate could be considered linear in axial direction such that its value at the node mid-plane provides an accurate approximation of the axially averaged quantity. This axial integration scheme of the bilinearly weighted reaction rate can be improved by analytically integrating the axial shapes of the bilinearly weighted reaction rates in each extruded finite element such that the limitations on the axial node size can be reduced.

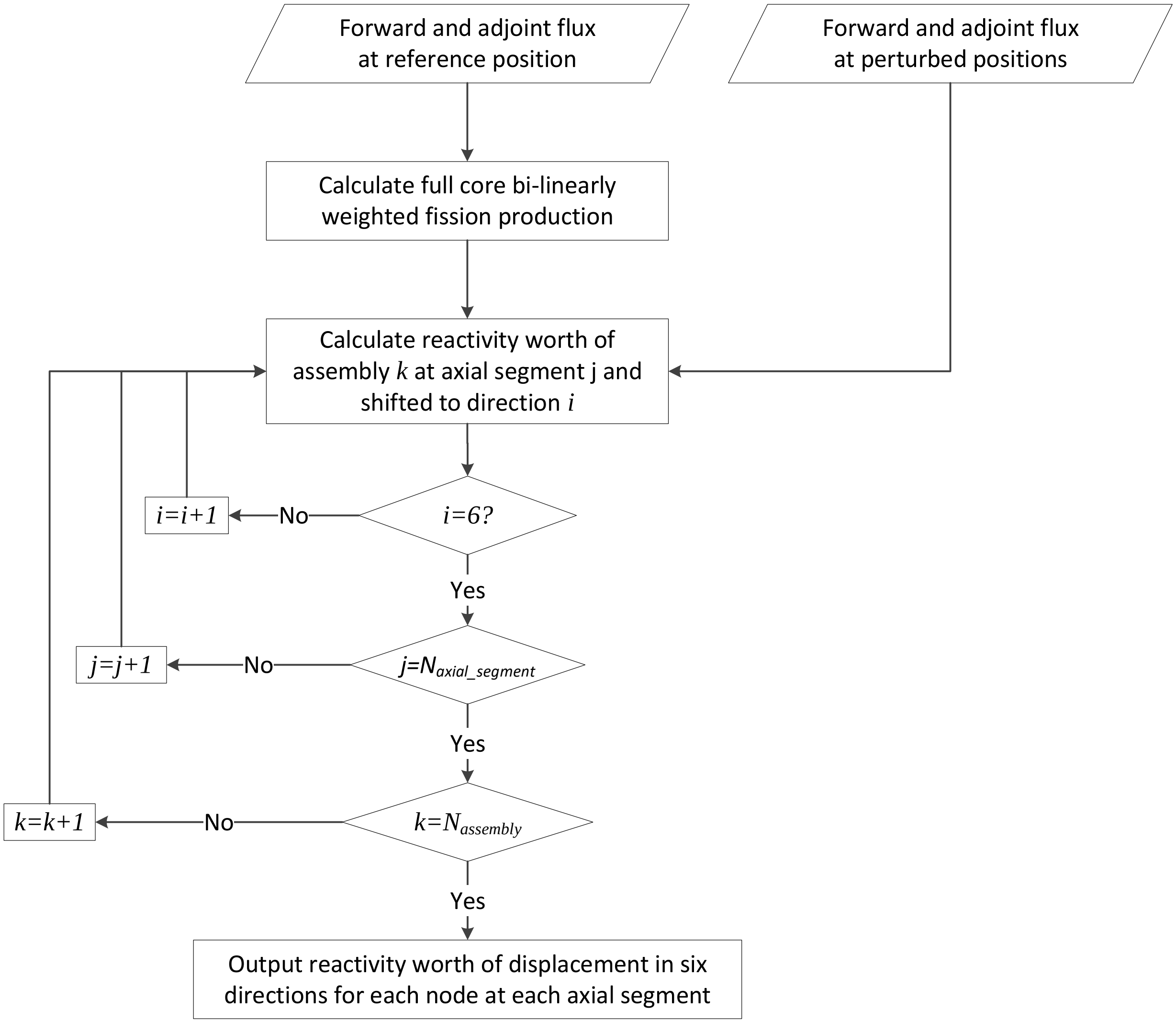

Figure 6.5 Procedures for Perturbation Calculation of Reactivity Changes Due to Assembly Displacements

The procedure for the perturbation calculations of the reactivity changes due to fuel axial expansion is shown in Figure 6.6. The calculation starts from evaluating the bilinearly weighted fission production term I_F over the whole core, which provides the denominator of the perturbation formula. With assumed axial expansion for each fuel assembly, the perturbed nuclide density was calculated for the perturbed regions including fuel, bound sodium and fission gas plenum. Then the program proceeds to calculate the reactivity changes in those regions and gives the reactivity worth due to fuel axial expansion for each assembly. The final output is the fuel axial expansion worth for unit length of expansion for each assembly.

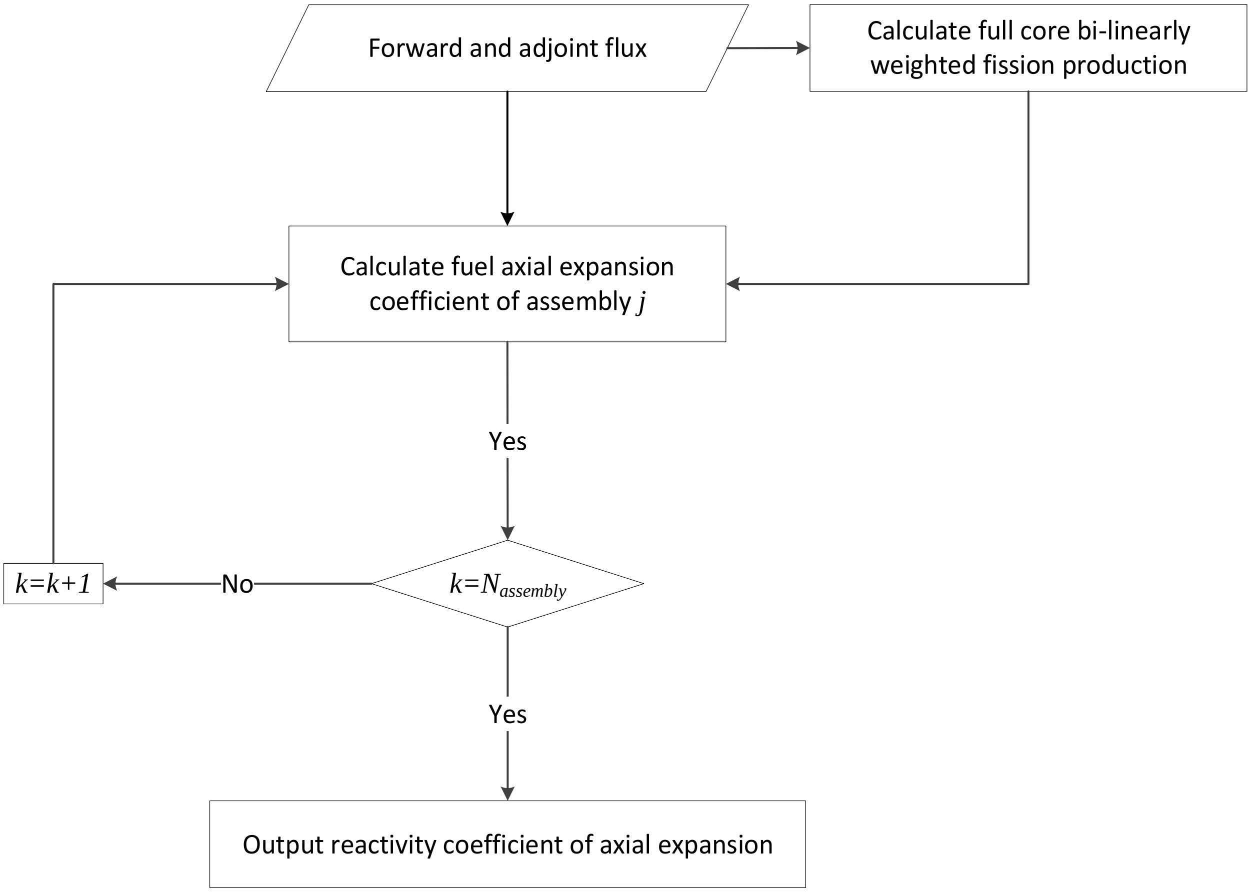

Figure 6.6 Procedures for Perturbation Calculation of Reactivity Changes Due to Fuel Axial Expansion

6.3 RAINBOW Input and Output Descriptions

The user-friendly ‘namelist’ input format is adopted in the RAINBOW code. There are three namelist blocks: &ProblemSpecs, &AssemblySpecs and &InterfaceFiles. The descriptions of the three namelist blocks are shown in Table 6.1, Table 6.2 and Table 6.3. The RAINBOW output file has a simple structure. It contains a core map denoting the assembly ordering followed by a matrix of reactivity changes due to assembly displacements (in pcm) for each assembly in each of six directions. The assembly displacement data matrix is repeated for each axial level in 3D calculations. A sample input and output files are also provided in Appendix D.

Table 6.1 Descriptions of the ProblemSpecs Block

Keyword	Type	Description
Problem%UseFormFE	Logical	.FAULSE. indicates the FormFE file does not exist and user should provide HDF5 output file from PROTEUS calculation. .TRUE. indicates use of FormFE file
Problem%Keffective	Real	Multiplication factor
Problem%NumGroup	Integer	Number of energy group
Problem%Dims	Integer	Number of problem dimension
Problem%ScatOrder	Integer	Legendre order used for expanding the scattering source
Problem%AngularOrder	Integer	Legendre order used for expanding the angular fluxes
Problem%NumAssembly	Integer	Total number of assemblies in the core module
Problem%NumActiveAssembly	Integer	Number of assemblies for perturbation calculations
Problem%NumAssemblyType	Integer	Number of difference assembly types
Problem%AssemblyMap(:,:)	Integer	The arrangement of active assemblies, inactive assemblies are specified as 0.

Table 6.2 Descriptions of the AssemblySpecs Block

Keyword	Type	Description
Assembly(:)%Height	Real	Assembly height (cm), required if Problem%Dims=3
Assembly(:)%NumAxialNode	Integer	Number of axial node in the assembly, required if Problem%Dims=3
Assembly(:)%NumElement	Integer	Number of finite element in the assembly
Assembly(:)%NumVertex	Integer	Number of finite element vertices in the assembly
Assembly(:)%Shift	Real	Distance (cm) of assembly displacement from its origin

Table 6.3 Descriptions of the InterfaceFiles Block

Keyword	Type	Description
PROTEUS_Interface%ForwardFlux	Character	PROTEUS HDF5 output file name for forward calculation, required if Problem%UseFormFE=.FAULSE.
PROTEUS_Interface%AdjointFlux	Character	PROTEUS HDF5 output file name for adjoint calculation, required if Problem%UseFormFE=.FAULSE.
PROTEUS_Interface%FormFunction	Character	FormFE file name generated from previous execution of RAINBOW code, required if Problem%UseFormFE=.FAULSE.
PROTEUS_Interface%Assignment	Character	Assignment input file name adopted from PROTEUS calculation
MCC_Interface%ISOTXS	Character	File name for the ISOTXS dataset generated from MC^3-2 code
VARIANT_Interface%NHFLUX	Character	File name for the NHFLUX dataset generated from VARIANT code
VARIANT_Interface%NAFLUX	Character	File name for the NAFLUX dataset generated from VARIANT code
VARIANT_Interface%GEODST	Character	File name for the GEODST dataset generated from VARIANT code

7. VERIFICATION TESTS OF RAINBOW CODE

Verification tests of the RAINBOW code for perturbation theory calculation of reactivity changes due to assembly displacements were performed using two dimensional (2D) and three dimensional (3D) mini-core models. The reactivity change was calculated for an assembly (or an assembly axial segment) displacement by 2 mm in each of six directions normal to the duct wall surfaces. Reference solutions were obtained from MCNP6 Monte Carlo simulations and PROTEUS-SN deterministic calculations by taking the difference in eigenvalue between the perturbed and unperturbed cases.

7.1 Mini-Core Models

The mini-core models were derived from the ABTR design by reducing the number of assemblies. Two-dimensional core models were obtained from the core configuration at the mid-plane. Two mini-core configurations were developed in this study as shown in Figure 7.1. The mini-core model A consists of three rings of fuel assemblies, three rings of reflector assemblies and one ring of shield assemblies. The mini-core model B consists of four rings of fuel assemblies, two rings of reflector assemblies and one ring of shield assemblies. In the fuel region, three control assemblies are located in the third ring. A 3D mini-core model was developed by extruding the 2D mini-core model A in axial direction by 100 cm.

The multiplication factors for the unperturbed base configurations of the mini-core models were calculated using the VARIANT code and compared with the reference MCNP6 results. Two cases were considered for the mini-core model B: one with three B_4C control assemblies in and the other with control assemblies out. In the case of control assemblies out, the control assembly positions are filled with sodium. The MCNP6 simulations were performed with 1,000,000 particles per cycle and 800 inactive and 2000 active cycles. For each core configuration, two MCNP6 calculations were performed: one with homogenized assembly model and the other with the partially heterogeneous assembly model. One standard deviation of the resulting eigenvalue reported by the MCNP6 code was one pcm for all calculations. The VARIANT calculations were performed with 6th order polynomial approximations for the intra-nodal flux and source distributions and a quadratic polynomial approximation for the nodal interface current distribution. A P_5 angular approximation of flux was used with an anisotropic scattering order of 5.

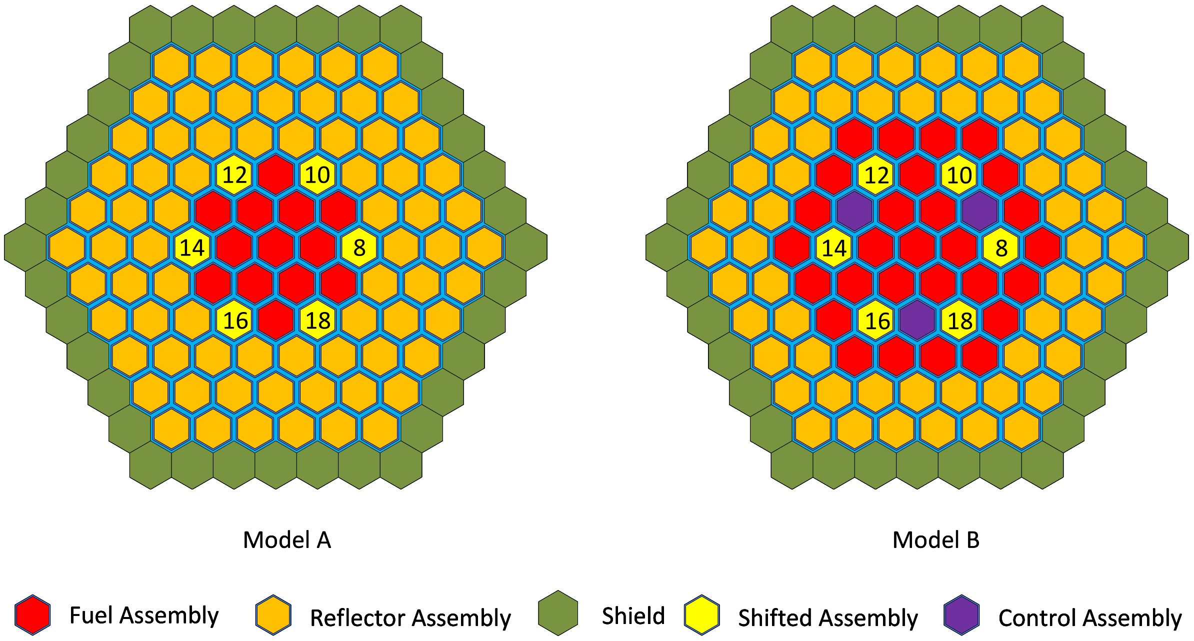

Figure 7.1 Radial Layouts of Mini-core Models without (A) and with (B) Control Assemblies

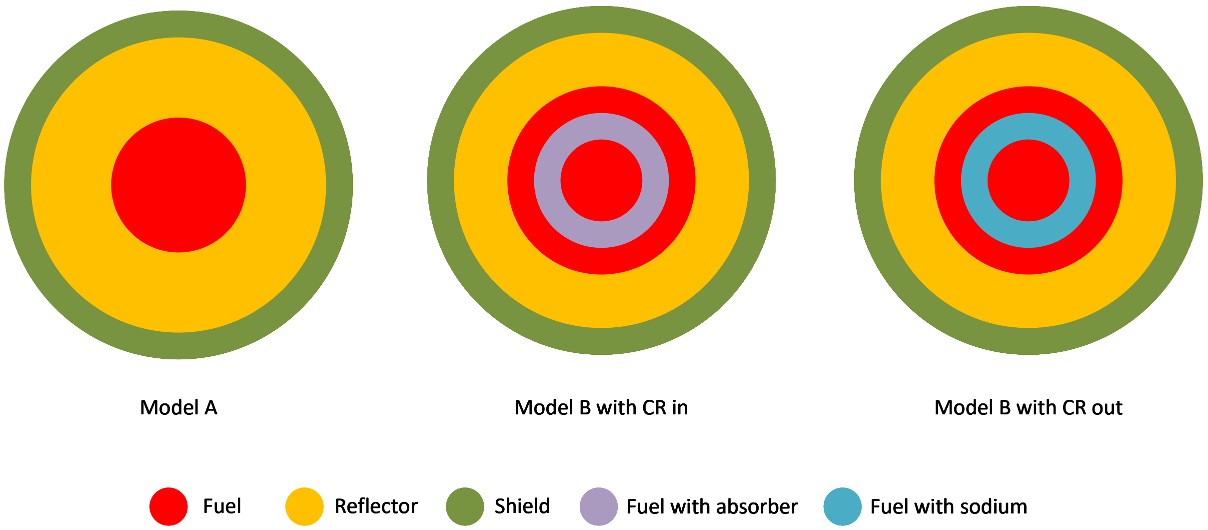

Figure 7.2 TWODANT Models for Mini-core Models

The resulting multiplication factors for 2D and 3D mini-core models are summarized in Table 7.1. The difference in multiplication factor between the VARIANT and MCNP6 results is mainly due to the assembly heterogeneity effects, since the VARIANT calculations were performed with fully homogenized assemblies (including inter-assembly gap sodium) while MCNP6 calculations were done with partially homogenized assemblies where the assembly duct and the inter-assembly sodium are explicitly modeled. It is noted that the 3D mini-core models were deeply subcritical with original ABTR assembly composition due to large leakage. The Pu-239 faction in the fuel was increased from 14% to 19% to yield a critical 3D mini-core models. The multiplication factors for critical 3D mini-core models are summarized in Table 7.2.

Table 7.1 Multiplication Factors for Mini-core Models Calculated by VARIANT and MCNP6 with ABTR Assembly Composition

	VARIANT	MCNP6	Difference (pcm)
2D Mini-core A	1.00419	1.00918±0.00001	-499
2D Mini-core B with CR in	0.99252	0.99281±0.00001	-29
2D Mini-core B with CR out	1.11077	1.11131±0.00001	-54
3D Mini-core A	0.85347	0.85512±0.00001	-165
3D Mini-core B with CR in	0.85578	0.85407±0.00001	171
3D Mini-core B with CR out	0.92119	0.91991±0.00001	128

Table 7.2 Multiplication Factors for Critical 3D Mini-Core Models Calculated by VARIANT and MCNP6

	VARIANT	MCNP6	
		Homogenous	Heterogeneous
3D Mini-Core A	1.00726	1.00691	1.00952
3D Mini-Core B with CR in	0.93539	0.93288	0.93568
3D Mini-Core B with CR out	1.00508	1.00427	1.00652

7.2 Verification of RAINBOW Perturbation Results against MCNP6 Reference

7.2.1 2D Mini-Core

The first set of tests was performed using the mini-core model A. The displacement worth of the assembly 8 (according to the NHFLUX node ordering shown in Figure 6.3) was calculated by shifting the assembly by 2 mm from its origin in each of the six directions normal to the duct wall surfaces (see Figure 7.3). Table 7.3 compares the reactivity worth from RAINBOW perturbation calculation and MCNP6 eigenvalue subtractions.

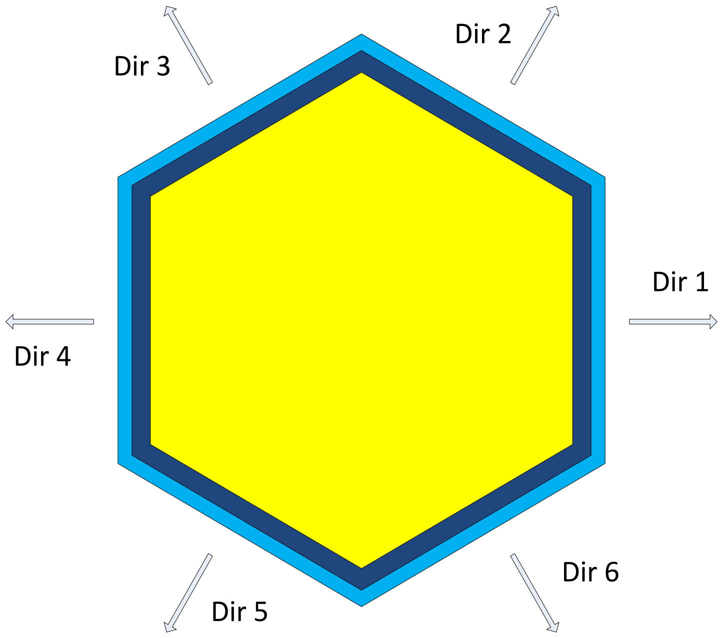

Figure 7.3 Assembly Displacements in Six Directions

Table 7.3 Comparison of RAINBOW and MCNP6 Reactivity Changes (pcm) of Fuel Assembly Displacements in the Third Ring of Mini-core Model (A)

Assembly Displacement	RAINBOW	MCNP6
Assembly 8 Shifted in Direction 1	-19.16	-15.71±1.4
Assembly 8 Shifted in Direction 2	-9.62	-7.86±1.4
Assembly 8 Shifted in Direction 3	9.53	11.78±1.4
Assembly 8 Shifted in Direction 4	19.15	19.63±1.4
Assembly 8 Shifted in Direction 5	9.53	11.78±1.4
Assembly 8 Shifted in Direction 6	-9.63	-7.86±1.4
Assemblies 8, 10, 12, 14, 16 and 18 Shifted Outwards	-114.94	-108.13±1.4
Assemblies 8, 10, 12, 14, 16 and 18 Shifted Inwards	114.89	112.79±1.4

It can be seen that the assembly displacement worth predicted by RAINBOW agrees well with the MCNP6 results. The maximum reactivity worth in magnitude is obtained when the assembly is shifted in the direction 1 (outward from the core center) and in the direction 4 (inward toward the core center). The MCNP6 results show that the displacement worth for the inward direction is larger in magnitude than that for the outward direction by about 3 standard deviations, suggesting that the flux gradient in the inner side of the assembly 8 is larger than that in the outer side of the assembly 8. On the other hand, the RAINBOW results show similar magnitudes for these two directions. However, it is later found that this difference is not physical but due to the statistical uncertainty of MCNP6 calculation.

To introduce a larger perturbation and thus reduce the MCNP6 statistical error, the reactivity worth was calculated by shifting the six assemblies at the third ring. As shown in Table 7.3, the MCNP6 result is -108.13±1.4 pcm for the outward shift and 112.79±1.4 pcm for the inward shift. The absolute values are very close to each other. This indicates that the observed difference in displacement worth between the inward and outward shifts of the assembly 8 resulted from the MCNP6 statistical error. The RAINBOW perturbation calculation result is -114.94 pcm for the outward shift and 114.89 pcm for the inward shift, which agree very well with the MCNP6 results. The perturbation calculation slightly overestimates the reactivity worth in magnitude due to the first order perturbation approximation under which the interaction effects of multiple assembly shifts were neglected.

Additional perturbation calculations were made with inward displacements of the assembly 8 by 1.2 mm, 1.6 mm and 2.0 mm. The reactivity worth results of MCNP6 and RAINBOW calculations are compared in Figure 7.4. It can be seen that the RAINBOW results agree well with the MCNP6 results and that the reactivity worth of assembly displacement increases in proportional to the amount of displacement for these small perturbations. The linearity of the assembly displacement worth indicates that the perturbation theory of first order is adequate for evaluating small perturbation of the assembly geometry.

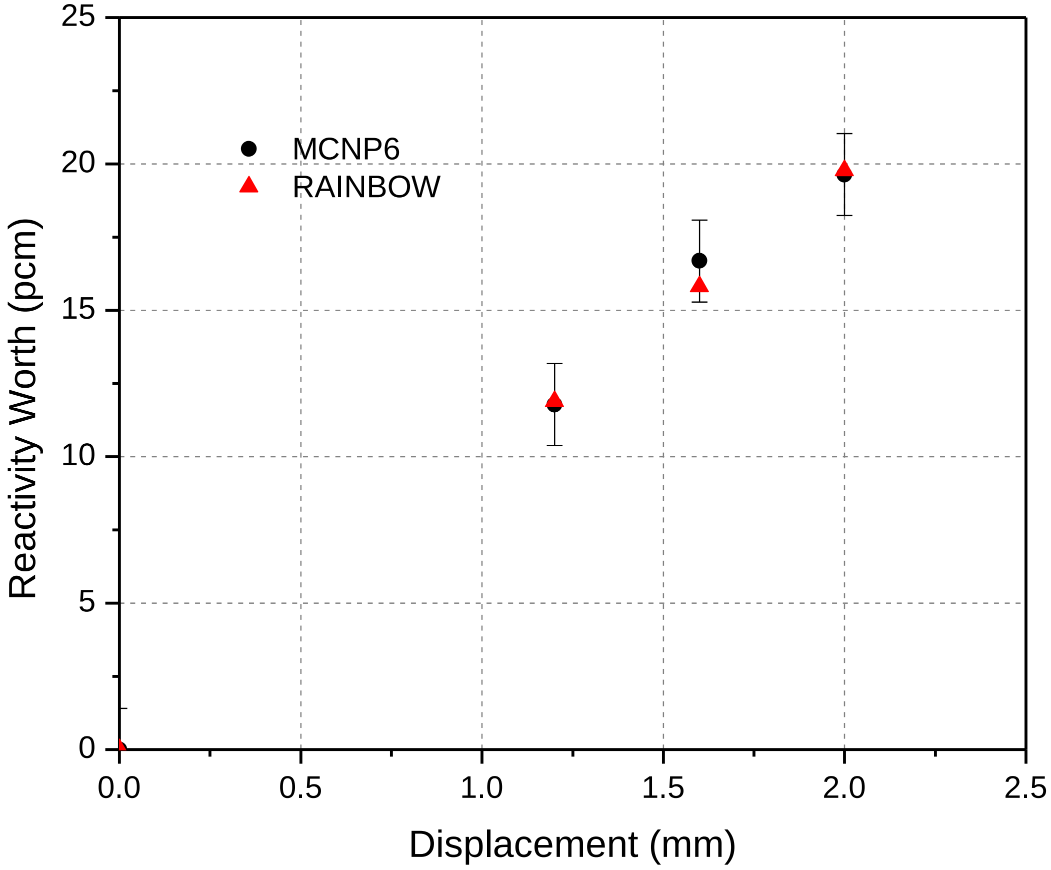

Figure 7.4 Comparison between MCNP6 and RAINBOW Results with Different Amount of Displacements

A second set of tests were performed using the mini-core model B, which provides more heterogeneous configuration in the fuel region. Using the RAINBOW and MCNP6 codes, the reactivity change due to displacement was calculated for the assemblies 2, 8 and 20 (see the NHFLUX node ordering shown in Figure 6.3) by displacing each of these assemblies by 2 mm. The MCNP6 solutions were obtained to yield one pcm standard deviation in the multiplication factor to minimize the effect of Monte Carlo statistical uncertainties. As a result, the standard deviation for the reactivity change is 1.4 pcm. Table 7.4 compares the reactivity changes due to assembly displacement obtained from RAINBOW and MCNP6 calculations for the configuration of control assemblies out. The three control assembly positions are filled with sodium. The RAINBOW results show good agreement with the MCNP6 results. For most of the cases, the difference from the MCNP6 result is within one or two standard deviation of the MCNP6 results.

Table 7.5 shows a statistical analysis of the results. Among the total 18 reactivity changes, 12 RAINBOW values (i.e., 67%) agree with the MCNP6 results within one standard deviation, 17 values (i.e., 94%) agree within two standard deviations, and all 18 values agree within three standard deviations. This distribution of the RAINBOW results is close to the normal distribution, indicating that the RAINBOW results are statistically consistent with the MCNP6 results.

Table 7.4 Comparison of RAINBOW and MCNP6 Reactivity Changes (pcm) of Assembly Displacements in the Third Ring of Mini-core Model B with Control Assembly Out

Assembly	Method	Dir 1	Dir 2	Dir 3	Dir 4	Dir 5	Dir 6
2	MCNP6	-4.86	-1.62	4.86	6.48	2.43	-3.24
	RAINBOW	-4.99	-2.99	1.98	4.94	2.94	-2.02
8	MCNP6	-4.86	-3.24	1.62	7.29	4.05	-1.62
	RAINBOW	-5.59	-3.76	1.80	5.57	3.73	-1.88
20	MCNP6	-4.86	-4.86	3.24	8.10	4.05	-3.24
	RAINBOW	-6.26	-3.16	3.11	6.27	3.15	-3.12

Table 7.5 Statistical Analysis of RAINBOW Results with Respect to MCNP6 Standard Deviations for Mini-core Model B with Control Assembly Out

	< 1 sigma	< 2 sigma	< 3 sigma
Number of cases	12	17	18
Percentage of cases	67%	94%	100%
Probability in normal distribution	68%	95%	99%

The reactivity change due to assembly displacement was also calculated for the case with control rod inserted, which allows larger variations in the flux distributions. Table 7.6 compares the RAINBOW and MCNP6 results for the displacements of assemblies 2, 8 and 20. The RAINBOW results agree well with the MCNP6 results. Table 7.7 shows the statistical analysis of the RAINBOW results with respect to the MCNP6 standard deviations. Nine RAINBOW values (i.e., 50%) agree with the MCNP6 results within one standard deviation, 16 values (i.e., 89%) agree within two standard deviations, and all 18 values (i.e. 100%) agree within three standard deviations, indicating the RAINBOW results are statistically consistent with the MCNP6 results.

Table 7.6 Comparison of RAINBOW and MCNP6 Reactivity Changes (pcm) of Assembly Displacements in the Third Ring of Mini-core Model B with Control Assembly In

Assembly	Method	Dir 1	Dir 2	Dir 3	Dir 4	Dir 5	Dir 6
2	MCNP6	-7.10	-3.04	6.09	9.13	5.07	-1.01
	RAINBOW	-8.02	-3.40	4.55	7.93	3.39	-4.61
8	MCNP6	-11.16	-7.10	3.04	10.14	8.12	2.03
	RAINBOW	-10.51	-9.05	1.53	10.61	8.98	-1.55
20	MCNP6	-8.12	-4.06	4.06	9.13	7.10	-2.03
	RAINBOW	-7.97	-5.58	2.36	7.97	5.58	-2.42

Table 7.7 Statistical Analysis of RAINBOW Results with Respect to MCNP6 Standard Deviations for Mini-core Model B with Control Assembly In

	< 1 sigma	< 2 sigma	< 3 sigma
Number of cases	9	16	18
Percentage of cases	50%	89%	100%
Probability in normal distribution	68%	95%	99%

Figure 7.5 shows the reactivity map of assembly displacement for all the fuel assemblies generated by RAINBOW calculations. It is noted that a negative reactivity is induced due to enhanced leakage and reduced fission productions when a fuel assembly is shifted outward from the core center. In general, the assembly displacement worth decreases (i.e., become more negative) as the location moves from the core center to the core periphery because the global flux gradient is larger near the core periphery. The variations in local flux distribution resulting from the control assemblies also affect the assembly displacement worth.

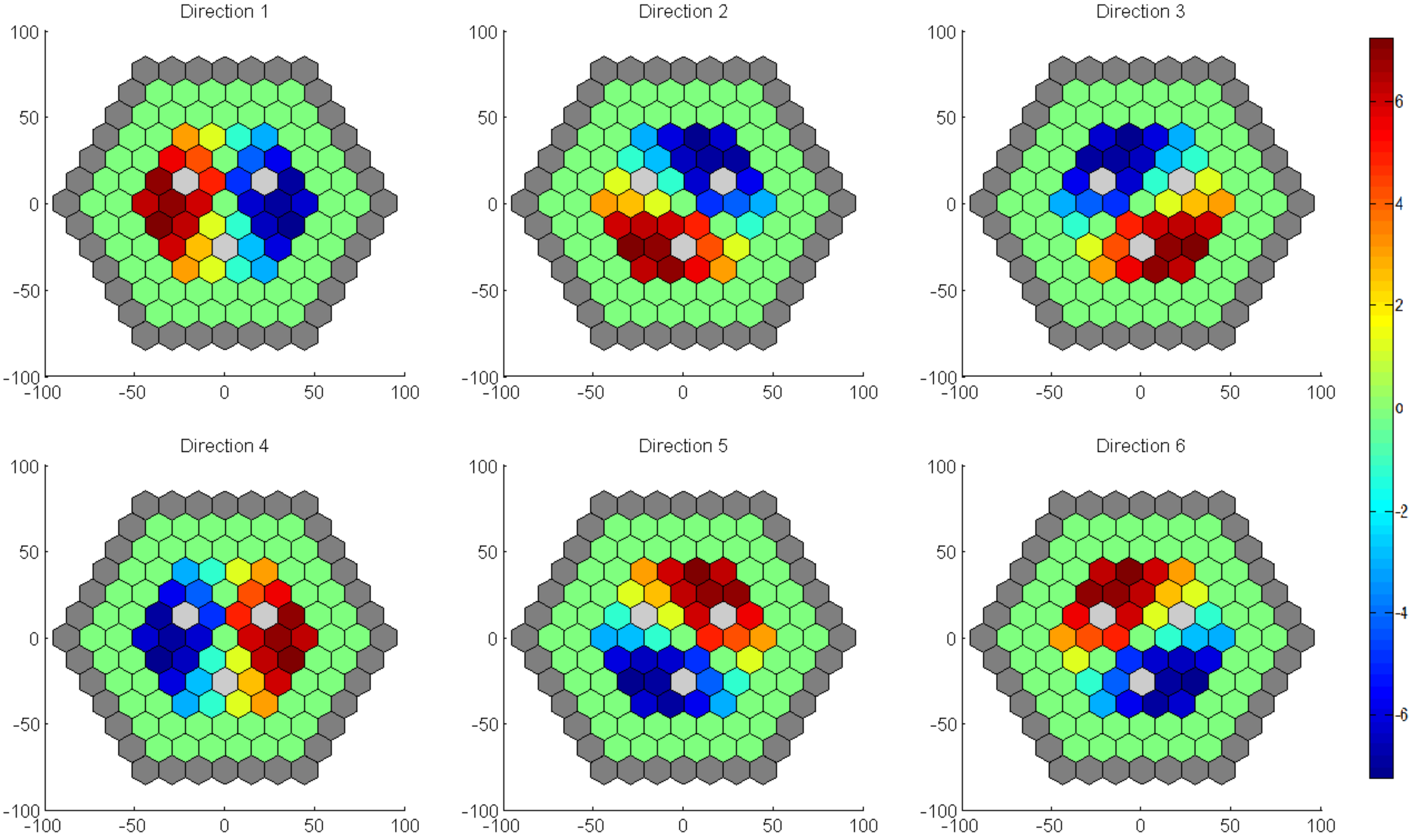

Figure 7.5 Directional Reactivity Worth of Fuel Assemblies

7.2.2 3D Mini-Core

Numerical tests were also performed for the 3D perturbation theory calculation capability of the RAINBOW code using a 3D configuration obtained by extruding the 2D mini-core A by 100 cm as shown in Figure 7.6. Based on the very smooth behavior observed in the bi-linearly weighted reaction rates as shown in Figure 7.7, a relatively large axial mesh size of 10 cm was selected for perturbation calculations. The perturbation calculations were performed for the upper five axial segments of the assembly, since the results for the lower half of the assembly will be exactly the same as the upper one due to the symmetry.

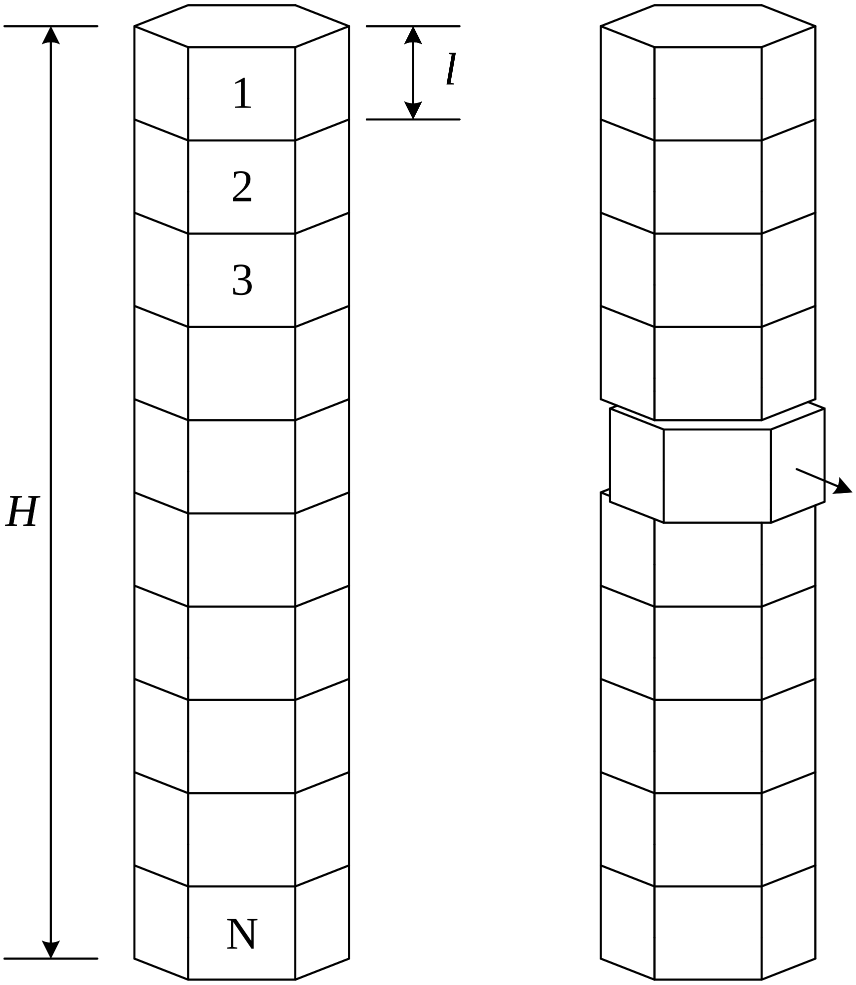

Figure 7.6 Displacement of an Axial Segment of Three-Dimensional Assembly Model

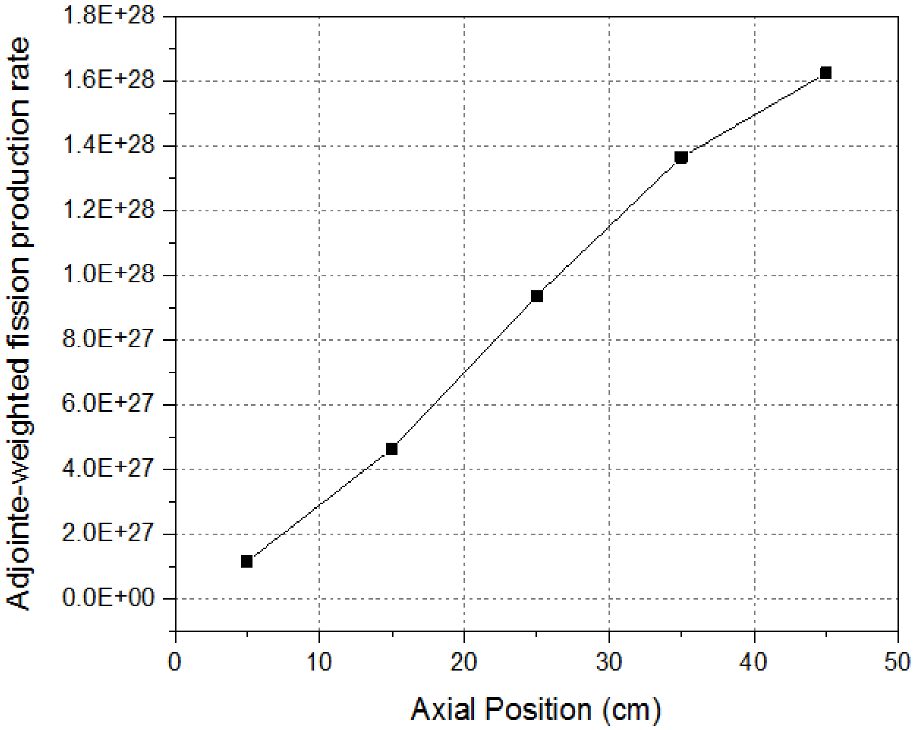

Figure 7.7 Bi-linearly weighted Fission Production Rate as a Function of Segment Axial Position

Reactivity changes were calculated for the displacement of the upper five axial segments of one or six assemblies in the third ring (assemblies 8, 10, 12, 14, 16 and 18 in Figure 6.3). Table 7.8 compares the reactivity changes obtained from RAINBOW perturbation calculations and MCNP6 eigenvalue calculations for assembly 8. The results show limited agreement with MCNP6 reference results mainly due to the MCNP6 statistical uncertainties since the displacement of single axial segment results in a tiny change in eigenvalue.

In addition, as the distance from the core center increases, the RAINBOW results decrease almost linearly due to the reduced fuel worth as shown in Figure 7.8. However, this is hardly seen from the MCNP6 results since the reactivity change due to a single axial segment displacement is so small that it is comparable with MCNP6 standard deviations. Further verification calculations need to be performed with reduced effect of Monte Carlo simulation uncertainties.

Table 7.8 Comparison of RAINBOW and MCNP6 Reactivity Changes (pcm) of Single Assembly Axial Segment Displacements

	Assembly 8		
	RAINBOW	MCNP6	Error
Segment 1	-1.31	-2.34±1.4	1.01
Segment 2	-2.24	1.17±1.4	-3.41
Segment 3	-3.49	-3.51±1.4	0.02
Segment 4	-4.65	-3.51±1.4	-1.14
Segment 5	-5.34	-4.68±1.4	-0.66

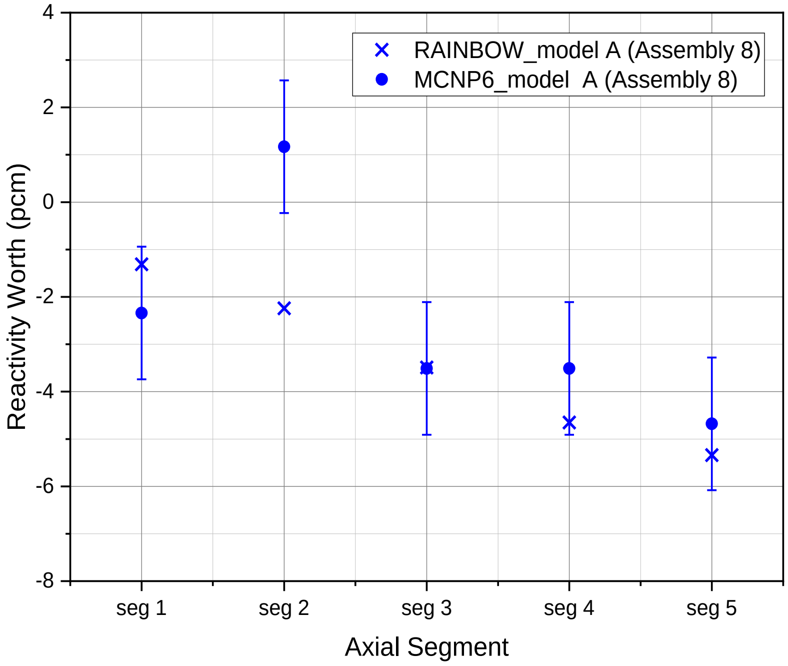

Figure 7.8 Reactivity Worth Due to Displacement of Five Axial Segments

In order to introduce a large perturbation relative to the standard deviation of MCNP6 results, the six assemblies were simultaneously shifted outward from the core center by 2 mm from their original positions. Table 7.9 compares the reactivity changes obtained from RAINBOW perturbation calculations with the MCNP6 results determined by the eigenvalue difference between the base and perturbed cases for the mini-core model A. For most of the cases, the RAINBOW results agree with the reference MCNP6 results within one or two standard deviation of the MCNP6 results. The magnitude of the reactivity change due to assembly segment displacement decreases nearly in proportional to the distance of the segment from the core center as shown in Figure 7.9, since the neutron importance in the core center is higher.

Table 7.9 Comparison of RAINBOW and MCNP6 Reactivity Changes for Axial Segment Displacements of Six Assemblies 8, 10, 12, 14, 16 and 18 in Mini-Core Model A

	RAINBOW (pcm)	MCNP6 (pcm)	difference (pcm)
Segment 1	-6.36	-7.85±1.40	-1.49
Segment 2	-10.98	-12.76±1.40	-1.78
Segment 3	-16.98	-17.67±1.40	-0.69
Segment 4	-22.62	-24.54±1.40	-1.92
Segment 5	-25.92	-23.56±1.40	2.36

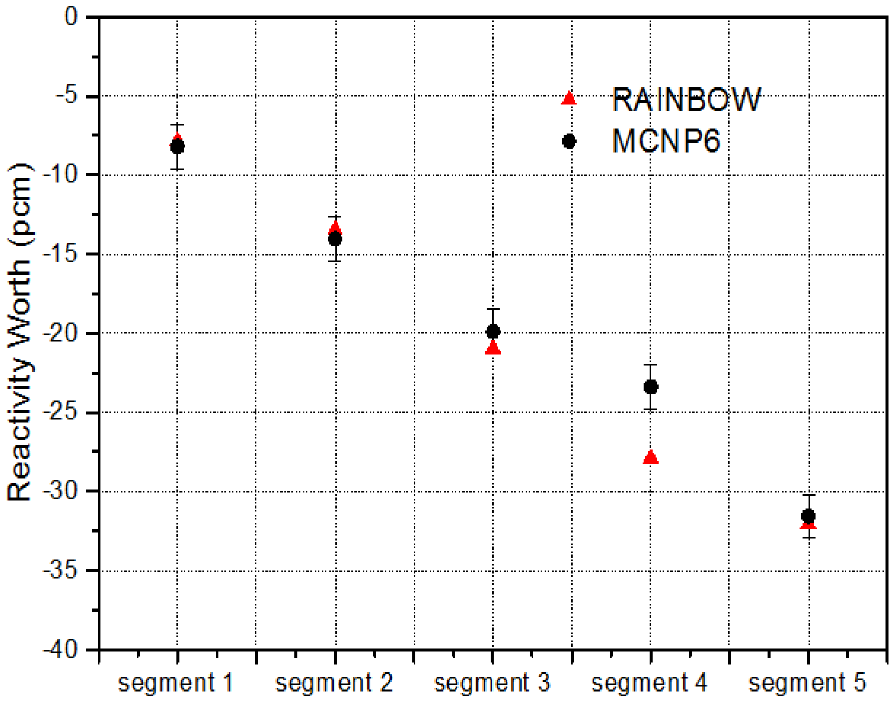

Figure 7.9 Reactivity Changes of Six Axial Segments Displacements

Table 7.10 and Table 7.11 compare the reactivity changes obtained from RAINBOW perturbation calculations with the MCNP6 results determined by the eigenvalue difference between the base and perturbed cases for the mini-core model B with control assemblies in and the mini-core model

B with control assemblies out, respectively. The RAINBOW results for the control absorber inserted case agree well with the MCNP6 results. However, the displacements of the segments 3 and 4 in the mini-core model B with control assemblies out show exceptionally large differences. These large differences appear to be due to the statistical uncertainties of the MCNP6 calculations since the MCNP6 results of these two cases deviate significantly from the monotonically decreasing trend of reactivity worth with respect to the distance from the core center as shown in Figure 7.10.

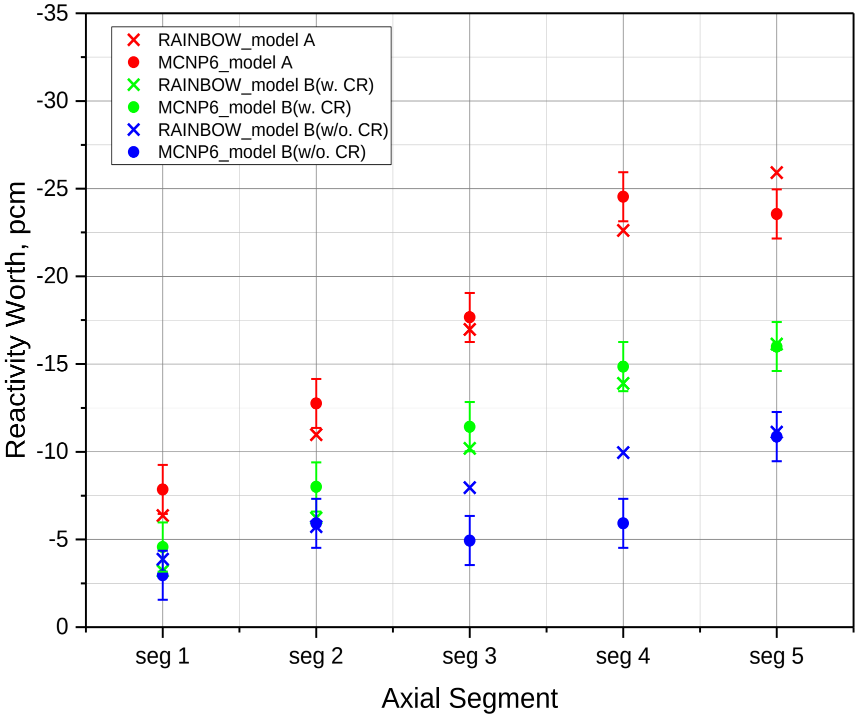

Figure 7.10 Reactivity Worth Due to Displacement of Six Axial Segments

Table 7.10 RAINBOW and MCNP6 Reactivity Changes for Axial Segment Displacements of Six assemblies 8, 10, 12, 14, 16 and 18 in Mini-Core Model B with Control Assemblies In

	RAINBOW (pcm)	MCNP6 (pcm)	difference (pcm)
Segment 1	-3.21	-4.57±1.51	-1.36
Segment 2	-6.23	-8.00±1.51	-1.76
Segment 3	-10.19	-11.42±1.51	-1.23
Segment 4	-13.90	-14.85±1.51	-0.95
Segment 5	-16.14	-15.99±1.51	0.14

Table 7.11 RAINBOW and MCNP6 Reactivity Changes for Axial Segment Displacements of Six assemblies 8, 10, 12, 14, 16 and 18 in Mini-Core Model B with Control Assemblies Out

	RAINBOW (pcm)	MCNP6 (pcm)	difference (pcm)
Segment 1	-3.87	-2.96±1.41	0.91
Segment 2	-5.73	-5.92±1.41	-0.19
Segment 3	-7.96	-4.94±1.41	3.02
Segment 4	-9.95	-5.92±1.41	4.03
Segment 5	-11.12	-10.86±1.41	0.26

Table 7.12 shows a statistical analysis of RAINBOW results with respect to MCNP6 standard deviations. Among the total 15 reactivity changes, 8 RAINBOW values (i.e., 53%) agree with the MCNP6 results within one standard deviation, 13 values (i.e., 87%) agree within two standard deviations, and all 15 values agree within three standard deviations. This distribution of the RAINBOW results deviates somewhat from the normal distribution, indicating either a physical difference between the RAINBOW and MCNP6 results or the inaccurate uncertainties of the MCNP6 results.

Table 7.12 Statistical Analysis of RAINBOW Results with Respect to MCNP6 Standard Deviations

	<1 σ	<2 σ	<3 σ
Number of cases	8	13	15
Percentage of cases	53%	87%	100%
Probability in normal distribution	68%	95%	100%

Based on the fact that a Monte Carlo simulation yields an underestimated standard deviation of multiplication factor because of the neglect of the inter-cycle correlation of fission source, the observed inconsistency between the RAINBOW and MCNP6 results are likely due to the inaccuracy in the reported MCNP6 standard deviations. For further investigation, the standard deviations were estimated statistically for the base and perturbed cases of the three mini-core models by repeating the MCNP6 simulation five times with different random seed numbers. Table 7.13, Table 7.14 and Table 7.15 show the eigenvalues of five independent MCNP6 simulations for the base and five perturbed cases. It can be seen that the statistically estimated standard deviations are 3.29 times larger in maximum than the reported MCNP6 standard deviation of 1 pcm.

Table 7.13 Eigenvalues of Five Independent MCNP6 Simulations for Base and Five Perturbed Cases of Mini-core Model A

	Seed 1	Seed 2	Seed 3	Seed 4	Seed 5	Mean	STD (pcm)
Base	1.00952	1.00951	1.00950	1.00944	1.00951	1.00950	3.21
Segment 1	1.00944	1.00944	1.00943	1.00943	1.00943	1.00943	0.55
Segment 2	1.00938	1.00940	1.00934	1.00939	1.00938	1.00938	2.28
Segment 3	1.00934	1.00935	1.00933	1.00934	1.00930	1.00933	1.92
Segment 4	1.00927	1.00930	1.00923	1.00927	1.00926	1.00927	2.51
Segment 5	1.00928	1.00926	1.00922	1.00920	1.00922	1.00924	3.29

Table 7.14 Eigenvalues of Five Independent MCNP6 Simulations for Base and Five Perturbed Cases of Mini-core Model B with Control Assemblies In

	Seed 1	Seed 2	Seed 3	Seed 4	Seed 5	Mean	STD (pcm)
Base	0.93568	0.93568	0.93568	0.93568	0.93570	0.93568	0.89
Segment 1	0.93564	0.93564	0.93566	0.93566	0.93563	0.93565	1.34
Segment 2	0.93561	0.93563	0.93560	0.93562	0.93559	0.93561	1.58
Segment 3	0.93558	0.93559	0.93556	0.93560	0.93559	0.93558	1.52
Segment 4	0.93555	0.93555	0.93558	0.93557	0.93555	0.93556	1.41
Segment 5	0.93554	0.93553	0.93552	0.93554	0.93553	0.93553	0.84

Table 7.15 Eigenvalues of Five Independent MCNP6 Simulations for Base and Five Perturbed Cases of Mini-core Model B with Control Assemblies Out

	Seed 1	Seed 2	Seed 3	Seed 4	Seed 5	Mean	STD (pcm)
Base	1.00652	1.00653	1.00651	1.00657	1.00653	1.00653	2.28
Segment 1	1.00649	1.00646	1.00649	1.00649	1.00648	1.00648	1.30
Segment 2	1.00646	1.00647	1.00647	1.00647	1.00647	1.00647	0.45
Segment 3	1.00649	1.00644	1.00643	1.00647	1.00645	1.00646	2.41
Segment 4	1.00646	1.00642	1.00641	1.00642	1.00643	1.00643	1.92
Segment 5	1.00641	1.00642	1.00640	1.00642	1.00645	1.00642	1.87

Table 7.16, Table 7.17 and Table 7.18 compares the RAINBOW results with the MCNP6 reference solutions determined by the statistical average of five independent MCNP6 results. It can be seen that the RAINBOW results agree well with the MCNP6 reference results.

Table 7.16 Comparison of RAINBOW and Statistically Estimated MCNP6 Reactivity Changes for the Mini-Core Model A

	RAINBOW (pcm)	MCNP6 (pcm)	Difference (pcm)
Segment 1	-6.36	-6.08±3.23	0.28
Segment 2	-10.98	-11.58±3.90	-0.60
Segment 3	-16.98	-16.10±3.71	0.88
Segment 4	-22.62	-22.57±4.04	0.05
Segment 5	-25.92	-25.52±4.55	0.40

Table 7.17 Comparison of RAINBOW and Statistically Estimated MCNP6 Reactivity Changes for the Mini-Core Model B with Control Assemblies In

	RAINBOW (pcm)	MCNP6 (pcm)	Difference (pcm)
Segment 1	-3.21	-4.34±1.72	-1.13
Segment 2	-6.23	-8.45±1.94	-2.22
Segment 3	-10.19	-11.42±1.88	-1.23
Segment 4	-13.90	-14.17±1.79	-0.27
Segment 5	-16.14	-17.36±1.31	-1.23

Table 7.18 Comparison of RAINBOW and Statistically Estimated MCNP6 Reactivity Changes for the Mini-Core Model B with Control Assemblies out

	RAINBOW (pcm)	MCNP6 (pcm)	Difference (pcm)
Segment 1	-3.87	-4.94±2.61	-1.06
Segment 2	-5.73	-6.32±2.31	-0.59
Segment 3	-7.96	-7.50±3.30	0.46
Segment 4	-9.95	-10.27±2.96	-0.31
Segment 5	-11.12	-11.06±2.93	0.06

In addition, the reactivity worth of axial segment displacements predicted by RAINBOW and MCNP6 calculations show a linear dependence on the distance from the core center as shown in Figure 7.11. For 14 cases out of 15, RAINBOW result agrees with the mean value of five MCNP results within one standard deviation. The remaining one case agrees within two standard deviations.

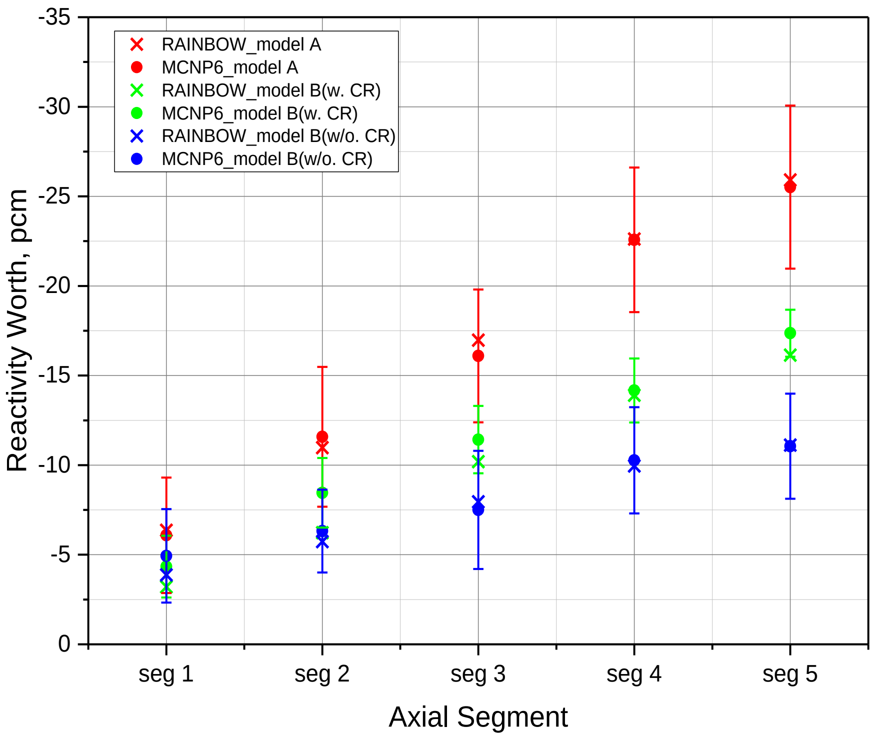

Figure 7.11 Comparison of RAINBOW Reactivity Changes with MCNP6 Results Obtained by Statistical Average of Five Independent MCNP6 Simulations

7.3 Verification of RAINBOW Perturbation Results against PROTEUS-SN Reference

As discussed in the previous section, the MCNP6 statistical errors affect the accuracy of the reference results for the small reactivity perturbation. Thus, we performed deterministic calculations using PROTEUS-SN code, which also has the capability to represent heterogeneous assembly geometries explicitly by using finite element methods, to further verify the RAINBOW code. The calculations are based on the same 2D and 3D mini-core model (A) used for MCNP6 calculations.

7.3.1 2D Mini-Core

The perturbation calculations are performed with assembly 8 (according to the NHFLUX node ordering shown in Figure 6.3) of mini-core model A shifted in six directions that are normal to the assembly duct wall surfaces (see Figure 7.3). The radial layout of the core model is shown in Figure 7.12. Partially heterogeneous assembly model was used in the PROTEUS-SN calculation. The PROTEUS-SN use the same 33-group cross section set with VARIANT calculations, which was generated using the MC^2-3/TWODANT codes.

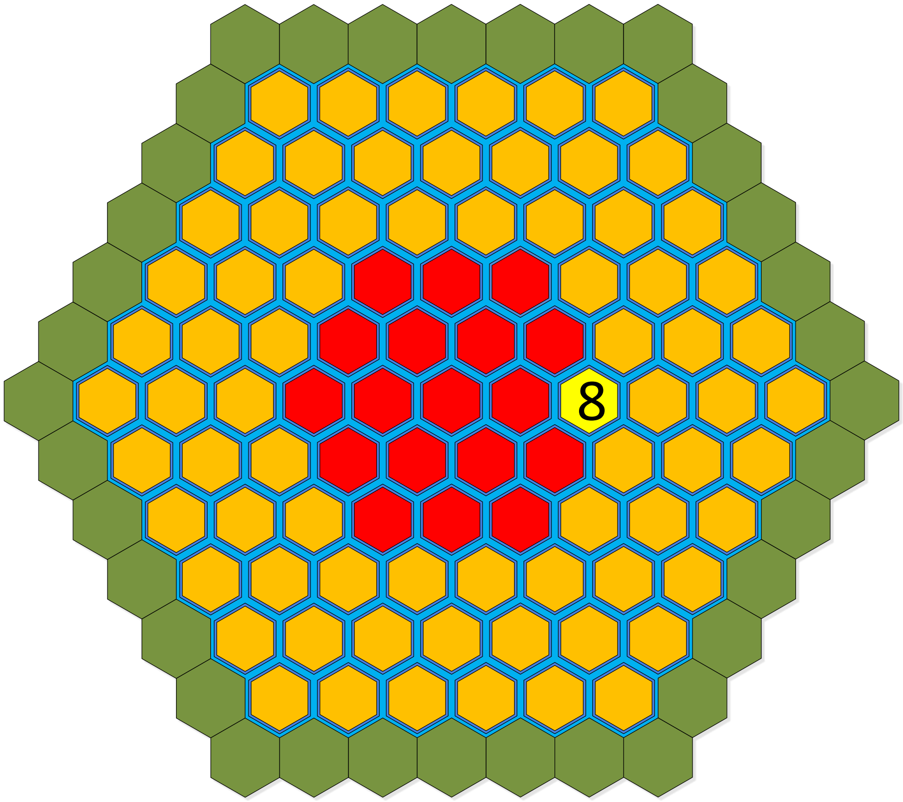

Figure 7.12 Radial Layout of 2D Mini-Core Model A with Displaced Assembly 8

Table 7.19 compares the effective multiplication factors calculated by PROTEUS-SN and MCNP6 codes based on the base model and the models with assembly 8 shifted in six directions. The PROTEUS-SN calculations show about 400 pcm errors in eigenvalue compared to the MCNP6 calculations. This is mainly due to the use of 33-group cross section. Further refinement of the broad group structure results in a converged solution as discussed in section 5.2.3.

Table 7.19 Effective Multiplication Factors Calculated Using PROTEUS-SN and MCNP6 for Base Model and Models with Assembly 8 Displaced in Six Directions

	PROTEUS-SN	MCNP6
Base	1.00524	1.00918±0.00001
Dir 1	1.00506	1.00902±0.00001
Dir 2	1.00515	1.00910±0.00001
Dir 3	1.00534	1.00930±0.00001
Dir 4	1.00543	1.00938±0.00001
Dir 5	1.00534	1.00930±0.00001
Dir 6	1.00515	1.00910±0.00001

Table 7.20 compares the RAINBOW perturbation results with the reference solutions obtained from PROTEUS-SN and MCNP6 calculations. It can be seen that the RAINBOW results agree better with PROTEUS-SN results compared with the MCNP6 results. The maximum difference between RAINBOW and PROTEUS-SN results is 1 pcm while the maximum difference between RAINBOW and MCNP6 results is more than 3 pcm. This indicates the differences between RAINBOW and MCNP6 results are largely due to the MCNP6 statistical errors.

Table 7.20 Comparison of the RAINBOW Results (pcm) with Both Reference Solutions (pcm) Obtained Using PROTEUS-SN and MCNP6 Codes

	RAINBOW	Reactivity Worth		Difference	
		PROTEUS-SN	MCNP6	PROTEUS-SN	MCNP6
Dir 1	-19.16	-18.16	-15.71±1.4	-1.00	-3.45
Dir 2	-9.62	-9.20	-7.86±1.4	-0.42	-1.77
Dir 3	9.53	9.17	11.78±1.4	0.36	-2.25
Dir 4	19.15	18.56	19.63±1.4	0.59	-0.48
Dir 5	9.53	9.15	11.78±1.4	0.38	-2.25
Dir 6	-9.63	-9.22	-7.86±1.4	-0.41	-1.77

In addition, the PROTEUS-SN results for the reactivity changes induced by the displacements of assembly 8 in direction 1 (outwards) and in direction 4 (inwards) are similar in magnitude and have opposite signs, indicating the radial flux distribution across the assembly 8 is nearly linear. The RAINBOW results show the same trend. However, the corresponding MNCP6 results are significantly different in magnitude due to statistical uncertainties.

7.3.2 3D Mini-Core

The verification test of the RAIBOW code for 3D calculations against PROTEUS-SN code was performed based on the 3D mini-core model developed by extruding the 2D mini-core model A, which is the same with the model used in Section 7.2.2. However, the 2D mesh used for the 2D PROTEUS-SN calculation cannot be directly used for the 3D calculation, since the 3D mesh developed by extruding this 2D mesh cannot model the assembly with a shifted segment. A new 2D mesh has been made such that the 3D assembly model with a shifted segment can be obtained by extruding the 2D mesh. The mesh was generated using the Trelis meshing software. The Trelis scripts for generating the new 2D mesh is included in Appendix E. The new 2D mesh has slightly larger number of vertices and elements as shown in Table 7.21. The small difference in mesh results in almost no neutronics impact.

Table 7.21 Comparison of the New Mesh with the Original Mesh

	Original 2D mesh	New 2D mesh
Number of Vertices	168704	169235
Number of Elements	262382	262711
Number of Regions (Blocks)	381	385
Eigenvalues, Base	1.005244	1.005242
Eigenvalues, Perturbed	1.005061	1.005058
Worth (pcm)	-18.16	-18.26

Before proceeding to the PROTEUS-SN 3D calculations, a sensitivity study on axial resolution was performed. However, the computational resource available to the author cannot afford the 3D PROTESU-SN calculation with more than 20 axial meshes due to insufficient memory. Thus, the calculations are also performed with non-uniform meshes that allow finer mesh near the perturbed assembly segment. The axial meshes are summarized in Table 7.22.

Table 7.22 Axial Resolution for 3D PROTEUS-SN Calculations

Seg.	Number of intervals in axial segments						
	Mesh 1	Mesh 2	Mesh 3	Mesh 4	Mesh 5	Mesh 6	Mesh 7
1	1	2	3	3	2	2	2
2	1	2	3	3	3	2	2
3	1	2	2	3	3	3	2
4	1	2	2	2	3	3	3
5	1	2	2	2	2	3	3
6	1	2	2	2	2	2	3
7	1	2	2	2	2	2	2
8	1	2	2	2	2	2	2
9	1	2	2	2	2	2	2
10	1	2	2	2	2	2	2

Table 7.23 shows the reactivity worth due to assembly segment displacement using uniform axial meshes. The results indicate that 20 axial mesh might not yield a converged solution, since a significant difference is observed between the results calculated with 10 and 20 axial meshes. The results with non-uniform axial meshes are shown in Table 7.24. With finer meshes, the RAINBOW estimation of the segment displacement worth agrees better with the PROTEUS-SN results. However, the RAINBOW results show around 10% error compared with PROTEUS-SN result, indicating that the axial meshes are not fine enough to yield a converged PROTEUS-SN solution.

Table 7.23 Reactivity Worth Due to Assembly Segment Displacement Using Uniform Axial Meshes

	RAINBOW (pcm)	PROTEUS-SN (pcm)			
		Mesh 1	Diff (pcm)	Mesh 2	Diff (pcm)
Segment 1	-1.06	-1.47	0.41	-1.23	0.17
Segment 2	-1.83	-3.04	1.21	-2.26	0.43
Segment 3	-2.83	-4.41	1.58	-3.38	0.55
Segment 4	-3.77	-5.78	2.01	-4.41	0.64
Segment 5	-4.32	-6.40	2.08	-5.03	0.71

Table 7.24 Reactivity Worth Due to Assembly Segment Displacement Using Non-uniform Axial Meshes

	RAINBOW (pcm)	PROTEUS-SN			
		Base Eigenvalue	Perturbed Eigenvalue	Worth (pcm)	Difference (pcm)
Segment 1, Mesh 3	-1.06	1.00762317	1.00761142	-1.16	0.10
Segment 2, Mesh 4	-1.83	1.0076392	1.00761769	-2.12	0.29
Segment 3, Mesh 5	-2.83	1.00761807	1.00758552	-3.21	0.38
Segment 4, Mesh 6	-3.77	1.00763775	1.0075949	-4.22	0.45
Segment 5, Mesh 7	-4.32	1.00764937	1.00760049	-4.81	0.49

The convergence study is also performed for the x-y plane resolution. The number of elements in x-y plane is reduced to 91575 and 122100 from the original 169235 while the axil mesh is increased to 40 since the reduction in the number of x-y plane elements decreases the memory usage. The results are shown in Table 7.25. Only tiny difference in assembly segment displacement worth is observed by using both reduced numbers of x-y plane elements, indicating 91575 elements are sufficient for the calculation.

Table 7.25 Reactivity Worth (pcm) Due to Assembly Segment Displacement Using Different Radial Mesh

	RAINBOW	Case 1 (91575 elements)		Case 2 (122100 elements)	
		PROTEUS-SN	Difference	PROTEUS-SN	Difference
Segment 1	-1.06	-1.13	6.24%	-1.15	7.51%
Segment 2	-1.83	-2.04	10.23%	-2.06	11.07%
Segment 3	-2.83	-3.14	9.89%	-3.13	9.64%
Segment 4	-3.77	-4.12	8.59%	-4.13	8.77%
Segment 5	-4.32	-4.73	8.57%	-4.75	8.97%

The convergence study is also performed for angular cubature. In the previous 2D PROTEUS-SN calculation, the Legendre-Chebyshev cubature of order L5T5 was sufficient. The order of cubature is increased to L7T5 since the 3D case might requires a higher order approximation in polar angle. The results are shown in Table 7.25. Almost no difference is observed for the increased cubature order, indicating that the L5T5 is still sufficient for the 3D calculation. In addition, the calculations are performed using 50 axial meshes that is the maximum axial resolution allowed by the available memory with the current problem settings. The assembly segment displacement worth is still changing with the increased number of axial meshes.

Table 7.26 Reactivity Worth (pcm) Due to Assembly Segment Displacement Using Different Angular Cubature

	RAINBOW	L5T5		L7T5	
		PROTEUS-SN	Difference	PROTEUS-SN	Difference
Segment 1	-1.06	-1.12	5.07%	-1.12	5.72%
Segment 2	-1.83	-2.00	8.68%	-2.01	8.88%
Segment 3	-2.83	-3.07	7.92%	-3.07	7.96%
Segment 4	-3.77	-4.07	7.32%	-4.06	7.15%
Segment 5	-4.32	-4.663	7.35%	-4.661	7.31%

Given that the computational resource available cannot afford a converged calculation in terms of axial meshes, we seek for a different way to obtain the converged solution. We apply the Richardson extrapolation of the eigenvalue k by varying axial mesh size h. Let $k(h)$ be an approximation of $k^* = k(0)$, which linearly depends on mesh size h. The error function can be written as

$$k(h) = k^* + Ch + O(h^2) \tag{7.1}$$

With mesh size h_1 and h_2 ($h_2 = ah_1$), the eigenvalue with zero axial mesh size can be obtained as

$$k^* = \frac{k(h_2) - ak(h_1)}{1-a} \tag{7.2}$$

We use $a = 4/5$ in Eq. (7.2) for estimating the eigenvalue with zero axial mesh size. The extrapolated results are shown in Table 7.27.

Table 7.28 compares the reactivity changes due to assembly segment displacement obtained from RAINBOW and extrapolated PROTEUS-SN eigenvalues. The maximum absolute error is less than 0.1 pcm and the maximum relative error is 2.11%, indicating the RAINBOW results agree very well with the PROTEUS-SN results.

Table 7.27 Extrapolated Eigenvalues Using the PROTEUS-SN Results with 40 and 50 Axial Meshes

	40 meshes	50 meshes	Extrapolated eigenvalues
Base	1.007701	1.007745	1.007922
Segment 1	1.007689	1.007734	1.007911
Segment 2	1.007680	1.007725	1.007903
Segment 3	1.007669	1.007714	1.007893
Segment 4	1.007659	1.007704	1.007883
Segment 5	1.007653	1.007698	1.007877

Table 7.28 Comparison of Reactivity Changed Due to Assembly Segment Displacement Calculated Using RAINBOW and Extrapolated PROTEUS-SN Eigenvalues

	RAINBOW (pcm)	PROTEUS-SN (pcm)	Difference (pcm)	Rel. difference
Segment 1	-1.06	-1.06	-0.001	0.11%
Segment 2	-1.83	-1.87	-0.035	1.90%
Segment 3	-2.83	-2.80	0.026	-0.91%
Segment 4	-3.77	-3.84	-0.072	1.88%
Segment 5	-4.32	-4.41	-0.093	2.11%

7.4 Verification of RAINBOW Perturbation Results on Fuel Axial Expansion

The verification of the RAINBOW calculation on fuel axial expansion worth is performed using the 3D mini-core model with heterogeneous axial regions that has been described in Section 4.3. The axial and radial layouts of the mini-core model is shown in Figure 7.13. The fuel assembly in the third fuel ring is expanded by 3% with a expanded length of 82.4 cm for the perturbed case.

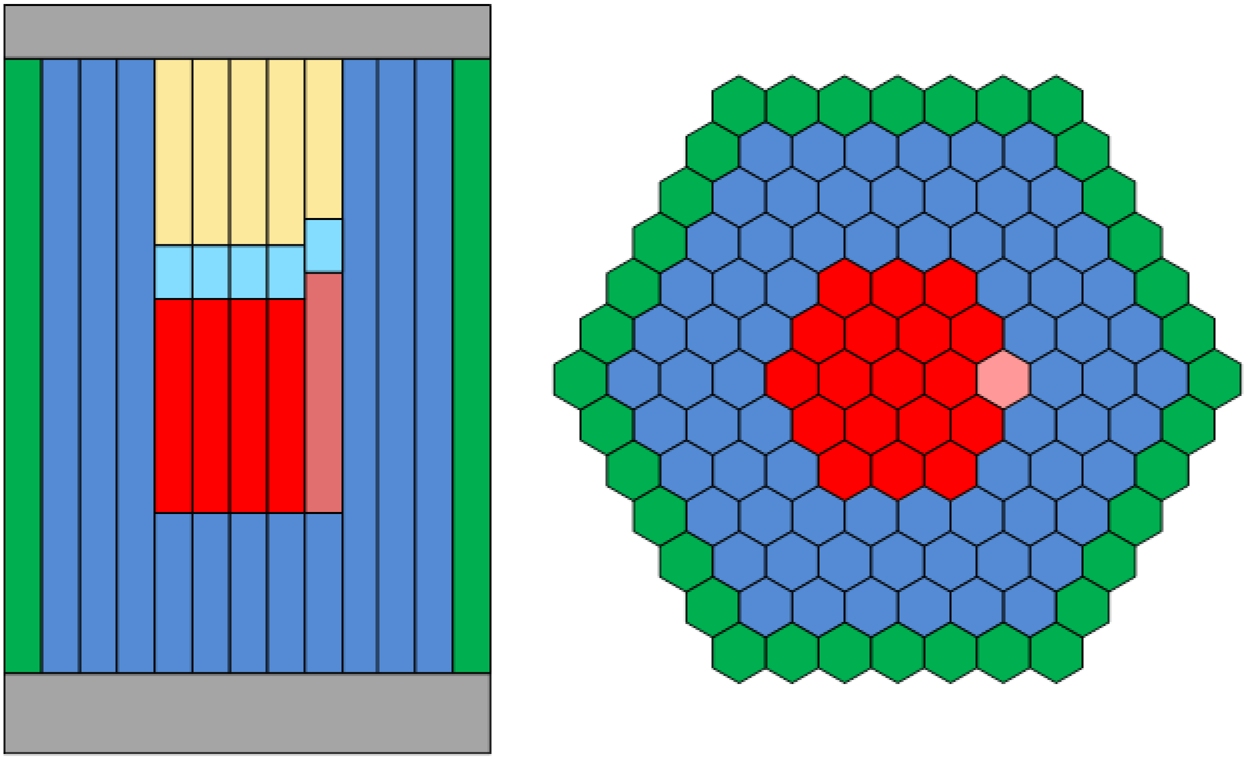

Figure 7.13 Axial and Radial Layout of the 3D Mini-Core Used for Fuel Axial Expansion Calculations

The reference MCNP and VARIANT results for the fuel axial expansion worth are -44.6±4.9 pcm and -44.7 pcm, respectively, as presented in Section 4.3. Table 7.29 show the RAINBOW results for the reactivity effect of the material density change in each axial segment due to axial expansion of fuel. The fuel region is divided into eight uniform segments of which density is reduced at the perturbed case. The bond sodium segment is at the top of fuel region and its lower 2.4 cm is occupied by the expanded fuel in the perturbed case. The lower 2.4 cm of the fission gas plenum segment above the bond sodium is replaced with the bond sodium. The total reactivity worth of the fuel assembly axial expansion is obtained by adding up the contributions of these ten axial regions. The RAINBOW estimation of the fuel axial expansion worth is -47.53 pcm, which agrees well with the reference results obtained from MCNP6 and VARIANT calculations.

Table 7.29 Reactivity Changed Due to Nuclide Density Perturbation in each Axial Segment/region

	Elevation of segment center (cm)	Reactivity worth (pcm)
Segment 1	95	-5.12
Segment 2	105	-7.94
Segment 3	115	-10.38
Segment 4	125	-11.72
Segment 5	135	-11.57
Segment 6	145	-9.97
Segment 7	155	-7.38
Segment 8	165	-4.56
Bond Sodium Segment	171.2	20.39
Gas Plenum Segment	191.2	0.71
Total	N/A	-47.53
MCNP6 Reference	N/A	-44.6±4.9
VARIANT Reference	N/A	-44.7

7.5 A Test on Fully Heterogeneous Model

We concluded in Section 4.1.1 that the fuel pin heterogeneity effect is not important for the bowing reactivity. However, the RAINBOW code retains the capability of modeling fully heterogeneous problem. A test on RAINBOW with a fully heterogeneous assembly model was performed. Figure 7.14 shows the finite element meshes for a partially heterogeneous model and a fully heterogeneous model. The finite element mesh for the partially heterogeneous assembly model has 1394 vertices and 2066 elements. For the fully heterogeneous assembly model, the numbers of vertices and elements were increased to 26891 and 29478, respectively, which implies a significantly longer calculation time.

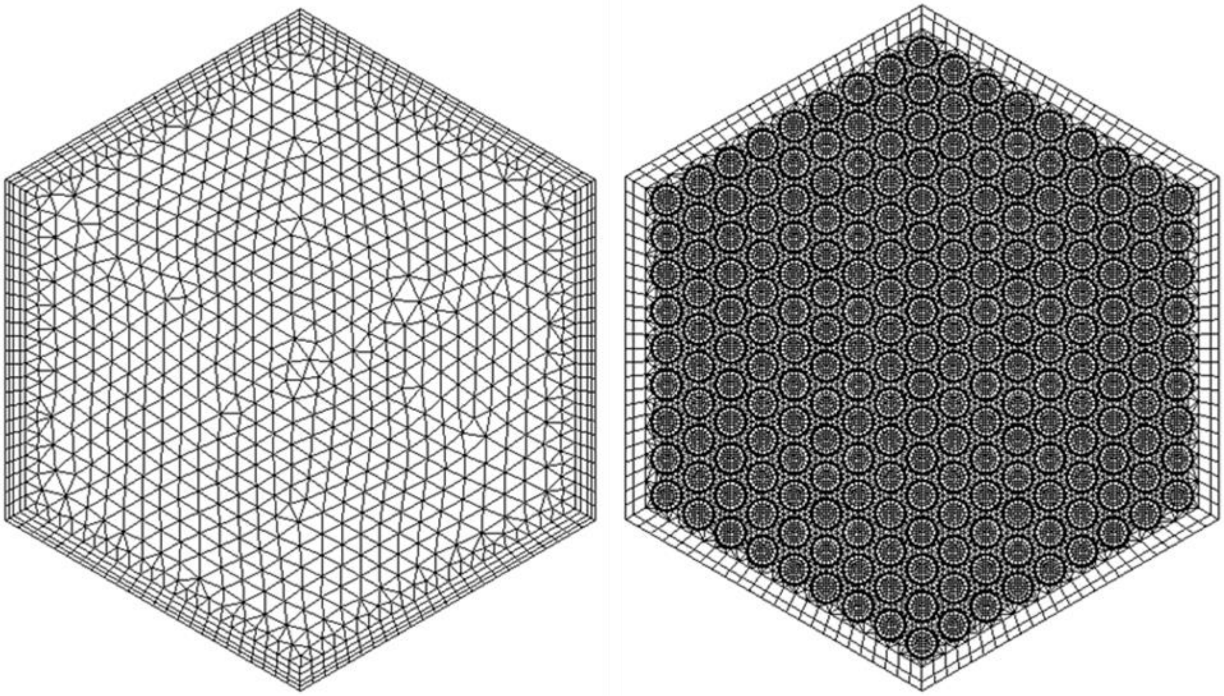

(a) Mesh 1 (b) Mesh 2

Figure 7.14 Finite Element Meshes for Partially Heterogeneous (Left) and Fully Heterogeneous (Right) Models

We use the RAINBOW code to calculate the reactivity worth due to a 2 mm displacement of the assembly 8 (see Figure 6.3) in the mini-core model (A). Three cases were tested using the heterogeneous assembly model with the axial mesh 2 in Table 7.22, the partially heterogeneous assembly model with the axial mesh 1, and the partially heterogeneous assembly model with the axial mesh 2. The results are compared with the reference value obtained from direct subtraction of PROTEUS-SN eigenvalues determined with the partially heterogeneous model and the axial mesh 1. As shown in Table 7.30, all three cases of RAINBOW calculation are nearly identical and agree well with the reference PROTEUS-SN solution. The results further confirm that the fuel pin heterogeneity effect on the assembly displacement worth is insignificant.

Table 7.30 Reactivity Changed (pcm) Due to Assembly Displacement Calculated using RAINBOW Based on Fully and Partially Heterogeneous Models

		Dir 1	Dir 2	Dir 3	Dir 4	Dir 5	Dir 6
RAINBOW	Hete. Model w. Mesh 2	-19.22	-9.65	9.56	19.21	9.56	-9.66
	Part. Hete. Model w. Mesh 1	-19.21	-9.65	9.55	19.19	9.55	-9.65
	Part. Hete. Model w. Mesh 2	-19.16	-9.62	9.53	19.15	9.53	-9.62
PROTEUS	Part. Hete. Model w. Mesh 1	-18.16	-9.20	9.17	18.56	9.15	-9.22

7.6 Timing Information

In this section, we discuss the computational time of the sequence of calculations required for evaluating the set of bowing reactivity coefficients based on the perturbation theory. The sequence of calculations includes the multi-group cross section generation using MC^2-3 code, VARIANT full core calculation, PROTEUS-SN single assembly calculation, and the reconstruction of heterogeneous flux and the perturbation calculation using the RAINBOW code. The selected test problem is based on the 2D mini-core model A presented in Section 7.1. The total computational time consumed by the perturbation calculation sequence for obtaining the core map of bowing reactivity coefficients is compared with the time estimated for the MCNP6 simulations for obtaining the same results.

The computational environment, problem settings, and computational time for those calculations are summarized from Table 7.31 to Table 7.35. The total computational time to obtainin the core map of bowing reactivity coefficients using the perturbation theory method is around 15 minutes. No parallel computing is adopted in running the sequence of codes. On the other hand, the MCNP6 eigenvalue calculation for single core configuration is around 8 hours with parallelized 256 processors. To obtain the set of bowing reactivity coefficients of all 19 assemblies displaced in 6 directions, we need to perform a total number of 105 MCNP calculations including one for the based case. It requires more than 200 cpu-month to finish the simulations.

Table 7.31 Computational Time of MC^2-3 Code for Generating Multi-Group Cross Section of 2D Mini-Core Model A

Computational Environment	
CPU	Intel(R) Xeon(R) CPU E5-2670 0 @ 2.60GHz
OS	Linux (Red Hat)
Parallel Computing	No
Problem Setting	
Ultrafine Group Transport Solver	TWODANT
Number of Broad Groups	33
Scattering Order	5
Regions	3
Computational Time	
Calculate rzmflx	~4 mins
Group Condensation	~49 seconds

Table 7.32 Computational Time of VARIANT Code with 2D Mini-Core Model A

Computational Environment	
CPU	Intel(R) Xeon(R) CPU E5-2670 0 @ 2.60GHz
OS	Linux (Red Hat)
Parallel Computing	No
Problem Setting	
Number of Energy Groups	33
Angular Expansion Order	5
Spatial Approximations	6-6-1 (source-flux-current)
Computational Time	
Computational Time (Include Adjoint)	~1 mins

Table 7.33 Computational Time of PROTEUS-SN Code with 2D Mini-Core Model A

Computational Environment	
CPU	Intel(R) Xeon(R) CPU E5-2670 0 @ 2.60GHz
OS	Linux (Red Hat)
Parallel Computing	No
Problem Setting	
Number of Energy Groups	33
Angular Cubature	Legendre-Tchebychev (L5T5)
Number of Spatial FE Elements Per Assembly	2066
Number of Spatial FE Elements for Full Core	262382
Computational Time	
Single Assembly Calculation (Forward)	~2 mins
Single Assembly Calculation (Adjoint)	~2 mins
Total	~4 mins

Table 7.34 Computational Time of RAINBOW Code to Produce a Set of Assembly Bowing Reactivity Coefficients for All Assemblies for 2D Mini-Core Model A

Computational Environment	
CPU	Intel(R) Core(TM) i7-3770 CPU @ 3.40 GHz
OS	Windows 7
Parallel Computing	No
Problem Setting	
Number of Energy Groups	33
Angular Expansion Order	5
Number of Spatial FE Elements per Assembly	2066
Computational time	
Flux Evaluation	< 1 mins
Perturbation Calculation	~4 mins
Total	~5 mins

Table 7.35 Computational Time of Single MCNP6 Simulation With 2D Mini-Core Model A

Computational Environment	
CPU	Intel(R) Xeon(R) CPU E5-2670 0 @ 2.60GHz
OS	Linux (Red Hat)
Number of Nodes	16
Number of Processors Per Node	16
Total Number of Processors	256
Problem Setting	
Number of Particles	1000000
Number of Cycles	2000
Eigenvalue Convergence	1 pcm
Computational Time	
Total	~ 8 hr

8. CONCLUSIONS AND SUMMARY

8.1 Study Objective

The evaluation of feedback reactivity due to core geometrical changes has been a long-standing challenge for the analysis of fast reactor core. The objective of this thesis work is to develop a perturbation theory method for accurate and efficient calculation of feedback reactivity due to core deformation. The following sections summarize the major findings and contributions presented in this dissertation.

8.2 Reactivity Feedback Effects Due to Core Deformation

A series of investigations was performed on various reactivity feedback components induced by core deformation in order to develop an efficient and accurate computational procedure to evaluate the feedback reactivity due to core deformation. The calculations were performed using the MCNP6 code with its ENDF/B-VII.0 library, which can model deformed core geometries exactly. A reactivity change caused by core deformation was obtained by direct eigenvalue subtractions between the cases of base and perturbed core configurations. Several conclusions were drawn from this study:

1. The fuel pin heterogeneity effect is negligible on assembly displacement worth, while the assembly duct heterogeneity effect amounts to several percent of the total assembly displacement worth. In order to estimate assembly bowing reactivity accurately, assembly ducts and inter-assembly gaps need to be modeled explicitly.

2. The reactivity worth of assembly segment displacement is additive in the anticipated range of variations. That is, the reactivity change induced by simultaneous displacements of multiple axial segments can be determined by adding the contributions of individual segments.

3. The assembly heterogeneity effect on the negative reactivity induced by radial expansion of the core grid plate is negligible. Therefore, it would be better to evaluate the reactivity feedback due to uniform radial expansion from direct VARIANT transport calculations

with homogenized assembly models (including the inter-assembly gap sodium) instead of the perturbation theory calculations.

4. The reactivity induced by axial fuel expansion is linear within the anticipated range of expansion, and the assembly heterogeneity effect on it is negligible. However, the reactivity worth of axial fuel expansion varies from assembly to assembly. Therefore, the first-order perturbation theory method based on the VARIANT transport solutions obtained with homogenized assembly models would be adequate for accurate evaluation of the feedback reactivity due to fuel axial expansion.

5. The reactivity induced by radial expansion of assembly duct is insignificant compared to other components of the core deformation reactivity, and thus it can be neglected.

8.3 Development of Perturbation Theory Method for Core Deformation Reactivity

A new perturbation theory method for evaluating the reactivity change due to assembly displacement has been developed based on the global VARIANT transport solutions with homogenized assembly models and the local PROTEUS-SN transport solutions with heterogeneous assembly models. A new numerical calculation scheme was developed by following the material movement, which is analogous to the ‘Lagrangian frame of reference’ in a fluid field. This scheme provides a unique convenience for modeling heterogeneous assembly displacements by eliminating the need to consider numerous intersections of finite element meshes of PROTEUS-SN and shifted assemblies.

The perturbation theory method for evaluating the reactivity change due to axial fuel expansion has also been developed. This method is based on the conventional perturbation theory formula that computes the material change in each axial region of fuel assembly. This method produces the reactivity coefficient of axial fuel expansion for individual fuel assemblies. The whole core reactivity change due to axial fuel expansion can be calculated by combining the axial fuel expansion coefficients and the magnitudes of axial expansion of individual fuel assemblies.

8.4 Reconstruction of Heterogeneous Flux Distribution

The forward and adjoint fluxes in heterogeneous assemblies used in the perturbation theory calculation are reconstructed from the VARIANT solution for the whole core model with homogenized assemblies and the PROTEUS-SN solutions for heterogeneous single-assembly models. The accuracy of the reconstructed flux distributions has been examined using a two-dimensional (2D) mini-core model. A local region-dependent broad group cross section set for the PROTEUS-SN calculation with heterogeneous assembly models was generated using the MC^2-3 code with the MOC transport calculation option to take into account the duct heterogeneity effect. The reconstructed heterogeneous flux distributions were compared with the reference PROTEUS-SN solution for the full core model with heterogeneous assemblies. The results indicate that the reconstructed flux distributions by combining the VARIANT core solution and the PROTEUS-SN assembly solution can reproduce the reference heterogeneous solution with sufficient accuracy.

8.5 Development of RAINBOW Code

A computer code RAINBOW has been developed to calculate the reactivity changes due to core deformation in sodium cooled fast rectors. Assembly bowing is modeled by shifting axially discretized assembly segments, and heterogeneous assembly configurations are represented by unstructured finite element meshes. A perturbation theory calculation capability has been implemented in RAINBOW to calculate the reactivity changes for the displacements of axial assembly segments in each of six directions normal to the duct wall surfaces. Benchmark tests of the RAINBOW code were performed using 2D and 3D mini-core models that were derived from the ABTR core design. Reference solutions were obtained from MCNP6 Monte Carlo simulations and PROTEUS-SN deterministic calculations by the difference in eigenvalue between the perturbed and unperturbed cases. The numerical results of 2D models showed that the assembly displacement worth obtained from RAINBOW perturbation calculations agree very well with the MCNP6 results. Statistical analysis shows that the RAINBOW results are statistically consistent with the MCNP6 results.

In the 3D calculation, the assembly was divided into 10 axial segments. The results for single assembly segment displacement show limited agreement with MCNP6 reference results mainly due to the MCNP6 statistical uncertainties since the displacement of single axial segment results in a tiny change in eigenvalue. In order to introduce a large perturbation relative to the standard deviation of MCNP6 results, the six assemblies in the third ring of assemblies were simultaneously shifted outward from the core center from their original positions. For 13 cases among the 15 perturbed cases considered, the RAINBOW results agreed with the reference MCNP6 results within two standard deviation of the MCNP6 results, but two cases showed exceptionally large differences. By recalculating the reference solutions by the statistical average of five independent MCNP6 simulations with different random seed numbers, it was found that the observed deviations are due to the underestimated standard deviations reported by MCNP6 simulations. When the statistically estimated MCNP6 reference solutions were used, the RAINBOW perturbation theory calculation results agreed well with the reference solutions.

The verification of the RAINBOW code has also been performed against PROTEUS-SN determinist results to eliminate the effect of Monte Carlo statistical uncertainties. The calculations are based on the same 2D and 3D mini-core models. In the 2D calculations, the RAINBOW results agree well with the PROTEUS-SN reference with all the errors within one pcm. In the 3D calculations, however, the required memory to obtain a mesh-converged PROTEUS-SN solution exceeds the computational resource currently available to the author. A simple estimate of memory requirement indicates more than 3 Terabyte memories are required for the PROTEUS-SN calculation based on 3D mini-core model. Therefore, the Richardson extrapolation scheme was applied to obtain a mesh-converged solution. The RAINBOW perturbation results agreed very well with the PROTEUS-SN reference solutions derived from the extrapolated eigenvalues.

Additional numerical tests were performed to verify the capability of the RAINBOW code to evaluate the fuel axial expansion reactivity. The calculations were based on a 3D mini-core with heterogeneous axial regions. The RAIBOW results agreed well with the reference results obtained using the MCNP6 and VARIANT codes.

8.6 Summary and Future Work

This doctoral work aims at tackling the long-standing challenge on evaluating the reactivity changes due to core deformation in fast reactors and results in an innovative perturbation theory method for such purpose. The perturbation theory method has been developed and implemented in a computer code named RAINBOW (ReActivity INduced by assembly BOWing). The RAINBOW code is still under development, but preliminary verification tests performed with mini-core models produced very satisfactory results. In the future, more extensive verification tests with realistic fast reactor core designs and validation tests against EBR-II and FFTF experiments need to be conducted.

APPENDIX A MINI CORE COMPOSTIONS

Mini-core fuel compositions

Isotope	Nuclide density adopted from ABTR	Nuclide density for critical mini-core
U234	**1.22252E-08**	**1.14719E-08**
U235	**3.22479E-05**	**3.02609E-05**
U236	**2.05609E-06**	**1.92940E-06**
U238	**2.02220E-02**	**1.89760E-02**
NP237	3.83873E-06	3.83873E-06
PU236	**1.39182E-11**	**1.83720E-11**
PU238	**9.58542E-07**	**1.26528E-06**
PU239	**3.49907E-03**	**4.61877E-03**
PU240	**3.73979E-04**	**4.93652E-04**
PU241	**2.45354E-05**	**3.23867E-05**
PU242	**1.75421E-06**	**2.31556E-06**
AM241	1.42088E-06	1.42088E-06
AM242	2.84750E-08	2.84750E-08
AM243	6.13383E-08	6.13383E-08
CM242	4.70831E-08	4.70831E-08
CM243	7.41385E-10	7.41385E-10
CM244	4.83054E-09	4.83054E-09
CM245	1.90641E-10	1.90641E-10
CM246	2.61116E-12	2.61116E-12
ZR90	3.75264E-03	3.75264E-03
ZR91	8.18360E-04	8.18360E-04
ZR92	1.25088E-03	1.25088E-03
ZR94	1.26766E-03	1.26766E-03
ZR96	2.04225E-04	2.04225E-04
MO92	1.44857E-04	1.44857E-04
MO94	9.02914E-05	9.02914E-05
MO95	1.55399E-04	1.55399E-04
MO96	1.62817E-04	1.62817E-04
MO97	9.32197E-05	9.32197E-05
MO98	2.35538E-04	2.35538E-04
MO100	9.40006E-05	9.40006E-05
sum	3.24319E-02	3.24319E-02

APPENDIX B POST-PROCESSING OF PROTEUS-SN SOLUTION

A computational module for post-processing of PROTEUS-SN solutions has been developed to generate element-averaged fluxes that will be used for calculating form functions in the RAINBOW code. The full solution of PROTEUS-SN code is stored in an HDF5 data format. As an example, the data structure of the HDF5 output file for a single pin cell problem is shown in Figure B.1. The pin cell model has three blocks representing three regions with different material assignments. The output flux is on the finite element vertices and stored in the dataset VERTEXDATA. The dataset XYZ stores the coordinates of each vertex. The dataset GLOBALID provides the information on to which element each vertex belongs. With these datasets, we can calculate the element-averaged flux used to generate the assembly form functions.

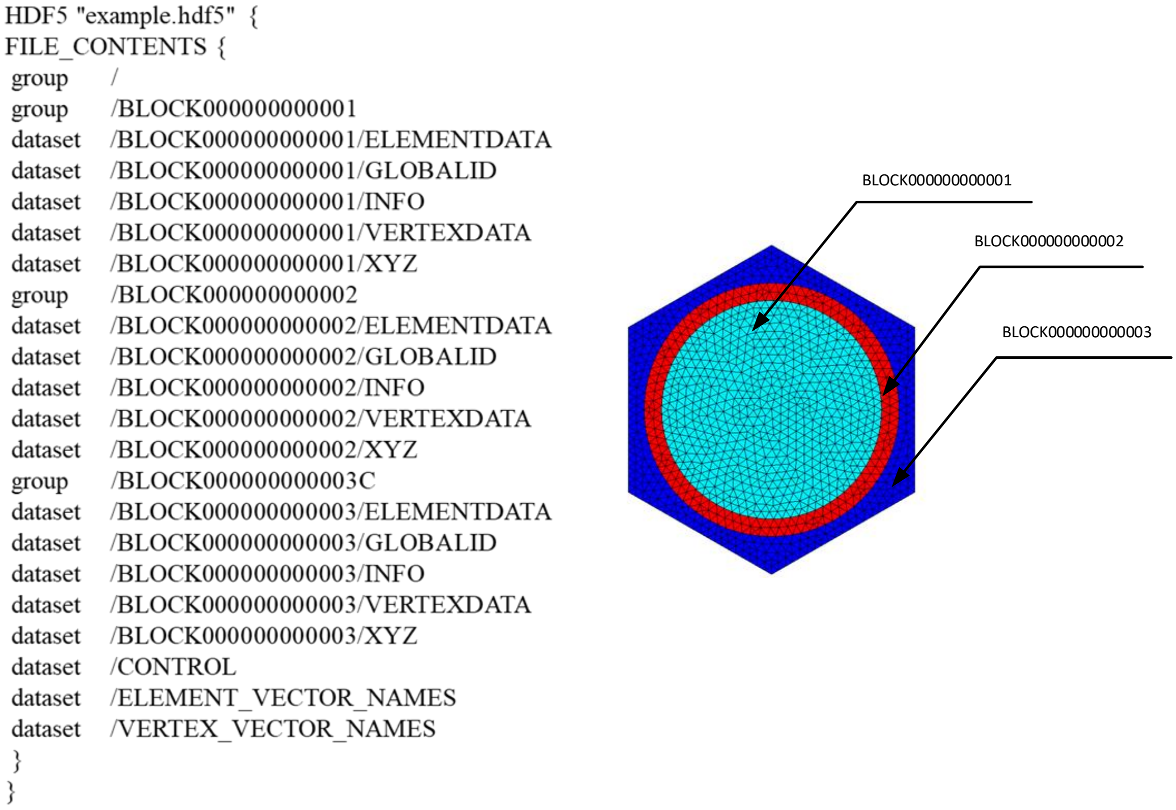

```
HDF5 "example.hdf5"  {
FILE_CONTENTS {
 group      /
 group      /BLOCK000000000001
 dataset    /BLOCK000000000001/ELEMENTDATA
 dataset    /BLOCK000000000001/GLOBALID
 dataset    /BLOCK000000000001/INFO
 dataset    /BLOCK000000000001/VERTEXDATA
 dataset    /BLOCK000000000001/XYZ
 group      /BLOCK000000000002
 dataset    /BLOCK000000000002/ELEMENTDATA
 dataset    /BLOCK000000000002/GLOBALID
 dataset    /BLOCK000000000002/INFO
 dataset    /BLOCK000000000002/VERTEXDATA
 dataset    /BLOCK000000000002/XYZ
 group      /BLOCK000000000003C
 dataset    /BLOCK000000000003/ELEMENTDATA
 dataset    /BLOCK000000000003/GLOBALID
 dataset    /BLOCK000000000003/INFO
 dataset    /BLOCK000000000003/VERTEXDATA
 dataset    /BLOCK000000000003/XYZ
 dataset    /CONTROL
 dataset    /ELEMENT_VECTOR_NAMES
 dataset    /VERTEX_VECTOR_NAMES
 }
}
```

Figure B.1 Output Structure of PROTEUS-SN in HDF5 Format

In the preliminary RAINBOW code, we only deal with 3-node triangular element and 4-node quadrilateral element that appears in the heterogeneous assembly model as shown in Figure B.2. Additional types of element including higher order elements need to be added to the RAINBOW code in the future development.

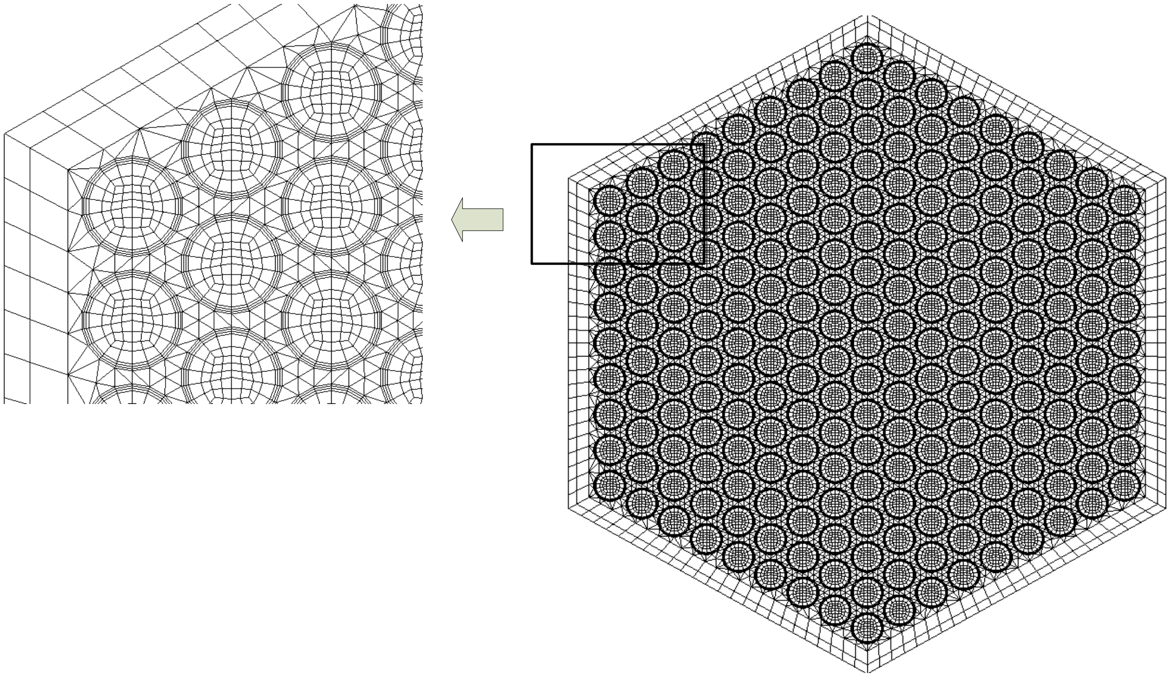

Figure B.2 Finite Element Mesh for Heterogeneous Assembly Model with 3-Node Triangular Element and 4-Node Quadrilateral Element

The 3-node triangular element and 4-node quadrilateral element in Cartesian coordinates are pictured in Figure B.3. The 3-node triangular element is linear, that is, a within-element distribution of quantity z (such as flux) can be written as

$$z = ax + by + c\,. \tag{B.1}$$

For linear triangular element, the element-averaged value is equivalent to the volume underneath the triangle divided by the element area. After some algebra, we have

$$V = \frac{\left|(z1 + z2 + z3) * \left[(x1y2 - x2y1) + (x2y3 - x3y2) + (x3y1 - x1y3)\right]\right|}{6}, \tag{B.2}$$

$$A = \frac{\left|(x1y2 - x2y1) + (x2y3 - x3y2) + (x3y1 - x1y3)\right|}{2}, \tag{B.3}$$

$$\overline{z} = \frac{V}{A} = \frac{(z1 + z2 + z3)}{3}. \tag{B.4}$$

Eq. (B.4) can also be obtained directly from the linearity of the element.

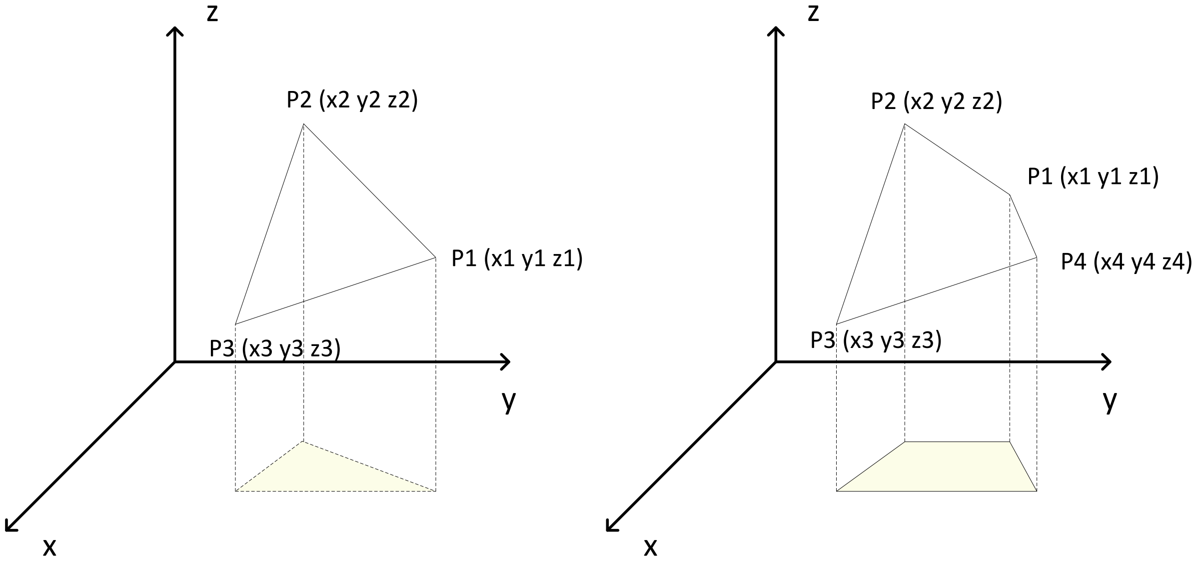

Figure B.3 Illustrations of 3-Node Triangular Element (Left) and 4-Node Quadrilateral Element (Right)

The 4-node quadrilateral element is bilinear element, that is, it is linear at the edges and the within element flux is given by

$$z(x, y) = a1 + a2 \cdot x + a3 \cdot y + a4 \cdot xy = u(x, y). \tag{B.5}$$

To calculate the element averaged flux, we can use an iso-parametric mapping to translate the element to a square as shown in Figure B.4. The shape functions are given by

$$\begin{array}{l} N1(s,t) = \frac{1}{4}(1+s)(1+t) \\ N2(s,t) = \frac{1}{4}(1-s)(1+t) \\ N3(s,t) = \frac{1}{4}(1-s)(1-t) \\ N4(s,t) = \frac{1}{4}(1+s)(1-t) \end{array}. \tag{B.6}$$

Then we have

$$\begin{aligned}
x(s,t) &= N1(s,t)x1 + N2(s,t)x2 + N3(s,t)x3 + N4(s,t)x4 \\
y(s,t) &= N1(s,t)y1 + N2(s,t)y2 + N3(s,t)y3 + N4(s,t)y4\,. \\
v(s,t) &= N1(s,t)u1 + N2(s,t)u2 + N3(s,t)u3 + N4(s,t)u4
\end{aligned} \tag{B.7}$$

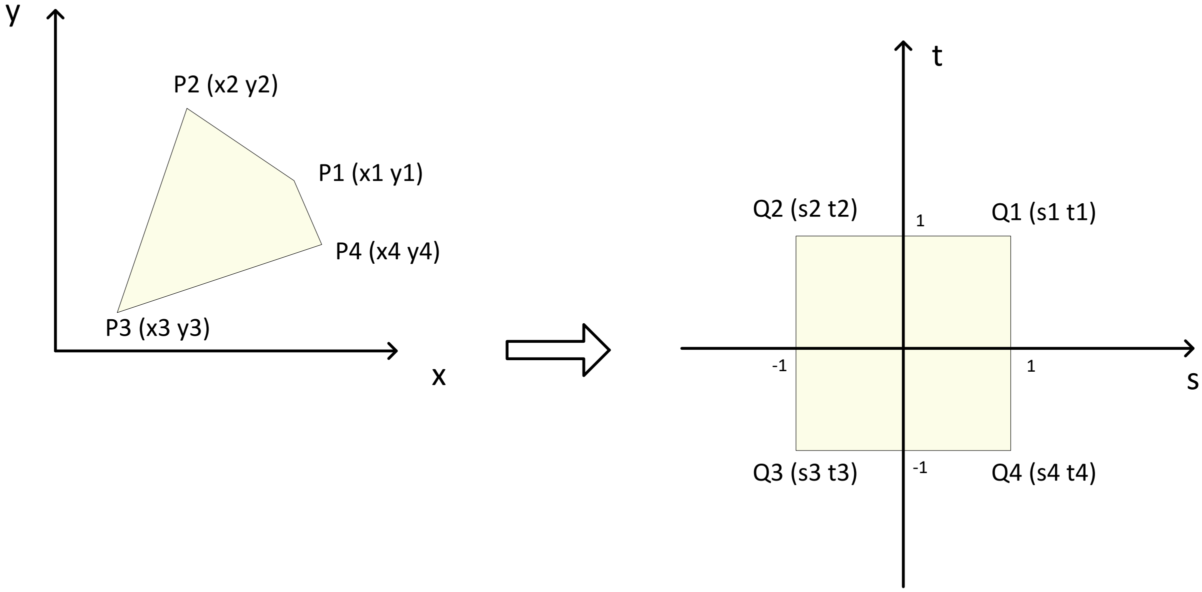

Figure B.4 Isoparametric Mapping

Representing the shape function in a matrix form, we have

$$\vec{N}(s,t) = \frac{1}{4} \cdot \begin{bmatrix} 1 & 1 & 1 & 1 \\ 1 & -1 & 1 & -1 \\ 1 & -1 & -1 & 1 \\ 1 & 1 & -1 & -1 \end{bmatrix} \begin{bmatrix} 1 \\ s \\ t \\ st \end{bmatrix} = N \cdot \vec{p}\,, \tag{B.8}$$

with

$$\vec{p} = \begin{bmatrix} 1 \\ s \\ t \\ st \end{bmatrix}. \tag{B.9}$$

Then, we can write Eq. (B.7) in a matrix form as

$$\begin{aligned}
x(s,t) &= \vec{x}^{\mathrm{T}} \cdot \vec{N}(s,t) = \vec{x}^{\mathrm{T}} \cdot N \cdot \vec{p} = \overrightarrow{xst}^{\mathrm{T}} \cdot \vec{p} \\
y(s,t) &= \vec{y}^{\mathrm{T}} \cdot \vec{N}(s,t) = \vec{y}^{\mathrm{T}} \cdot N \cdot \vec{p} = \overrightarrow{yst}^{\mathrm{T}} \cdot \vec{p}\,, \\
v(s,t) &= \vec{u}^{\mathrm{T}} \cdot \vec{N}(s,t) = \vec{u}^{\mathrm{T}} \cdot N \cdot \vec{p}
\end{aligned} \tag{B.10}$$

where we have

$$\overrightarrow{xst} = N^T \vec{x} , \tag{B.11}$$

and

$$\overrightarrow{yst} = N^T \vec{y} . \tag{B.12}$$

The integration of flux over the element is

$$I_e = \iint u(x,y)dxdy = \iint v(s,t)\left|J\right|dsdt , \tag{B.13}$$

where

$$\left|J\right| = \mathrm{Det}\begin{bmatrix} \frac{\partial x}{\partial s} & \frac{\partial y}{\partial s} \\ \frac{\partial x}{\partial t} & \frac{\partial y}{\partial t} \end{bmatrix} . \tag{B.14}$$

We need to find the expressions for $v(s,t)$ and $\left|J\right|(s,t)$.

Let

$$v(s,t) = a1 + a2 \cdot s + a3 \cdot t + a4 \cdot st = a^{\mathrm{T}} \cdot \vec{p} . \tag{B.15}$$

Comparing Eq. (B.15) to Eq. (B.10), we have

$$a = N^{\mathrm{T}} \cdot \vec{u} . \tag{B.16}$$

Let

$$\left|J\right|(s,t) = b1 + b2 \cdot s + b3 \cdot t + b4 \cdot st = b^{\mathrm{T}} \cdot \vec{p} . \tag{B.17}$$

By using Eq. (B.14), we can obtain

$$\vec{b} = \begin{bmatrix} xst(2)yst(3) - yst(2)xst(3) \\ xst(2)yst(4) - yst(2)xst(3) \\ xst(4)yst(3) - yst(4)xst(3) \\ 0 \end{bmatrix} . \tag{B.18}$$

Expand the integration in Eq. (B.13), the element total flux can be written as

$$I_e = \iint v(s,t)\left|J\right|dsdt = \int_{-1}^{1}\int_{-1}^{1} (a1 + a2 \cdot s + a3 \cdot t + a4 \cdot st) \cdot (b1 + b2 \cdot s + b3 \cdot t + b4 \cdot st)dsdt . \tag{B.19}$$

By performing the integration in Eq. (B.19), we have the algebraic expression of the total flux as

$$I_e = 4a1b1 + \frac{4}{3}(a2b2 + a3b3) + \frac{4}{9}a4b4 . \tag{B.20}$$

The numerical test of the PROTEUS-SN post-processing module has been performed based on a simple two-dimensional model shown in Figure B.5. The core has two rings of fuel assembly with fully heterogeneous assembly model. We extracted the power data of fuel assembly 5 from the HDF5 output and calculated the element averaged flux using the method presented in this section. The element-averaged data is visualized using MATLAB [70] and compared with the results obtained using data processing software VisIt [71] as shown in Figure B.6. The element-averaged power for assembly 5 calculated using the post-processing module is identical to that obtained from VisIt.

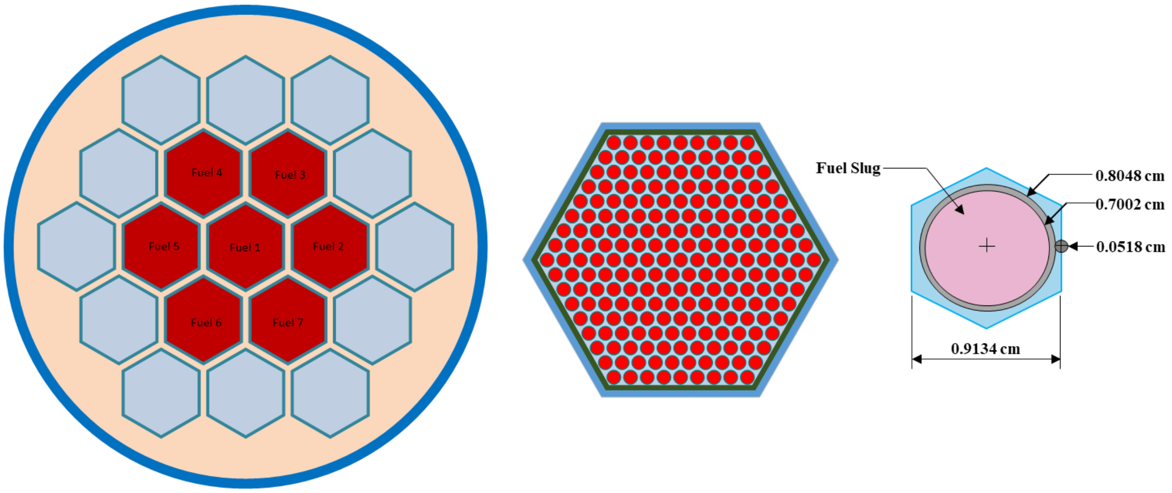

Figure B.5 A 2D Toy Model for Testing PROTESU-SN Post-Processing Module

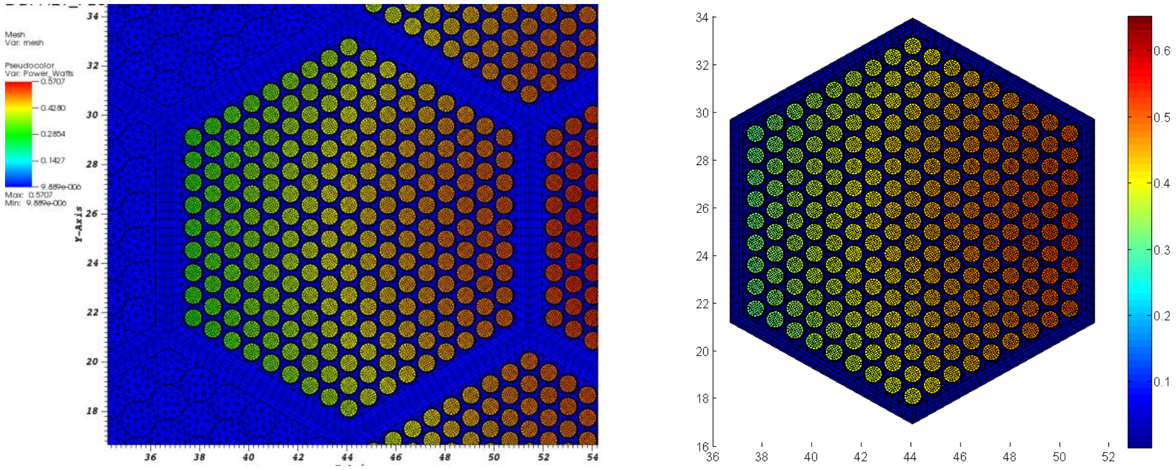

Figure B.6 Element Averaged Power In Assembly 5 obtained using the Post-Processing Module (Right) and VisIt (Left)

APPENDIX C BROAD GROUP STRUCTURES

33-group structure in ev

Group	Energy	Group	Energy	Group	Energy	Group	Energy
1	1.42E+07	10	1.83E+05	19	2.03E+03	28	2.26E+01
2	1.00E+07	11	1.11E+05	20	1.23E+03	29	1.37E+01
3	6.07E+06	12	6.74E+04	21	7.49E+02	30	8.32E+00
4	3.68E+06	13	4.09E+04	22	4.54E+02	31	3.93E+00
5	2.23E+06	14	2.48E+04	23	2.75E+02	32	5.32E-01
6	1.35E+06	15	1.50E+04	24	1.67E+02	33	4.17E-01
7	8.21E+05	16	9.12E+03	25	1.01E+02		
8	4.98E+05	17	5.53E+03	26	6.14E+01		
9	3.02E+05	18	3.35E+03	27	3.73E+01		

70-group structure in ev

Group	Energy	Group	Energy	Group	Energy	Group	Energy
1	1.42E+07	19	1.43E+05	37	1.58E+03	55	1.76E+01
2	1.00E+07	20	1.11E+05	38	1.23E+03	56	1.37E+01
3	7.79E+06	21	8.65E+04	39	9.61E+02	57	1.07E+01
4	6.07E+06	22	6.74E+04	40	7.49E+02	58	8.32E+00
5	4.72E+06	23	5.25E+04	41	5.83E+02	59	6.48E+00
6	3.68E+06	24	4.09E+04	42	4.54E+02	60	5.04E+00
7	2.87E+06	25	3.18E+04	43	3.54E+02	61	3.93E+00
8	2.23E+06	26	2.48E+04	44	2.75E+02	62	3.06E+00
9	1.74E+06	27	1.93E+04	45	2.14E+02	63	2.38E+00
10	1.35E+06	28	1.50E+04	46	1.67E+02	64	1.86E+00
11	1.05E+06	29	1.17E+04	47	1.30E+02	65	1.45E+00
12	8.21E+05	30	9.12E+03	48	1.01E+02	66	1.13E+00
13	6.39E+05	31	7.10E+03	49	7.89E+01	67	8.76E-01
14	4.98E+05	32	5.53E+03	50	6.14E+01	68	6.83E-01
15	3.88E+05	33	4.31E+03	51	4.79E+01	69	5.32E-01
16	3.02E+05	34	3.35E+03	52	3.73E+01	70	4.17E-01
17	2.35E+05	35	2.61E+03	53	2.90E+01		
18	1.83E+05	36	2.03E+03	54	2.26E+01		

116-group structure in ev

Group	Energy	Group	Energy	Group	Energy	Group	Energy
1	1.42E+07	30	2.73E+06	59	3.02E+05	88	4.53E+03
2	1.35E+07	31	2.47E+06	60	2.87E+05	89	4.10E+03
3	1.28E+07	32	2.39E+06	61	2.73E+05	90	3.35E+03
4	1.22E+07	33	2.27E+06	62	2.47E+05	91	2.86E+03
5	1.16E+07	34	2.23E+06	63	2.24E+05	92	2.61E+03
6	1.11E+07	35	2.02E+06	64	2.02E+05	93	2.25E+03
7	1.05E+07	36	1.92E+06	65	1.83E+05	94	1.84E+03
8	1.00E+07	37	1.83E+06	66	1.66E+05	95	1.58E+03
9	9.51E+06	38	1.65E+06	67	1.58E+05	96	1.36E+03
10	9.05E+06	39	1.57E+06	68	1.43E+05	97	1.17E+03
11	8.61E+06	40	1.50E+06	69	1.29E+05	98	1.06E+03
12	8.19E+06	41	1.35E+06	70	1.17E+05	99	9.61E+02
13	7.79E+06	42	1.22E+06	71	1.11E+05	100	5.83E+02
14	7.41E+06	43	1.16E+06	72	8.65E+04	101	3.54E+02
15	7.05E+06	44	1.05E+06	73	6.74E+04	102	2.14E+02
16	6.70E+06	45	1.00E+06	74	5.95E+04	103	1.30E+02
17	6.54E+06	46	9.54E+05	75	5.25E+04	104	7.89E+01
18	6.22E+06	47	8.63E+05	76	4.09E+04	105	4.79E+01
19	5.92E+06	48	7.81E+05	77	3.61E+04	106	2.90E+01
20	5.77E+06	49	7.07E+05	78	3.18E+04	107	1.76E+01
21	5.22E+06	50	6.39E+05	79	2.81E+04	108	1.07E+01
22	4.97E+06	51	5.78E+05	80	2.48E+04	109	6.48E+00
23	4.72E+06	52	5.23E+05	81	2.13E+04	110	3.93E+00
24	4.49E+06	53	4.98E+05	82	1.93E+04	111	2.38E+00
25	4.07E+06	54	4.50E+05	83	1.50E+04	112	1.45E+00
26	3.68E+06	55	4.08E+05	84	1.17E+04	113	8.76E-01
27	3.33E+06	56	3.69E+05	85	9.12E+03	114	6.83E-01
28	3.17E+06	57	3.34E+05	86	7.10E+03	115	5.32E-01
29	3.01E+06	58	3.17E+05	87	5.53E+03	116	4.17E-01

APPENDIX D SAMPLE INPUT AND OUTPUT OF RAIBOW

Sample input file

```
&ProblemSpecs
      Problem%UseFormFE=.FAULSE.
      Problem%Keffective=1.00419
      Problem%NumGroup=33
      Problem%Dims=2
      Problem%ScatOrder=5
      Problem%AngularOrder=5
      Problem%NumAssembly=91
      Problem%NumActiveAssembly=19
      Problem%NumAssemblyType=1
      Problem%AssemblyMap(1:13,1:13)=0 0 0 0 0 0 0 0 0 0 0 0 0
                                     0 0 0 0 0 0 0 0 0 0 0 0 0
                                     0 0 0 0 0 0 0 0 0 0 0 0 0
                                     0 0 0 0 0 0 0 0 0 0 0 0 0
                                     0 0 0 0 1 1 1 0 0 0 0 0 0
                                     0 0 0 0 1 1 1 1 0 0 0 0 0
                                     0 0 0 0 1 1 1 1 1 0 0 0 0
                                     0 0 0 0 0 1 1 1 1 0 0 0 0
                                     0 0 0 0 0 0 1 1 1 0 0 0 0
                                     0 0 0 0 0 0 0 0 0 0 0 0 0
                                     0 0 0 0 0 0 0 0 0 0 0 0 0
                                     0 0 0 0 0 0 0 0 0 0 0 0 0
                                     0 0 0 0 0 0 0 0 0 0 0 0 0
/

&AssemblySpecs
      Assembly(1)%NumElement=2066
      Assembly(1)%NumVertex=1394
      Assembly(1)%Shift=0.20
/

&InterfaceFiles
      PROTEUS_Interface%ForwardFlux='FUEL_ASSEMBLY_Forward.hdf5'
      PROTEUS_Interface%AdjointFlux='FUEL_ASSEMBLY_Adjoint.hdf5'
      PROTEUS_Interface%Assignment='FUEL_ASSEMBLY.assign'
      MCC3_Interface%ISOTXS='MiniCore2D.33g.ISOTXS'
      VARIANT_Interface%NHFLUX= MiniCore2D.NHFLUX'
      VARIANT_Interface%NAFLUX= MiniCore2D.NAFLUX'
      VARIANT_Interface%GEODST= MiniCore2D.GEODST'
/
```

Sample Output file

```
                                              _____
                                             /     \
                                       _____/  10   \_____
                                      /     \       /     \
                                _____/  11   \_____/   9   \_____
                               /     \       /     \       /     \
                              /  12   \_____/   3   \_____/   8   \
                              \       /     \       /     \       /
                               \_____/   4   \_____/   2   \_____/
                               /     \       /     \       /     \
                              /  13   \_____/   1   \_____/  19   \
                              \       /     \       /     \       /
                               \_____/   5   \_____/   7   \_____/
                               /     \       /     \       /     \
                              /  14   \_____/   6   \_____/  18   \
                              \       /     \       /     \       /
                               \_____/  15   \_____/  17   \_____/
                                     \       /     \       /
                                      \_____/  16   \_____/
                                            \       /
                                             \_____/

               ************** DIRECTIONAL REACTIVITY WORTH OF ASSEMBLY DISPLACEMENT **************

                 Direction 1    Direction 2    Direction 3    Direction 4    Direction 5    Direction 6
ASSEMBLY   1       -0.111         -0.116         -0.117         -0.115         -0.110         -0.109
ASSEMBLY   2      -14.388         -7.256          7.066         14.254          7.072         -7.250
ASSEMBLY   3       -7.251         14.390         -7.256          7.067         14.257          7.072
ASSEMBLY   4        7.069         -7.254        -14.390         -7.252          7.071         14.257
ASSEMBLY   5       14.256          7.067         -7.256        -14.389         -7.251          7.071
ASSEMBLY   6        7.071         14.255          7.067         -7.255        -14.389         -7.251
ASSEMBLY   7       -7.252          7.068         14.253          7.068         -7.252        -14.387
ASSEMBLY   8      -19.157         -9.622          9.529         19.149          9.528         -9.625
ASSEMBLY   9      -15.939         15.940         -0.087         15.853         15.855         -0.085
ASSEMBLY  10       -9.621         19.149         -9.616          9.526         19.139          9.522
ASSEMBLY  11       -0.085         15.935        -15.934         -0.086         15.849         15.850
ASSEMBLY  12        9.520         -9.619        -19.145         -9.615          9.525         19.135
ASSEMBLY  13       15.846         -0.088        -15.934        -15.931         -0.083         15.849
```

ASSEMBLY 14	19.140	9.528	-9.615	-19.150	-9.624	9.520
ASSEMBLY 15	15.854	15.857	-0.084	-15.940	-15.942	-0.088
ASSEMBLY 16	9.524	19.150	9.534	-9.619	-19.158	-9.629
ASSEMBLY 17	-0.084	15.864	15.862	-0.089	-15.949	-15.947
ASSEMBLY 18	-9.622	9.534	19.152	9.526	-9.629	-19.162
ASSEMBLY 19	-15.946	-0.087	15.859	15.860	-0.084	-15.945

APPENDIX E. GENERATING FINITE ELEMENT MESH FOR SHIFTED ASSEMBLY

Block Decomposition for Finite Element Mesh of Shifted Assembly

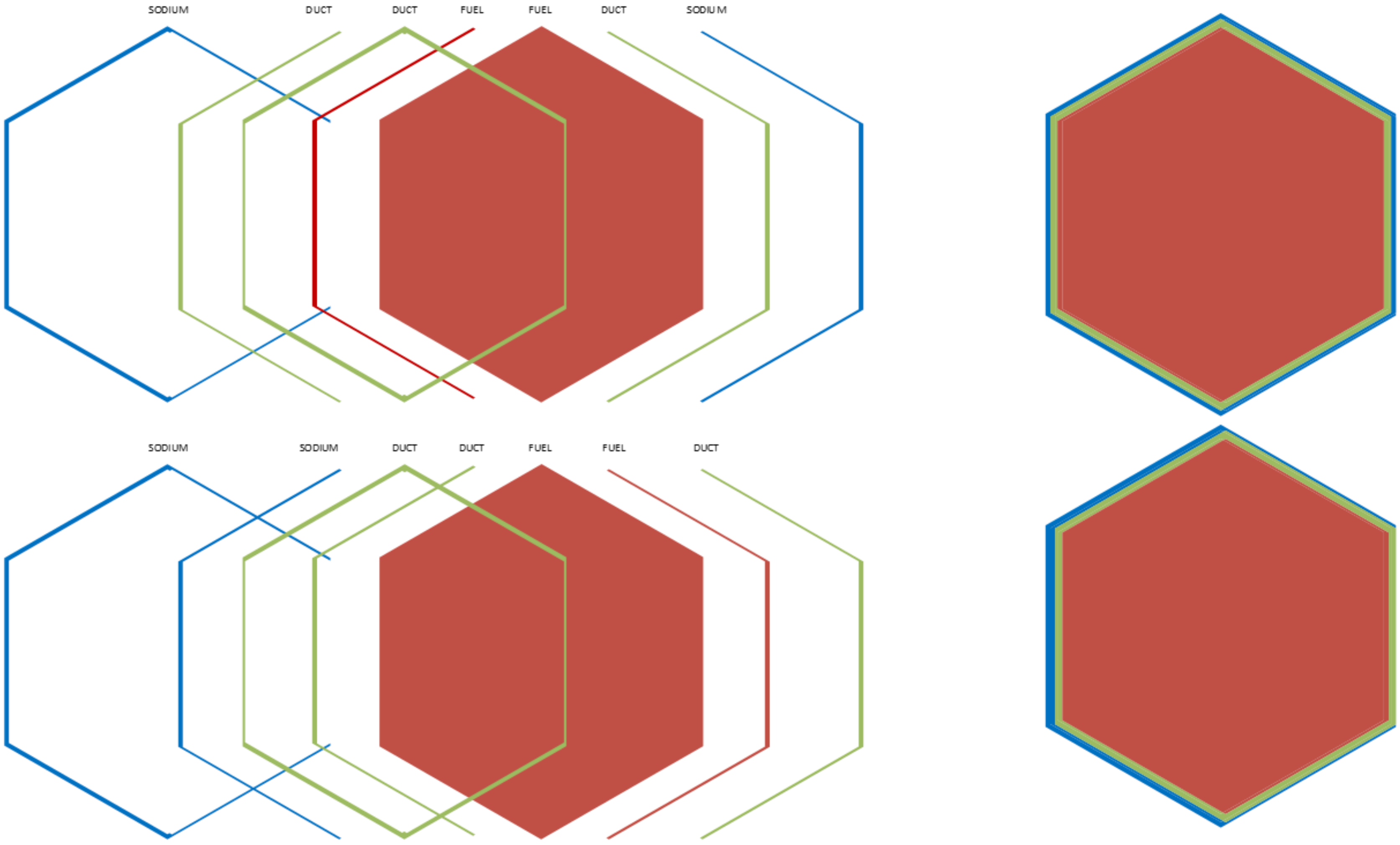

Trelis Scripts for Generating the Finite Element Mesh for Shifted Assembly

```
#########################################################
# INPUT DATA:
#########################################################

#{NUM_FUEL_RINGS=3}
#{NUM_REFL_RINGS=3}
#{ASSEMBLY_HEIGHT=1}
#{ASSEMBLY_PITCH=14.6850}
#{ASSEMBLY_SHIFT = 0.2012}
#{OUTER_DUCT_PITCH=14.2826}
#{INNER_DUCT_PITCH=13.6790}
#{ASSEMBLY_RADIUS=ASSEMBLY_PITCH/sqrt(3)}
#{OUTER_DUCT_RADIUS=OUTER_DUCT_PITCH/sqrt(3)}
#{INNER_DUCT_RADIUS=INNER_DUCT_PITCH/sqrt(3)}
#{NUM_SIDES=6}

######################################################
# BUILD MODEL:
######################################################

#Create volume 'SODIUM'
create Prism height {ASSEMBLY_HEIGHT} sides {NUM_SIDES} radius {ASSEMBLY_RADIUS}
volume 1 name 'SODIUM'
create Prism height {ASSEMBLY_HEIGHT} sides {NUM_SIDES} radius {OUTER_DUCT_RADIUS}
move volume 2 x {ASSEMBLY_SHIFT} y 0 z 0
subtract volume 2 from volume 1
create Prism height {ASSEMBLY_HEIGHT} sides {NUM_SIDES} radius {OUTER_DUCT_RADIUS}
subtract volume 3 from volume 1

#Create volume 'DUCT_SODIUM'
create Prism height {ASSEMBLY_HEIGHT} sides {NUM_SIDES} radius {OUTER_DUCT_RADIUS}
volume 4 name 'DUCT_SODIUM'
create Prism height {ASSEMBLY_HEIGHT} sides {NUM_SIDES} radius {OUTER_DUCT_RADIUS}
move volume 5 x {ASSEMBLY_SHIFT} y 0 z 0
```

```
subtract volume 5 from volume 4

#Create volume 'SODIUM_DUCT'
create Prism height {ASSEMBLY_HEIGHT} sides {NUM_SIDES} radius {OUTER_DUCT_RADIUS}
volume 6 name 'SODIUM_DUCT'
move volume 6 x {ASSEMBLY_SHIFT} y 0 z 0
create Prism height {ASSEMBLY_HEIGHT} sides {NUM_SIDES} radius {OUTER_DUCT_RADIUS}
subtract volume 7 from volume 6

#Create volume 'FUEL_DUCT'
create Prism height {ASSEMBLY_HEIGHT} sides {NUM_SIDES} radius {INNER_DUCT_RADIUS}
volume 8 name 'FUEL_DUCT'
create Prism height {ASSEMBLY_HEIGHT} sides {NUM_SIDES} radius {INNER_DUCT_RADIUS}
move volume 9 x {ASSEMBLY_SHIFT} y 0 z 0
subtract volume 9 from volume 8

#Create volume 'DUCT_FUEL'
create Prism height {ASSEMBLY_HEIGHT} sides {NUM_SIDES} radius {INNER_DUCT_RADIUS}
volume 10 name 'DUCT_FUEL'
move volume 10 x {ASSEMBLY_SHIFT} y 0 z 0
create Prism height {ASSEMBLY_HEIGHT} sides {NUM_SIDES} radius {INNER_DUCT_RADIUS}
subtract volume 11 from volume 10

#Create volume 'DUCT'
create Prism height {ASSEMBLY_HEIGHT} sides {NUM_SIDES} radius {OUTER_DUCT_RADIUS}
volume 12 name 'DUCT'
create Prism height {ASSEMBLY_HEIGHT} sides {NUM_SIDES} radius {INNER_DUCT_RADIUS}
subtract volume 13 from volume 12
volume 4 copy
subtract volume 14 from volume 12
volume 10 copy
subtract volume 15 from volume 12

#Create volume 'FUEL'
create Prism height {ASSEMBLY_HEIGHT} sides {NUM_SIDES} radius {INNER_DUCT_RADIUS}
volume 16 name 'FUEL'
volume 8 copy
```

```
subtract volume 17 from volume 16
imprint all
merge all

######################################################
# MESH SURFACES:
######################################################

#Define intervals
##FUEL boundary
curve 232 238 282 288 interval 22
curve 239 289 interval 24
##FUEL_DUCT boundary
curve 197 199 interval 23
curve 198 interval 24
curve 241 242 interval 1
##DUCT_FUEL boundary
curve 246 250 interval 23
curve 245 interval 24
curve 291 292 interval 1
## DUCT boundary
curve 132 138 139 182 188 189 interval 24
## DUCT_SODIUM boundary
curve 84 89 interval 23
curve 87 interval 24
curve 76 82 interval 1
## SODIUM_DUCT boundary
curve 38 51 interval 23
curve 145 interval 22
curve 92 94 interval 1
## SODIUM boundary
curve 2 3 4 5 6 scheme pinpoint location 0.11616287 0.49098392 0.86580496 1.240626 1.61544705 ..
1.99026809 2.36508913 2.73991018 3.11473122 3.48955226 3.86437331 4.23919435 4.61401539 ..
4.98883644 5.36365748 5.73847853 6.11329957 6.48812061 6.86294166 7.2377627 7.61258374 ..
7.98740479 8.36222583
curve 53 54 interval 1
```

```
surface 216 scheme pave
surface 108 131 193 62 85 42 scheme trimesh
mesh surface 216 108 131 193 62 85 42

######################################################
# DEFINE BLOCKS AND BOUNDARIES
######################################################

block 993 surface 216
block 993 element type QUAD4
block 994 surface 108
block 994 element type TRI3
block 995 surface 131
block 995 element type TRI3
block 996 surface 193
block 996 element type TRI3
block 997 surface 62
block 997 element type TRI3
block 998 surface 85
block 998 element type TRI3
block 999 surface 42
block 999 element type TRI3

sideset 999 curve 2 3 4 5 6 53 54 145

######################################################
# EXPORT MESH
######################################################

export mesh "FUEL_ASSEMBLY_SHIFTED.e"
```

REFERENCES

1. IAEA PRIS Database on Nuclear Power Reactors, URL: https://www.iaea.org/pris/
2. Generation IV International FORUM (GIF), "A Technology Roadmap for the Generation IV Nuclear Energy Systems," GIF-002-00 (2002).
3. M. J. Lineberry and T. R. Allen. "The Sodium-Cooled Fast Reactor (SFR)," American Nuclear Energy Symposium (ANES 2002), Miami, Florida, October 16-18, 2002.
4. H. P. Planchon, J. I. Sackett, G. H. Golden and R. H. Sevy, "Implications of the EBR-II Inherent Safety Demonstration Test", Nuclear Engineering and Design **101**, 75-90 (1987).
5. D. M. Lucoff, "Passive Safety Testing at the Fast Flux Test Facility", Nuclear Technology **88**(1), 21-29 (1989).
6. Alan E. Waltar, Donald R. Todd, Pavel V. Tsvetkov, "Fast Spectrum Reactors," Springer, New York (2012).
7. E. Bojarsky, K. Mueller, and H. Reiser, "Inherently Effective Shutdown System with Curie Point Controlled Sensor/switch Unit," KFK-4989, Germany (1992).
8. J. B. Waldo, A. Padilla Jr., D. H. Nguyen, S. W. Claybrook, "Application of the GEM Shutdown Device to the FFTF Reactor," Trans. Am. Nucl. Soc, 53, 312 (1986).
9. G. C. Slovik, G. J. Van Tuyle, and R. J. Kennett, "Analysis of unscrammed loss of flow and heat sink for PRISM with GEM," Trans. Am. Nucl. Soc., 317-319 (1991).
10. Y. BILIBIN, "Nuclear Reactor Shutdown Control Rod Assembly," U. S. Patent 4, 764, 252 (1988).
11. K. O. Ott, W. A. Bezella, "Introductory Nuclear Reactor Statics," Chapter 5, American Nuclear Society (1989).
12. W. S. YANG, "Fast Reactor Physics and Computational Methods," Nuclear Engineering and Technology **44** (2011).
13. H. S. Khalil and R. N. Hill, "Evaluation of Liquid-Metal Reactor Design Options for Reduction of Sodium Void Worth," Nuclear Science and Engineering **109** (3), 221-266 (1991).

14. V. M. Poplavsky, A. M. Tsiboulia, Y. S. Khomyakov, V. I. Matveev, V. A. Eliseev, A. G. Tsikunov, and M. R. Farakshin, “Core Design and Fuel Cycle of Advanced Fast Reactor with Sodium Coolant. In Int. Conf. on Fast Reactors and Related Fuel Cycles: Challenges and Opportunities (FR09), December 7, pp. 7-11 (2009).

15. F. Varaine, P. Marsault, M. S. Chenaud, B. Bernardin, A. Conti, P. Sciora, C. Venard, B. Fontaine, N. Devictor, L. Martin, A. C. Scholer, “Pre-conceptual Design Study of ASTRID Core,” American Nuclear Society, 555 North Kensington Avenue, La Grange Park, IL 60526, July 1 (2012).

16. S. Qvist, “Safety and Core Design of Large Liquid-Metal Cooled Fast Breeder Reactors” (Ph.D. thesis) University of California Berkeley, Nuclear Engineering, Berkeley, CA, USA (2013)

17. R. A. Wigeland and T. J. Moran, “Radial Core Expansion Reactivity Feedback in Advanced LMRs: Uncertainties and Their Effects on Inherent Safety,” *Proc. Topl. Mtg. on Safety of Next Generation Power Reactors*, April 1-5, 1988, Seattle, WA.

18. J. J. Grudzinski and C. Grandy, “Fuel Assembly Bowing and Core Restraint Design in Fast Reactors,” Proc. of the ASME 2014 International Mechanical Engineering Congress and Exposition, November 14-20, 2014, Montreal, Quebec, Canada.

19. W. H. Sutherland, “Overview of Core Designs and Requirements/criteria for Core Restraint Systems,” No. HEDL-SA-3211-FP; CONF-8410199-2, Hanford Engineering Development Lab, Richland, WA (1984).

20. Sutton, H. G., and J. A. Rylatt, “Design of the Core Support and Restraint Structures for FFTF and CRBRP” Technical report, Westinghouse Handford Company, 244 Bibliographie (1977).

21. “Koch: Remembering the EBR-I”, Nuclear News, p30-35, November (2001).

22. B. Fontaine, G. Prulhière, A. Vasile, P. Masoni, P. Barret, D. Rochwerger, J. Gros, R. Dupraz, N. Moussallam and M. Chassignet, “Description and Preliminary Results of PHENIX Core Flowering Test,” Nuclear Engineering and Design, **241** (10): 4143-51 (2011).

23. E. R. Shemon, C. H. Lee, M. A. Smith and A. Marin-Lafleche, “NEAMS Neutronics: Development and Validation Status,” *Proc. ICAPP* 2014, Charlotte, North Carolina, April 6-9, 2014.

24. G. A. McLennan, “NUBOW-3D (Inelastic): A FORTRAN Program for the Static Three-Dimensional Structural Analysis of Bowed Reactor Cores Including the Effects of Irradiation Creep and Swelling,” ANL-CT-78-19, Argonne National Laboratory, 1978.

25. T. J. Moran, “Core Restraint Contributions to Radial Expansion Reactivity”, *Proc. of Joint ASME/ANS Nuclear Power Conference*, Ju1y 20-23, 1986, Philadelphia, PA.

26. Perturbation theory. N. N. Bogolyubov, jr., Encyclopedia of Mathematics. URL: http://www.encyclopediaofmath.org/index.php?title=Perturbation_theory&oldid=11676

27. E. P. Wigner, “Effect of Small Perturbations on Pile Period,” Nuclear Energy, Springer Berlin Heidelberg, 540-552 (1992).

28. J. Lewins, “The Time-dependent Importance of Neutrons and Precursors,” Nuclear Science and Engineering, **7** (3): 268-274 (1960).

29. M. Becker, J. Lewins editors, “Sensitivity and Uncertainty Analysis of Reactor Performance Parameters,” Plenum Press, New York (1982).

30. A. Gandini, “Time-Dependent Generalized Perturbation Methods for Burnup Analysis,” RT/FI(75)4, Comitato Nazionale Energia Nucleare, Roma (1975).

31. A. Gandini, “A Generalized Perturbation Method for Bi-Linear Functionals of the Real and Adjoint Neutron Fluxes,” Journal of Nuclear Energy **21** (10): 755-765 (1967).

32. P. J. Finck, “A Technique for Computing the Reactivity Feedback Due to Core-Assembly Bowing in LMFBR’s,” FRA-TM-159, Argonne National Laboratory (1987).

33. K. L. Derstine, “DIF3D: A Code to Solve One-, Two-, and Three-Dimensional Finite-Difference Diffusion Theory Problems,” ANL-82-64, Argonne National Laboratory (1984).

34. M. A. Smith, E. E. Lewis, and E. R. Shemon, “DIF3D-VARIANT 11.0: A Decade of Updates,” ANL/NE-14/1, Argonne National Laboratory (2014).

35. E. W. Larsen, G. c. Pomraning, “Boundary Perturbation Theory,” Nuclear Science and Engineering **77**: 415-425 (1981).

36. F. Rahnema and G. C. Pomraning, “An Anomaly in the Use of Perturbation Theory,” Technical Notes, Nuclear Science and Engineering **78**: 393-437 (1981).

37. G. C. Pomraning, “Perturbation Theory in the Diffusion Approximation,” Nuclear Science and Engineering **83**: 72-74 (1983).
38. F. Rahnema, “Internal Interface Perturbations in Neutron Transport Theory,” Nuclear Science and Engineering **86**: 76-90 (1984).
39. J. A. Favorite, K. C. Bledsoe, “Eigenvalue Sensitivity to System Dimensions,” Annals of Nuclear Energy **37**: 522-528 (2010).
40. J. A. Favorite, “Adjoint-Based Eigenvalue Sensitivity to Geometry Perturbations,” Trans. Am. Nucl. Soc., **102**: 240-243 (2010).
41. J. A. Favorite, “Adjoint-Based Eigenvalue Sensitivity to Geometry Perturbations, and a Warning,” Trans. Am. Nucl. Soc., **103**: 393-395 (2010).
42. S. B. Shikhov. “The Effect of Dimensional Change on the Critical Mass of a Fast Reactor, Calculated by Perturbation Theory,” J. Nucl. Energy. Part A: Reactor Science **11**: 214 -219 (1960).
43. D. E. Cullen. “Mass and Density, Criticality Relationships,” UCRL-ID-143496, Lawrence Livermore National Laboratory (2001).
44. D. E. Cullen. “Mass and Density, Criticality Relationships, Generalized,” UCRL-ID-204988, Lawrence Livermore National Laboratory (2004).
45. J. Kupitz, G. Van Goethem, “Transient and Accident Analysis of BN-800 Type LMFR with Near Zero Void Effect, IAEA-TECDOC-1139, p 15-16, International Atomic Energy Agency (2000).
46. M. Reed, “The ‘Virtual Density’ Principle of Neutronics and Its Application to Perturbation Theory,” Trans. Am. Nucl. Soc., **107**: 997-980 (2012).
47. M. Reed, K. Smith, B. Forget, “The ‘Virtual Density’ Principle of Neutronics: Toward Rapid Computation of Reactivity Effects in Practical Distortion Scenarios,” Proceeding of M & C, p 1151-1164, Sun Valley, ID, 5-9 May (2013).
48. M. Reed, K. Smith and B. Forget, “The Virtual Density Theory of Neutronics: A Generic Method for Geometry Distortion Reactivity Coefficients,” *Proc. PHYSOR 2014*, Kyoto, Japan, Sep. 28 – Oct. 3, 2014.

49. M. Reed, "The '''Virtual Density' Theory of Neutronics" (Ph.D thesis), Massachusetts Institute of Technology, Cambridge, MA (2014).

50. M. Reed, K. Smith, B. Forget, "'Virtual Density' and Traditional Boundary Perturbation Theories: Analytic Equivalence and Numeric Comparison", Annals of Nuclear Energy **112**: 531-548 (2018).

51. M. Reed, K. Smith, B. Forget, "'Virtual Density' Theory of Neutronics", Annals of Nuclear Energy **112**: 549-596 (2018).

52. M. Gentili, B. Fontaine, G. Rimpault, "Deformed Core Reactivity Evaluation with Mesh Projection-based Method," Nuclear Technology **192** (1): 11-24 (2015)

53. M. Gentili, B. Fontaine, G. Rimpault, "Evaluation of SFR Deformed Core Reactivity," Proceedings of ICAPP, Nice (France), May 03-06 (2015).

54. G. M. Greenman, "Calculation of the Reactivity Feedback due to Core-Assembly Bowing in LMFBRs", CONF-831047--67, Argonne National Laboratory (1983).

55. G. M. Greenman, "Calculation of the Reactivity Feedback due to Core Assembly Bowing in LMFBRs", CONF-840901--8, Argonne National Laboratory (1984).

56. E. E. Lewis and W. F. Miller, Jr, "Computational Methods of Neutron Transport," Chapter 1, American Nuclear Society, Inc., La Grange Park, Illinois (1993).

57. G. Palmiotti , E. E. Lewis and C. B. Carrico, "VARIANT : VARIational Anisotropic Nodal Transport for Multidimensional Cartesian and Hexagonal Geometry Calculation," ANL-95/40, Argonne National Laboratory (1995).

58. Y. I. Chang, P. J. Finck, and C. Grandy, "Advanced Burner Test Reactor Preconceptual Design Report," ANL-ABR-1 (ANL-AFCI-173), Nuclear Engineering Division, Argonne National Laboratory, September 5 (2006).

59. T. Goorley, et al., "Initial MCNP6 Release Overview", LA-UR-11-07082, Los Alamos National Laboratory (Dec 2012).

60. M. B. Chadwick, et al., "ENDF/B-VII.0: Next Generation Evaluated Nuclear Data Library for Nuclear Science and Technology," Nuclear Data Sheet, UCRL-JRNL-225066, Oct 6 (2006).

61. W. S. Yang, T. K. Kim, S. J. Kim and C. H. Lee, “Preliminary Validation Studies of Exisiting Neutronics Analysis Tools for Advanced Burner Reactor Design Applications,” ANL-AFCI-186, Argonne National Laboratory. (2007).

62. F. Brown, “ A Review of Best Practices for Monte Carlo Criticality Calculations”, LA-UR-09-03134, Los Alamos National Laboratory. (2009).

63. C. H. Lee and W. S. Yang, “MC^2-3: Multigroup Cross Section Generation Code for Fast Reactor Analysis,” ANL/NE-11-41 Rev.2, Argonne National Laboratory (2013).

64. C. H. Lee and Y. S. Yang, “MC^2-3: Multigroup Cross Section Generation Code for Fast Reactor Analysis,” *Nucl. Sci. Eng*., **187**, 268-290 (2017).

65. R. E. Alcouffe, F. W. Brinkley, D. R. Marr, and R. D. O’Dell, “User’s Guide for TWODANT: A Code Package for Two-Dimensional, Diffusion-Accelerated, Neutral-Particle Transport,” LA-10049-M, Los Alamos National Laboratory (1990).

66. Yeon Sang Jung and Won Sik Yang, “Implementation of 2-D Transport Calculation Capabilities in MC^2-3,” Nuclear Reactor Design Simulation Laboratory, Purdue University, July 14, 2015.

67. E. R. Shemon, M. A. Smith, and C. Lee, “PROTEUS-SN User Manual”. United States, doi:10.2172/1240157, (2016).

68. The HDF Group. Hierarchical Data Format, version 5, URL: http//www.hdfgroup.org/HDF5/. (1997-2014).

69. R. Douglas O’Dell, “Standard Interface Files and Procedures for Reactor Physics Code, Version IV,” LA-6941-MS, Los Alamos Scientific Lab (1977).

70. MATLAB version 9.1.0.441655 (R2016b). Natick, Massachusetts: The MathWorks Inc., 2016.

71. Childs H., Brugger E., Whitlock B. et al, “VisIt: An End-User Tool for Visualizing and Analyzing Very Large Data”, High Performance Visualization-Enabling Extreme-Scale Scientific Insight, Boca Raton, 357-372 (2012).

PUBLICATIONS

Journal papers:

1. T. Jing and W. S. Yang, “Reactivity Feedbacks Due to Core Deformation in Fast Reactors,” in preparation for submitting to *Nuclear Science and Engineering*.
2. T. Jing, G. Yang, Y. S. Jung and W. S. Yang, “Stationary Liquid Fuel Fast Reactor SLFFR – Part I: Core design,” *Nuclear Engineering and Design*, **310**, 484-492, 2016.
3. T. Jing, Y. S. Jung and W. S. Yang, “Stationary Liquid Fuel Fast Reactor SLFFR – Part II: Safety analysis,” *Nuclear Engineering and Design*, **310**, 493-506, 2016.

Conference proceedings:

1. T. Jing and W. S. Yang, “Development of RAINBOW Code to Calculate Reactivity Changes Due to Assembly Bowing in Sodium Fast Reactors,” PHYSOR2018 (accepted), Cancun, Mexico, April 22-26, 2018.
2. T. Jing, W. S. Yang, “A Perturbation Theory Method for Evaluating Reactivity Worth of Assembly Displacements in Fast Reactors,” *Trans. Am. Nucl. Soc.*, 117, 1407–1411, 2017.
3. T. Jing, Y. S. Jung and W. S. Yang, “Passive safety characteristics of Stationary Liquid Fuel Fast Reactor (SLFFR),” *Proc. of PHYSOR2016*, Sun Valley, ID, May 1-5, 2016.
4. T. Jing, G. Yang, Y. S. Jung and W. S. Yang, “An optimized core design of passively safe liquid fuel reactor SLFFR for TRU burning,” *Trans. Am. Nucl. Soc.*, 113, 1095–1098, 2015.

Technical reports:

1. W. S. Yang and T. Jing, “FY 2017 Annual Report – Perturbation Theory Method for Calculating Reactivity Feedbacks Due to Core Deformation,” UM/NRDSL-17/01, University of Michigan, September 30, 2017.
2. W.S. Yang P. Deng, G. Yang, B. K. Jeon, T. Jing and T. K. Kim “FY 2016 Annual Report – Fuel Pin and Duct Wall Heating Calculation Based on Neutron and Gamma Transport Solutions,” PU/NE-16/16, Purdue University, September 30, 2016.

3. W. S. Yang, T. Jing, Y. S. Jung, S. Shi, G. Yang, C. Grandy, A. Borowski, L. Krajtl and T. Jonhnson, “Final Report on Stationary Liquid Fuel Fast,” PU/NE-15/08, Purdue University, September 30, 2015.
4. W.S. Yang, T. Jing, Y. S. Jung, C. Grandy and T. Johnson, “FY 2014 Annual Report on Stationary Liquid Fuel Fast,” PU/NE-14/09, Purdue University, September 30, 2014.